Modern Aspects of Electrochemistry 47

Su-Il Pyun
Jong-Won Lee *Editors*

Progress in Corrosion Science and Engineering II

Springer

MODERN ASPECTS OF ELECTROCHEMISTRY

No. 47

For further volumes:
http://www.springer.com/series/6251

Modern Aspects of Electrochemistry

Topics in Number 45 include:

- The cathodic reduction of nitrate and electrochemical membrane technology
- Non-haloaluminate ionic liquids
- The properties of nanowires composed of metals and semiconductors.
- Ammonium electrolysis as a renewable source of fuel
- The usefulness of synchrotron x-ray scattering to a wide range of electrode phenomena

Topics in Number 46 include:

- Structure, passivation and localized corrosion of metal surfaces.
- Anodic oxide films on aluminum: their significance for corrosion protection and micro- and nano- technologies.
- Electrochemical, microscopic and surface analytical studies of amorphous and nanocrystalline alloys.
- Physicochemical characterization of passive films and corrosion layers by differential admittance and photocurrent spectroscopy.

Su-Il Pyun • Jong-Won Lee
Editors

Progress in Corrosion Science and Engineering II

Springer

Editors
Su-II Pyun
Department of Materials Science
and Engineering
Korea Advanced Institute
of Science and Technology
Daejeon
Republic of Korea
sipyun@kaist.ac.kr

Jong-Won Lee
Fuel Cell Research Center
Korea Institute of Energy
Research
Daejeon
Republic of Korea
jjong277@kier.re.kr

ISSN 0076-9924
ISBN 978-1-4419-5577-7 e-ISBN 978-1-4419-5578-4
DOI 10.1007/978-1-4419-5578-4
Springer New York Dordrecht Heidelberg London

Library of Congress Control Number: 2009934519

Preface

The present volume of Modern Aspects of Electrochemistry is the second in a two-volume set (No. 46 and 47) that covers important technological progress in recent years in the fields of electrochemical corrosion and materials engineering.

The first chapter, by Macdonald, discusses electrochemical and corrosion phenomena of metals and alloys in supercritical aqueous media. The author reviews the corrosiveness of supercritical water oxidation (SCWO) media operating at temperatures up to 650 ^{o}C and at pressures of several hundred bars and the technical issues that need to be resolved for practical use of SCWO technology. The topics include the development of *in-situ* sensors for measuring pH and redox potential and the electrochemical polarization and corrosion studies in SCWO media.

In Chapter 2, Ohtsuka provides an *in-situ* characterization study of passive oxide films on iron and steels using optical techniques. A wide range of optical techniques – including ellipsometry, Raman spectroscopy, potential modulation reflectance and photo-electrochemical technique - are rigorously discussed to make a step further towards understanding what really happens during the passivation process. A comprehensive description is given of the growth mechanism, composition, and semiconducting properties (e.g., energy band gap, flat band potential, donor density, etc.) of the passive oxide films.

Chapter 3, by Oltra and Vuillemin, deals with experimental characterization and theoretical simulation of galvanic coupling phenomena in localized corrosion. The chapter offers a succinct, easy-to-follow introduction to the mathematical formulation of electrochemical reactions problems, followed by extensive coverage of localized galvanic corrosion modeling. The authors present several examples for galvanic corrosion on galvanized steel and aluminum alloys, which indicate the crucial role of current/potential distribution and homogeneous/heterogeneous chemical processes in localized corrosion.

In Chapter 4, Shin and Liu review some recent developments in fabrication of hierarchical 3-dimensional porous structures for energy storage and conversion by an electrochemical deposition process, an area in which electrochemistry and materials science are intertwined. These authors briefly present typical porous structures observed in materials for electrochemical devices, and then discuss the preparation of 3-dimensional electro-deposits with micro-/nano-hierarchical pores that could make the transport of electro-active species easier.

S.-I. Pyun
Korea Advanced Institute of Science and Technology
Daejeon, Republic of Korea

J.-W. Lee
Korea Institute of Energy Research
Daejeon, Republic of Korea

Contents

Chapter 2

PASSIVE OXIDE FILMS ON IRON BY IN-SITU DETECTION OF OPTICAL TECHNIQUES

Toshiaki Ohtsuka

Chapter 3

PROBING AND MODELLING OF GALVANIC COUPLING PHENOMENA IN LOCALIZED CORROSION

Roland Oltra and Bruno Vuillemin

Chapter 4

PREPARATION OF HIERARCHICAL (NANO/MESO/MACRO) POROUS STRUCTURES USING ELECTROCHEMICAL DEPOSITION

Heon-Cheol Shin and Meilin Liu

List of Contributors, MAE 47

Meilin Liu
Center for Innovative Fuel Cell and Battery Technologies,
School of Materials Science and Engineering,
Georgia Institute of Technology,
Atlanta, GA 30332-0245, USA

Digby D. Macdonald
Center for Electrochemical Science and Technology
The Pennsylvania State University
201 Steidle Building
University Park, PA 16802

Toshiaki Ohtsuka
Division of Materials Science, Graduate School of Engineering,
Hokkaido University, Kita13 Nishi 8, Kita-ku, Sapporo 060-8628 Japan
Tel.: +81-11-706-6351
Fax: +81-11-706-6351
E-mail: ohtsuka@eng.hokudai.ac.jp

Roland Oltra
Institut Carnot de Bourgogne, UMR 5209 CNRS - Université de Bourgogne, Electrochimie Interfaciale - Corrosion (EIC/IRM) 9 Av. A. Savary, BP 47 870 F-21078 DIJON Cedex, France
Tel: +33 380 39 61 62
Fax: +33 380 39 61 32
E-mail: roland.oltra@u-bourgogne.fr

Heon-Cheol Shin
School of Materials Science and Engineering, Pusan National University, Geumjeong-Gu, Busan 609-735, Republic of KOREA
Tel.:+82-51-510-3099
Fax: +82-51-514-4457;
E-mail: hcshin@pusan.ac.kr

Bruno Vuillemin
Institut Carnot de Bourgogne, UMR 5209 CNRS - Université de Bourgogne, Electrochimie Interfaciale - Corrosion (EIC/IRM) 9 Av. A. Savary, BP 47 870 F-21078 DIJON Cedex, France
Tel: +33 380 39 61 62
Fax: +33 380 39 61 32

1

Advances in the Study of Electrochemical and Corrosion Phenomena in High Subcritical and in Supercritical Aqueous Solutions

Digby D. Macdonald

Center for Electrochemical Science and Technology, The Pennsylvania State University, 201 Steidle Building, University Park, PA 16802

I. INTRODUCTION

Supercritical Water Oxidation (SCWO) is a promising technology for destroying highly toxic organic waste (including physiological agents) and for reducing the volume of low-level nuclear waste. For example, SCWO has been chosen by the US Army to destroy chemical agents, such as VX hydrolysate (product obtained by hydrolyzing the chemical agent VX with caustic) and a facility for meeting this goal is now operating in Newport, Indiana. However, other chemical agents as listed in Table 1 are scheduled to be treated in a similar manner. Note that the various agents contain sulfur, phosphorous, fluorine, and nitrogen (in the form of cyanide), so that complete oxidation is expected to produce the oxyacids and/or (depending upon the pH) oxyanions of these elements. The US Navy has also explored SCWO for destroying shipboard waste, including oils and greases, solvents, and paints. Various

S.-I. Pyun and J.-W. Lee (eds.), *Progress in Corrosion Science and Engineering II*, Modern Aspects of Electrochemistry 47, DOI 10.1007/978-1-4419-5578-4_1,

Table 1
The Composition and Nomenclature for Several Chemical Agents. Reprinted from Ref. 1, Copyright (2008) with permission from ___

Agent	Composition
VX	O-ethyl S-diisopropylamino-methyl methylphosphonothiolate
GF	Cyclohexyl methylphosphonofluoridate
GB (Sarin)	Isopropyl methylphosphonofluoridate
HD (Mustard)	Bis-2-(chloroethyl)sulfide
GD (Soman)	Pinacolylmethyl-phosphonofluoridate
GA (Tabun)	O-ethyldimethyl-amidophosphorylcyanide

pilot plant commercial facilities have been built in the United States, Europe, and Japan with the goal of demonstrating the efficacy of the method for destroying resilient organic waste. A variant of SCWO that operates under less severe conditions has been developed by SRI International in the form of Assisted Hydrothermal Oxidation (AHO). This technology is now offered on a commercial basis by Mitsubishi Heavy Industries, who operate a commercial pilot plant in Nagasaki, Japan. Given the increasing sensitivity of regulatory agencies and the general public to toxic waste, there is little doubt that the commercial and governmental application of SCWO will expand rapidly in the foreseeable future.

SCWO is accomplished at elevated temperatures (up to 650^{o}C) and pressures (in excess of 300 MPa) in a pressure vessel manufactured from a corrosion resistant material. A typical design of a SCWO system is shown schematically in Fig. 1. Typically, high nickel base alloys, such as Inconel 625, Alloy C-22, and Alloy 59 have been used with generally less-than-satisfactory results, because of the high corrosion rates that are encountered. The corrosion rates of the nickel base alloys were sufficiently high in the Newport, Indiana facility, which is being used to destroy VX hydrolysate, that a platinum liner was employed, necessitating the borrowing of platinum from the strategic reserve. However, even platinum exhibited significant material loss, which was attributed to the formation of PtO_2 under the highly oxidizing conditions present. The loss is postulated to be due to volatilization, rather than corrosion, because of the high vapor pressure of PtO_2 at 650^{o}C.

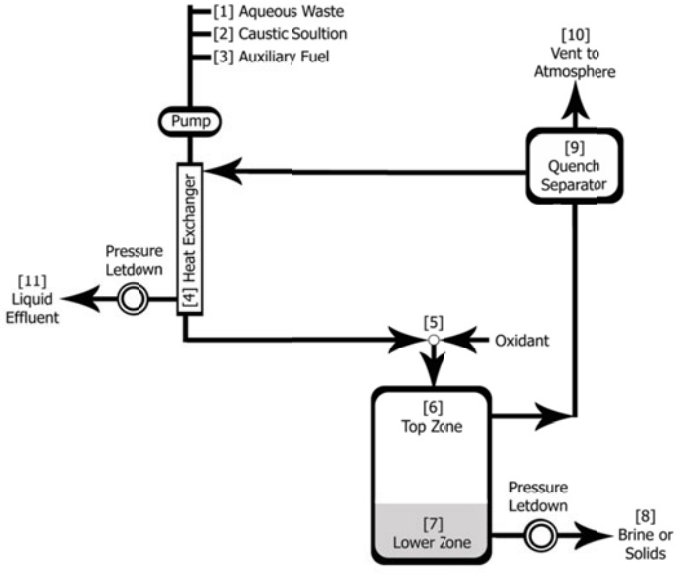

Figure 1. Schematic representation of a vertical down flow SCWO reactor. Reprinted from Ref. 1, Copyright (2008) with permission from NACE International.

In this system, the waste [1] along with caustic [2] are injected into the system as indicated in the figure. Initially, an auxiliary fuel [3], such as kerosene, is also injected to initiate combustion of the waste and the mixture is heat exchanged [4] with the outlet of the reactor after quench separation of reaction products. The mixture is then combined with an oxidant (air, oxygen, or hydrogen peroxide) [5] and is then injected into the top of the reactor, where combustion takes place. The temperature in the top of the reactor is of the order of 650°C. Separation of salts occurs in the reactor [7], because of the low solubility of salts in the supercritical environment; these salts are removed via the blow-down [8] from the reactor bottom. The fluid effluent exits the top of the reactor, flows

through the quench separator and then through the hot side of the heat exchanger [4], where heat is exchanged with the incoming mixture. Note that the auxiliary fuel is only added initially; the reaction becomes self-sustaining on the organic waste once conditions have stabilized.

Supercritical water (SCW) is also the coolant of choice in supercritical thermal power plants and has been selected as the coolant for one of the Generation IV nuclear power plant technologies (Fig. 2). In the latter application, the high heat capacity, high thermal stability, low cost, ready availability of water in ultrapure form, and wide temperature range of operation has made water the preferred coolant for supercritical nuclear power plants, as well. These applications tend to use *clean* fluids that do not contain salts or other components that might otherwise form precipitates that could foul heat-transfer surfaces or cause corrosion. For example, in supercritical fossil-fueled power plants the coolant is commonly pure water, although some high subcritical systems may contain *pH* and redox control chemicals, such as AVT (e.g., ammonia) and hydrazine (N_2H_4), respectively, with the latter being added to scavenge oxygen. Finally, one should note that water, under supercritical conditions, is Nature's *universal solvent*, being responsible for the dissolution, transport, and deposition of such inert materials as gold and the noble metals in fissured rock deep within the Earth's crust.

In this chapter, some of the chemical and electrochemical properties of high subcritical and supercritical aqueous systems are reviewed. Topics that are addressed include:

(a) the development of in-situ sensors,
(b) the development and functioning of reference electrodes,
(c) measurement of pH,
(d) electrochemical kinetic studies, including the effects of temperature and pressure of the polarization characteristics of metals and alloys, and
(e) corrosion of metals and alloys in supercritical aqueous media, particularly with regard to selection of materials for service in SCWO reactors and SCTPPs.

SCWO offers a number of unique advantages over other waste destruction technologies, such as incineration and pyrolysis (e.g., in plasmas), as previously noted. These advantages include:

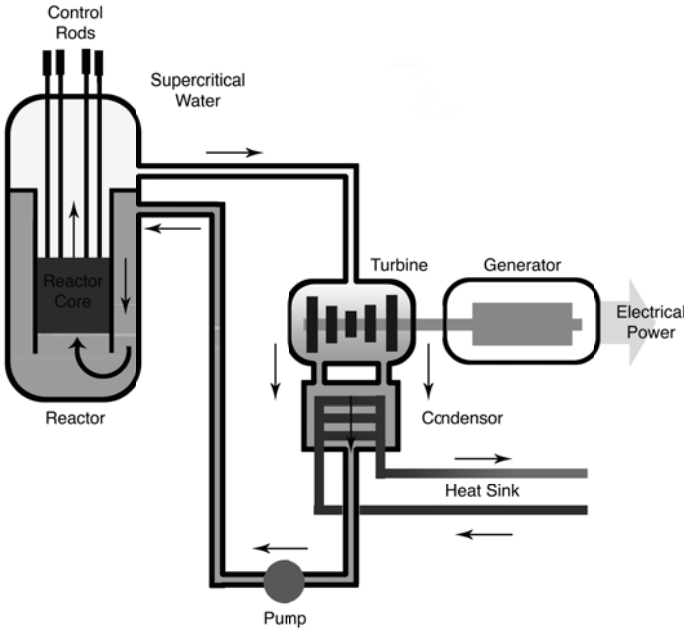

Figure 2. Coolant circuit of a supercritical water nuclear reactor. Note that the entire coolant circuit operates at a temperature above the critical temperature of 374.15°C. Reprinted from http://en.wikipedia. org/wiki/ Supercritical water reactor.

- Zero emissions to the environment.
- Very high destruction efficiencies (> 99.999%), for even the most resilient waste.
- Relatively low cost.
- Remote siting through minimal need for services (electricity, etc.)

Nevertheless, the full and effective implementation of SCWO faces major challenges, depending upon the nature of the waste. Perhaps the greatest challenge is the selection of materials that can withstand the harsh oxidizing conditions that exist in the reactor and in downstream components. Thus, a major problem inhibiting the wide implementation of SCWO is the lack of fundamental knowledge about various physico-chemical and corrosion processes in SCW environments.

II. DEFINITION OF THE ENVIRONMENT

Before any discussion is possible of the interaction of a material with its environment, the properties of the environment must be carefully defined, and the corrosion of metals and alloys in supercritical aqueous systems is no exception. As noted above, the environments employed in SCWO systems can be extraordinarily aggressive, by virtue of the acid produced by the thermal hydrolysis of organic waste, the high operating temperature, and the high redox potential (due to the high partial pressure of oxygen or the high concentration of hydrogen peroxide, which are used as oxidants). In discussing this subject, it is useful to first characterize the environment in terms of the phase behavior of pure water as shown in Fig. 3. Thus, the figure compares the operating conditions for conventional water-cooled reactors (BWRs and PWRs) and the proposed operating conditions for a Generation IV super

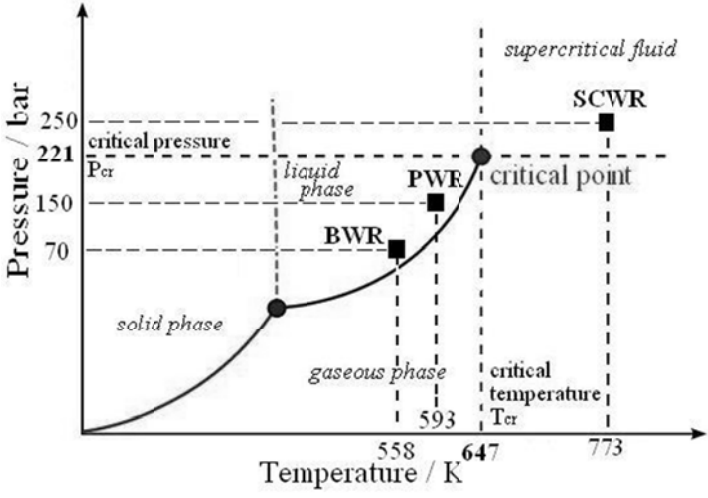

Figure 3. Phase diagram for pure water showing the critical conditions and the conditions of operation of a supercritical water (nuclear) reactor.[2]

critical water (nuclear) reactor. The latter system operates with its entire coolant system at above the critical temperature of water (374.15^{o}C). The advantages that accrue by operating under these conditions include a higher thermodynamic efficiency (45%) compared with a conventional BWR (35%); no boiling, and hence no formation of concentrated solutions on heat transfer surfaces; and a simpler coolant circuit.

It is important to note that at a temperature that is above the critical temperature a liquid phase cannot be produced by increasing the pressure, as can be done at subcritical temperatures by condensation. Instead, supercritical water is best described as being a *fluid*, whose density is a continuous function of pressure (unlike a subcritical system for which the density is a discontinuous function of pressure at the condensation pressure). Supercritical aqueous systems range in their physical characteristics from low density *steam* to dense fluids, depending upon the pressure.

The two most important parameters in defining the chemical and electrochemical properties of any aqueous environment are the potential and pH. The electrochemical potential, which is the potential of an indicator or *working* electrode measured against a suitable reference electrode in the same environment, and preferably expressed on the thermodynamically viable Standard Hydrogen Scale (SHE), provides a measure of the electrochemical driving force of whatever process might be occurring on the indicator electrode surface. If the indicator electrode is inert, the potential is established by various redox couples that exist in the system and it is referred to as the *redox* potential. On the other hand, if the indicator electrode participates electrochemically in the processes that occur on the surface, by being oxidized, for example, the potential is referred to as being the *corrosion* potential. All corrosion and redox potentials are *mixed* potentials that arise from a balance of non-conjugate partial anodic and cathodic reactions (e.g., $Fe \leftrightarrows Fe^{2+} + 2\ e^{-}$ and $H^{+} + e^{-} \leftrightarrows \frac{1}{2}\ H_2$, respectively) on the surface, and hence the system can never be at thermodynamic equilibrium. However, if only a single redox couple exists in the system (e.g., $H^{+} + e^{-} \leftrightarrows \frac{1}{2}\ H_2$) the redox potential is an equilibrium potential, with the value of the potential being determined by the activity of H^{+} and the fugacity of H_2 in accordance with the Nernst equation. If more than one redox couples exists simultaneously in the system (e.g., $H^{+} + e^{-} \leftrightarrows \frac{1}{2}\ H_2$ and $O_2 + 4\ H^{+} + 4\ e^{-} \rightarrow 2\ H_2O$) and the ex-

change current densities are sufficiently high, the measured potential is, again, a mixed potential and not an equilibrium potential, except in the trivial case where the two redox reactions have come to equilibrium with the concentrations of H_2 and O_2 being related by the equilibrium $H_2O \rightarrow H_2 + ½\ O_2$.

Potential-pH (Pourbaix) diagrams for iron and nickel in aqueous solutions above the critical temperature of water are shown in Figs. 4A and 4B, respectively.[3,4] The lack of detail, compared to their ambient temperature counterparts,[5] reflects the lack of thermodynamic data for species at supercritical temperatures, particularly for hydrolyzed ionic species, and the lack of stability of dissolved ionic species in the low dielectric constant supercritical medium.

The diagram in Fig. 4A was constructed for iron for a temperature of 400°C and for a pressure of 500 bar, and for reference the approximate region in potential-pH space for the operation of supercritical water oxidation (SCWO) reactors, without pH neutralization, and supercritical thermal power plants (SCTPPs) are also shown. The dotted lines (a) and (b) correspond to the equilibrium conditions for the H_2/H_2O and O_2/H_2O reactions, respectively, both corresponding to unit gas fugacity. The other lines correspond to Fe/Fe^{2+} (line 1), Fe/Fe_3O_4 (line 3), Fe/Fe_3O_4 (line 13), Fe_3O_4/Fe_2O_3 (line 12), Fe^{2+}/Fe_3O_4 (line 14), and Fe^{2+}/Fe_2O_3 (line 10). Note that no stability regions appear for Fe^{3+} and $HFeO_2^-$; the thermodynamic data indicate that these ionic species are so unstable at temperatures above the critical temperature that they can be ignored in the present analysis. Note also the extensions of lines 12 and 13 into the Fe^{2+} stability field; these extensions define the conditions for the formation of Fe_3O_4 and Fe_2O_3 as metastable phases (potentials above lines 13 and 12, respectively), which are responsible for any passivity that iron might exhibit in SCWO environments.

The diagram for nickel (Fig. 4B), constructed for a temperature of 450°C and a pressure of 500 bar is deceptively simple, primarily because of a lack of thermodynamic data for hydrolyzed cationic species under the conditions of interest. Furthermore, at the temperature of interest (450°C), the hydroxide, $Ni(OH)_2$, is not thermodynamically stable, so that only the oxide (NiO) is considered in constructing the diagram. No data could be found for other compounds in the Ni-O system (e.g., Ni_3O_4, Ni_2O_3, NiO_2), nor could data be found for possible anionic species (e.g., NiO_2^{2-}).

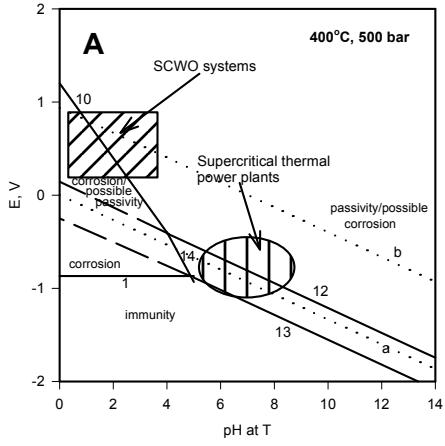

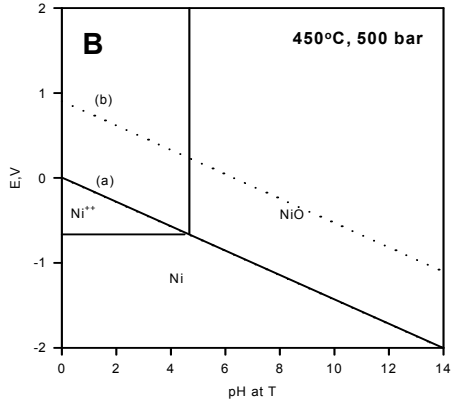

Figure 4. Potential-pH diagram for iron (A) and nickel (B) in supercritical aqueous solutions at 400°C and 450°C, respectively, P = 500 bar. The hydrogen equilibrium line for unit hydrogen fugacity is coincident with the Ni/NiO equilibrium line. The diagram for iron shows the approximate regions in potential-pH space for the operation of SCWO reactors and supercritical thermal power plants (SCTPPs). Reprinted from Ref. 5, Copyright (1997) with permission from Elsevier.

Accordingly, these species have been omitted from the diagram. Nevertheless, the diagram for nickel shown in Fig. 4B provides some important information on the corrosion properties of this metal, which forms the base of many of the corrosion-resistant alloys that are used in SCWO service (e.g., Alloys C-276 and C-22). Note that the extrapolation of the equilibrium line for Ni/NiO into the Ni^{2+} stability field defines the conditions for the formation of metastable NiO, in the same way as that described above for iron.

The first important feature to note is that the pH of neutral water ($pH = pK_w/2$) under the conditions of interest is calculated to be 6.87 (molal scale) or 7.27 (molar scale), where the two scales are related approximately by pH(molar scale) ≈ pH(molal scale) – log(ρ), where ρ is the density. The approximate sign arises from the fact that the *pH* on the molal and molar scales is defined as $-\log(\gamma_{\pm} m_{H+})$ and $-\log(y_{\pm} c)$, respectively, where m and c are the molal and molar concentrations and $\gamma_{\pm}$. and $y_{\pm}$ are the corresponding mean activity coefficients. The activity coefficients have slightly different values when calculated for the two scales. At the low end of the pH scale, incomplete acid dissociation plays a major role in determining the acidity of the system (see later). This is illustrated in Fig. 5, in which is plotted the pH and $-\log(m_{HCl})$ against $\log(m^o_{HCl})$, where m^o_{HCl} is the stoichiometric HCl concentration in the solution. The important point is that as m^o_{HCl} increases the pH does not change in a proportionate manner, because of the lower degree of dissociation of HCl at a higher m^o_{HCl}. Thus, HCl, which is no longer a strong acid under the conditions of interest ($T > 374.15^oC$, $P < 1000$ bar), effectively buffers the pH.

With regards to the potential-pH diagrams shown in Fig. 4, incomplete dissociation implies that the pH will not decrease in a logarithmic manner with increasing stoichiometric HCl concentration, m^o_{HCl}, particularly at low density. This situation parallels that encountered in developing potential-pH diagrams for metals in concentrated alkali metal hydroxide solutions, where it was found that plotting the potential against $\log(m^o_{HCl})$ offered some advantages over the classical form.[6]

Finally, examination of Fig. 4A shows that SCWO systems generally operate under much more aggressive conditions than do SCTPPs, with respect to both potential and pH. Indeed, because most SCWO systems operate at very high redox potential (high

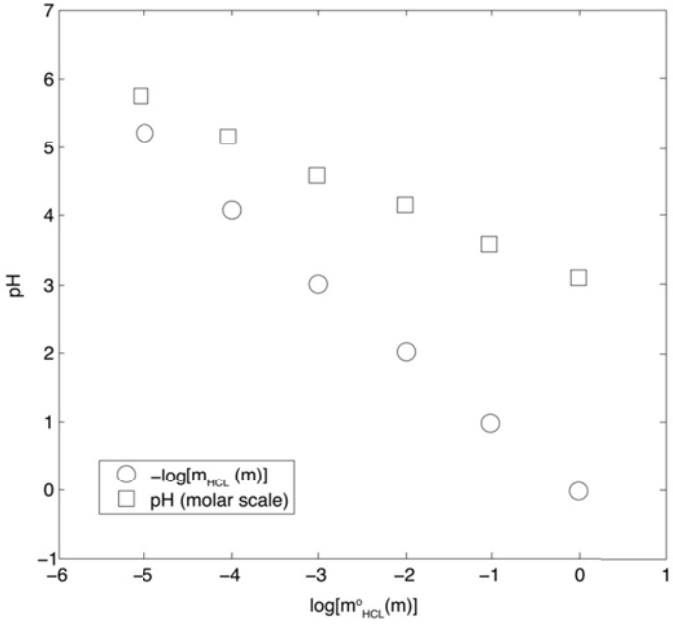

Figure 5. Plot of pH (molar scale) and –log[$m_{HCl(m)}$] versus log of the stoichiometric HCl concentration. If HCl was completely dissociated, the pH should be nearly coincident with –log[$m^{o}_{HCl(m)}$]. Reprinted from Ref. 11, Copyright (1998) with permission from NACE.

p_{O_2} or [H_2O_2]), the potential generally lies toward the upper boundary of the shaded box. On the other hand, SCTPPs commonly employ low oxygen levels, or even reducing agents, such as hydrazine or ammonia, and the potential is estimated to lie within the lower half of the oval. In the SCWO case, even if the pH is increased by neutralization (e.g., by the addition of caustic), the potential is so high that intense attack occurs on structural materials, due to passivity breakdown.

1. Properties

Most properties of liquid (subcritical) water, including density, viscosity, and dielectric constant change gradually with increasing temperature up to about 300°C. With increasing temperature above that value, the properties begin to change much more rapidly and once the critical temperature (T_c = 374.15°C) is reached some properties (e.g. heat capacity and compressibility) exhibit singularities (i.e., their values go to infinity at T_c). For our present purposes, we are mostly interested in the density, dielectric constant, and viscosity, because these properties determine, to a great extent, the tendency of acids and bases to ionize as well as determining solubility, phase behavior, and the rate of mass transport of reactants to a metal surface.[3]

In order to illustrate how these properties change at supercritical temperatures, we show in Figs. 6 to 8 plots of density, dielec-

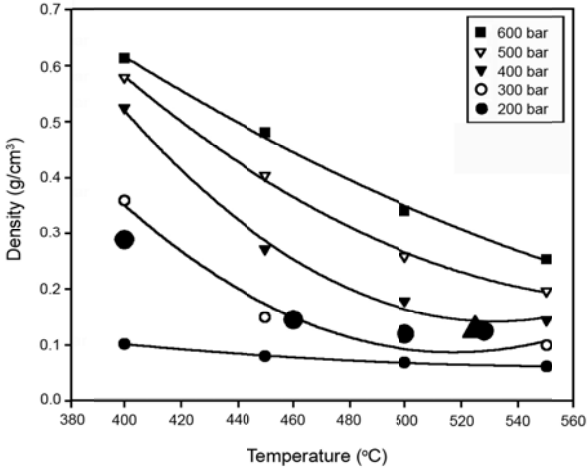

Figure 6. Plots of density versus temperature for supercritical water as a function of pressure. The conditions employed in the experimental determination of pH for 0.01 M HCl solution are indicated by the large filled circles. Reprinted from Ref. 5, Copyright (1997) with permission from Elsevier.

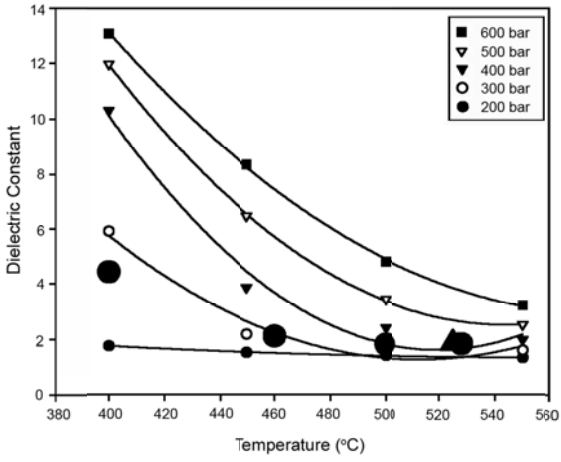

Figure 7. Plots of dielectric constant versus temperature for supercritical water as a function of pressure. The conditions employed in the experimental determination of pH for 0.01 m HCl solution are indicated by the large filled circles. Reprinted from Ref. 5, Copyright (1997) with permission from Elsevier.

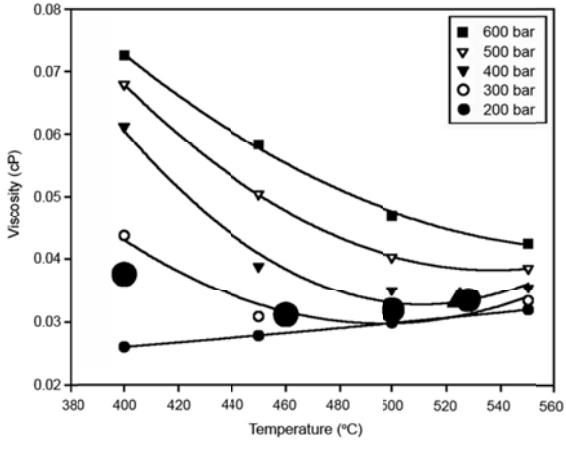

Figure 8. Plots of viscosity versus temperature for supercritical water as a function of pressure. The conditions employed in the experimental determination of pH for the 0.01 m HCl calibrating solutions are indicated by the large filled circles, whereas those for the CCl_4 solution are depicted by the filled triangle (see later). Reprinted from Ref. 5, Copyright (1997) with permission of Elsevier.

tric constant, and viscosity, respectively, as functions of temperature and pressure.[3] As a point of comparison, nitrogen gas at 25°C and at a pressure of 100 atm has a density of about 0.1 g/cm^3, which is comparable to that exhibited by supercritical water at 500°C and at a pressure of 300 atm (Fig. 6). Accordingly, as far as the volumetric properties are concerned, SCW, under conditions that are characteristic of SCWO systems, is best described as being a *dense gas*, rather than a *liquid* as we know water to be under ambient conditions.

The dielectric constant, which determines the extent to which ions are stabilized electrostatically in condensed media, also decreases strongly with increasing temperature and decreasing pressure (density) under supercritical conditions, as shown in Fig. 7. Indeed, the dielectric constant decreases to values that are typical of non-polar solvents, such as hexane (a hydrocarbon). The principal consequence of this drop in the dielectric constant is that electrolytes (e.g., HCl, NaCl, NaOH) that are essentially fully ionized in water at ambient temperature and pressure (where the dielectric constant is ~78) are very poorly ionized under supercritical conditions. This is a most important point, because supercritical aqueous systems begin to acquire *gas-like* properties as the temperature increases above T_c and the density decreases. Accordingly, in many respects, supercritical aqueous systems may be described as representing the interface between the *liquid* phase and the *gas* phase in many properties, including corrosion. However, it is still possible to perform electrochemical measurements in this low density, poorly ionizing environment, as shown by the filled circles and triangle that correspond to the conditions at which potentiometric pH measurements have been performed (see below).

The transport properties of a medium determine that rate at which corrodents (e.g., O_2, H^+ and HCl) are transferred to a metal surface, and hence determine the maximum rate at which a reaction can proceed. To a good approximation, the transport properties can be described by a Walden-type equation:

$$D\eta = \text{constant} \tag{1}$$

where D is the diffusivity of the species of interest (e.g., O_2) and η is the dynamic viscosity of the medium. The importance of Eq. (1)

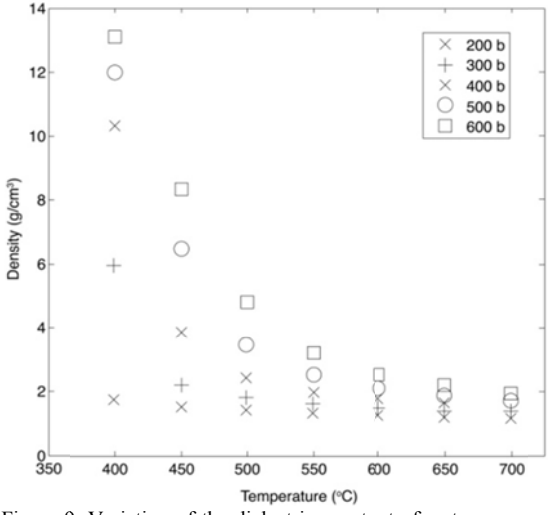

Figure 9. Variation of the dielectric constant of water over extended ranges in temperature and pressure, with temperature being the primary independent variable. Reprinted from Ref. 11, Copyright (1998) with permission of NACE International.

is *not* that it indicates a relationship between diffusivity and viscosity, but that it indicates an *inverse* relationship. Thus, as the viscosity drops (and it does so precipitously as the temperature exceeds T_c, Fig. 8), there is a correspondingly large increase in species diffusivity and hence mass transport controlled reaction rate.

Above the critical temperature, temperature and pressure are independent variables, as dictated by Gibbs' phase rule. Accordingly, any discussion of the properties of supercritical media (aqueous systems included) must include examination of the pressure dependencies over extended ranges of temperature and pressure. Figures 9 and 10 show plots of the dielectric constant of water as a function of temperature and pressure, respectively, as the primary independent variables extend to values that are characteristic of SCWO systems (T = 650°C, P = 300 bar) in the highest temperature operating zone.[3] These plots show that not only does the dielectric constant decrease to a very low value, but it becomes essentially independent of T and P. Accordingly, the solubility of

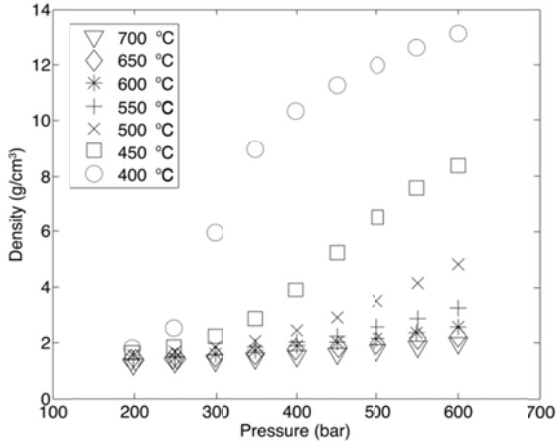

Figure 10. Variation of the dielectric constant of water over extended ranges in temperature and pressure, with pressure being the primary independent variable. Reprinted from Ref. 11, Copyright (1998) with permission of NACE international.

salts (e.g., NaCl, Na_2CO_3, and NaOH) are expected to be low and relatively independent of the conditions that exist within the high temperature reaction zone of a SCEO reactor (Fig. 1), with the consequence that salt deposition occurs more-or-less uniformly in this region. As the temperature decreases towards the exit of the reactor, the dielectric constant and salt solubility, progressively increase, giving rise to a zone where deposited salts redissolve into solution. To a large extent, these simple relationships dominate the dynamics of salt deposition and release from the reaction zone in a SCWO reactor.

Because of the non-polar properties of supercritical water, salts display low solubility and are readily precipitated as solid phases when supercritical conditions are achieved; this is in contrast with the majority of non-polar gas-water and water-organic systems, in which the components are fully miscible under comparable conditions. Depending on whether critical behavior is observed in saturated solutions, salt-water systems are consequently classified into two types.[7] Type 1 systems exhibit high salt solubility in the vicinity of the critical temperature of water, whereas

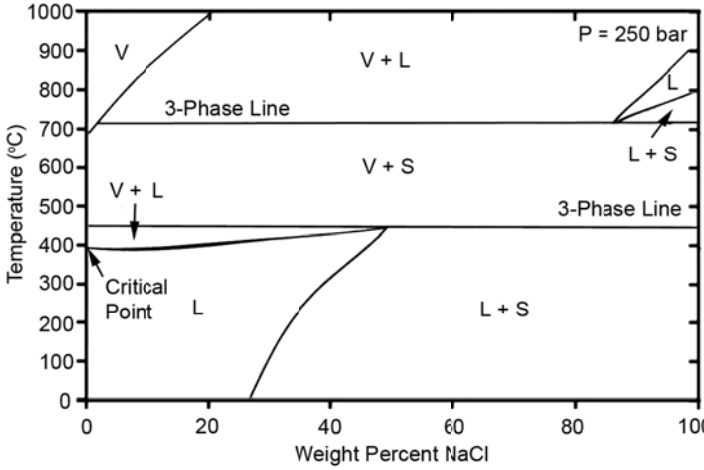

Figure 11. Temperature-composition phase diagram for NaCl-H_2O at 250 bar. Reprinted from Ref. 8, Copyright (2004) with permission from Elsevier.

Type 2 systems have low salt solubility. Classical examples of Type 1 and 2 are NaCl-H_2O and Na_2SO_4-H_2O system, respectively (Figs. 8 and 9).[8] There are several interesting features in Fig. 11; two lines of S-L-V (solid-liquid-vapor) equilibrium (solidus) exist at 450°C and 720°C between which there is no liquid phase present, the critical curves separating the liquid and liquid + vapor phase (L/V + L), and the saturation lines separating the liquid and liquid + solid phase (L/L + S). It is more convenient to select several concentrations to explain the phase changes that occur with increasing temperature. For the 20% (weight percentage) NaCl-H_2O system, starting from the lowest temperature shown in the diagram (Fig. 11), the system maintains a single phase (an unsaturated NaCl solution) until it crosses the critical curve, where it becomes a 2-phase system: a vapor phase (supercritical fluid) and a liquid phase (NaCl saturated solution). After that, as the temperature is increased further, the system moves along the critical curve, with the NaCl concentration in the liquid progressively increasing, until the critical temperature of the saturated liquid is reached. At this point (450°C and ≈ 48 wt% NaCl), a *eutectic-like* reaction occurs in the system with the formation of a *dry salt* and super-

critical water containing a very low concentration of NaCl. For the 40 wt% NaCl case, the system starts as a saturated solution with precipitated solid salt and, as the temperature increases, the NaCl solubility in the liquid solution also increases until the saturation line is met at about 300°C. At higher temperatures, the liquid phase is unsaturated and no solid salt exists in the system. However, at a still higher temperature, the system intersects the critical line resulting in two phases; a supercritical water (*vapor*) phase and a salt solution, as described above. The concentration of the salt solution increases with further increases in temperature until the critical curve intersects the 3-phase line at 450°C, at which point solid NaCl precipitates. Starting at 80 wt% NaCl, the behavior of the system is basically the same as the previous case, except that the solution at subcritical temperatures never becomes unsaturated and a solid NaCl phase always exists in the system. At the temperature of 720°C, another eutectic reaction occurs whence the system produces a supercritical water phase containing a finite concentration of NaCl and a liquid comprising molten salt containing a certain amount of H_2O. Note that water depresses the melting temperature of NaCl. For the Na_2SO_4-H_2O system (Fig. 12), one obvious distinction is the lack of low-temperature intersection of the L+S

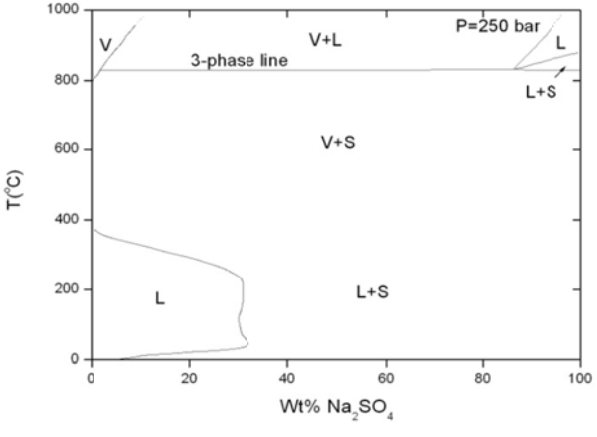

Figure 12. Temperature-composition phase diagram for Na_2SO_4-H_2O at 250 bar. Reprinted from Ref. 8, Copyright (2004) with permission from Elsevier.

saturation line with the S-L-V curve in the phase diagram; instead the saturated fluid displays a continuous transition from liquid-like to gas-like behavior as the temperature increases. Note also the two turning points on the saturation line at the lower part of the diagram; the solubility of Na_2SO_4 begins a slow decrease at the first point ($T \approx 40°C$) and decreases dramatically above the second point (approximately 200°C) until $T = 374.5°C$, where the system is separated into 2 phases: supercritical fluid and solid salt.

It is clear from the above discussion that the phase behavior of supercritical aqueous solutions in a complicated matter, brought on primarily by the decrease in the dielectric constant of water. Unfortunately, as is evident from an examination of the literature, the phase behavior of supercritical aqueous solutions is poorly understood, but an appreciation of that behavior is vital for interpreting corrosion and electrochemical phenomena in supercritical aqueous media.

2. Standardization of pH Scale

As noted previously, the two most important chemical/electrochemical properties of any aqueous system are the pH and the electrochemical (redox or corrosion) potential. The pH is defined as

$$\mathrm{pH} = -\log_{10}(a_{\mathrm{H}^+}) \tag{2}$$

where a_{H^+} is the thermodynamic activity of hydrogen ion, which, in turn, is defined as

$$a_{\mathrm{H}^+} = \gamma\left(\frac{m_{\mathrm{H}^+}}{m^0_{\mathrm{H}^+}}\right) \tag{3}$$

In this latter definition, $m_{\mathrm{H}^+}, m^0_{\mathrm{H}^+}$, and γ are the molal concentration[4] of H^+, the standard state molal concentration of the same species [$m^0_{\mathrm{H}^+}$ = 1 mol/kg(H_2O)], and the activity coefficient for hydrogen ion, respectively. Knowledge of the pH of the solution is

of particular importance for the SCWO process, because the corrosion of structural materials can be attributed to acid attack (H^+ and possibly molecular HCl). While the importance of pH as been long recognized, practical methods of measuring this parameter at temperatures above the critical temperature were lacking until about a decade, or so, ago. At that time, Kriksunov and Macdonald[9,10] significantly extended the temperature and pressure ranges of utilization of the YSZ (Yttria-Stabilized Zirconia) ceramic membrane based *pH* sensors and External Pressure Balanced Reference Electrodes (EPBRE) to include aqueous systems at high subcritical and at supercritical temperatures ($T > 500^oC$). The authors proposed the use of these electrodes for defining the practical pH scale for supercritical aqueous systems, as discussed below. A brief outline of that proposal follows.

A viable pH scale for supercritical aqueous systems must be *practical*, in the sense that it must be accessible via experiment, yet fulfill the theoretical need for an accurate measure of the activity of hydrogen ion in the system. As in the case of systems at ambient temperature and pressure, standardization of the pH scale for supercritical systems is based upon somewhat arbitrary model assumptions and standard solutions. The pH of standard solutions at relatively low temperatures ($T < 100^oC$) is usually assigned by assuming values for the dissociation constants of the electrolytes, by employing model calculations of activity coefficients, and in some cases, by estimating liquid junction potentials (E_{LJ}) of the reference electrodes employed. The pH of any other solution is then determined by measuring the potential (E) of the cell comprising a *pH*-sensitive electrode, which has been calibrated in the standard solution, and a *pH*-independent reference electrode. Because of the paucity of data on possible standard (*buffer*) solutions at temperatures above ca. 300°C, the options that are available for calibrating pH electrodes in high subcritical/supercritical solutions are severely limited, compared with the ambient temperature case.

It is also important to note that pH at ambient temperature is defined thermodynamically as the negative logarithm of the activity of hydrogen ion (a_{H^+}), as noted above. The activity at ambient temperatures is usually based on the molar (mol/L) concentration scale. This volume-based scale is highly inconvenient for supercritical systems, where the volume (density) depends upon temper-

ature and pressure (see above). Accordingly, Kriksunov and Macdonald[10,11] suggested the use of the molal scale (mol/kg H_2O) in *pH* standardization at high subcritical and supercritical temperatures, in which the concentration is independent of T and P.

The unambiguous choice of standard solutions for supercritical aqueous systems is more complicated, in comparison with those for subcritical solutions, because of the poor dissociation of even strong electrolytes in the former, and because of the relatively low activity coefficients. Experimental data for determining those parameters are scarce, and data for estimating the isothermal liquid junction potential for the reference electrode (E_{LJ}) are practically absent (although calculations of E_{LJ} for supercritical aqueous solutions have been reported recently.)[3,11,12] Additional problems arise from the fact that many fundamental properties of high subcritical and supercritical aqueous solutions are strongly pressure-dependent. In this regard, aqueous solutions at the same (supercritical) temperature, but at significantly different pressures, should be considered as being different systems, thereby greatly complicating the specification of pH standards. Large changes in the density, dielectric constant, and the dissociation constant of water (K_w) with pressure, and the pressure-dependence of electrolyte dissociation constants, obviously complicate the specification of pH standards. The complication is even further compounded by the pressure dependence of the potential of the reference electrode, due to pressure dependencies of the thermal liquid junction potential (TLJP) potential (regardless of whether the reference electrode is an *internal* or an *external* pressure balanced type) and the isothermal liquid junction potential (ITLJP).[13]

To overcome these difficulties, a practical pH scale for supercritical systems was defined somewhat arbitrarily,[10,11] based upon available estimates of dissociation constants (K_d) and activity coefficients (γ) for solutions of some common 1-1 electrolytes, such as HCl and NaOH, in much the same way as has been done for aqueous systems at low subcritical systems. The concentration was chosen to be reasonably low, to allow for complete solubility and to yield reliable model estimates for K_d and γ, but at the same time the concentration of the buffering system should be much higher than the concentrations of potential impurities and corrosion products. As a compromise of all of these factors, 0.01 m solutions of HCl and NaOH were proposed as the primary pH standards.[10,11]

In the proposed standardization procedure, we assume that the contribution from the isothermal liquid junction potential (ITLJP) of the reference electrode to the cell potential, due to interfacing the internal reference electrode solution with the external solution, is negligible or has been calculated with sufficient accuracy.[3,12,13] The concentration of hydrogen ion in the HCl solution (m_{H^+}), for example, may be estimated by considering the HCl dissociation reaction,[5]

$$HCl \rightarrow H^+ + Cl^- \tag{4}$$

along with water dissociation

$$H_2O \rightarrow H^+ + OH^- \tag{5}$$

For reactions (2) and (3), we establish the following system of four equations, which include the mass action constants together with the mass balance and charge balance constraints:

$$K_d = \frac{m_{H^+} m_{Cl^-} \gamma_{\pm}^2}{m_{HCl} \gamma_{HCl}} \tag{6}$$

$$K_w = m_{H^+} m_{OH^-} \gamma_{\pm}^2 \tag{7}$$

$$m^0_{HCl} = m_{Cl^-} + m_{HCl} \tag{8}$$

$$m_{H^+} - m_{Cl^-} + m_{OH^-} = 0 \tag{9}$$

Here $\gamma_{\pm}$ is the mean molal activity coefficient, and m^o_{HCl} is the total (stoichiometric) molal concentration of HCl in solution.[14]

Combining Eqs. (6)–(9), and assuming $\gamma_{HCl} = 1$, we obtain,

$$m^3_{H^+} + m^2_{H^+} \frac{K_d}{\gamma^2_{\pm}} - m_{H^+} \left[\frac{K_W}{\gamma^2_{\pm}} + \frac{m^o K_d}{\gamma^2_{\pm}} \right] - \frac{K_d K_W}{\gamma^4_{\pm}} = 0 \tag{10}$$

For sufficiently dilute solutions, the activity coefficients can be estimated using Debye-Hückel theory in extended form,[14] provided that the ionic strength, *I,* is not too high ($I < 0.1$M), which is nearly always the case, because of the very small dissociation constants for electrolytes. Thus, to a good approximation, the activity coefficient is given by[14]

$$\log \gamma_{\pm} = -\frac{z_i^2 A\sqrt{I}}{1 + aB\sqrt{I}} \tag{11}$$

where the ionic strength, I, is defined as $I = 0.5\Sigma C_i z_i^2$; a is the *distance of closest approach* of the ions; and A (the Debye-Hückel limiting slope) and B are constants that depend on density (pressure) and the dielectric constant of the medium; the molal dissociation constant of HCl, K_d, can be obtained from the data of Frantz and Marshall[14] or by using the Supcrt 92 computer program, developed by Johnson et al.[15] Data for the density of water, and for K_W as a function of temperature and pressure (density) were taken from Ref. 16. The Debye-Huckel limiting slopes for the temperature range of interest were estimated by employing the dielectric constant and density of water as given in Ref. 3 and 17. Solution of the system of Eqs. (6) to (11) yields the molal concentration and activity coefficient of hydrogen ion. A similar model was developed for the proposed 0.01m NaOH standard.[3]

With data on the activity of hydrogen ion in the standard solution available from model estimations, relationships between the pH and cell potential, and hence a practical pH scale, for supercritical systems was developed.[10,11] The potential of the cell comprising a pH sensor (yttria stabilized zirconia membrane) and a reference electrode (silver/silver chloride external pressure balanced electrode) ($E_{meas.}$) can be written in the following form:[10,11]

$$E_{meas.} = E_{E.S.P.} - \frac{2.303RT}{F}\left[\mathrm{pH} - \mathrm{pH}_{st.sol.}\right] + \frac{2.303RT}{2F}\log\frac{a_{\mathrm{H_2O}}^{\mathrm{st.sol}}}{a_{\mathrm{H_2O}}} \tag{12}$$

where $E_{E.S.P.}$ represents the effective standard potential, in other words, the potential of the cell measured in the standard solution, $E_{E.S.P.} = m_{meas.}^{st.sol.}\mathrm{pH}_{\mathrm{st}.sol.}$ is the value of the pH in the standard solu-

tion and a_{H2O} is the activity of water. From Eq. (12), the pH for the solution of interest is obtained as

$$\mathrm{pH} = \frac{F}{2.303RT}\left[E_{E.S.P.} - E_{meas.}\right] + \mathrm{pH}_{st.sol.} + \frac{1}{2}\log\frac{a_{\mathrm{H2O}}^{\mathrm{st.sol}}}{a_{\mathrm{H2O}}} \qquad (13)$$

Clearly, an accurate derivation of pH requires knowledge of the activity of water in the test solution as well as in the standard solution.

In summary, the proposed pH standard is based on the concept of a standard solution and effective standard potential of the cell, just as the practical pH scale is defined under ambient conditions. This standard requires only one reference measurement in the standard solution at the temperature and pressure of interest, in exactly the same way as in subcritical systems. However, as is shown below, the fact that temperature and pressure are independent variables over the entire state space in supercritical systems considerably complicates the practical definition of the system for which the pH is measured or calculated.

3. Contribution of the Activity of Water

In order to accurately interpret the results of EMF measurements at supercritical temperatures, it is necessary to estimate the activity of water in the fluid, as noted above, because the activity of water appears in the equation for the electrode potential of the YSZ membrane as:[10,11]

$$E = E_{YSZ}^{o} - \frac{2.303RT}{F}\mathrm{pH} - \frac{2.303RT}{2F}\log\frac{a_{\mathrm{H_2O}}}{a_{\mathrm{H_2O}}^{\mathrm{o}}} \qquad (14)$$

For subcritical systems, the activity of water is simply defined as the ratio of the vapor pressure of water over the solution of interest to the vapor pressure of pure water under identical conditions. However, for supercritical systems this definition is no longer useful or practical, because of the absence of a liquid phase. Instead, for supercritical water systems, which are essentially dense gases, it is more convenient (and descriptive) to use the con-

cept of fugacity instead of activity. Fugacity is essentially pseudo pressure or *corrected* pressure, which permits the use of ideal gas equations for real gases. The relationship between fugacity (*f*) and activity of water is given as

$$\frac{a_{H_2O}}{a^{o}_{H_2O}} = \frac{f}{f^{o}} \tag{15}$$

where superscript "o" indicates a reference or standard state (corresponding to pure water for subcritical systems). There exist several means of estimating the fugacity of a gas. Kriksunov and Macdonald[10,11] used the technique based on determining the difference between the isothermal expansion work functions for ideal and real gases. Thus, the work of isothermal expansion of an ideal gas from pressure P_2 to P_1 can be written as $A_{id}=RTln(P_2/P_1)$. For a real gas, the same work should be written using fugacities (*f*): $A_{re}=RT\ ln(f_2/f_1)$. The difference between A_{id} and A_{re} is the excess expansion work:

$$\Delta A = RT \ln \frac{P_2}{P_1} - RT \ln \frac{f_2}{f_1} = RT \ln \frac{P_2 f_1}{P_1 f_2} \tag{16}$$

We must choose as P_1 a suitably low pressure, such that the real gas behaves practically as an ideal gas. In that case, $P_1 = f_1$ and ΔA becomes:

$$\Delta A = RT \ln \frac{P_2}{f_2} \tag{17}$$

From the last equation, one obtains the fugacity as

$$f_2 = P_2 \exp(-\frac{\Delta A}{RT}) \tag{18}$$

and the fugacity coefficient as:

$$\gamma_2 = \frac{f_2}{P_2} = \exp(-\frac{\Delta A}{RT}) \tag{19}$$

The value of ΔA is then easily estimated as

$$\Delta A = A_{id} - A_{re} = \int_{P_2}^{P_1} V_{id}\,dP - \int_{P_2}^{P_1} V_{re}\,dP = \int_{P_2}^{P_1} (V_{id} - V_{re})\,dP \tag{20}$$

Taking into account that, for one mole of ideal gas, $PV = RT$, we obtain:

$$\Delta A = \int_{P_2}^{P_1} (\frac{RT}{P} - V_{re})\,dP \tag{21}$$

The values of ΔA were estimated for water at supercritical temperatures and at several P_2 over the range 1–1000 bars from Eq. (21) using specific volumes obtained from the ASME Steam Tables.[18] Water vapor at a pressure of 1 bar and at the temperature of interest was chosen as the standard state, but it is emphasized that other standard states are readily defined.

Calculated values for γ_2 are presented in the Fig. 13 as a function of pressure for temperatures of 400 and 500°C. It is clear that the fugacity coefficient drops precipitously at pressures higher than about 100 bars, especially so at low supercritical temperatures. This is due to the increasing impact of molecular interactions in the fluid that tend to make the system less compliant with the ideal gas equation and hence less *ideal*. An increase in temperature, as one would expect, makes the fluid more *ideal*, so that at higher temperatures the fugacity coefficient decreases more slowly with pressure than it does at lower temperatures.

It is emphasized that the activities (fugacity) of water calculated above are for pure water only. In order to obtain activities of water in solutions, it is necessary to employ *PVT* data for corresponding systems. However, for relatively dilute solutions, the effect of the solute upon the properties of the solvent can be neglected and, hence, fugacity data calculated from the properties of

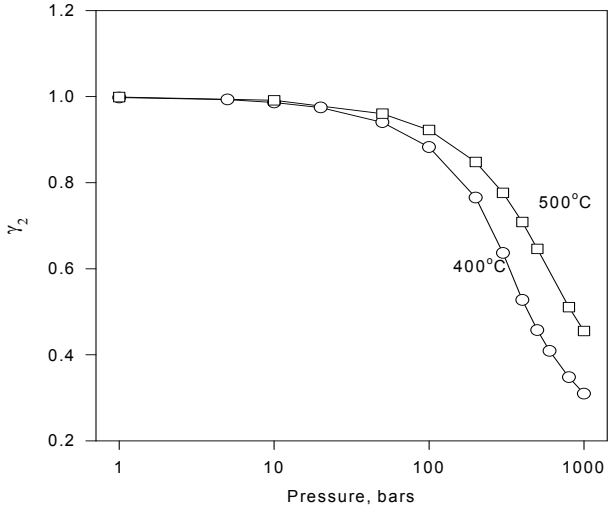

Figure 13. Fugacity coefficient of water as a function of pressure for two supercritical temperatures. Reprinted from Ref. 11, Copyright (1998) with permission from NACE International.

$$\Delta E = \frac{2.303RT}{2F} \log f_{H_2O} \tag{22}$$

pure water may be used to a first approximation for the present application.

The effect of fugacity on cell potential can now be estimated as:[10,11]

Values for ΔE are plotted against pressure in Fig. 14 for temperatures of 400 and 500°C. Note that the effects of pressure are significant. Thus, for a change in pressure from 500 to 1000 bar at 500°C, the effect of the change in fugacity on cell potential would be (0.192 – 0.204) V = –0.012 V. This value may be compared

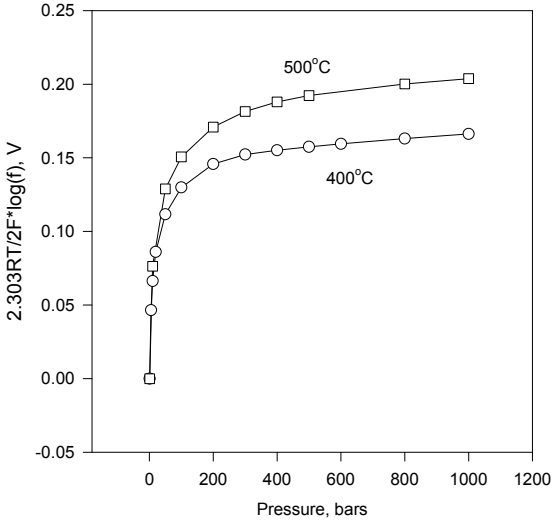

Figure 14. Contribution of water fugacity to the potential of the YSZ pH sensor as a function of pressure for two supercritical temperatures. Reprinted from Ref. 5, Copyright (1997) with permission from Elsevier.

with that of $2.303RT/F = 0.153$ V at 500°C. Accordingly, the fugacity correction is significant (≈ 0.08 pH unit) for highly accurate work, but is probably of little consequence for many technological applications.

III. SENSORS

A principal goal of early work by the author and his colleagues on supercritical aqueous systems was to develop simple, rugged sensors that were capable of measuring pH and redox potential at temperatures up to about 550°C. As discussed earlier in this review, these two parameters are of prime interest, because the hydrothermolysis of organic material produces acid (which may be

neutralized by the addition of sodium hydroxide) and because a typical SCWO reactor utilizes a high partial pressure of oxygen or even additions of hydrogen peroxide. These conditions are necessary, in order to destroy the most resilient wastes. However, they are also the conditions that lead to exceptionally high corrosion rates that render even the most corrosion resistant, nickel-based alloys generally unsuitable for use in SCWO reactors unless protected by a suitable liner. Indeed, even the noble metals, such as platinum, are found to corrode at tens of mils per year in some supercritical aqueous environments.

The key to measuring electrochemical potentials in any environments is the availability of a viable reference electrode and a viable indicator electrode. The generally accepted attributes of a *viable* reference electrode are as follows:

- The potential should be stable and reproducible over extended periods of time.
- The potential should be independent of compositional changes in the system or, at least, the change in the potential should be predictable from the compositional changes.
- The reference potential should be established by an electroactive couple at equilibrium, so that the reference potential may be placed on an accepted thermodynamic scale.

In many cases, only the first two conditions can be fulfilled, with the result that the measured potential of an indicator electrode cannot be placed upon a viable thermodynamic scale (e.g., the Standard Hydrogen Scale, SHE, see below). In this case, the reference electrode is referred to as a *pseudo reference electrode* or PREs, which might be capable of internal calibration against some potential-determining process that occurs at the indicator electrode. PREs have been used extensively in corrosion studies in high subcritical and supercritical aqueous systems, as described below, and are generally serviceable provided that limited accuracy is acceptable.

1. Internal Reference Electrodes

(*i*) *Hydrogen Electrodes*

From the theoretical point of view, the hydrogen electrode is perhaps the most ideal reference electrode for high temperature work. Thus, the Standard Hydrogen Electrode (SHE) has been selected in thermodynamics as the zero of the potential scale and it is the electrode against which the standard potentials of all other half cells are expressed. However, it is important to note that the SHE is a hypothetical construct, in which the activity of H^+ (a_{H^+}) and the fugacity of H_2 (f_{H2}) are both equal to one at the specified temperature and pressure. Although it is possible to devise a practical hydrogen electrode that conforms closely to the SHE, by choosing the appropriate concentration of H^+ and pressure of H_2, such that the activity and fugacity, respectively, are unity, this is seldom, if ever done, because of the ease of relating the potential of a practical hydrogen electrode to the SHE scale (see below) and because of the difficulty in interfacing a gas (hydrogen of precisely controlled pressure) with a high temperature/high pressure aqueous solution. Even so, with appropriate care, the hydrogen electrode has proven to be rugged and reversible, but it can only be used in systems that are stable against reduction by hydrogen. For example, it cannot be used in potentiometric studies of Fe^{3+} hydrolysis, because of the occurrence of the reaction

$$Fe^{3+} + \tfrac{1}{2}\, H_2 \rightarrow Fe^{2+} + H^+ \tag{23}$$

According to the 1960 Stockholm Convention, the half-cell reaction for the hydrogen electrode is expressed as:

$$2\, H^+ + 2\, e^- \leftrightarrows H_2 \tag{24}$$

with the potential being given by the Nernst equation

$$E_{H^+/H_2} = -\frac{2.303RT}{2F}\log(f_{H_2}) - \frac{2.303RT}{F}\mathrm{pH} \tag{25}$$

in which pH = –log(a_{H^+}). The fugacity of hydrogen is related to the molal (mol/kg H_2O) concentration of dissolved hydrogen by Henry's Law as:

$$f_{H_2} = K_{H_2} \cdot \gamma_{H_2} \cdot m_{H_2} \tag{26}$$

where K_{H2} and γ_{H2} are the Henry's constant and activity coefficient for dissolved hydrogen, respectively.

For the hydrogen electrode to be used as a reference electrode, the pH of the medium and the fugacity of the hydrogen must be accurately known. The first condition is readily achieved by employing a well characterized buffer solution, as described above. Suitable buffers are available for temperatures up to ca. 300°C, primarily through the work of the Oak Ridge National Laboratory group, but few are available for use at temperatures up to or above the critical temperature. The few studies that have been performed in supercritical systems have employed HCl and NaOH solutions as pH standards, with the pH values being calculated from dissociation constant data in the literature that were obtained from conductance studies. Note that both electrolytes are poorly dissociated at supercritical temperatures and hence are classified as being a weak acid and a weak base, respectively.[3] Furthermore, the corresponding, fully dissociated salts, which would be required for an effective buffer to be formulated, do not exist. However, in most applications of the hydrogen electrode being used as a reference electrode, the major experimental problem is the accurate measurement of the hydrogen fugacity, as noted above. For instance, a temperature fluctuation of ±1°C at 300°C can easily cause an error in the estimated hydrogen partial pressure of greater than ±1 atm, which will be reflected in an uncertainty in the reference electrode potential of nearly 60 mV (if only the total pressure is known).[18] Although values for the hydrogen fugacity coefficients are well known, it is generally necessary to employ extra-thermodynamic assumptions to estimate the fugacity coefficients in the presence of a high solvent (water) vapor pressure. For example, it is often assumed that partial pressures of the solvent (water) and hydrogen are additive, an assumption that has not been rigorously tested, to the author's knowledge.

The problem of the uncertainty in the hydrogen fugacity was overcome by the development in the early 1970s of the hydrogen concentration cell by Mesmer and Baes[19-23] for high temperature potentiometric studies. Various versions of the high temperature aqueous hydrogen concentration cell were subsequently developed by Mesmer and coworkers,[19-23] Palmer and/or Wesolowski and coworkers[25-31] and Macdonald et al.[32-34] Results using similar cells have also been reported by Shoesmith and Woon,[35] Giasson and Tewari,[36] Matsushima and coworkers[37] and Bilal and Mueller.[38] One classical example of the hydrogen concentration cell is shown in Fig. 15.[33] The cell is formally represented as

$$\mathrm{Pt, H_2/H^+(a_1), KCl \mid H^+(a_2), KCl/H_2, Pt\ (with\ liquid\ junction)} \quad (27)$$

in which the vertical bar depicts the liquid junction, the slash represents a phase boundary, and the comma separates two components in the same phase. The central compartment contains a buffered solution of accurately known pH-temperature characteristics and serves as the reference electrode, while the outer compartment contains the solution under study. The inner and outer compartments are connected via a porous Teflon plug, so that the cell con-

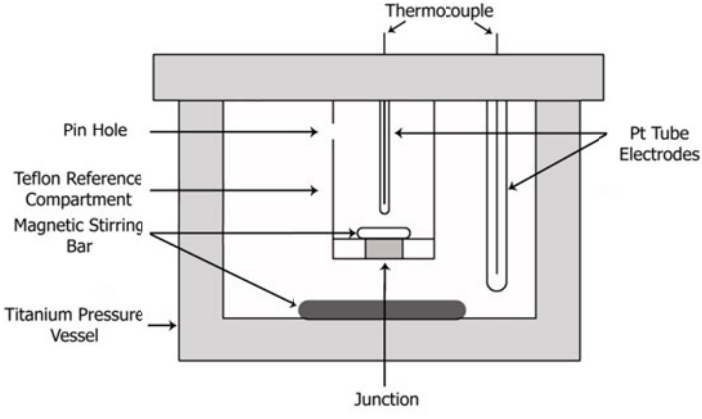

Figure 15. Schematic of a high temperature aqueous hydrogen concentration cell. Reprinted from Ref. 32, Copyright (1973) with permission from Canadian Journal of Chemistry.

tains a liquid junction, as indicated above, with the liquid junction potential being suppressed by using a high background concentration of KCl. Both compartments contain platinized platinum hydrogen electrodes and, during operation, the system is pressurized with hydrogen gas. Since the inner (reference) and outer (test) compartments are connected via a small hole above the liquid surface, the fugacity of hydrogen in both compartments is the same, but does not need to be known accurately, because the terms containing the hydrogen fugacity in the Nernst equation cancel in the expression for the cell potential. Accordingly, the cell potential varies only with the change of the pH of the test solution.

One important variation of the hydrogen concentration cell, the *flowing emf cell,*[23] was developed by Sweeton et al. for studies of volatile reactants. The cell, shown in Fig. 16,[23] comprises of two electrode chambers and a liquid junction chamber. The lateral holes in the bottom of each piece allow solution to come in from each electrode chamber and then flow upwards into grooves cut in

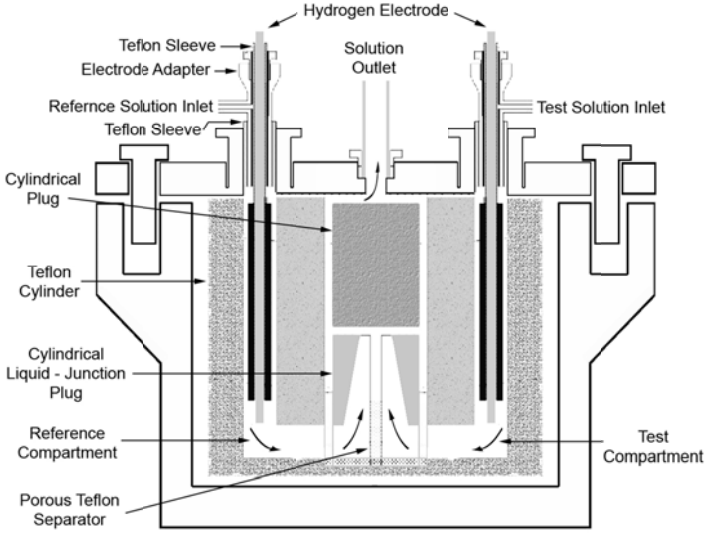

Figure 16. Schematic cross section of flowing hydrogen concentration cell. Reprinted from Ref. 22, Copyright (1973) with permission from J. Physics.

the connecting inside surfaces. The converging solutions are separated mechanically by a Teflon separator inserted between the two half-cylinders (the cylindrical liquid-junction plug). The two flowing streams join before leaving this split plug, then pass along a small groove cut along the outside surface of the upper plug to the outlet. The porous Teflon separator is intended to form and maintain a stable interface and to reduce convection that might result from slight differences in densities of the two solutions and from heat released at the interface by the mixing of the solutions. This emf cell with a flowing liquid junction is capable of operating at pressures to 100 atm and at temperatures up to 300°C.

One application of the cell is the determination of the dissociation quotient for water (Q_W). The cell used for this purpose can be represented as

$$\mathrm{Pt,H_2(m_1)/HCl(m_2),KCl(m_3)|KCl(m_3),KOH(m_2)/H_2(m_1),Pt} \quad (28)$$

The accuracy of the measured results was ± 0.02 in $\log[Q_W]$ at temperatures ranging from 0 to 50°C. When the cell was tested as an HCl concentration cell (using different concentrations, c_1 and c_2, of HCl, instead of HCl and KOH, on both sides, see Eq. 27) with the potential between the electrodes being given as:

$$\Delta E = -\frac{2.303RT}{F}\log(c_2/c_1) + E_{LJ} \quad (29)$$

the measured potential could be used to calculate the concentration ratio of HCl on the two sides. The measured ratios were found to be in good agreement with the true values over the full temperature range of 0 to 300°C.[23]

The hydrogen concentration cell has been used to investigate the dissociation of water in KCl solution, to characterize buffer systems, including boric acid (50–290°C),[21] phosphoric acid (up to 300 °C),[22] and ammonia (50–295°C),[24] to investigate the hydrolysis of Al^{3+} (up to 200°C),[20] to explore the precipitation of boehmite (γ-AlOOH) (200°C),[34] and to measure transport numbers for H^+ and Cl^- in aqueous HCl solutions at temperatures as high as 200°C,[35] among other systems, where the upper temperatures are given in parentheses. One instrumental restriction on the applicable temperature of the cell comes from the use of PTFE, which is

unstable at temperatures above 300°C. Hydrogen concentration cells have proven to be capable of precise in situ pH measurement (with uncertainties of no greater than ±0.01 pH unit), even over long periods of time (up to one month or more).[28] Indeed, it is fair to say that essentially all of the high-precision *pH* measurements at moderate, subcritical temperatures (100–300°C) reported to date has been performed using hydrogen concentration cells of the type first introduced by Mesmer, Sweeton, and Baes more than thirty years ago.

Although the hydrogen concentration cell can provide precise pH measurement at temperatures up to 300°C, and could possibly be used up to T_c, when employing a flowing cell,[23] it has several inherent disadvantages:

(a) It cannot be used in systems that are unstable in the presence of hydrogen;
(b) it requires the use of a buffer solution whose *pH*-temperature characteristics are accurately known, which is difficult to fulfill under high subcritical temperatures and at supercritical temperatures, as noted above; and
(c) a suitably high back ground concentration of an indifferent electrolyte, such as KCl, must be employed to suppress the isothermal liquid junction potential (ILJP) between the reference and test compartments.

Of these three issues, the first two are the most serious, with the first severely limiting the systems that can be studied to those that are stable in the presence of hydrogen, and the second limiting the upper temperature. The third constraint is not a major issue in high subcritical systems, because the transference numbers of the ions of most, if not all, binary electrolytes tend toward 0.5 with increasing temperature; however, at temperatures above the critical temperature the solubility of a salt is severely restricted and it may not be possible to attain a sufficiently high concentration to suppress the liquid junction potential. Note that the isothermal liquid junction is most effectively suppressed if the transference numbers of the cation and the anion of the background electrolyte are equal, a condition that is fulfilled by KCl at ambient temperature (and hence the reason for the choice of KCl in ambient temperature studies).

The hydrogen (reference) electrode has also been used extensively to explore the thermodynamics of the yttria-stabilized zirconia membrane electrode (YSZME) in high subcritical and in supercritical aqueous systems. The use of the YSZME in subcritical systems was first described in 1980 by Niedrach[39] and soon thereafter by Tsuruta and Macdonald,[40] Danielson et al.[41,42] and Bourcier et al.[43] The YSZME with a Cu/CuO internal element was initially used as a reference electrode by Niedrach[40,44-47] for measuring corrosion potentials of stainless steel components in nuclear reactor coolant circuits. The work of Macdonald et al.[41,48-52] and later by Lvov and others[53] concentrated on exploring the thermodynamics of the YSZME, as noted above, because of its utility as a primary pH sensor (i.e., one that does not need to be calibrated). Since these initial studies, the YSZME with a Ag/O_2 internal element has been used to sense acidity in aqueous solutions at temperatures as high as 528°C using an External Pressure Balanced Reference Electrode (EPBRE) based upon the Ag/AgCl, KCl (sat), electroactive element.[54,55] This work is described further below. Regardless of whether the YSZME is employed as a reference electrode (in a medium of known *pH* versus temperature characteristics, as in the initial application by Niedrach)[39,46-47] or as a pH sensor, it is necessary to establish the theoretical response of the electrode in order that the potential can be related to the SHE scale.

For the YSZME electrode employing a Hg/HgO internal element, the half-cell reaction is written as:

$$HgO + 2\,H^+ + 2\,e^- \leftrightarrows Hg + H_2O \tag{30}$$

with the corresponding Nernst equation being:

$$E_{YSZ} = E^0_{Hg/HgO} - \frac{2.303RT}{2F}\log(a_{H_2O}) - \frac{2.303RT}{F}\,pH \tag{31}$$

where $E^0_{Hg/HgO}$ is the standard potential of the Hg/HgO couple and a_{H2O} is the activity of water. By combining Eqs. (25), (26), and (31), we obtain the potential of the cell H_2/H^+, YSZME as:

$$\Delta E = [E^0_{\mathrm{Hg/HgO}} + \frac{2.303RT}{2F}\log(\frac{K_{\mathrm{H}} \cdot \gamma_{\mathrm{H_2}}}{a_{\mathrm{H_2O}}})] + \frac{2.303RT}{2F}\log(m_{\mathrm{H_2}}) \tag{32}$$

The first term of Eq. (32) is a constant for a given temperature, pressure, and ionic strength, so that the cell voltage is linearly related to the logarithm of the dissolved hydrogen concentration. In other words, using the hydrogen electrode as an indicator electrode and the YSZME as the reference electrode, the cell

$$\mathrm{Pt,H_2/H^+(aq.)/ZrO_2(Y_2O_3)/HgO/Hg} \tag{33}$$

may be employed as a hydrogen sensor to obtain the concentration of hydrogen at given temperature and pressure by measuring the potential difference between the two electrodes.[49,52] To test this concept, Ding and Seyfried Jr.[59] used the same electrochemical cell depicted above to measure the fugacity and Henry's constant for hydrogen at supercritical temperatures. At a temperature of 400°C and at a pressure of 400 bar, the measured potential of the cell displays a good Nernstian response to dissolved hydrogen concentration that agrees with the theoretical value. The experiments also demonstrated the excellent stability of the sensor during month-long operation.[57]

Eklund et al.[60] also employed the hydrogen electrode and YSZ electrode to measure Henry's constant for hydrogen in NaOH solutions at temperatures ranging from 25°C to 450°C and at a pressure of 275 bar. The system that they used can be written in the form:

$$\mathrm{Hg/HgO/ZrO_2\,(Y_2O_3)/NaOH\ (aq.)/H_2,\ Pt} \tag{34}$$

The results agreed well with those of Fernandez-Prini and Crovetto[61] for temperatures up to 350°C and with Kishima and Sakai's work[62] for temperatures up to 450°C.

According to Ding and Seyfried Jr.,[63] two problems of the platinum/hydrogen electrode are the poisoning by sulfide ion and the solubility of hydrogen in the metal at elevated temperatures. We regard the first of these concerns to be legitimate, but it is difficult to reconcile the second with thermodynamic principles. Ding and Seyfried Jr.[63] evaluated gold hydrogen-sensing electrodes, as

alternatives to platinum, for the in situ measurement of dissolved hydrogen in supercritical aqueous fluid (temperature: 375–400°C, pressure: 400 bar). With the same cell potential expressed by Eq. (32), at 400°C and 400 bar, the experimental data reveals a slope of 0.0668 ± 0.0027 V (measured potential with respect to logarithm of dissolved H_2 concentration), which is in excellent agreement with the theoretical values of 0.0668 V (from Eq. 32) compared with that for a platinum electrode under the same conditions (0.054 V, see Ref. 57). The present authors consider the latter result to be too far different from the theoretical value that attribution of the difference to the different noble metals employed is not reasonable. Instead, the difference is probably due to experimental error, given the high level of difficulty in performing experiments of this type.

A significant problem with potentiometric measurements in high subcritical and in supercritical aqueous systems is corrosion of the apparatus, which can result in large changes in the pH. This problem was addressed by Lvov, Gao, Zhou, and Macdonald[64-66] by devising flow through reference electrodes (Ag/AgCl and the YSZME) and indicator electrodes (H_2/H^+), such that the incoming solution was never in contact with corrodible metal surfaces. In this way, contamination of the solution could be prevented or at least minimized. Sue et al.[67] subsequently employed this concept by using two identical high-temperature platinum/hydrogen electrodes as the working and reference electrodes (Fig. 17). The cell is depicted as:

$$\text{Cu/Pt, } H_2\text{/Ref. Solution} \mid \text{Test Solution/}H_2\text{, Pt/Cu} \tag{35}$$

$$T_1 \rightarrow |\leftarrow T_2 \rightarrow |\leftarrow T_1$$

in which T_2 is the higher working temperature and T_1 is the ambient reference temperature. The corresponding cell potential is written as

$$E = \frac{1}{F}\left[\mu_{H^+}(L) - \frac{1}{2}\mu_{H_2}(L) + \frac{1}{2}\mu_{H_2}(R) - \mu_{H^+}(R)\right] + \Delta\Phi_{LJ} + \Delta\Phi_{STR}(L) + \Delta\Phi_{STR}(R) \tag{36}$$

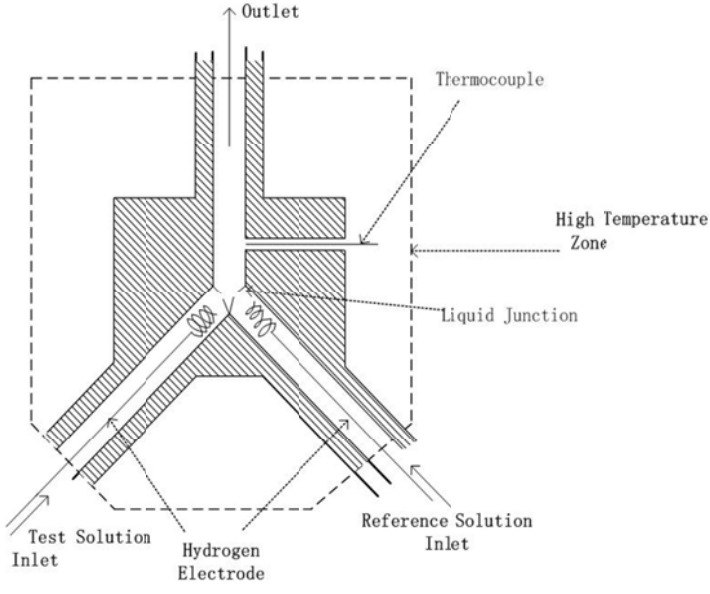

Figure 17. Schematic of flow-through electrochemical cell. Reprinted from Ref. 64, Copyright (1997) with permission from Elsevier.

in which μ_{H+} and μ_{H2} are the chemical potentials of H^+ and H_2, respectively, $\Delta\Phi_{LJ}$ and $\Delta\Phi_{STR}$ are the isothermal liquid junction potential and the steaming potentials, and *L* and *R* designate the left and right side of the cell, respectively. In a manner similar to that previously described by Lvov et al.,[64-66] measurement of the cell potential for Test Solutions 1 and 2 yields the expression:

$$\Delta E_{ap} = \frac{RT}{F} \ln \frac{m_{\mathrm{H}^+,test(2)} \gamma_{\pm,test(2)}}{m_{\mathrm{H}^+,test(1)} \gamma_{\pm,test(1)}} + \Delta\Phi_{LJ} \qquad (37)$$

in which m_{H+} and $\gamma_{\pm}$ are the hydrogen ion molality and the mean ionic activity coefficient, respectively. The mean molal activity coefficient, $\gamma_{\pm}$, can be calculated using extended Debye-Huckel theory and $\Delta\Phi_{LJ}$ can be estimated by using the Henderson equation. They also described procedures to reduce the instability of the

measured potential, including adjustment of the electrode coiled tip lengths, etc., although the exact theoretical basis for the procedures remains obscure. Sue et al.[67] compared the calculated and measured values for ΔE_{ap} and concluded that an accuracy of ±0.02 of a logarithmic (pH) unit was achieved at temperatures from 19.6 to 392.9°C and at pressures from 0.1 to 29.8 MPa. The cell was also used to determine the first dissociation constant of sulfuric acid at temperatures from 375.2 to 399.8°C and at pressures from 28.1 to 32.5 Mpa.[67]

(*ii*) *Silver/Silver Chloride Electrodes*

Silver/silver chloride electrodes have been used extensively as reference electrodes in high temperature electrochemical studies. The first potentiometric measurement of pH at elevated temperatures, at Oak Ridge National Laboratory by Lietzke,[68] employed Pt-H_2 electrodes coupled with Ag/Ag-salt reference electrodes to investigate the thermodynamic properties of HCl and other strong acids in electrolytes to 225°C. Ag/AgCl electrodes are considered to be among the most serviceable electrodes under high temperature conditions, and have been found to perform satisfactorily at temperatures up to 573K (300°C).[19] Thus, the early work of Greeley and Lietzke,[69-70] subsequently reviewed by Macdonald,[18] attests to the utility of the Ag/AgCl electroactive element, in particular.

One of the major problems experienced with all Ag/AgX, X ≡ Cl, Br, I electrodes, when used in hydrogen-rich systems, are the reduction of AgX by hydrogen to metallic silver:

$$AgX + \tfrac{1}{2} H_2 \rightarrow Ag + H^+ + X^- \tag{38}$$

This reaction results in a mixed potential (rather than equilibrium potential) being generated at the electroactive element and in the activity of X^- at the electroactive element varying with time. Further, as noted above, the thermohydrolysis of AgX,

$$2\ AgX + H_2O \rightarrow Ag_2O + 2\ H^+ + 2\ X^- \tag{39}$$

readily occurs at elevated temperatures and the reaction product will also result in a mixed potential. Furthermore, Ag_2O decom-

poses to Ag at temperatures greater than about 160°C,[70] so that the ultimate product of thermohydrolysis is silver metal. Both phenomena preclude true thermodynamic equilibrium, thus the results obtained from Ag/AgCl electrodes under those conditions should be regarded with caution.

Ding and Seyfried Jr.[73] used the silver/silver chloride internal reference electrode in the direct measurement of pH in NaCl-bearing fluids at 400°C and 40 MPa. The electrochemical cell that was employed can be described as:

$$Ag/AgCl/Cl^{-}(aq.),H^{+}(aq.)/ZrO_2(Y_2O_3)/HgO/Hg \qquad (40)$$

with the cell potential being related to the pH of the solution by the equation:

$$\Delta E(V)_{T,p} = \Delta E^0 - \frac{2.303RT}{F}[\log a_{Cl^-} - \frac{1}{2}\log a_{H_2O})] + \frac{2.303RT}{F}\mathrm{pH}_{T,p} \qquad (41)$$

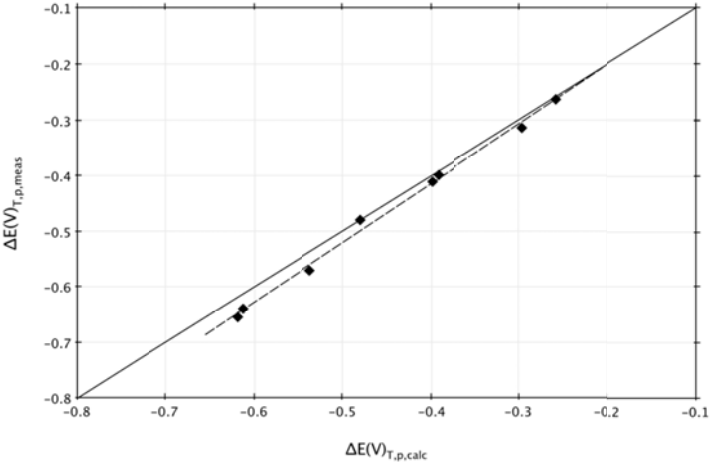

Figure 18. Measured cell potential $\Delta E\ (V)_{T,p,meas}$ versus theoretically predicted cell potential, $\Delta E(V)_{T,p,calc}$, in the aqueous NaCl-HCl system (NaCl 0.57 m) (thermocell $Ag/AgCl/Cl^{-}(aq.),H^{+}(aq.)/ZrO_2(Y_2O_3)/HgO/Hg$, Eq. 40) at 400°C and 40 MPa.[71]

Ding et al.[75] measured the *pH* of concentrated NaCl-HCl fluids (0.57 m NaCl) and compared the results with calculated cell potential data using various thermodynamic databases and codes.[16,72-76] The comparisons are shown in Figs. 18 and 19. The good agreement observed between $\Delta E(V)_{T,p,meas}$ and $\Delta E(V)_{T,p,calc}$ shown in Fig. 18 demonstrates that the cell response is consistent with available thermodynamic data. Furthermore, Fig. 19 shows an excellent linear relationship between $\Delta E(V)_{T,p,meas}$ and $pH_{T,p,calc}$ over the entire range investigated. Importantly, the slope of the regression line is 0.140 ± 0.004 V, which is quite close to the value of 0.134 V predicted from the Nernst equation for a temperature of 400°C.

(*iii*) *Other Internal Reference Electrodes*

Other internal reference electrodes have been devised for use in high subcritical and in supercritical aqueous solutions. For example, Dobson et al.,[81-83] Macdonald and coworkers,[84] and Nagy et

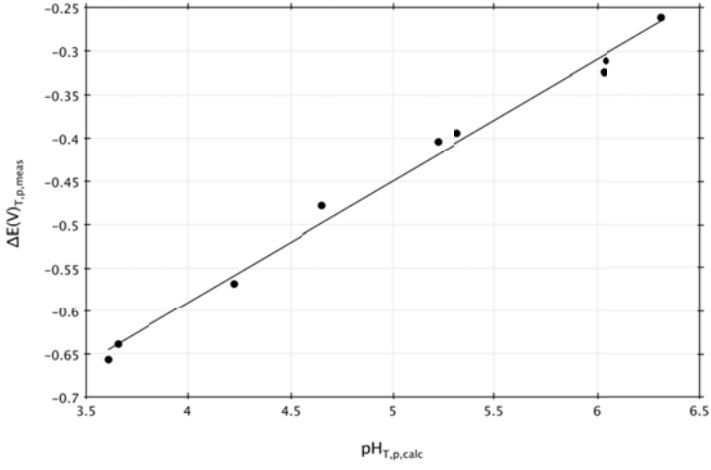

Figure 19. Measured cell potential $\Delta E\ (V)_{T,p,meas}$ against theoretically predicted $pH_{T,p,calc}$ [thermocell $Ag/AgCl/Cl^-(aq.),H^+(aq.)/ZrO_2(Y_2O_3)/HgO/Hg$, Eq. 40] at 400°C and 40 MPa. The buffer solution is NaCl-HCl aqueous system (NaCl 0.57m), with the pH being varied by adding HCl.[71]

al.[85] explored the palladium/hydrogen system as a reference electrode as well as a pH indicator electrode. The work by Dobson[81-83] and Macdonald[84] used palladium wire electrodes that had been cathodically charged into the β region of the Pd-H phase diagram, where solid palladium hydrides are formed. Hydrogen was then allowed to desorb from the lattice and the system passed into the α + β region, where hydrogen in solid solution (the α phase) is in equilibrium with the hydrides. Under these conditions, the activity of H in the lattice is fixed by the Gibbs phase rule, so that the potential due to the reaction

$$H^+ + e^- \leftrightarrows H \tag{42}$$

depends only on the pH and temperature, provided that the composition remains in *the* $\alpha + \beta$ region of the phase diagram for the Pd-H system. Once the composition moves into the α-region, where the activity of H depends on composition, the potential varies with time. Thus, as the potential decays from the cathodically-charged state, it exhibits a plateau over which the activity of H in the lattice is established internally. This removes one of the principal objections to the hydrogen electrode as a reference electrode: the need to accurately control the hydrogen fugacity. However, the Pd-H phase diagram exhibits an upper consolute temperature for the α + β region of the phase diagram of about 275°C.[80,82] At temperatures above this value, the $\alpha + \beta$ region no longer exists, so that the establishment of a fixed activity of H does not occur.

A variant of the Pd-H_2 electrode was explored by Macdonald and coworkers[84] and later by Nagy et al.[85] in the form of a Pd (or Pd-Ag) thimble with a known H_2 pressure on the inside with the external surface being exposed to the solution. Diffusion of hydrogen through the Pd wall establishes a fixed activity of H (or fugacity of H_2) at the outer surface where the potential determining reaction occurs. The electrode potential is stable and the electrode can serve as a viable reference electrode, provided that the pH is known. Again, like the Pd-H_2 electrode, the Pd thimble electrode removes the difficulty with the classical hydrogen electrode of establishing a known hydrogen activity (fugacity) in the system. However, unlike the Pd-H_2 electrode, the maximum temperature of operation is not limited by the thermodynamics of the Pd-H sys-

tem. Of course, these reference electrodes are viable only in systems that are stable in the presence of hydrogen.

Finally, attempts have been reported to develop various solid state electrolyte internal reference electrodes for use in high subcritical and supercritical aqueous systems. Among these was an attempt by Hettiarachchi and Macdonald[86] to develop a solid polymer electrolyte (epoxy + KCl solution, which sets as a rubber) reference electrode containing an Ag/AgCl electroactive element (Fig. 20)[87] and a KCl (aq.)/epoxy electrolyte. The electrode displayed reversible behavior at temperatures as high as 280°C for over 40 hours, but, because the activities of Cl^- in water-containing epoxy are not known, the electrode needs to be calibrated. A variation on this theme was reported by Jayaweera et al.[87] who used a ziconia + alumina + KCl + silica electrolyte, together with an Ag/AgCl electroactive element, as a reference electrode for supercritical systems. The electrode was found to exhibit a constant

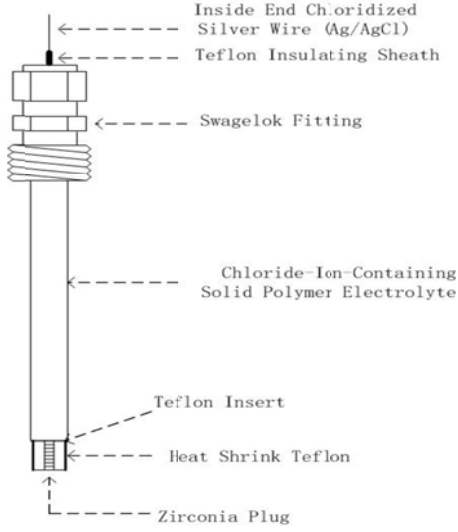

Figure 20. Assembly of an internal polymer electrolyte reference electrode. Reprinted from Ref. 83, Copyright (1973), reproduced by permission of The Electrochemical Society.

potential, but it suffers from the same disadvantage as does the polymer electrolyte reference electrode: the need to calibrate, which requires a primary standard whose potential can be accurately related to the SHE scale.

2. External Reference Electrodes

Because of the harsh working conditions in high subcritical and in supercritical water systems, the stability of electroactive element becomes a major practical and theoretical issue in reference electrode technology. The most frequent problem is the thermal hydrolysis of one or more phases in the electroactive element, such as AgCl in the Ag/AgCl internal reference electrode, as described above. One solution to this problem is to locate the electroactive element at ambient temperature, where thermal hydrolysis does not occur, and connect the element to the high temperature region of the system by a non-isothermal electrolyte bridge. Early variants of this scheme used a non-isothermal bridge together with a compressed porous plug to reduce the pressure to ambient at the electroactive element (Jones and Masterson,[88] Macdonald and Owen,[89] and Macdonald[84]) with only limited success. In this case, two irreversible potentials are created by the junction. The first is the steaming potential due to the non-isobaric junction, which is eliminated by the use of pressure-balanced electrolyte bridges. The second is the thermal diffusion potential, which remains as the main problem of all external pressure-balanced electrodes.

External pressure-balanced reference electrodes (EPBREs) have been developed and evaluated extensively over the past three decades. The first variant was described in 1978 by Macdonald et al.[90] and was patented in the same year, with the invention being assigned to the Electric Power Research Institute. The electrode won the EPRI *Invention-of-the-Year Award* in 1979. The EPBRE that was first evaluated is described thermodynamically as the thermocell:

$$(25°C)\ \mathrm{Ag/AgCl/KCl\ (M)/AgCl/Ag}\ (T°C) \tag{43}$$

in which T was varied from 25 to 275°C and the concentration of KCl was varied from 0.0050 to 0.505 M.[88] An important feature of the original, Macdonald et al.[91] electrode was the reliance of pres-

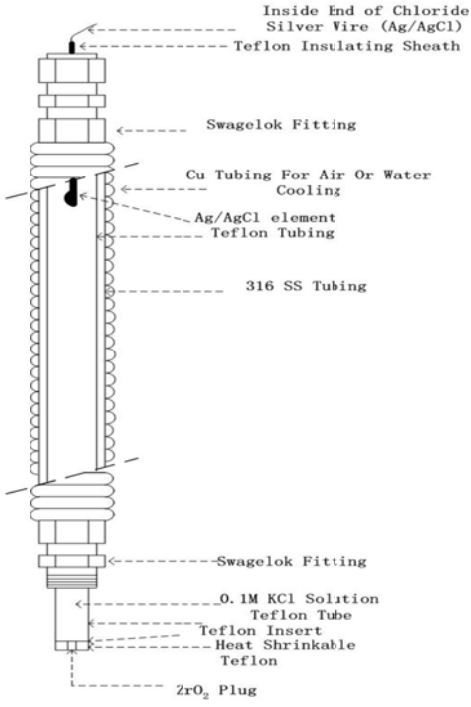

Figure 21. Assembly of an external pressure-balanced reference electrode (EPBRE). Reprinted from Ref. 50, Copyright (1992) with permission from Plenum.

sure pulsations transmitted into the flexible (PTFE) inner compartment from the flow-activating pump, to inhibit the tendency of thermal diffusion to occur and hence to maintain the solution composition uniform and hence to maintain the non-isothermal electrolyte bridge in the Soret initial state (Fig. 21). This was an important, but often ignored, caveat of the operation of an EPBRE. If thermal diffusion occurs, the potential will drift as the electrolyte diffuses toward the cold end of the junction (the tendency predicted by thermal diffusion theory). The theory of thermal diffusion of the electrolyte applies strictly to subcritical systems, where the properties of the system can be described in terms of classical elec-

trolyte theory. No comparable theory has been developed for supercritical aqueous systems, to the author's knowledge. In spite of the theoretical shortcomings, EPBREs have been used extensively in supercritical aqueous systems to demonstrate the thermodynamic viability of YSZMEs[49,52,88] and to measure pH in high subcritical and in supercritical aqueous solutions (using YSZMEs as pH electrodes).[51,84,89,90] In the early 1990s, using an YSZME with a Ag/O_2 internal element and an EPBRE, Kriksunov and Macdonald significantly extended the temperature of direct acidity measurement up to 528°C.[53,55,56] To the author's knowledge, this still represents the highest temperature at which acidity measurements have been made.

The original flow-through technique for reference electrodes was first developed by Danielson in 1983[94] with the purpose of eliminating thermal diffusion by continually refreshing the inner compartment. In this way, the electrolyte in the inner compartment could be maintained in the Soret initial state (i.e., by maintaining a uniform concentration along the non-isothermal bridge). The flow rate was adjusted to be sufficiently high to maintain a uniform concentration, but to be sufficiently low to maintain the temperature gradient along the non-isothermal electrolyte bridge. The original Danielson cell, which was restricted to moderate, subcritical temperatures ($T < 300^oC$), proved to be quite successful, in that the potential remained stable at the expected value over extended periods of time. Later, this same concept was adopted by Lvov et al. (Fig. 22)[65,66] for high subcritical and low supercritical temperatures ($374.15^oC < T < 400^oC$), with the result that highly accurate potentiometric measurements could be made.[65,66,92] This required careful calibration of the reference electrode against a hydrogen electrode in a flow-through system and against theoretical calculation, knowing the pH and the fugacity of hydrogen. In any event, while this type of electrode represents the current state-of-the-art, it is judged to be too difficult to apply in the field and is perhaps too difficult to apply even in the research laboratory (the same problem with the EPBRE). The reference potential was also found to depend on flow rate of the electrolyte through the inner compartment, presumably arising from the streaming potential and possibly also from the modified temperature gradient down the thermal liquid junction. The fact that the potential is flow rate dependent is

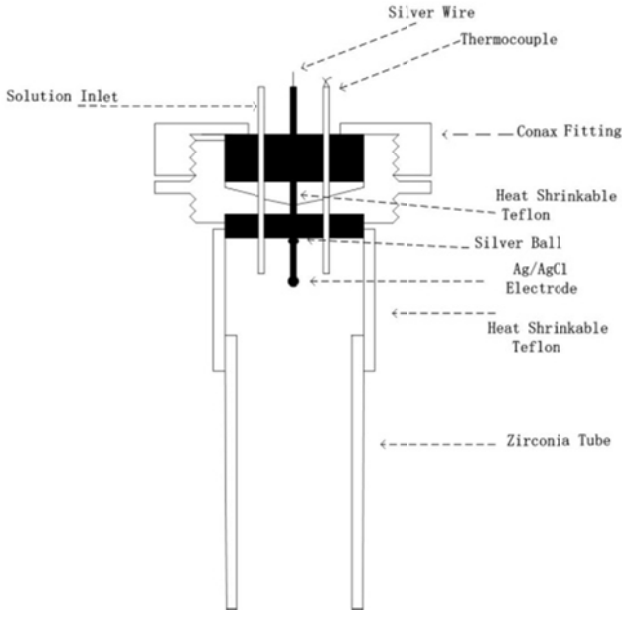

Figure 22. Schematic of the flow-through external pressure-balanced reference electrode (FTEPBRE). Reprinted from Ref. 62, Copyright (1984) with permission from Elsevier.

a significantly complicating factor, because of the need to calibrate the electrode in each system studied.

As noted above, an external pressure-balanced electrode suffers from two irreversible thermodynamic potentials: the isothermal liquid junction potential and the thermal liquid junction potential (thermal diffusion potential). The external pressure balanced reference electrode (EPBRE) is amenable to formal thermodynamic analysis in terms of Thermocell I:[63]

$$|\leftarrow T_1 \rightarrow|\leftarrow T_2 \rightarrow|\leftarrow T_1 \rightarrow|$$

$$\text{Cu/Ag/AgCl/KCl (aq.) | HCl (aq.)/H}_2\text{, Pt/Cu} \qquad (44)$$

The initial voltage (corresponding to the Soret initial state) of the cell is given by (i.e., no concentration gradient):

$$E = -\frac{1}{F}\int_{T_1}^{T_2} \bar{\bar{S}}_{e,\mathrm{Pt}}\, dT + E_{TLJ} + E_D(T_2) + \frac{1}{F}\Big[\mu_{\mathrm{H}^+}(T_2) + \mu_{\mathrm{Cl}^-}(T_1) - \frac{1}{2}\mu_{\mathrm{H}_2}(T_2) - \mu_{\mathrm{AgCl}}(T_1) + \mu_{\mathrm{Ag}}(T_1)\Big] \tag{45}$$

in which $\mu_{H^+}(T_2)$ and $\mu_{H2}(T_2)$ are the chemical potentials of the hydrogen ion and the hydrogen molecule in the high temperature (T_2) region, respectively. The quantities $\mu_{Ag}(T_1)$, $\mu_{AgCl}(T_1)$, and $\mu_{Cl^-}(T_1)$ are the chemical potential of Ag, AgCl, and Cl^- in the low temperature (T_1) zone. The term $\bar{\bar{S}}_{e,Pt}$ is the transported entropy of an electron in the platinum wire. $E_D(T_2)$ and E_{TLJ} are, respectively, the isothermal liquid junction potential and thermal liquid junction potential, which are discussed below.

(*i*) *Isothermal Liquid Junction Potential*

Both internal and external reference electrodes possess an interface between the internal solution and the external environment. This interface is commonly established within a porous junction and is designed to permit electrolytic communication while preventing flow. In any event, the junction gives rise to the isothermal liquid junction potential (ILJP), $E_D(T_2)$, which develops, because some ions diffuse faster than others, thereby generating an electric field that opposes the process. Integration of the electric field across the junction yields the isothermal liquid junction potential. Bard and Faulkner provide a detailed discussion of the thermodynamics of the isothermal liquid junction.[93] For dilute solutions, the potential can be calculated from Henderson's equation. In the case of Thermocell I, the isothermal liquid junction potential is expressed by:

$$E_D(T_2) = \frac{\sum_i \frac{|z_i|u_i}{z_i}(m_i^{\mathrm{HCl}} - m_i^{\mathrm{KCl}})}{\sum_i |z_i|u_i(m_i^{\mathrm{HCl}} - m_i^{\mathrm{KCl}})} \frac{RT_2}{F} \ln \frac{\sum_i |z_i|u_i m_i^{\mathrm{KC}l}}{\sum_i |z_i|u_i m_i^{\mathrm{HCl}}} \tag{46}$$

where u_i and z_i are the mobility of and charge on species i, respectively. The quantities m_i^{KCl} and m_i^{HCl} are the molal concentration of the i^{th} species of the right (HCl) and left (KCl) sides of the junction. The isothermal liquid junction potentials for various $B(OH)_3$/LiOH aqueous systems at a number of temperatures have been calculated by Macdonald[84] and have been used to correct the measured results in Ref. 94.

The Henderson's equation assumes ideal solution behavior, which renders it suitable only for dilute solutions. For more concentrated solutions, Harper has provided an alternative expression.[95] The equation is reckoned to achieve an accuracy of 0.1 mV for a simple junction between two identical electrolytes of different concentrations, and 1–2 mV uncertainty for more complex junctions.

As noted above, the ILJP can be suppressed by employing a high concentration of a binary electrolyte whose ions have similar transference numbers. Traditionally, in ambient temperature studies, KCl has been used for this purpose, because of the near equality of the transference numbers: $t^0_{K+} = 0.491$ and $t^0_{Cl-} = 0.509$ at 25°C. As shown by Macdonald and Owen[34] the transference numbers for H^+ and Cl^- approach equality as the temperature increases toward 200°C, and ionic conductance data indicate that this is a general trend, suggesting that the ILJP issue is of less importance at higher temperatures. However, the trend toward equality of the transference numbers is countered by the larger value of RT/F, so that the effect of temperature on the ILJP is not easily gleaned by inspecting Eq. (46) alone. In the case of supercritical aqueous solutions (SCASs), ion association occurs to such a large extent that, even for solutions of high stoichiometric concentrations, the concentrations of free ions is always quite small, even at high pressure (density). Accordingly, the SCAS case is always dilute and the isothermal liquid junction potential may be adequately estimated using the ideal expression, Eq. (46).

(*ii*) *Thermal Liquid Junction Potentials*

The quantity E_{TLJ} in Eq. (45) is the thermal liquid junction potential, or the *thermal diffusion potential*, which arises from the coupling between heat flow and mass flow (diffusion) in accord-

ance with Curie's Principle in irreversible thermodynamics. In the electrolyte solution, a small, but definite, increase in concentration occurs at the cold end of a non-isothermal electrolyte bridge as the system evolves towards a Soret steady-state. This transport phenomenon is denoted as *thermal diffusion* and is due to coupling between the heat flux from the hot end to the cold end and the ion flux, as noted above. Thermal diffusion in liquid systems was first discovered by Ludwig in 1856, but was examined more closely in 1879–1881 by Soret, and so is now named the *Soret effect.*[96] The state when no obvious thermal diffusion has occurred is designated the *Soret initial state.*[97] Concentration gradients due to the Soret effect lead to the establishment of a diffusion potential and an internal electric field due to the migration of ions. The sum of these two potentials is designated the *thermal diffusion potential*. Thermal diffusion continues until backward, *chemical diffusion* (from the more concentrated cold end to the hot end of the junction) causes the system to attain a steady state. This state is referred to as the *Soret final state.* Attainment of the Soret steady (final) state may take many days or weeks, depending upon the electrolyte, temperature gradient, and the length of the junction. Clearly, it is impractical to operate an EPBRE in the Soret steady state, so that emphasis was originally placed on devising methods for maintaining the system in the Soret initial state (e.g., by transmitting pressure pulses into the inner compartment of an EPBRE, as discussed above). The importance of thermal diffusion in electrochemical cells has been discussed at length by Engelhardt, Lvov, and Macdonald.[101]

In 1979, Macdonald et al.[102] successfully measured the initial thermal liquid junction potential of the thermal cell

$$(298.15\text{K})\text{Ag/AgCl/KCl(aq.)/AgCl/Ag}(T) \qquad (47)$$

in which the temperature of the hot end of the cell (T) was varied from 298.15 K (25°C) to 548.15 K (275°C) and the KCl concentration was varied from 0.005 to 0.505 m. Macdonald et al. calculated the Nernstian thermal cell potential by employing Gibbs energies of formation for the cell components based upon an absolute, 298.15 K, standard state. The difference between the Nernstian potential and the observed potential (Fig. 23) is the initial state thermal liquid junction potential (Fig. 24). The thermal liquid junc-

tion potential was found to increase in a parabolic manner with the temperature difference between T and 298.15 K (in Ref. 100), E_{TLJ} is represented as a cubic equation in ΔT, the temperature difference between the hot and cold ends of the cell). Another important feature of the measured thermal liquid junction potential is that it is only weakly dependent on concentration. Other studies on measuring or calculating thermal liquid junction potentials are described in Refs. 81 and 100.

Lvov and Macdonald[100] attempted to calculate the TLJP of Thermal Cell I from fundamental theory using the general expression for the potential as given by:

$$E_{TLJ} = -\frac{1}{F}\int_{T_1}^{T_2}\sum_i \frac{t_i S_i^*}{z_i} dT \tag{48}$$

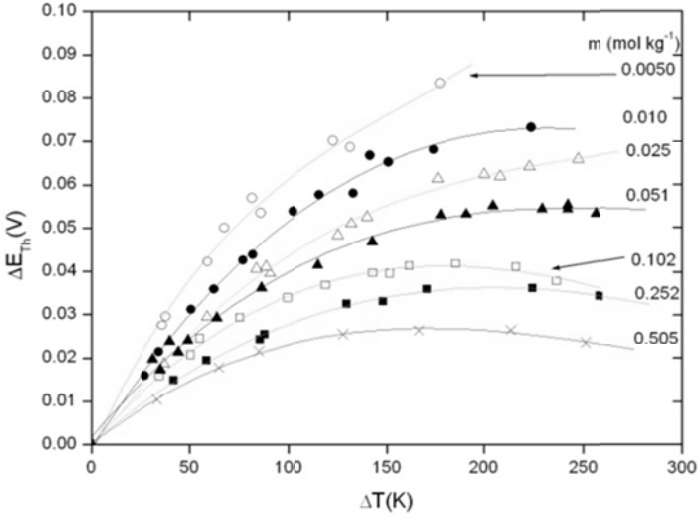

Figure 23. Voltages for the thermocell (298.15 K)Ag/AgCl/ KCl(aq.)/AgCl/ Ag(T) (Eq. 47) as a function of ΔT (= T – 298.15) and KCl concentration (m). The numbers shown on the right side of the figure are the KCl concentrations in the unit of mol kg^{-1}. Reproduced with permission from Ref. 99, Copyright (1969), The Electrochemical Society.

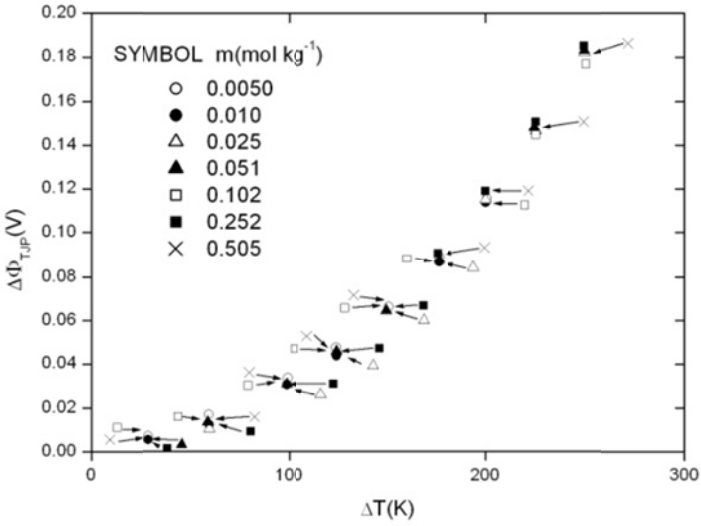

Figure 24. Thermal liquid junction potentials for the thermocell (298.15 K)Ag/AgCl/KCl(aq.)/AgCl/Ag(*T*) (Eq. 47) as a function of ΔT (= T – 298.15 in K) for various KCl concentration. The numbers shown on the left side of the figure are the KCl concentrations in the unit of mol kg^{-1}. Reproduced with permission from Ref. 99, Copyright (1969), The Electrochemical Society.

in which t_i, S_i^* and z_i are the transport number, the entropy of transport, and the charge of the i^{th} ion , respectively, in the thermal bridge solution. To calculate the thermal diffusion potential, the following information is required:

(a) The ionic composition of the thermal liquid junction, in terms of the total composition of the solution at a given temperature and pressure.
(b) The transference numbers, t_i, of all ions in the aqueous solution at a given temperature and pressure.
(c) Eastman entropies of transport, S_i^*, of all ions in the solution.

First, Lvov and Macdonald used a free-energy minimization code,[104] which employs standard Gibbs energies of formation of the species (as calculated using the SUPCR92 software package.)[16] The activity coefficients for all charged species were calculated

using extended Debye-Huckel theory, and activity coefficients for all neutral species, including water, were set equal to unity. Secondly, the ionic transference numbers are calculated using the equation:

$$t_i \approx \frac{|z_i|\lambda_i^0 c_i}{\sum_i |z_i|\lambda_i^0 c_i} \tag{49}$$

where λ_i^0 is the limiting equivalent ionic conductivity of the i^{th} ion. Lvov and Macdonald used the ionic limiting equivalent conductivities of K^+(aq.), Na^+(aq.), Cl^-(aq.), H^+(aq.) and OH^-(aq.) given by Quist and Marshall.[105] The parameter c_i is the molar concentration of the i^{th} species, which was calculated as described above. Equation (49) was proved to be a very good approximation for dilute solutions.

To derive the entropies of transport for ionic species, Lvov and Macdonald[100] extrapolated the standard entropies of transport of electrolytes, $S_i^{*,0}$, from lower temperatures to higher temperatures by applying Agar's hydrodynamic theory. The low-temperature experimental data were taken from Refs. 103 and 104. Lvov and Macdonald[100] employed previously measured differences between E_{TLJ} values for different electrolytes, MCl_n(aq.), so as to test the viability of the extrapolation. The results are shown in Fig. 25. As can be seen, good agreement exists between the calculated and observed data. Lvov and Macdonald[100] also calculated thermal liquid junction potentials for different electrolytes over a wide range of temperature (Figs. 25 and 26). From the calculated data, it can be seen that E_{TLJ} depends strongly on both the temperature and the type of the electrolyte, and the difference could be more than ±150 mV. To our knowledge, these data represent the only reported attempt to estimate the thermal liquid junction potential for external pressure balanced reference electrodes.

All of the calculations described above correspond to Soret's initial state, i.e., to a state where the concentration of electrolyte along the bridge is constant. As noted above, maintaining the thermal junction in the initial state has been a vital problem in the operation of external pressure balanced reference electrodes. As also noted above, in the original design of the EPBRE[88] (Fig. 21),

the thermal junction consisted of a PTFE tube and a porous ZrO_2 plug at the end. The PTFE tube was also used to transmit the pressure pulses from the flow-inducing, positive displacement pump to the internal reference solution. Thus any thermal diffusion tendency was counteracted by the pressure pulses. When the EPBRE was used under supercritical conditions,[49,51,52] a ceramic bridge was used in the high temperature ($T > 300^oC$) part of the junction, and it was connected via a PTFE tube to the lower temperature region (since the highest temperature PTFE can sustain is about 573 K). The uncertainty of the electrode potential was measured to be ±15–25 mV at temperatures below 573 K, and up to 100 mV at supercritical temperatures, and the measured potential was found to be extremely sensitive to pressure changes.

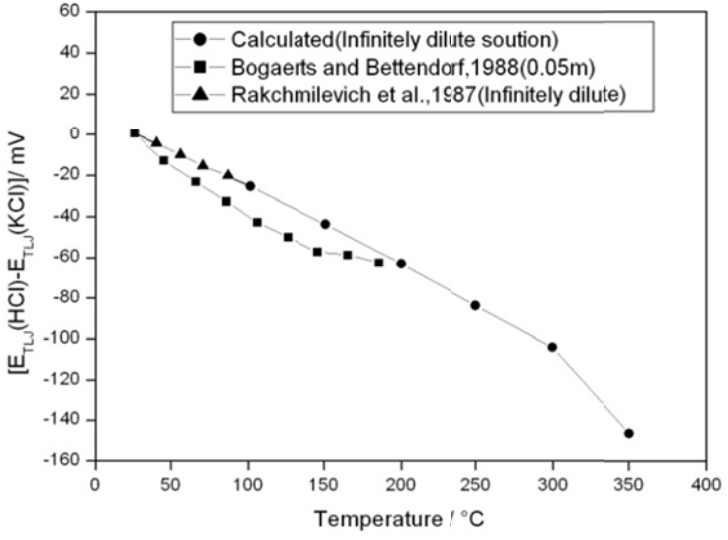

Figure 25. Comparison of the calculated and observed $E_{TLJ}(HCl) - E_{TLJ}(KCl)$ values (Thermocell I, Eq. 44) as a function of temperature. The citations are given in Ref. 97. Reprinted from Ref. 97, Copyright (1997) with permission from Elsevier.

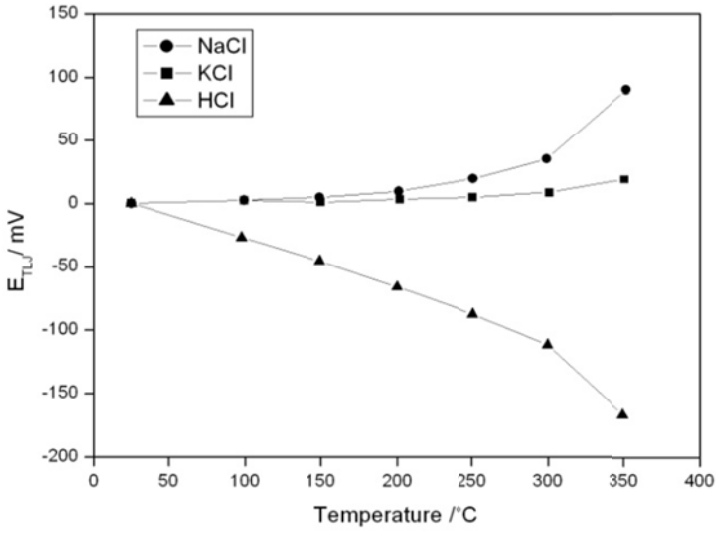

Figure 26. Temperature dependence of E_{TLJ} (Thermocell I) for standard, infinitely dilute NaCl, KCl and HCl aqueous solutions. Reprinted from Ref. 97, Copyright (1997) with permission from Elsevier.

Concentration dependence of E_{TLJ} (Thermocell I) for very dilute aqueous KCl and HCl solutions was studied by Lvov and Macdonald, and it is shown in Fig. 27.

A variation of the external reference electrode concept was reported by Tsuruta and Macdonald to measure the pH of a high temperature solution (Fig. 28). The ceramic membrane pH-measuring system is represented by

$$|\leftarrow T_I(25°C) \rightarrow|\leftarrow T \rightarrow|\leftarrow T_I(25°C) \rightarrow|$$

$$\text{Ag/AgCl/InternalSolution/TestSolution/}ZrO_2(Y_2O_3)\text{/InternalSolution/Ag/AgC} \quad (50)$$

By using an YSZME containing a buffered internal solution (0.1 m KCl + 0.01 m $B(OH)_3$ + 0.01 m KOH) and a matched EPBRE containing the identical solution (with a liquid junction of porous ZrO_2), and by equipping both with Ag/AgCl electroactive elements at ambient temperature (Fig. 20), it was postulated that

the thermal liquid junction potentials could be matched and hence eliminated from the measured cell potential. The measured cell potential is then given by

$$\Delta E = E_D + \Delta\Phi_m \tag{51}$$

where E_D and $\Delta\Phi_m$ are the isothermal liquid junction potential of the external reference electrode and the membrane potential, respectively. E_D can be obtained via Henderson's equation and the estimates were used to correct the measured cell potentials. A theoretical analysis shows that the membrane potential should exhibit a Nernstian pH response except for a small deviation due to the difference in the activity of water in the internal and test solutions. To test the concept, a platinized platinum hydrogen electrode was added to the test cell containing different buffers as indicated in the caption to Fig. 29, in order to compare the results with the ceramic membrane electrode. Various test solutions were em-

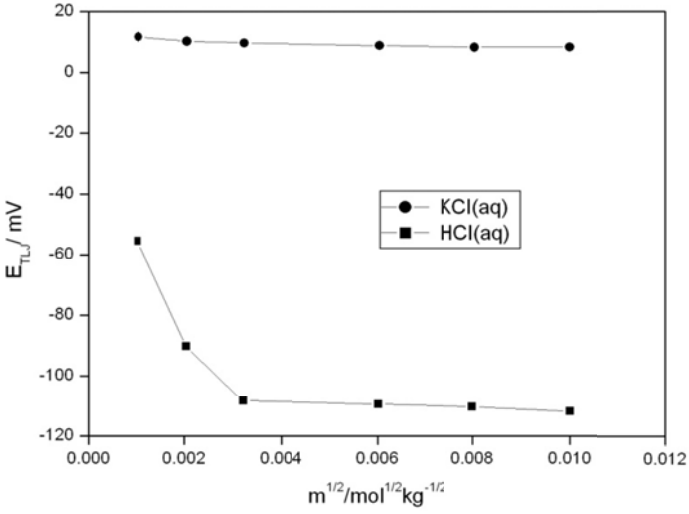

Figure 27. Concentration dependence of E_{TLJ} (Thermocell I) for very dilute aqueous KCl and HCl solutions at 300°C. Reprinted from Ref. 97, Copyright (1997) with permission from Elsevier.

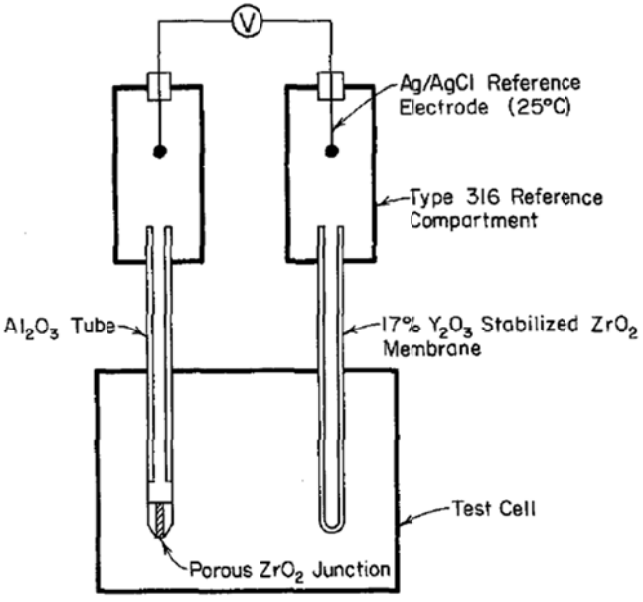

Figure 28. Schematic of the ceramic membrane pH-measuring system (Eq. 50). Reprinted from Ref. 94, Copyright (1983) with permission from The Electrochemical Society.

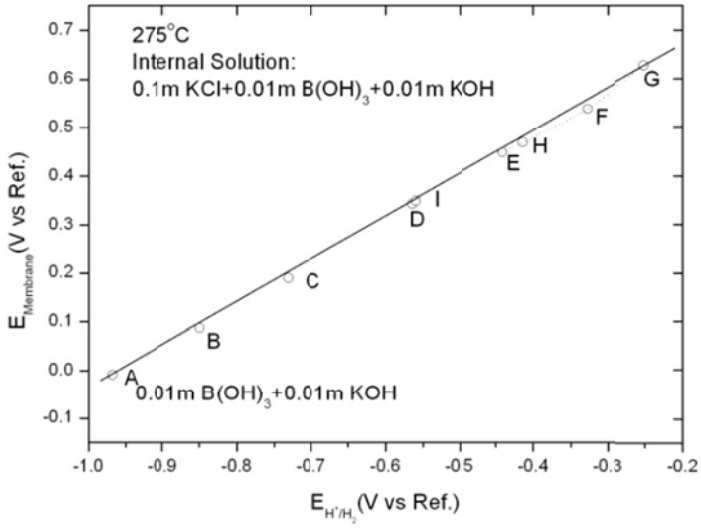

Figure 29. Potential vs. pH_T response for the ceramic membrane electrode (Eq. 50) in various $B(OH)_3$/KOH and H_2SO_4/Na_2SO_4 systems at 275°C. The various test solutions are: (A) 0.01m KOH+0.01m $B(OH)_3$, (B) 10^{-3}m KOH+0.01m $B(OH)_3$, (C)10^{-4}m KOH+0.01m $B(OH)_3$, (D) 0.01m $B(OH)_3$, (E) 0.00005m H_2SO_4, (F) 0.0005m H_2SO_4, (G) 0.005m H_2SO_4, (H) 0.005m H_2SO_4+0.005m Na_2SO_4, (I) 0.005m H_2SO_4+0.045m Na_2SO_4. Reprinted from Ref. 94, Copyright (1983) with permission from The Electrochemical Society.

ployed to calibrate the pH response of the ceramic membrane. The measured membrane potentials were plotted against the hydrogen electrode potentials at temperatures from 100°C to 275°C, with Fig. 26 showing data at 275°C. It is indicated that the ZrO_2 (17% Y_2O_3) membrane does not exhibit a strictly Nernstian pH response, especially at the lower temperatures and in weakly acidic systems. Tsuruta and Macdonald[97] have analyzed the possible reason, concluding that the rest of error might be attributed to the effect of ionic strengths on the buffer properties of the internal solution and to errors in the estimates of E_D. Retrospectively, it is now believed that the use of a silica *sintering aid* by the manufacturer of the YSZ ceramic tubes, resulting in abnormally high membrane impedance, is the principal cause of the deviations from theory at the lower temperatures. While this approach is clearly a most promis-

ing way of eliminating the TLJP in high temperature pH measurement, it has yet to be fully explored.

Macdonald and Kriksunov employed an YSZME (with an internal element of Ag/O_2) against the EPBRE to explore changes in acidity of dilute HCl and NaOH solutions for temperature ranging from 400° C to 528° C as the solution cycled from 0.01 m HCl to 0.01 m NaOH, as shown in Fig. 30.[55] The utility of the sensor for detecting pH changes in response to changes in solution composition at temperatures well above the critical point is clearly indicated from the figure. By using the calculated pH values and the measured cell potentials, Macdonald and Kriksunov calibrated the reference electrode and obtained the pH of CCl_4 solution (Fig. 30) assuming complete hydrolysis of CCl_4 (Fig. 31).[55] This topic is discussed further below under Measurement of pH.

The pH of the CCl_4 solution was found to be a little higher than that calculated, assuming complete thermal hydrolysis of carbon tetrachloride. However, the level of agreement is still acceptable, considering the unknown actual extent of CCl_4 thermal hydrolysis and the uncertainty in the calibrating cell voltages. While the level of uncertainty perhaps does not satisfy the need for accurate thermodynamic work, it is satisfactory for monitoring SCWO systems.[3]

In the flow-through external pressure-balanced reference electrodes[62,63] (Fig. 22), fluid flow was employed instead of pressure pulses to suppress thermal diffusion. This was done by pumping the internal reference solution through the inner compartment at a delicately set rate. The flow rate must be high enough to yield a constant electrolyte concentration along the non-isothermal bridge, but also not too high so as to maintain the temperature gradient along the electrolyte bridge. Since the concentration is kept constant along the bridge, the Soret initial state can be maintained and the thermal diffusion potential is constant for a given temperature difference across the junction. Thus, the uncertainty of the thermal liquid junction potential is assumed to be eliminated at any given temperature and pressure.

To test this assumption, Lvov, Gao, and Macdonald[65] employed two hydrochloride solutions of different concentrations (0.01mol kg^{-1} and 0.001mol kg^{-1} HCl) as the test solutions, and measured the potential difference of the thermocell:

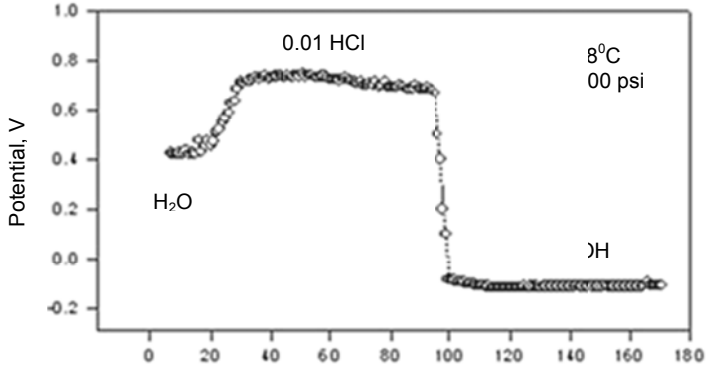

(a)

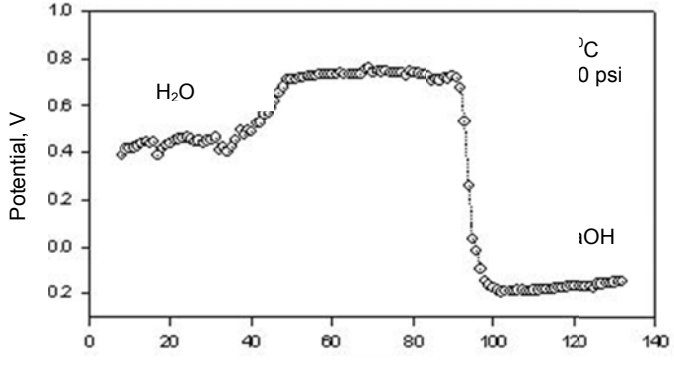

(b)

Figure 30. Measured potential vs. time for dilute HCl and NaOH solutions and for carbon tetrachloride in supercritical aqueous systems at temperature (a) 528°C and (b) 525°C. Reprinted from Ref. 5 , Copyright (1997) with permission by Elsevier.

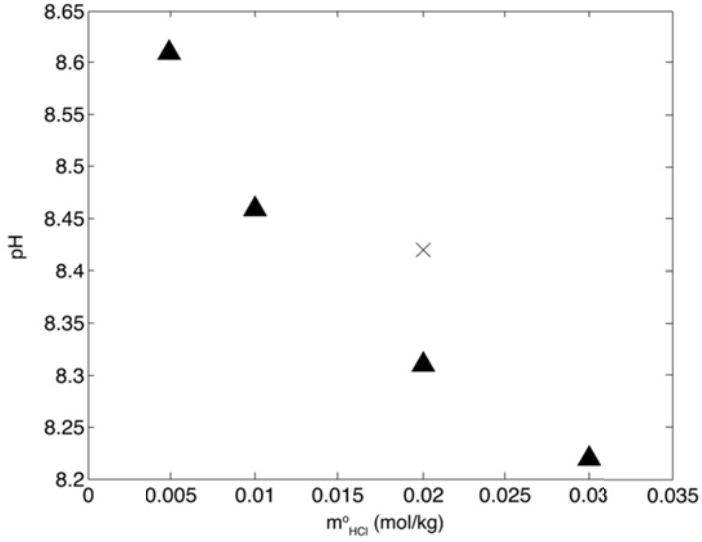

Figure 31. Plot of calculated pH against stoichiometric HCl concentration for T = 525°C and P = 5000 psi (closed circles). The measured pH for the hydrolyzed CCl_4 solution is given by the closed triangle.[55] Reprinted from Ref. 5 , Copyright (1997) with permission by Elsevier.

$$|\leftarrow T_1 \rightarrow|\leftarrow T_2 \rightarrow|\leftarrow T_1$$

$$\text{Cu/Ag/AgCl/0.1mol·kg}^{-1}\text{NaCl(aq.)|0.1mol·kg}^{-1}\text{NaCl(aq.) + HCl(aq.)/H}_2\text{,Pt/Cu} \tag{52}$$

with the potential difference being:

$$\Delta E = E\ (10^{-2}\,\text{mol}\cdot\text{kg}^{-1}\text{HCl}) - E\ (10^{-3}\,\text{mol}\cdot\text{kg}^{-1}\text{HCl})$$
$$= \frac{RT_2}{F}\ln\frac{m_{H^+}(1)\gamma_{H^+}(1)}{m_{H^+}(2)\gamma_{H^+}(2)} + E_D[\text{HCl}(1)/\text{NaCl}] - E_D[\text{HCl}(2)/\text{NaCl}] \tag{53}$$

The potential difference for the two different solutions was shown to be independent of the thermal diffusion potential and can be calculated theoretically. The calculated and measured poten-

tials, listed in Table 2, show good agreement and demonstrate the effectiveness of the flow-through technique in maintaining the Soret initial state. At the higher temperatures (350–360°C), the difference between the measured and calculated potentials was of the order of 10mV, corresponding to an uncertainty in a measured pH value (if it was used for that purpose) of about 0.08 (± 0.04).

Lvov, Zhou, and Macdonald[66] used a flow-through electrochemical cell (comprising a flow-through external Ag/AgCl pressure-balanced reference electrode and a modified flow-through platinum hydrogen electrode) to measure pH at temperatures up to 400°C and pressures up to 25.3 MPa. The measured accuracy was demonstrated to be better than ±0.03 logarithmic (pH) units, in good agreement with the estimate calculated above.

A similar FTEPBRE has been employed by Lvov et al.[108] in a four-way, once-through electrochemical cell (composed of one flow-through reference electrode, one flow-through Pt-H_2 electrode, one flow-through YSZ electrode, and a thermocouple). Because the same dependence on the temperature, pressure, flow rate, and solution component of the platinum electrode and YSZ electrode exist, the cell was run at 320°C and 350°C (pressure 23.0 and 24.8MPa) to test the precision and response time of the YSZ electrode as a pH-sensing electrode.

Table 2
Experimental and Theoretical Differences in Potentials *E* (10^{-2} m^{-1} HCl) – *E* (10^{-3} m^{-1} HCl) of the Thermocell (Eq. 52) as a Function of Temperature and Pressure.[57]

Temperature (K)	Pressure (bar)	*E* (0.01 m HCl) – *E* (0.001 m HCl)	
		Experimental observed (mV)	Theoretically calculated (mV)
298	275	64.5	59.1
298	338	61.4	59
373	275	81	74
473	275	97.8	93.7
573	275	100.3	109.8
623	275	93.4	102.2
623	338	97.4	106.2
633	338	91.7	102.4

Using a similar concept, Sue et al.[109] designed another flow-through external pressure balanced reference electrode using a platinum/hydrogen electrode instead of Ag/AgCl electrode. The cell they developed can be depicted by:

$$\text{Cu/Pt,H}_2\text{/Test solution} \mid \text{Reference solution/H}_2\text{,Pt/Cu} \qquad (54)$$

$$T_1 \quad \rightarrow\leftarrow T_2 \rightarrow\leftarrow T_1 \rightarrow$$

in which T_2 is the higher temperature and T_1 is the lower (ambient) temperature. The platinum/hydrogen electrode on the right side is the flow-through external pressure balanced reference electrode, while that on the left side is the indicator electrode. This electrochemical cell has been used to measure pH at temperatures from 23.9°C to 400.2°C and pressures from 25.0 to 35.1MPa. The difference between the measured pH and the calculated pH proved to be less than 0.03 logarithmic (pH) units. Sue et al. also used the cell to measure the dissociation constant of phenol (PhOH).[110]

The development of FLEPBRE represents a significant advance in the quest to make possible accurate pH measurements in supercritical aqueous systems. However, there are also a number of issues that need to be resolved. One is the delicate setting of flow rate to simultaneously maintain the system in the Soret initial state and maintain the temperature gradient down the non-isothermal bridge, which greatly complicates the system and makes the FTEPBRE unlikely to be used in many practical field situations (e.g. SCWO system). The second is the calibration of the reference electrode. Since the reference potential (measured against a hydrogen electrode) strongly depends on the flow rate of reference solution, it needs to be calibrated against a known standard over wide ranges of temperature, pressure, and solution type and composition, at accurately known flow rates. This feature, alone, indicates that the flow through concept, which was initially introduced by Danielson[94] more than twenty years ago, is not the panacea in reference electrode technology.

3. Measurement of pH

A variety of sensors have been developed to measure the activity of H^+ in high temperature aqueous solutions, including Pd/H elec-

trodes, Pt/H_2 electrodes, metal/metal oxide electrodes, glass electrodes, and most importantly yttria-stabilized zirconia [ZrO_2 (Y_2O_3)] electrodes.[111] The latter [ZrO_2 (Y_2O_3)] sensors have now been used for monitoring pH in supercritical systems at temperatures to 528°C, which is more than 150 °C higher than the critical temperature.[5,10,11] For this reason, the present discussion of pH sensors will be restricted to the yttria-stabilized zirconia membrane system, with particular reference to the (Ag),O_2/ZrO2(Y_2O_3)/H^+, H_2O electrode. Physically, this sensor comprises a closed end ZrO_2 (Y_2O_3) tube containing porous silver as an internal element and platinum wire as an ohmic contact with the silver. The porous Ag internal element is readily formed by the thermal decomposition of Ag_2O at temperatures above ca 200°C. Although back filled with alumina cement, the inside of the tube is assumed to be in contact with ambient air with $p_{O2} = 0.21$ atm. It is important to note that this pH sensor is essentially identical to that described many years ago by Danielson,[112] which he used to measure pH in subcritical systems ($T < 300$°C, in this case).

Thermodynamic analysis of this sensor has been carried out by noting that the equilibrium processes that occur on the outside (solution side) and the inside (dry side) of the membrane are written as

$$V_O^{\bullet\bullet} + H_2O \rightarrow O_O + 2\,H^+ \tag{55}$$

and

$$\tfrac{1}{2}\,O_2 + V_O^{\bullet\bullet} + 2\,e^- \rightarrow O_O \tag{56}$$

Where $V_O^{\bullet\bullet}$, O_O, and e^- are the oxygen vacancy, oxide ion in a normal anion site in the YSZ lattice, and an electron in the metal (Ag). Thus, the half-cell reaction for the sensor becomes

$$\tfrac{1}{2}\,O_2 + 2\,H^+ + 2\,e^- \rightarrow H_2O \tag{57}$$

provided that the activity of $V_O^{\bullet\bullet}$ is uniform across the membrane wall. Note that if this latter condition holds, the thermodynamics of the system is independent of the properties of the ceramic, which constitutes a great advantage of YSZ ceramic membrane pH sensors.[112]

Application of equilibrium thermodynamics to this system yields the equilibrium potential as

$$E^e = E^o - \frac{2.303RT}{2F}\log_{10}\left[a_{H_2O} / f_{O_2}^{1/2}\right] - \frac{2.303RT}{F}pH \qquad (58)$$

where a_{H_2O} and f_{O_2} are the activity of water on the solution side and the fugacity of oxygen on the *dry* (internal) side of the membrane, respectively, and pH = –log(a_{H^+}). $E°$ is the standard potential, as given by

$$E^O = -\Delta G^O / 2F \qquad (59)$$

where ΔG^0 is the change in standard Gibbs energy for the cell reaction

$$H_2 + ½\ O_2 \rightarrow H_2O \qquad (60)$$

Typical potential vs. time plots for a O_2(Ag)/ZrO_2(Y_2O_3) /H^+,H_2O sensor measured against an Ag/AgCl/KCl(sat) external pressure balanced reference electrode (EPBRE) for temperatures ranging from 400°C to 528°C as the solution is cycled from 0.01m HCl to 0.01m NaOH are shown in Fig. 10.[10,11] It is evident that the cell potential responds to change in pH in a reproducible manner. In one case, a 0.1m NH_3 solution was pumped through the cell resulting in a potential that is more positive than that for 0.01 m NaOH, as expected from the relative basicity. While a full analysis of these data has yet to be made, the utility of the sensor for detecting changes in pH in response to changes in solution composition at temperatures well above the critical temperature is clearly indicated.

It is also important to note that the YSZ electrode is a primary pH sensor[109] and hence (in principle) does not require calibrating. However, this is not the case with the EPBRE, which forms the other half of the cell. At the present time, no method exists for calculating the reference electrode potential, a priori, so that calibration is the only course for devising a practical pH sensor. Calibration requires knowledge of the activity of H^+ and the fugacity

of water in the calibrating solution (see Eq. 60), both of which can be calculated from the thermodynamics of the system, provided that equilibrium constants, etc. are known (see above).

The utility of the pH sensor described above for following the course of a reaction is illustrated by the data shown in Fig. 32(d). In this particular experiment, an aerated 0.005 m CCl_4 solution (a *resilient* waste) was injected into the high temperature zone at a temperature of 525°C and at a pressure of 5000 psi (340.2 atm). The voltage of the sensor increased in the positive direction, indicating acidification of the solution. Assuming that the carbon tetrachloride is completely hydrolyzed,

$$CCl_4 + 2\ H_2O \rightarrow CO_2 + 4\ HCl \qquad (61)$$

the HCl concentration should be 0.02 m. The observed potential is in good agreement with that measured for 0.01 m HCl, being slightly more positive than that for the latter. Because both the thermal hydrolysis and the oxidation of organic materials produces acid, monitoring of the pH using sensors of the type described in this work appears to be an effective means of monitoring the progress of a reaction. By using the calculated pH values and the measured cell potentials, it is possible to calibrate the external pressure balanced reference electrode (EPBRE). From this calibration it is possible to then obtain the pH of the CCl_4 solution, as shown in Fig. 31. Also plotted in this figure are the calibrating data. The pH of the CCl_4 solution is judged to be slightly high (by about 0.15 pH units). However, the level of agreement is satisfactory considering that the extent of CCl_4 thermal hydrolysis is unknown and that the uncertainties in the calibrating cell voltages are such that the derived pH is unlikely to be more accurate than ±0.15 units. While this level of uncertainty is not satisfactory for accurate thermodynamic work, it is satisfactory for monitoring SCWO systems. In this regard, we note that attempts are now underway to develop techniques (including reference electrodes) for measuring pH to better than ±0.05 at supercritical temperatures and at the time of preparation of this article measurements of this precision have been made at temperatures to 400°C.[113]

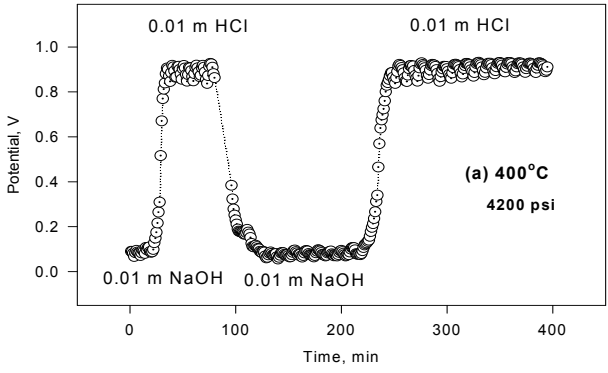

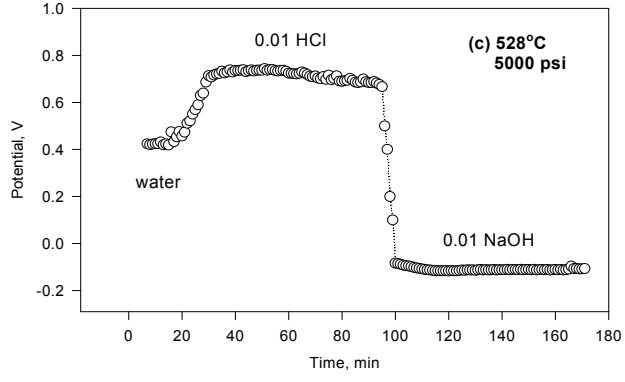

Figure 32. Measured potential vs. time for dilute HCl and NaOH solutions and for carbon tetrachloride in supercritical aqueous systems at temperatures ranging from 400°C to 528°C. Reprinted from Ref. 5, Copyright (1997) with permission by Elsevier.

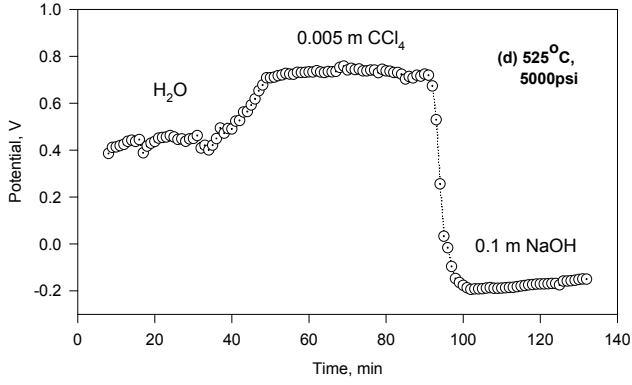

Figure 32. Continuation.

The pH measurements reported in this review are summarized in Fig. 33, in which are plotted the calculated pH values for the 0.01 m HCl calibrating solutions and the measured pH for the CCl_4 solution, as a function of temperature and pressure. Note that, at a temperature of 528°C and a pressure of 300 bar, the neutral pH is $pK_w/2$ = 10.4, so that a pH of 8.4 under these conditions corresponds to an acidic system. Also note that the density of the systems at the highest temperatures (525°C and 528°C) are of the order of 0.15 g/cm^3, which renders the systems more *gas-like* than "liquid-like", as previously noted. The fact that pH measurements can be made under these conditions is remarkable and demonstrates an additional, peculiar property of SCW. Finally, while the data plotted in Fig. 33 clearly correspond to dilute HCl solutions and to hydrolyzed CCl_4, they are believed to be representative of SCWO systems in general that do not employ neutralization.

It is evident from the material presented above and earlier in this paper that the pH of a high subcritical aqueous solution or of a supercritical aqueous fluid is dominated by incomplete dissociation of even the strongest acids and bases. The importance of acid dissociation in determining the pH is best illustrated by using HCl as a calculational probe. Thus, in Fig. 34, is plotted the calculated degree of dissociation of a dilute HCl solution (0.01 m) as a func-

tion of temperature (25°C to 600°C) at pressures ranging from 400 bar to 1000 bar. At temperatures below 325°C, HCl is almost completely dissociated and hence behaves as a strong acid. At higher temperatures, however, the degree of dissociation drops precipitously and becomes highly pressure dependent. The pressure dependence at supercritical temperatures is such that the degree of dissociation increases with increasing density and dielectric constant, corresponding to progressively more effective stabilization of the ions. At the highest temperature (600°C) and lowest pressure (400 bar), the degree of dissociation corresponds to little more than one part per million, illustrating that overwhelmingly chloride exists in the form of undissociated HCl.

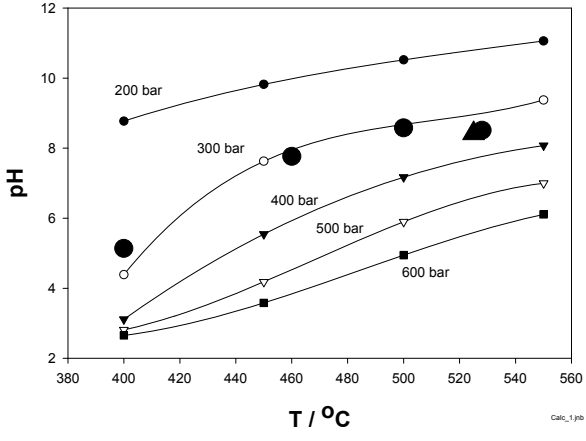

Figure 33. Plot of calculated pH against temperature for a stoichiometric HCl concentration of 0.01 m (closed circles). The measured pH for the hydrolyzed CCl_4 solution is given by the closed triangle. Reprinted from Ref. 5, Copyright (1997) with permission by Elsevier.

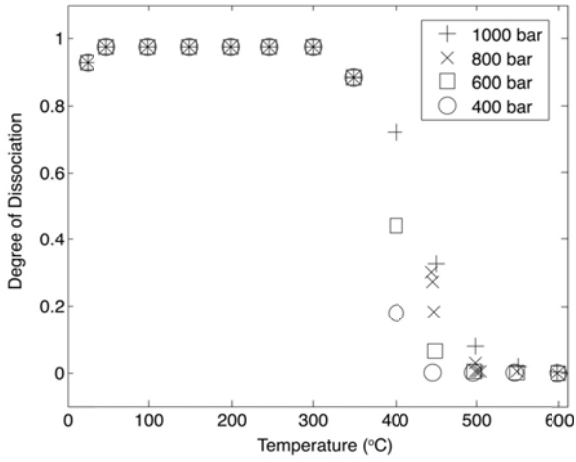

Figure 34. Calculated degree of dissociation of 0.01 m HCl as a function of temperature and pressure. Reprinted from Ref. 5, Copyright (1997) with permission by Elsevier.

That the degree of dissociation dominates the pH is shown by a comparison between Figs. 34 and 35. The pH of the system at the lowest pressure (density) displays the greatest deviation from $-\log(m^{o}_{HCl}) \approx 2$, rising to about 9 at 600°C. We emphasize, however, that while HCl is strongly associated under these conditions, the solutions are still acidic, even though the pH is as high as 9. This is evident by comparing the data shown in Fig. 35 with those displayed in Fig. 36, in which is plotted the pH (on both scales) of pure water as a function of temperature for a pressure of 400 bar. Note that at the lowest pressure (also the lowest density and dielectric constant) the pH of the 0.01 m HCl solution is calculated to be only slightly less positive (by 1–2 pH units), attesting to the strong influence of association in buffering the pH.

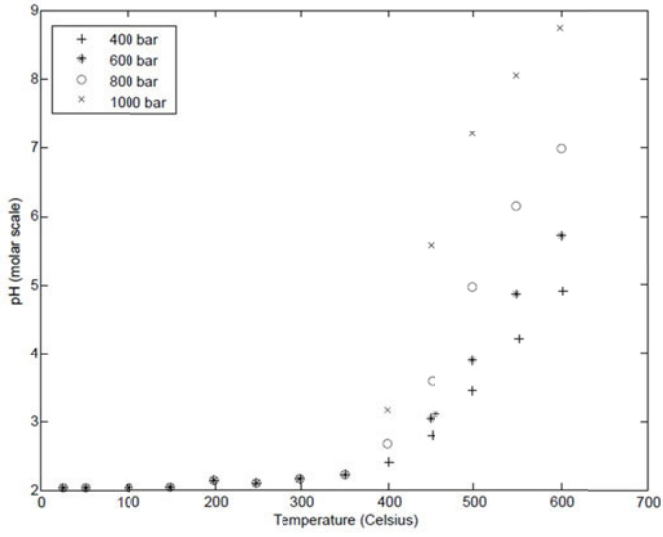

Figure 35. Calculated molar scale pH for 0.01 m HCl as a function of temperature and pressure. Reprinted from Ref. 5, Copyright (1997) with permission by Elsevier.

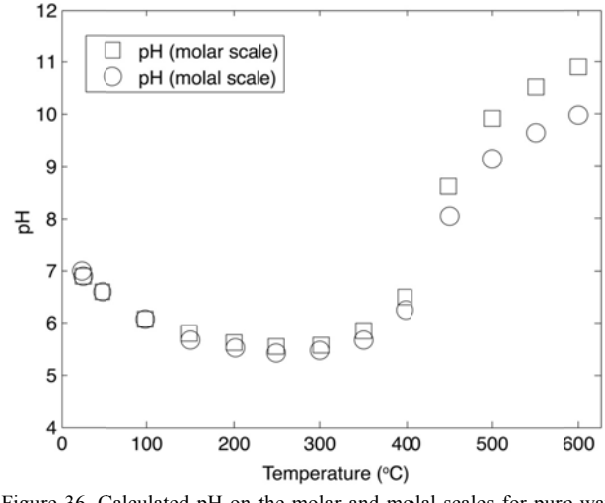

Figure 36. Calculated pH on the molar and molal scales for pure water as a function of temperature for a pressure of 400 bar. Reprinted from Ref. 5, Copyright (1997) with permission by Elsevier.

4. Redox and Combination Sensors

The chemical and electrochemical properties of SCWO systems and other supercritical aqueous solutions are determined in large part, by the concentration of oxygen, hydrogen, and other redox species. The presence of oxygen often causes extensive general and/or localized corrosion attack, including pitting corrosion and stress corrosion cracking. In many industrial environments, such as those found in nuclear power industry, various forms of corrosion can be prevented or significantly diminished by maintaining the potential of structural metals and alloys exposed to the aqueous environment within certain ranges. This is usually achieved by modifying the water chemistry, e.g. as in hydrogen water chemistry, which is now used in Boiling Water Reactors to mitigate and control stress corrosion cracking of sensitized stainless steels.[114] However, in applying these techniques, it is important to monitor the amount of oxidant (or redox potential) in the system *on line* and in situ, in order to avoid excessive corrosion damage. Our ability to do so depends critically upon having available an in situ redox sensor that is both effective and practical under the conditions of interest. One such sensor that was developed in the author's laboratory is shown in Fig. 37.[115]

This sensor was developed for monitoring oxygen, hydrogen, and redox potential in aqueous solutions at temperatures extending above the critical temperature of water. The sensor is based on a combination of two electrodes that are structurally combined into a single unit: a redox insensitive yttria stabilized zirconia (YSZ) membrane pH electrode, of the type described in the previous section, and a Pt electrode. The potential of this latter electrode is, of course, sensitive to oxygen and hydrogen concentration and to pH. The potential of the YSZ membrane can be represented as

$$E = E^{o}_{YSZ} - \frac{2.303RT}{F} pH - \frac{2.303RT}{2F} \log a_{H_2O} \qquad (62)$$

where a_{H2O} is the activity of water and E^{o}_{YSZ} is the standard potential for the internal couple (O_2/H_2O) used in the YSZ membrane. The potential of the platinum electrode in a hydrogenated environment can be written as

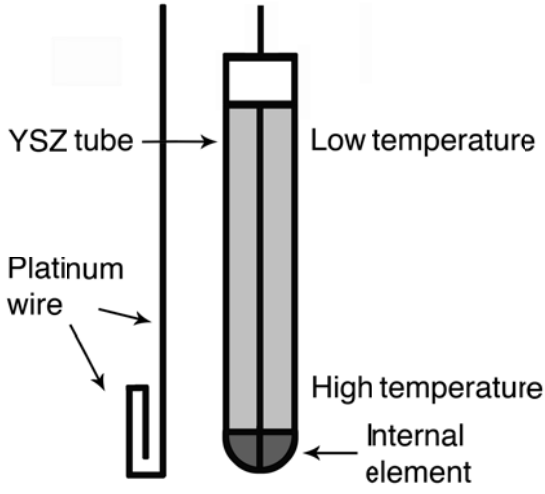

Figure 37. Oxygen, hydrogen and redox potential combination sensor. Reprinted from Ref. 5, Copyright (1997) with permission by Elsevier.

$$E = -\frac{2.303RT}{F} pH - \frac{2.303RT}{2F} log\ f_{H_2} \tag{63}$$

Where f_{H2} is the fugacity of hydrogen. Similarly, the potential of the reversible oxygen electrode can be written as follows:

$$E = E^{o}_{OX} - \frac{2.303RT}{F} pH - \frac{2.303RT}{4F} \log f_{O_2} - \frac{2.303RT}{2F} \log a_{H_2O} \tag{64}$$

where $E_{OX}{}^{0}$ is the standard potential for the O_2/H_2O couple and f_{O2} is the fugacity of oxygen.

Importantly, Eqs. (62)–(64) contain the same dependence of the electrode potential on pH. Hence, the potential difference between the YSZ electrode and Pt electrode in both hydrogenated and oxygenated environments will be pH independent, under ideal conditions, provided that the electrodes are at equilibrium. For hydrogenated environments, we obtain by subtracting Eq. (63) from (62):

$$\Delta E = E^{o}_{YSZ} + \frac{2.303RT}{2F}\log f_{H_2} - \frac{2.303RT}{2F}\log a_{H_2O} \quad (65)$$

From this last equation, it is apparent that we can estimate the hydrogen fugacity in the solution, independently of the solution pH, as:

$$\log f_{H_2} = 2F(\Delta E - E^{o}_{YSZ})/2.303RT + \log a_{H_2O} \quad (66)$$

Likewise, subtracting Eq. (64) from Eq. (62) we obtain for oxygenated environments:

$$\Delta E = (E^{o}_{YSZ} - E^{o}_{OX}) + \frac{2.303RT}{4F}\log f_{O_2} \quad (67)$$

and hence

$$\log f_{O_2} = 4F(\Delta E - E^{o}_{YSZ} + E^{o}_{OX})/2.303\mathrm{RT} \quad (68)$$

Because all of the quantities on the right hand sides of Eqs. (66) and (68) are known or can be measured, the sensors are primary sensors and, in principle, do not need calibrating. Note that the sensor is the same in both cases. We should emphasize that Equation (66) for hydrogenated environments contains the activity of water, which can be estimated for dilute solutions from the PVT properties of water, as previously described. Another important issue is that both Eqs. (66) and (68) contain thermodynamic fugacity (activity) of dissolved gases. Fugacity coefficients under SCWO operating conditions might be significantly different from

unity and, because of this, the practical determination of the concentration of dissolved gas may require calibration of the sensor in solutions of known gas concentrations.

Experiments were performed at temperatures in excess of 500°C and at pressure of 3500-4000 psi.[116] Several different designs of the sensor were explored. The sensor was found to respond to changes in oxygen and hydrogen concentration in the solution, as determined by saturating the feed solution with the corresponding gas (Figs. 38–41). The response time of the sensor is mostly determined by the hydrodynamics of the high-temperature / high-pressure loop and cell. In particular, for the system employed, the time required for the solution of a new concentration to reach the measurement zone dominates the sensor response time.

From the data summarized in Figs. 38 to 40, is apparent that the sensor responds rapidly to changes in the concentrations of oxygen and hydrogen and, correspondingly, to the redox potential in the solution.[116] For example, Fig. 38 presents potential data from the sensor measured in a stainless steel cell at a low pH that was established by the addition of 0.01 m HCl to the system and at a temperature of 400°C. As the hydrogen partial pressure in the ambient temperature reservoir is changed systematically from 0.01 atm to 1.0 atm, the potential is observed to change systematically in like fashion. In this mode, the sensor acts as a *hydrogen* sensor. The addition of oxygen to the reservoir gives rise to a large shift in the potential (by about 720 mV) in the negative direction. In this case, a systematic variation in the oxygen partial pressure in the reservoir results in a corresponding variation in the potential. Thus, in this case, the sensor acts as an *oxygen* sensor. When both hydrogen and oxygen are simultaneously present in the system, the sensor measures the redox potential, corresponding to values between the pure hydrogen and pure oxygen limits discussed above.

Similar, but more extensive data for oxygenated supercritical solutions are shown in Fig. 36.[116] These data were measured in a 0.002 m NaOH solution at a temperature of 430°C and at a pressure of 4000 psi. Again, the sensor is found to respond systematically to changes in the oxygen partial pressure in the reservoir. Comparison of these data with those given in Fig. 38, albeit at dif-

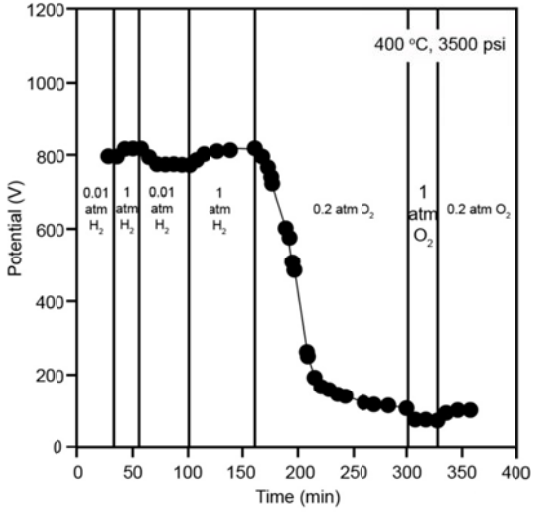

Figure 38. Potential of the combination redox sensor in 0.01 m HCl at a temperature of 400°C and at a pressure of 3000psi (204 atm) upon cycling the concentrations of hydrogen and oxygen in the feed. Reprinted from Ref. 5, Copyright (1997) with permission by Elsevier.

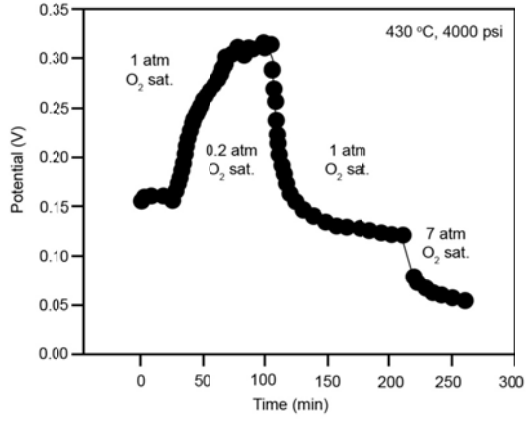

Figure 39. Potential of the combination redox sensor in 0.002 m NaOH at a temperature of 430°C and at a pressure of 4000psi (272.2 atm) upon changing the oxygen concentration in the feed. Reprinted from Ref. 11, Copyright (1998) with permission from NACE International.

ferent temperatures, shows that the sensor response is insensitive to the change in pH, which, of course, was one of the primary goals in developing the combination sensor. Finally, Fig. 40 shows the response of the combination redox sensor to changes in H_2 and O_2 concentration in pure water at 465°C and at a pressure of 4000 psi, demonstrating the utility of the sensor in a more resistive environment. Again, comparison of the data for oxygenated solutions in Fig. 40 with those in Figs. 38 and 39 confirms the insensitivity of the sensor towards changes in pH.

We also tested a modification of the combination redox sensor described above, in which the yttria stabilized zirconia tube was replaced by a tungsten/tungsten oxide electrode. Elsewhere, we have shown that this electrode is pH sensitive and is practically insensitive to oxygen and hydrogen,[116] at least at low subcritical temperatures (T < 300°C). In Fig. 41, we present typical data on the response of this sensor to the changes in the gas concentration

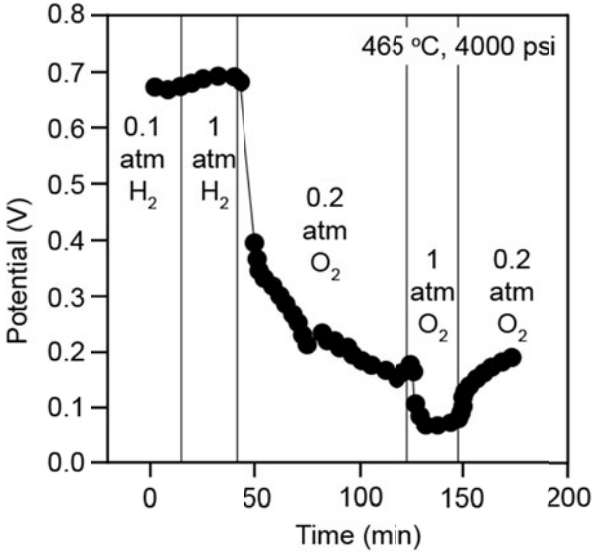

Figure 40. Potential of the combination redox sensor in water at a temperature of 465°C and a pressure of 4000psi (272.2 atm) upon cycling the concentrations of H_2 and O_2 in the feed. Reprinted from Ref. 5, Copyright (1997) with permission by Elsevier.

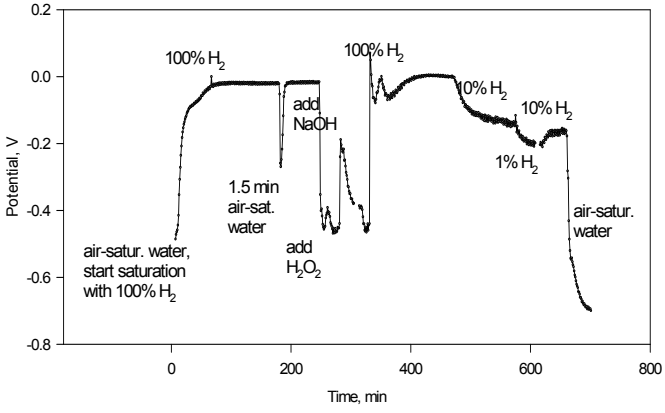

Figure 41. Response of the W/WO_3-Pt combination sensor to changes in oxygen and hydrogen concentrations in pure water at 300 °C. Reprinted from Ref. 5, Copyright (1997) with permission by Elsevier.

in the solution reservoir. This tungsten/tungsten oxide/platinum redox sensor, which is exceptionally rugged (consisting of an oxidized tungsten wire and a platinum wire), clearly responds to changes in the redox conditions in the solution in a manner that parallels the response of the sensor containing the YSZ ceramic tube.

The major advantages of the combination sensors described above include:

(a) absence of a traditional reference electrode (such as a Ag/AgCl external pressure balanced reference electrode);
(b) the possibility of employing the sensor up to very high temperatures (YSZ membranes are routinely used in fuel cells and oxygen sensor applications at temperatures in excess of 700°C in gas phase);
(c) the fact that this is a universal oxygen, hydrogen, and redox combination sensor, auto corrected for the pH of the solution, and;

(d) the sensor is very resistant to corrosion (YSZ, and Pt are probably the most corrosion resistant materials known for use in high subcritical and supercritical aqueous solutions). The corrosion properties of tungsten in SCWO environments are presently unknown.

Applications of the sensor include monitoring oxygen and hydrogen concentration, and redox potential in SCWO systems, as well as for monitoring the chemistry of the heat transport fluid (water) in supercritical thermal power plants. Because the sensor contains an independent pH-sensitive electrode, it can be used, in conjunction with a suitable reference electrode for simultaneous pH monitoring. If the value of pH in the system is kept constant, the YSZ membrane electrode of the sensor could also be utilized as a reference electrode, in order to monitor corrosion potentials of structural components.

IV. CORROSION STUDIES

Because of the technological importance of supercritical aqueous solutions, as evidenced by their use as reaction media in the destruction of toxic waste and as a heat transport medium, it is not surprising that the corrosion of structural materials has been studied in some depth. This is especially true recognizing the well-known aggressiveness of supercritical aqueous solutions, which raises great challenges in materials selection. Indeed, it is likely that SCWO and SCTPPs will continue to drive the development of the science and engineering base of the corrosion of metals and alloys in supercritical aqueous solutions over the foreseeable future.

1. General Corrosion

From a strictly engineering viewpoint, corrosion studies need to:

- identify the type of attack occurring on a surface, and;
- characterize the rate.

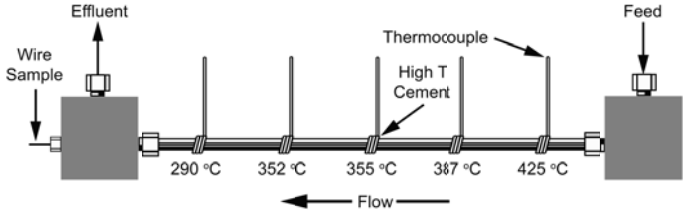

Figure 42. The experimental configuration employed for assessing wire samples over an extensive temperature range. A similar design, excluding the wire sample and fitting, was also used for assessing tube samples. Reprinted from Ref. 1, Copyright (2008), with permission of NACE International.

It is for this reason and because of the difficulty in performing electrochemical experiments in supercritical aqueous environments that much of the work reported to date has been of the *expose-and-examine* type in which examination is carried out post-test.

An experimental configuration employed by Mitton et al.[1] for assessing wire samples over an extensive temperature range is shown in Fig. 42.

The form of attack was found to be dealloying and the depth, as determined by post-test metallographic examination, is plotted as a function of temperature in Fig. 43. It is seen that the extent of attack passes through a maximum at a temperature of about 350°C. As discussed later in this review, the increase in the extent of attack upon increasing the temperature from 290°C to 350°C is due to the increase in the rate constant as described by the Arrhenius equation. Over this temperature range, HCl is essentially fully dissociated (see Fig. 34). However, upon increasing the temperature above 350°C, HCl becomes increasingly associated, because of the decrease in the dielectric constant (Fig. 7), and the concentration of free H^+ falls rapidly. Furthermore, the sharp decrease in the density of the medium that occurs with increasing temperature above the critical temperature (Fig. 6), results in a correspondingly sharp decrease in the volumetrically-based molar concentration. These two latter effects outweigh the increase in the rate constant with temperature at temperatures above 350°C, thereby resulting in a decrease in the extent of attack. The maximum in the rate is predicted by the model of Kriksunov and Macdonald[3] as discussed later in this review.

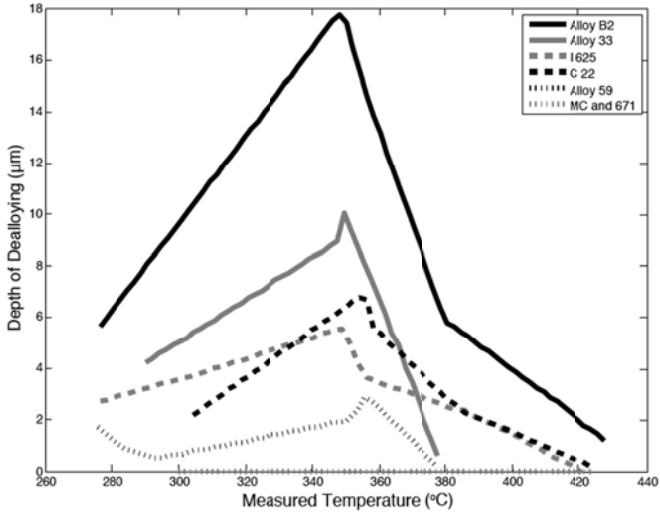

Figure 43. The depth of dealloying as a function of temperature for various high nickel alloys exposed to an acidic chlorinated feed stream. Reprinted from Ref. 1, Copyright (2008) with permission from NACE International.

Was et.al.[117] studied the corrosion of a series of austenitic alloys, including Type 304 (UNS S30400) and Type 316L (UNS S31603) stainless steels and the nickel-base alloys Alloy 625 (UNS N06625) and Alloy 690 (UNS N06690), in deaerated water at temperatures ranging from 400°C to 550°C at a pressure of 25 MPa (250 bar). Under these conditions, the density varies from about 0.1 g/cm^3 (550°C) to about 0.2 g/cm^3 (400°C). The weight gain was found to follow parabolic kinetics

$$w^2 = k_0 e^{-Q/RT} t \tag{69}$$

where W is the weight gain, k_0 is a rate constant, Q is the activation energy, and t is the time of exposure.

The Arrhenius plots displayed in Fig. 44 demonstrate that the corrosion rate (as reflected in the weight gain) demonstrate that the rate increases with increasing temperature at supercritical temperatures in contrast to the findings of Mitton, et al.[1] shown in Fig. 43.

In the case of Was et al.[117] the reaction medium was pure water containing no acidic electrolyte, so that the issue of dissociation is moot. Even though K_w decreases sharply over the 400°C to 550°C temperature range, the lack of a corrosive species (e.g., H^+) at significant concentration also negates the impact of density upon volumetric concentration and the rate becomes dominated by the activation process as reflected through the rate constant, thereby yielding linear Arrhenius plots with positive values for the activation energy (Fig. 44).

Extensive analyses of the oxide films formed on the alloys using electron back scattering diffraction (EBSD), orientation imaging microscopy (OIM), glancing X-ray Diffraction (GXRD), and X-ray photo-electron spectroscopy (XPS), together with scanning electron microscopy (SEM) / energy dispersive spectroscopy (EDS). The oxide scales formed on the stainless steels were found to be multilayer in morphology, with a chromium-rich spinel inner layer adjacent to the metal and a magnetite (Fe_3O_4) outer layer. In

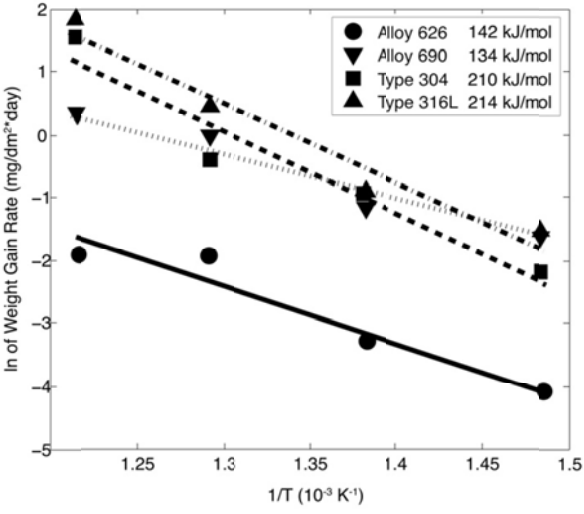

Figure 44. Arrhenius plots for oxide growth on austenitic stainless steels and nickel-base alloys in deaerated water at temperatures from 400°C to 550°C. Reprinted from Ref. 114, Copyright (1999) with permission from NACE International.

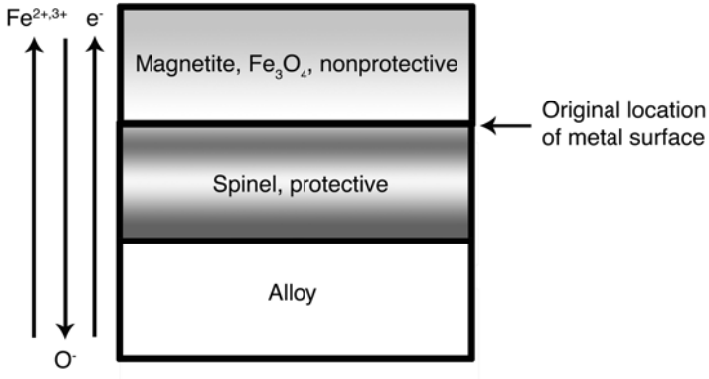

Figure 45. Model proposed by Was et.al.[117] to explain the oxidation of austenitic stainless steels and nickel-base alloys in supercritical, deaerated water. Reprinted from Ref. 114, Copyright (1999) with permission from NACE International.

the case of Alloy 690, the inner layer comprised chromia (Cr_2O_3), nickel oxide (NiO), and the spinel $Ni(Cr, Fe)_2O_4$. The oxide film on Alloy 625 was found to be too thin to be effectively analyzed. For the most part, the form of attack was general (uniform) corrosion; however, Alloy 625 also exhibited pitting attack with the pits ranging up to about 5 μm.

The model postulated by the authors to explain their results is depicted in Fig. 45. In this model, the inner layer is envisioned to grow directly into the metal, in agreement with the Point Defect Model[118] and other modern theories for the growth of barrier oxide layers, via the inward movement of oxygen ions via the counterflow of oxygen vacancies that are generated at the metal/inner layer interface and are annihilated at the inner layer/outer layer interface via the injection of oxygen ions from water. On the other hand, the magnetite outer layer on steels exposed to high temperature aqueous solutions form as crystalline phases as indicated in Fig. 46a. Each crystallite forms via an electrocrystallization process from the Fe^{2+} ions that are transmitted as interstitials through the inner layer and injected into the solution at the base of the porous outer layer[87] (Fig. 46b).

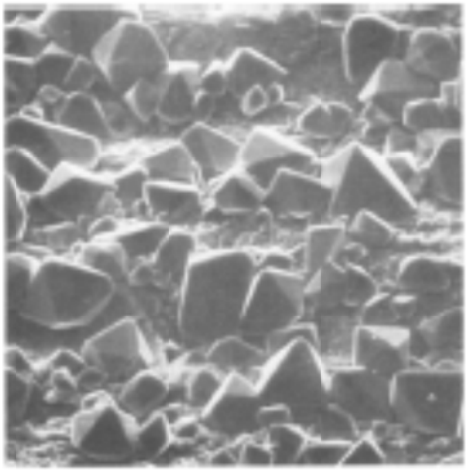

(a)

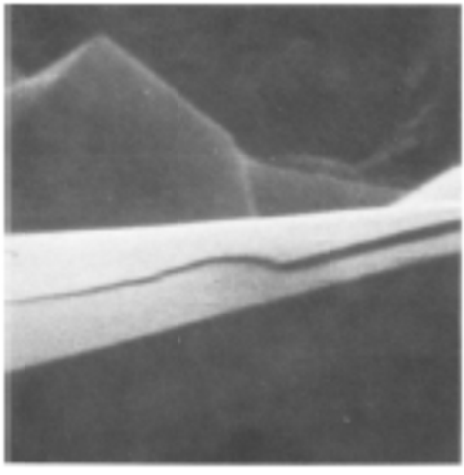

(b)

Figure 46. Morphology of the outer layer formed on iron in 1 M LiOH solution at 200°C for 24 hours at a potential of -1250 mV [Hg/Hg_2SO_4, K_2SO_4 (sat) at 22 °C], corresponding to open circuit. (a) Overview (900X). (b) Growth step on crystallite face (18000X). Reprinted from Ref. 86, Copyright (1973) with permission from The Electrochemical Society.

$$3\ Fe^{2+} + 4\ H_2O \rightarrow Fe_3O_4 + 8\ H^+ + 2\ e^- \qquad (70)$$

The authors note that the inner layer/outer layer interface remains at the location of the original metal/solution interface; a finding that was apparently first reported by Potter and Mann.[119]

Because the rates of growth of the inner and outer layers are proportional to the fluxes of oxygen vacancies and iron interstitials, respectively, with the volumes of the respective phase formed being corrected for the effective density, the constant volume nature of the barrier layer growth implies a relationship between the transport numbers for oxygen vacancies and cation interstitial in the inner layer. While a satisfactory atomic scale explanation of this phenomenon has yet to be given, it is likely that the relationship between the fluxes is such that the stress within the barrier layer and hence its Gibbs energy is minimized. Citing the work of Crouch and Robertson,[120] the authors conclude that diffusion of oxide ions through the inner layer occurs via *short circuit* paths along the grain boundaries. In this regard it is known that the inner (barrier) oxide layer that forms on iron comprises nanocrystallites,[121] such that a significant fraction of the surface is covered by highly disordered grain boundary phase through which rapid diffusion is envisioned to occur.

Similar studies have been reported by Ampornrat and Was[122] on ferritic-martensitic alloys (T91, HCM12A, HT-9), Chen et al.[123] on oxide dispersion strengthened 9Cr ferritic steel (9Cr ODS),[124] and by Motta et al.,[124] also on 9Cr ODS steel. The findings of these studies are all broadly similar; where measured, the oxidation follows a parabolic rate law and the oxide layer exhibits a bilayer (or, sometimes, a multilayer) structure comprising a chromium-rich spinel inner (barrier) layer and a porous, outer layer of magnetite. The proposed oxidation mechanisms are essentially the same as that articulated by Was et al.[117]

Because of the use of zirconium alloys for fuel cladding in nuclear power reactors and because of the intense interest in supercritical water reactors under the Generation IV reactor development program, it is not surprising that the corrosion of zirconium alloys in supercritical water have been extensively studied by Yilmazbayhan,[125] Peng,[126] Jeong,[124] and Motta.[128] Weight gain versus time data from the work of Jeong et.al.[127] for various zirconium alloys along with low alloy steels and austenitic iron- and

nickel-base alloys in supercritical pure water are plotted in Fig. 47. The reader will note that at short times the rate law is parabolic, but at longer times the increase in weight due to the formation of the oxide layer changes linearly with time. This behavior is a characteristic of the oxidation of zirconium alloys and the transition from parabolic kinetics to linear growth kinetics is attributed to the fracture of the oxide film due to the growth generated stresses within the film. The data show that while Zr sponge, crystal bar zirconium, and Zircaloy-4 showed accelerated corrosion rates in SCW, some of the experimental alloys exhibited good corrosion resistance that is comparable to those of the low alloy steels and austenitic alloys. The authors concluded that, as far as general corrosion is concerned, zirconium alloys should be considered for service in supercritical water nuclear reactors.

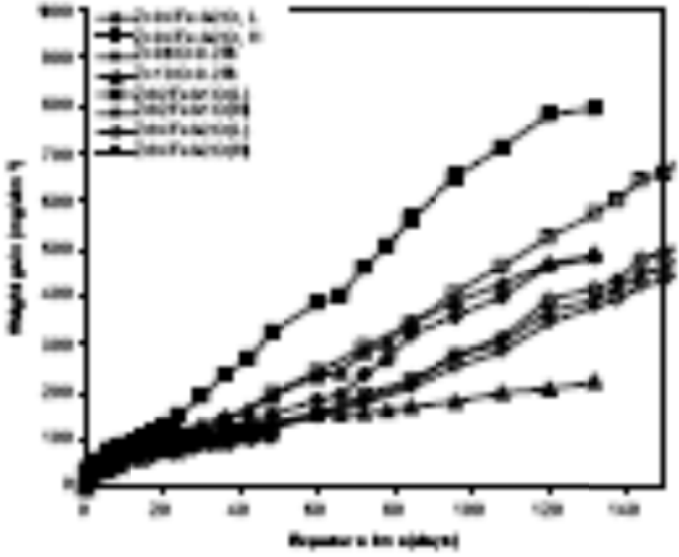

Figure 47. Weight gain versus time for various zirconium alloys, low alloy steels (T-91, HCM12A, HT-9), and austenitic alloys (304SS, 316SS, Inconel 625, Inconel 690) in steam and supercritical water at 500°C. Reprinted from Ref. 124, Copyright (2005) with permission from TMS.

2. Some Theoretical Aspects of General Corrosion Mechanisms

Prior to discussing the work that has been reported on the use of electrochemical noise analysis (ENA) or electrochemical emission spectroscopy (EES) as it is sometimes termed, it is worth discussing possible mechanisms for the corrosion of metals and alloys in high subcritical and supercritical aqueous media. The treatment that follows closely that reported by Kriksunov and Macdonald[3] and later by Guan and Macdonald.[129]

As noted elsewhere in this review, the density (ρ) and dielectric constant (ε) of high temperature water depend on the temperature and pressure of the system. For instance, $\rho = 0.6255$ g cm^{-3} and $\varepsilon = 14.85$ for $T = 350°C$, $P = 250$ bar (typical *high subcritical* conditions) and $\rho = 0.1090$ g cm^{-3} and $\varepsilon = 1.78$ for $T = 450°C$, P = 250 bar (typical *supercritical* conditions). The change of the dielectric constant of high temperature water corresponds to the change of the system density in a way that the dielectric constant decreases with increasing temperature and decreasing density. Solutes such as HCl and H_2SO_4 are fully dissociated under ambient conditions, in which the dielectric constant of water is relatively high at 78. On the other hand, strong electrolytes that are fully dissociated under ambient conditions may be very poorly ionized in low-density, supercritical aqueous systems, because of the low dielectric constant of the medium. Consequently, the corrosion of metals in high temperature aqueous systems is significantly influenced by the temperature and pressure of the systems, because of the impact that T and P have on the solvent stabilization of ions and ionic corrosion properties.

Due to the unique properties of high temperature water, the corrosion of metals and alloys in high subcritical and supercritical aqueous systems (SCAS) shows characteristics that can be attributed to either *electrochemical oxidation* (*EO*) or *chemical oxidation* (*CO*) mechanisms, depending upon the density and dielectric constant of the media, as suggested by the earlier work of Liu, et al.[130] A corrosion reaction involving partial interfacial charge transfer process, as envisioned by the Wagner-Traud hypothesis in relatively high-density subcritical and supercritical solutions is called

an *electrochemical oxidation* (*EO*) process, because the overall reaction can be decomposed into partial anodic and partial cathodic charge transfer reactions: $M \rightarrow M^{n+} + ne^-$ (partial anodic reaction) and $O_2 + 4\ H^+ + 4e^- \rightarrow 2\ H_2O$ (partial cathodic reaction) occurring on the surface.[128] The overall reaction is: $M + n/4\ O_2 + n\ H^+ \rightarrow M^{n+} + n/2\ H_2O$. Because charge species are stabilized in systems with higher dielectric constant, and because ions are more effectively hydrated at higher densities, the EO mechanism is favored in relatively high density solutions.

In general, low-density SCAS (supercritical aqueous solutions, which are often analogous to low pressure gas phases) have characteristics that include low dielectric constants; low degrees of dissociation for acids, bases, and salts; and low salt solubility. In addition, the hydrogen bonds that exist in low temperature solutions are extensively broken in low-density SCAS with the consequence that the fluid takes on less *water-like* properties as the temperature increases and the fluid density decreases. Furthermore, the dissociation constant of water (K_w) decreases sharply with increasing temperature and decreasing density as the temperature increases above the critical temperature. Likewise, base dissociation and acid dissociation constants decrease with increasing temperature and decreasing density with the result that both bases and acids become less *strong* with increasing temperature and decreasing density. Thus, the attenuated dielectric screening of solvents enhances the tendency of ions pairing in low-density SCAS.[132] Consequently, corrosion processes occurring in low-density SCAS are dominated by direct molecular processes and are termed as *chemical oxidation* processes. Unlike the EO mechanism, in which corrosion typically involves two or more coupled partial redox reactions at different sites on the corroding metal surfaces, the CO mechanism is envisioned to be a direct result of the reaction of the metal with the corrodent (e.g., O_2 or HCl) at a single site, as indicated by the reactions $M + O_2 \rightarrow MO_2$.[133] It is postulated that either a chemical or an electrochemical mechanism is the dominant corrosion mechanism under any given set of temperature/pressure conditions. In *condensed aqueous systems* (defined arbitrarily here as having $\rho > 0.1$ gm/cm^3) the EO mechanism is postulated to prevail, such that the electrochemical activity is detected in the form of electrochemical noise in the coupling current between two identical specimens. The CO mechanism is the dominant corrosion

process in *gaseous systems*, where the density is very low (< 0.1 gm/cm^3). A distinctive characteristic of the CO mechanism is that there are no electrons transferring from anodic sites to cathodic sites in corroding metals and no ions move through the aqueous phase between the same sites. In general, the chemical oxidation mechanism becomes important when:

(a) aggressive, nonionic components are present;
(b) the reaction medium has a low dielectric constant, and
(c) the medium has low density.

As expected, those conditions inhibit the EO corrosion processes.

The electrochemical oxidation (EO) corrosion reaction in a deaerated acidic solution can be expressed by a chemical reaction form such as $M + 2\ H^+ \rightarrow M^{2+} + H_2$, which is indistinguishable from a chemical oxidation (CO) corrosion reaction such as $M + 2\ HCl \rightarrow MCl_2 + H_2$. The activity (concentration) of H^+ has been widely used to indicate the corrosion susceptibility in condensed liquid solutions (pH is the independent variable in Pourbaix diagrams). On the other hand, undissociated, aggressive species such as HCl and H_2S become important in low-density supercritical aqueous systems, corresponding to the CO dominant corrosion processes. Consequently, the reaction rate of an electrochemical/chemical corrosion process in a deaerated, acidic, high subcritical and supercritical solution can be expressed by the chemical reaction rate law,

$$R = k\left[C_{H^+}\right]^a \tag{71}$$

where k is the heterogeneous rate constant. Based on the transition state theory, the rate constant can be expressed as $k = k^0 \exp(-\Delta G^{0,\neq}/R_g T)$, in which superscript "0" designates the reference conditions, $\Delta G^{0,\neq}$ is the change in standard Gibbs energy of activation and is defined as the difference in Gibb's energy between the reactants and the transition state, and R_g is the universal gas constant. C_{H+} in Eq. (71) is the volumetric concentrations of hydrogen ion and a is the corresponding reaction order. The dominant form of corrosion in high temperature, acidic solutions is acid attack. Therefore, the Y^- ion is not treated as an aggressive ion and the Y^-

ion-induced corrosion phenomena, such as pitting, is not included in Eq. (71).

The volumetric concentration (mol/l of the solution) of C_{H^+} in Eq. (71) is density dependent and can be expressed in terms of the molal (mol/kg of solvent) concentration by,

$$C = \frac{1000 m\rho}{1000 + mM_s} \tag{72}$$

where M_s is the molecular weight of the dissolved species (g/mol), m is the molal concentration (mol/kg), and ρ is the density of the solution (g/cm^3). For dilute solutions, we can approximate $C \approx m\rho$, because $mM << 1000$. Therefore, $C_{H^+} = m_{H^+}\rho$. A relative corrosion rate in deaerated, acidic solutions can be written as follows[134]

$$\frac{R}{R_0} = \left[\frac{m_{H^+}}{m_{H^+,0}}\right]^a \left[\frac{\rho}{\rho_0}\right]^a \exp\left(\frac{-\Delta G^{\neq}}{R_g T} + \frac{\Delta G^{\neq}}{R_g T_0}\right) \tag{73}$$

Equation (73) can be expressed in logarithmic form such as,

$$\ln\left(\frac{R}{R_0}\right) = a \ln\left[\frac{m_{H^+}}{m_{H^+,0}}\right] + a \ln\left[\frac{\rho}{\rho_0}\right] + \left(\frac{-\Delta G^{0,\neq}}{R_g T} + \frac{\Delta G^{0,\neq}}{R_g T_0}\right) \tag{74}$$

The first term in the right hand side of Eq. (74) is the temperature dependent degree of dissociation of H^+; the second term represents the effect of temperature on the volumetric concentration of the attacking species; and the last term corresponds to the temperature dependence of the reaction rate constant. The quantity $\Delta G^{0,\neq}$ is the change in standard Gibbs energy of activation for the reaction. The model shows that the temperature dependence of the corrosion rate can be attributed to two competing effects:

- the increase in the corrosion rate with increasing temperature due to the exponential (Arrhenius) dependence of the rate constant on temperature, and;

- the decrease in the corrosion rate with increasing temperature corresponding to the decrease in the dissociation of an associated species (e.g., an acid, such as HCl) that produces the attacking species (e.g., H^+) and the decreasing density of the medium.

One of the two corrosion mechanisms (chemical oxidation and electrochemical oxidation) should prevail under any given set of working conditions. Electrochemical noise (spontaneous potential and current emissions) should be observed only in the case of the electrochemical oxidation (EO) mechanism and not in the case of the chemical oxidation (CO) mechanism. This is postulated, because only in the EO case is the partial anodic and partial cathodic reactions spatially and temporally separated, resulting in current transients being induced in the wire coupling the identical, but spatially separated specimens. Thus, the noise in the coupling current between a pair of identical working electrodes in high pressure, high temperature aqueous environments has been measured as a function of pressure (up to 300 bar) and temperature (up to 500^{o}C). Each test was measured for 30 minutes and standard deviation of current noise was calculated for every test. It is assumed that the current noise (standard deviation of current noise) is proportional to the electrochemical corrosion rate, when the electrochemical mechanism is operative.[131,135]

3. ENA Studies of General Corrosion

Electrochemical noise analysis (ENA), which is also known as electrochemical emission spectroscopy (EES), was first introduced by Iverson for corrosion studies around 40 years ago and it has become one of very promising corrosion monitoring methods, due to its unique advantages, such as non-perturbative, *in-situ* application, and simplicity.[136,137] Electrochemical noise (EN) is a series of naturally-occurring transient events and is measured as fluctuations of coupling current noise between the two identical working electrodes, as measured using a zero resistance ammeter (ZRA) and as fluctuations in the potential of one of the specimens measured against a low noise reference electrode. Since the electrochemical noise is produced by the fluctuation in corrosion rates across the electrode surfaces, it has been proposed that the shape

and amplitude of the noise transients, among other characteristics of the EN data, are directly related to the electrochemical corrosion rates in the system.[138]

Mansfeld et al.[138] applied electrochemical noise analysis (ENA) to the study of corrosion process on iron in NaCl solution and they observed that the root mean square (RMS) of current noise is largest for iron in aerated NaCl solution in which significant corrosion occurs. By applying ENA to monitor corrosion processes of carbon steel and stainless steel in high temperature (including supercritical) aqueous systems, Macdonald et al.[130,133] suggested that the RMS of the electrochemical noise is related to the corrosion rate, with a high current noise being associated with a high corrosion rate. They also concluded that corrosion was the dominant source of electrochemical noise based on the correlation between the measured noise and the extent of corrosion. Recently, ENA has been successfully applied in monitoring and differentiating corrosion mechanisms in high subcritical and supercritical aqueous systems.[137] Consequently, ENA is a effective and convenient method for studying corrosion activity and rate in elevated temperature systems.

4. Effect of Temperature

Electrochemical noise analysis, ENA (sometimes termed electrochemical emission spectroscopy, ECS) has proven to be an effective method of following the kinetics of corrosion reactions in high subcritical and supercritical aqueous media, because the method can be applied *in situ* to obtain rate data without interrupting the experiment. The first application of ENA (ECS) to the study of metal corrosion in supercritical aqueous systems appears to be that of Liu et al.[130] on 1013 carbon steel in oxygenated water as a function of temperature and oxygen concentration. The study was based upon earlier, unpublished data by Macdonald and Chen,[139] who found that, under ambient conditions, the root mean square of the electrochemical noise generated between two identical steel electrodes and measured by a wide bandwidth zero resistance ammeter (ZRA) was proportional to the instantaneous corrosion rate. The apparatus used to record the coupling current noise is shown in Fig. 48. The apparatus included a band-pass filter, so that only noise having components within a specified frequency range were

analyzed. The cell and electrodes were conventional with the cell being located in a flow loop that was capable of operating at supercritical temperatures. Control of the oxygen concentration was affected by sparging the reservoir with O_2/N_2 mixtures of the appropriate compositions.

Upon increasing the temperature into the supercritical region, the RMS of the noise is found to pass through a maximum at about 440°C, as shown in Fig. 49, which is significantly higher that that observed for corrosion in acidic (HCl) environments. However, in this case, the dissociation of an acid (e.g., HCl) is not an issue, because the medium is pure water. Thus, with increasing temperature, only the change in density and hence the change in volumetric concentration is the issue and the latter reflects the change in density. In order to illustrate the impact of density, the density versus temperature is also plotted in Fig. 49. It is seen that the density decreases precipitously as the temperature increases above the critical temperature. While the maximum in the corrosion rate might have been expected to occur at a lower temperature, if the dominant effect had

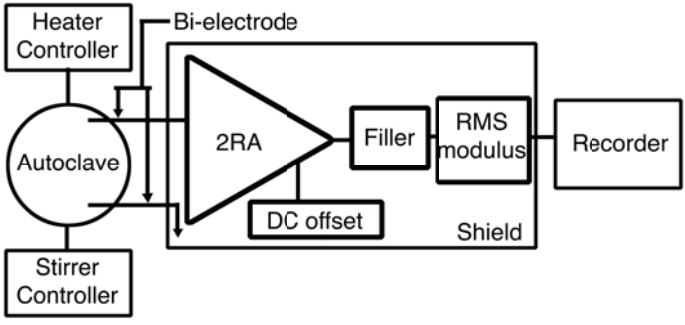

Figure 48. Electrochemical noise recording system. Reprinted from Ref. 127, Copyright (2005) with permission of NACE International.

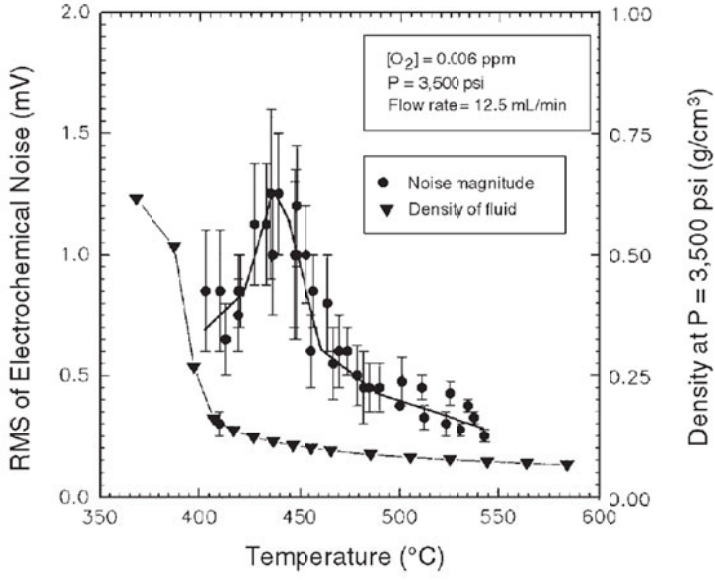

Figure 49. Dependence of the RMS of the noise in the coupling current between identical 1013 carbon steel specimens in oxygenated water at a pressure of 3500 psi (238 bar) on temperature. Also plotted is the density of the medium versus temperature. Reprinted from Ref. 127, Copyright (2005) with permission of NACE International.

been the change in volumetric concentratioon of oxygen, the corrosion rate data are not inconsistent with the density data when it is recognized that the impact of temperature on the rate constant of the reaction dominatess the rate of reaction over a range of temperature extending from 374°C to about 440°C even as the volumetric concentration falls. In any event, it is evident that the model that postulates that the rate of reaction is governed by a competition between the effect of temperature on the rate constant and on the dissociation of an electrolyte and the volumetric concentration of the reactant (O_2 and/or H^+) accounts for the observed behavior as proposed by Kriksunov and Macdonald.[3]

Figure 50 displays the RMS of the coupling current noise generated between two identical 1013 carbon steel specimens at 481°C as a function of pressure and density. It is evident that the corro-

sion rate depends on density and hence the volumetric concentration of oxygen, but the important lesson from this plot is that the rate of reaction, as measured by the RMS of the coupling current noise, does not extrapolate to zero at zero density. These data suggest that at densities below about 0.06 g/cm^3 a corrosion process exists that do not generate noise in the coupling current or even in a coupling current itself. It is argued later in this review that two corrosion processes do, indeed, exist; a *chemical oxidation* process that resembles *dry oxidation*, in which no separate partial anodic and cathodic processes exist on the surface, and the

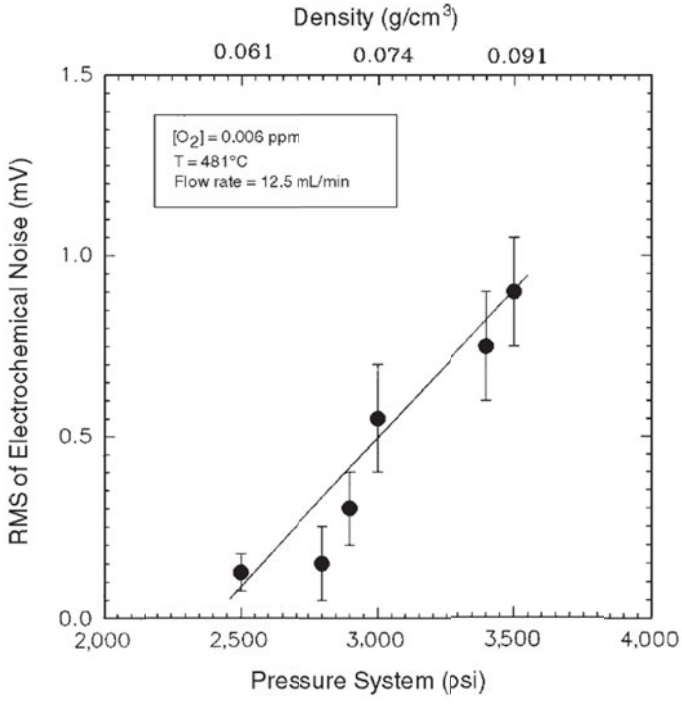

Figure 50. Dependence of the RMS of the noise in the coupling current between identical 1013 carbon steel specimens in oxygenated water at a pressure of 3500 psi (238 bar) as a function of pressure. Reprinted from Ref. 127, Copyright (2005) with permission of NACE International.

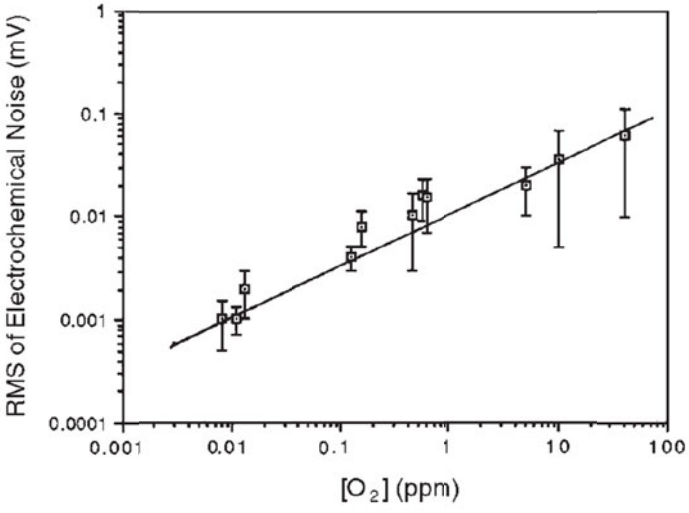

Figure 51. Dependence of the RMS of the noise in the coupling current between identical 1013 carbon steel specimens in oxygenated water at 250°C and at a pressure of 1400 psi (9.65 MPa) as a function of oxygen concentration. Reprinted from Ref. 127, Copyright (2005) with permission of NACE International.

electrochemical oxidation process that does result in the spatial separation of partial anodic and cathodic processes on the surface, whose momentary imbalance results in the coupling current and noise in that quantity. This issue will be explored further when the corrosion of stainless steels and titanium in HCl and NaOH solutions is considered later in this chapter.

The dependence of the RMS of the noise in the coupling current was also measured on 1013 carbon steel in subcritical water at 250°C and P = 9.65 MPa (Fig. 51) and in supercritical water at a pressure of 23.8 MPa and at a temperature of 410°C, and the data are plotted in Fig. 52. At both temperatures, the rate of the reaction is found to be half order in oxygen, provided that the oxygen concentration exceeds 0.2 ppm for the higher concentration. At lower oxygen concentration, the RMS of the noise and hence the reaction rate is independent of $[O_2]$ (i.e., the order of the reaction with respect to O_2 is zero). This observation is most readily accounted for by postulating two parallel reactions; one in which the corrodents

is O_2 and the other in which the corrodents is water; that is,

$$\text{Metal} + O_2 \rightarrow \text{Corrosion Products} \tag{75}$$

and

$$\text{Metal} + H_2O \rightarrow \text{Corrosion Products} \tag{76}$$

At 410°C, the rates of these two reactions are equal at an oxygen concentration of 0.2 ppm.

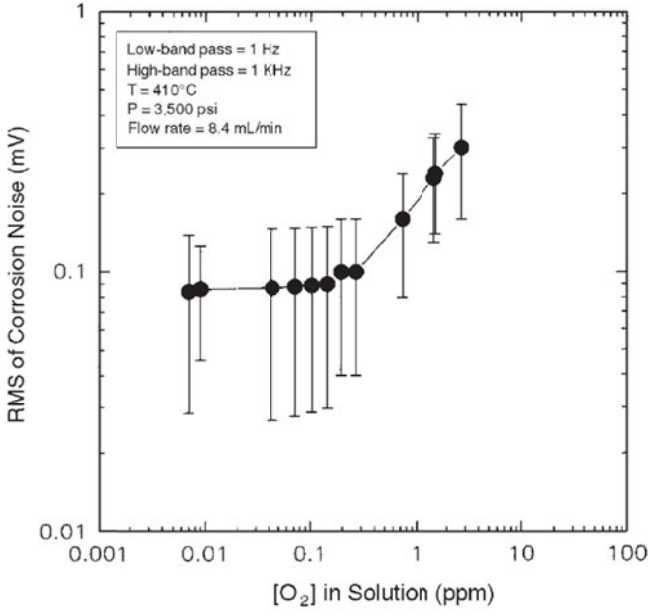

Figure 52. Dependence of the RMS of the noise in the coupling current between identical 1013 carbon steel specimens in supercritical oxygenated water at 410°C and at a pressure of 3500 psi (23.8 MPa) as a function of oxygen concentration. Reprinted from Ref. 127, Copyright (2005) with permission of NACE International.

In some instances, at 405°C and at P = 14.8 MPa (2150 psi), large excursions were observed in the RMS versus time traces, as shown in Fig. 53(a). These excursions were identified with the pitting attack shown in Fig. 53(b). However, if the pressure was increased to 18.9 MPa (2750 psi), the excursions were no longer observed and pitting attack did not occur. The origin of this form of localized attack is currently unknown.

In a later study, Zhou et.al.[139] studied the corrosion of Type 304 SS in 0.1m NaCl+0.01m HCl and 0.1m NaCl+0.001m HCl saturated with H_2 gas at ambient temperature ($[H_2] = 7.84 \times 10^{-4}$ m) at temperatures ranging from 150°C to 400°C, using the test system shown in Fig. 54.

The ENA sensor comprised two identical Type 304 SS wire electrodes and one platinum wire electrode that served as a low noise reference electrode (note that the potential of the Pt electrode is determined by the H_2/H^+ electrode reaction, with both the fugacity of H_2 and the activity of H^+ being fixed by the solution composition). The coupling current between the two steel electrodes was monitored using the ZRA while the potential of one of the SS electrodes was monitored using the Pt electrode. Every effort was made to mitigate contamination of the solution by corrosion products from the stainless steel apparatus; thus, the solution was delivered to the cell via PEEK tubing and, prior to coming in contact with the sensors, the solution was in contact with only zirconia or PTFE. The potential of the Pt wire versus the Ag/AgCl, Cl^- external reference electrode measured on the two solutions was consistent with the calculated pH difference, thereby demonstrating the viability of both reference electrodes.[140]

Typical potential and coupling current noise data are shown in Fig. 55(a) and (b), respectively.

Posttest examinations included determination of weight loss and SEM/EDS examination of the steel surface. A typical SEM micrograph of the corroded surface is displayed in Fig. 55. The form of attack was observed to be *scaling* with sections where it was apparent that exfoliation had occurred (Fig. 55b), as observed in other studies.[141] The exfoliated material is almost certainly the outer layer, which from passivity theory forms via the hydrolysis of cations (Fe^{2+}) that are transmitted as cation interstitials across the barrier oxide layer from the metal/barrier layer interface to the barrier layer/outer layer (solution in the pores of the outer layer) to

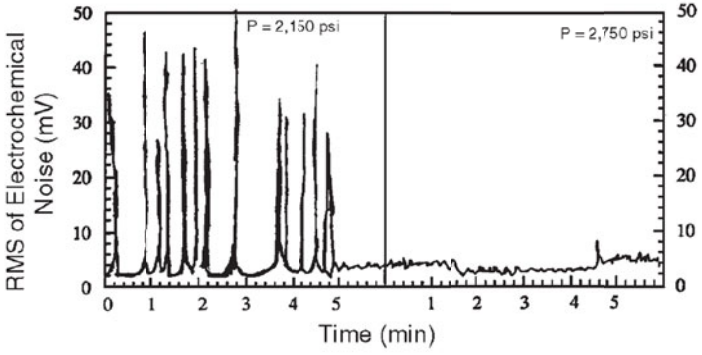

(a)

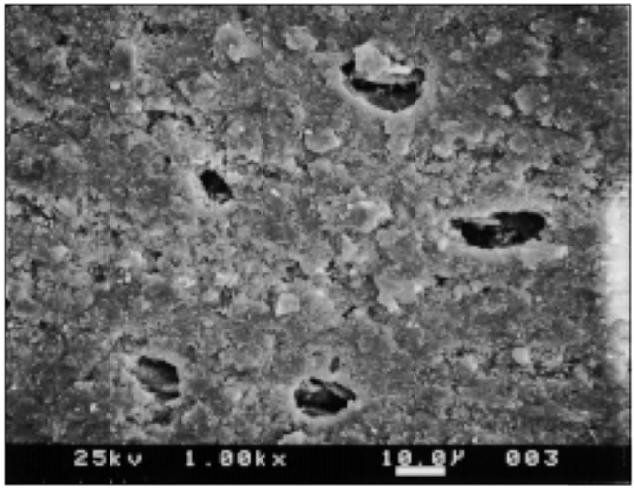

(b)

Figure 53. (a) RMS of the noise in the coupling current showing the large excursions that have been identified with the pitting attack shown in the micrograph (b). $T = 405^{o}C$, $P = 14.8$ MPa (2150 psi)/18.9 MPa (2750 psi), $[O_2] = 6$ ppb. Reprinted from Ref. 127, Copyright (2005) with permission of NACE International.

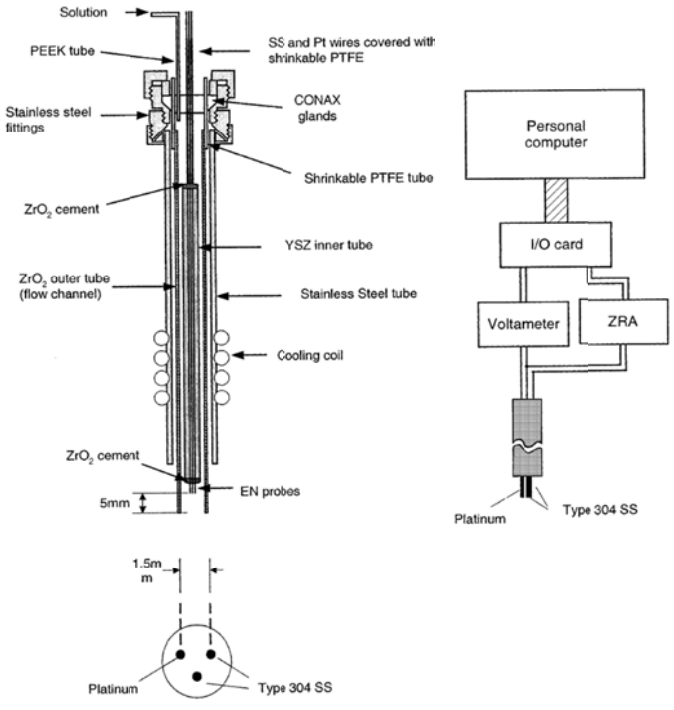

Figure 54. Test cell used for studying the general corrosion of Type 304 SS in HCl + NaCl solutions at temperatures ranging from 150°C to 400°C. (a) ENA sensor and data acquisition system. (b) Schematic of hydrothermal test cell. Reprinted from Ref. 140, Copyright (2009) with permission from Elsevier.

form porous magnetite via an electrocrystallization process (Fig. 46b). Previous studies on the oxide films that form on stainless steels in supercritical aqueous solutions[115] demonstrate that the barrier layer is a spinel, which the author postulates is a defective phase of the general stoichiometry $[Fe(Cr,Ni)]_{3+x}O_{4-y}$, indicating that the principal defects in the barrier layer are cation interstitials and oxygen vacancies. The former are formed by direct injection of cations into the film at the metal film interface, while the latter are generated at the

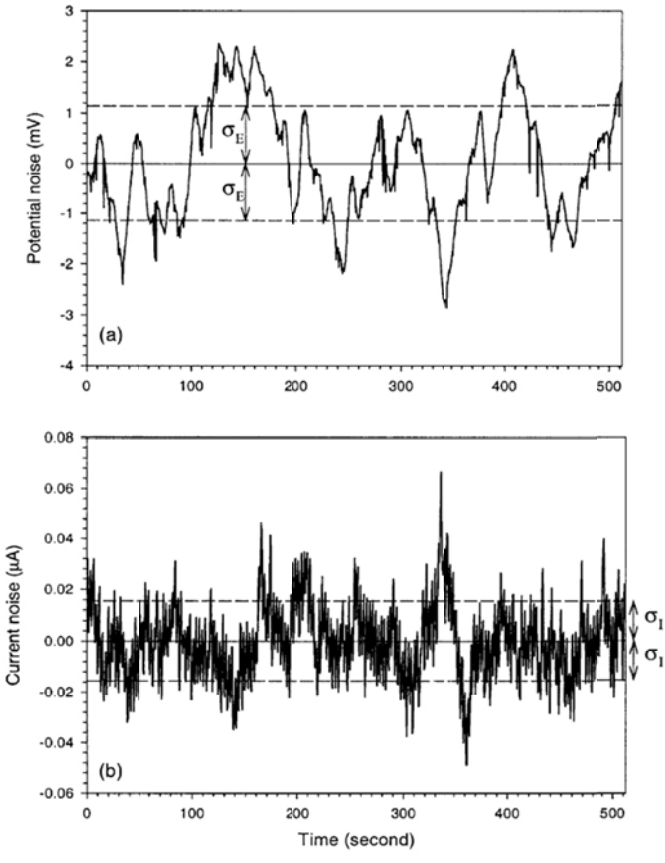

Figure 55. Potential and coupling current traces for Type 304 SS in hydrogenated 0.1 m NaCl + 0.01 m HCl solution at 350ºC and 25 MPa after correction for drift. Reprinted from Ref. 140, Copyright (2009) with permission from Elsevier.

same location by growth of the barrier layer into the metal.[116] The metal interstitials ($M_i^{\chi+}$) and the oxygen vacancies ($V_O^{\bullet\bullet}$) are annihilated at the barrier layer/outer layer (solution) interface via ejection from the layer and by injection of oxide ions from water, respectively. The latter process results in the growth of the barrier layer into the metal, while the former results in the growth of the outer layer. Thus the outer layer forms as a precipitated, somewhat

fragile layer that is subject to exfoliation, as observed (Fig. 56a). The measured weight loss was used to estimate a corrosion current density, assuming that the corrosion rate was constant over the exposure time, and the results are plotted in Fig. 55. The data indicate that the corrosion rate passes through a maximum at about 350°C, in keeping with the findings of other studies. Again, the maximum in the corrosion rate is attributed to a competition between the effect of temperature upon the rate constant of

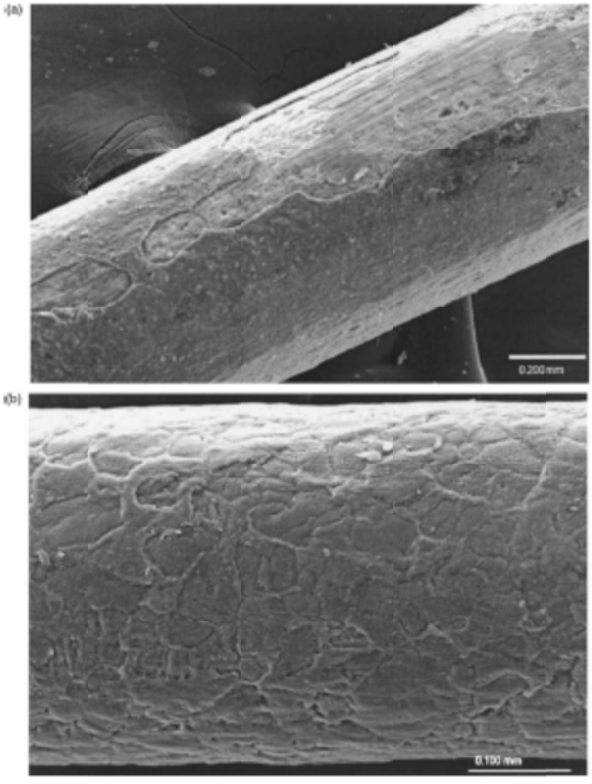

Figure 56. SEM micrographs of the surface of Type 304 SS after exposure to 0.1 m NaCl + 0.01 m HCl solution at: (a) 150 °C and (b) 390 °C at 25 MPa for 168 hours and 1 hour, respectively. Reprinted from Ref. 140, Copyright (2009) with permission from Elsevier.

the reaction, as described by the Arrhenius equation, and the effect of temperature on the dissociation of the electrolyte (e.g., HCl) and the volumetric concentration, as articulated by the model of Kriksunov and Macdonald.[3]

The corrosion rate calculated from the mass loss of Type 304 SS as a function of temperature and flow rate through the test cell is plotted in Fig. 57. The corrosion rate is found to increase slightly with increasing flow rate at all temperature, possibly because of enhanced mass transfer rates to the metal surface, although the effect is not strong. The important observation from these data is that the corrosion rate is observed to pass through a maximum at about 350°C, as observed by Mitton et al.[1] (Fig. 43) and Guan and Macdonald (Fig. 61) (see below).

The potential and coupling current versus time traces shown in Fig. 55 were used to calculate the *noise resistance* as the ratio of the standard deviation in the potential divided by the standard deviation in the current. The resulting noise resistance data are plotted along with the mass loss corrosion rate data versus temperature in Fig. 58. The two sets of data closely parallel one another

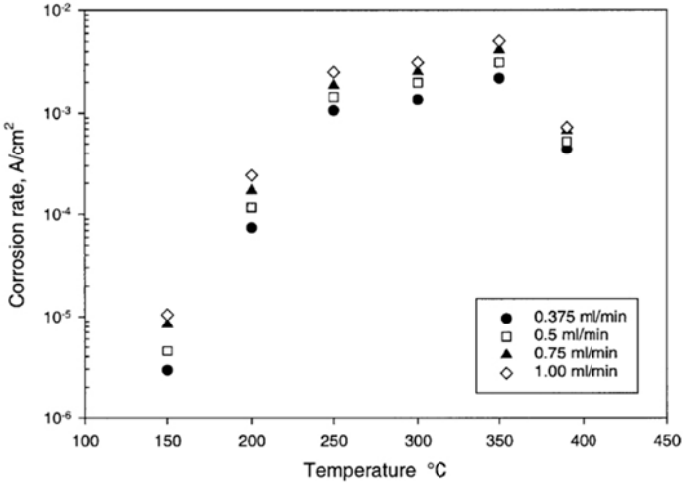

Figure 57. Corrosion current density calculated from mass loss versus temperature for Type 304 SS in 0.1 m NaCl + 0.01 m HCl solution at a pressure of 25 MPa. Reprinted from Ref. 140, Copyright (2009) with permission from Elsevier.

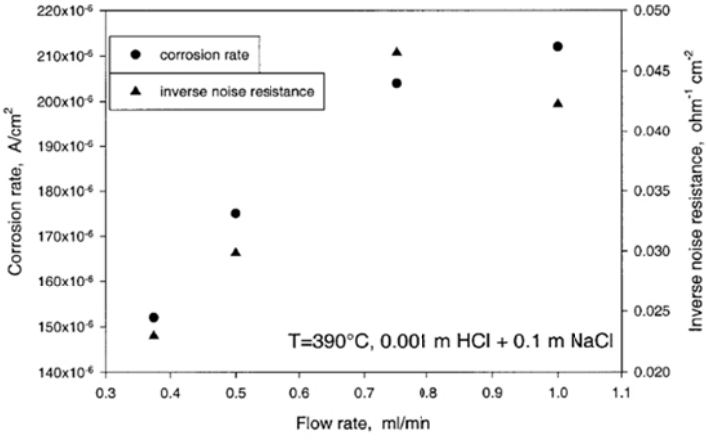

Figure 58. Comparison between the corrosion rate (expressed as an average current density as calculated from the weight loss using Faraday's law) and the reciprocal of the "noise resistance" as a function of temperature. Reprinted from Ref. 140, Copyright (2009) with permission from Elsevier.

and, again demonstrate that the corrosion rate passes through a maximum at about 350°C, although the noise resistance data are not as convincing in this aspect as are the mass loss data.

A comparison between the corrosion rate (expressed as an average current density as calculated from the weight loss using Faraday's law) and the reciprocal of the *noise resistance*, which is proportional to the corrosion rate via the Stern-Geary relationship, as a function of temperature. The Stern-Geary relationship for the corrosion current density, i_{corr}, is expressed as:

$$i_{corr} = \frac{1}{R_p} \frac{b_a b_c}{2.303(b_a + b_c)} \tag{77}$$

where R_p is the polarization resistance, which may be equated to the *noise resistance*, if the latter is measured over s sufficiently long time that the impedance corresponds to the steady-state, and b_a and b_c ate the inverse Tafel constants for the anodic and cathodic processes, respectively.

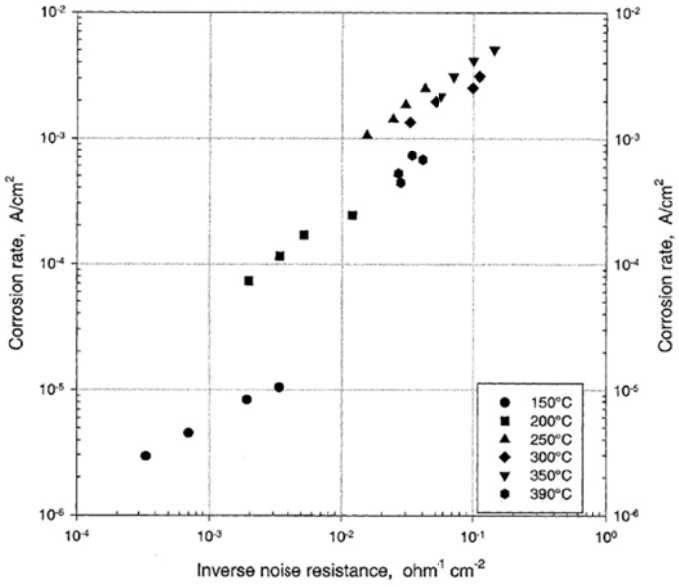

Figure 59. Relationship between the noise resistance as calculated from ENA data and the corrosion rate calculated from weight loss data. Reprinted from Ref. 140, Copyright (2009) with permission from Elsevier.

Finally, the data plotted in Fig. 59 demonstrate the relationship between the inverse of the noise resistance and the corrosion rate, expressed as corrosion current density as a function of temperature, as calculated from the Stern-Geary relationship and the noise resistance estimated from the ENA data. Generally good agreement is obtained, although there is clearly a discrepancy between the data sets for 150°C and for those for higher temperature. The origin of this discrepancy has not been identified.

In summary, the study by Zhou et al.[140] confirmed the findings of the prior work by Liu et al.,[130] that electrochemical noise analysis is an effective method for monitoring the corrosion rate of metals and alloys in high subcritical and supercritical aqueous solutions. The method is readily calibrated and, when used to estimate the noise resistance, and yields a quantity (the polarization resistance) that is directly related to the corrosion current density and hence the corrosion rate through the Stern-Geary relationship. This

relationship requires knowledge of the anodic and cathodic inverse Tafel constants in the form of the quantity, $b_a b_c/(b_a + b_c)$, which may be determined by calibration of the inverse noise (polarization) resistance data on mass loss data or by measuring b_a and b_c directly in polarization experiments. The former method was employed in the work of Zhou et al.[141] for temperatures up to 300°C, but the second method is also viable.

In a more recent study of the electrochemistry and corrosion behavior of Type 304 SS and titanium in high subcritical and supercritical aqueous solutions, Guan and Macdonald[129] monitored the noise in the coupling current

Following the work of Liu, et al.[130] and Zhou and coworkers,[134] Guan and Macdonald[129] carried out extensive studies of the corrosion of Type 304 SS and titanium in HCl solution at high subcritical and supercritical temperatures as a function of temperature and pressure. These studies again employed electrochemical noise analysis (ENA) as the principal tool for monitoring the corrosion rate in situ. The experiments were carried out in a high pressure/high temperature flow loop (Fig. 60) using an ENA sensor of the type shown in Fig. 54. Figure 61 shows the relationship between the standard deviation of the current noise (proportional to electrochemical corrosion rate) and temperature for Type 304 stainless steel in deaerated 0.01 m HCl. The working pressure was 250 bar and the HCl solution was deaerated by nitrogen gas sparging. The current noise is observed to increase to a maximum as the temperature rises to approximately 350°C, as also found by others. Then, the current noise decreases sharply after the temperature passes the critical point (374.15°C). This can be explained by the chemical/electrochemical corrosion mechanisms theory, as outlined earlier in this review. Below the critical temperature, the increased corrosion activity, due to increasing temperature (exponential dependence of the rate constant on temperature, as described by the Arrhenius equation), dominates over the effects of falling density and dielectric constant, resulting in the electrochemical corrosion rate increasing as the temperature increases. Beyond the temperature of the maximum in corrosion rate, the test solution changes from being a condensed, liquid aqueous phase to a gas-like phase and the density decreases sharply. Consequently,

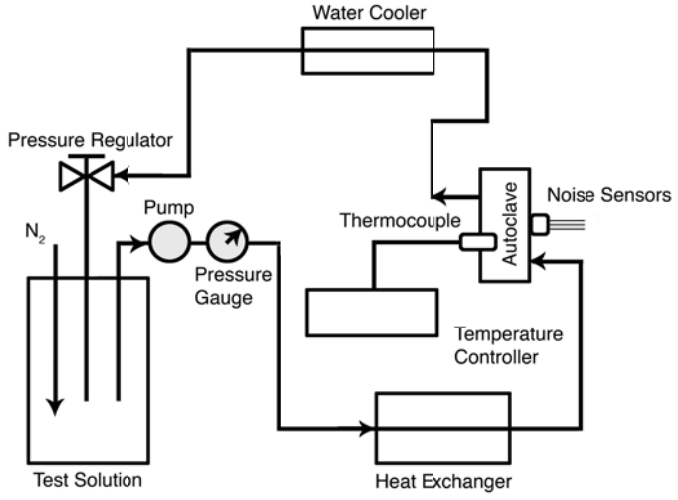

Figure 60. Schematic of the high temperature, high pressure circulating loop system. Reprinted from Ref. 142, Copyright (2009) with the permission from NACE International.

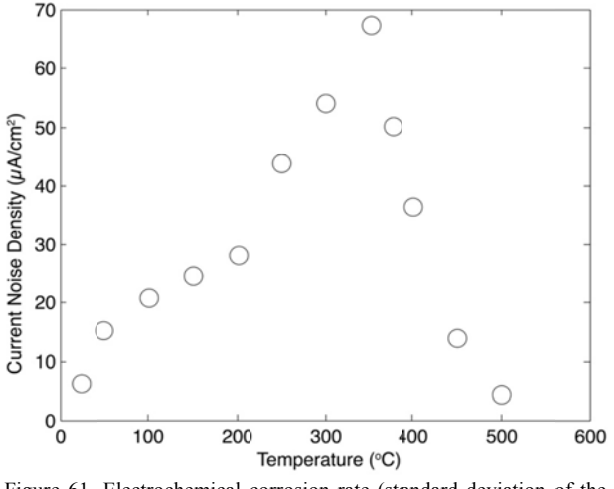

Figure 61. Electrochemical corrosion rate (standard deviation of the current noise) of Type 304 SS as a function of temperature at 250 bar in deaerated 0.01 m HCl. Reprinted from Ref. 140, Copyright (2009) with the permission from NACE International.

the molal concentration of H^+ decreases sharply with increasing temperature at high subcritical and supercritical temperatures and it decreases further with increasing temperature, because HCl becomes increasingly poorly dissociated, as noted above. Under those conditions, the electrochemical oxidation (EO) corrosion mechanism is less prevalent and the corrosion current noise decreases sharply due to the dominant effects of increasing temperature on the concentration of the aggressive species and on the dissociation of HCl. This result corresponds to experimental observations that severe corrosion damage occurs in those regions of a reactor that operate at temperatures just below the critical temperature, whereas less damage is observed at higher or lower temperature.

Figure 62 shows the effect of oxygen on the electrochemical corrosion rate of Type 304 SS in 0.01 m HCl as a function of temperature from ambient to 500°C. The solid points in the figure represent the electrochemical current noise of Type 304 SS in deaerated 0.01 m HCl (N_2 sparged) and the open points represent the electrochemical current noise of the steel in 0.01 M HCl purged with oxygen gas in the solution reservoir at ambient temperature and pressure. Thus, the oxygen concentration in the latter case was about 40 ppm ($2.5x10^{-3}$ m). The working pressures for both experiments were 250 bar. Similar to that observed for the corrosion of Type 304 SS in deaerated, 0.01 m HCl (Fig. 61), the current noise (which is proportional to electrochemical corrosion rate) of Type 304 SS in oxygenated 0.01 m HCl increases with increasing temperature and passes through a maximum prior to the temperature reaching the critical value of 374°C. Thereafter, the current noise amplitude decreases as the temperature passes the critical temperature of the medium. The electrochemical corrosion rate at the maximum at $T = 350$°C in the oxygenated environment is only marginally greater than that in the deaerated environment (Fig. 62). These data indicate that, by itself, oxygen is not a particularly aggressive solute, at least in this particular case, as indicated by the relative corrosion rates observed in the deaerated vs. the oxygenated environments. The graph shows that the presence of oxygen increases the corrosion rate within the temperature range of 150°C to 400°C, but only by 0–25%. Thus, at the peak, the increase is ~25 %. It is important to note that the drop-off of the current noise becomes

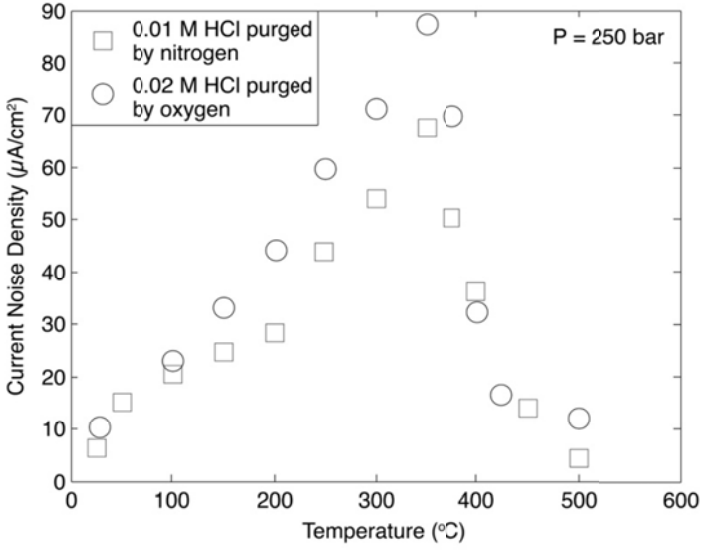

Figure 62. Comparison of electrochemical corrosion rates (standard deviations of current noise) of Type 304 SS in deaerated 0.01 m HCl and in 0.01 m HCl purged with oxygen gas as a function of temperature at 250 bar. Reprinted from Ref. 140, Copyright (2009) with the permission from NACE International.

less steep as temperature ascends above 400°C in both experiments. This indicates that, un-der constant pressure conditions, in a supercritical environment, the effect of temperature on the reaction rate is independent of the concentration of oxygen, suggesting that the dominant factor is the dissociation of HCl.

Figure 63 compares electrochemical amplitude of the current noise (proportional to the electrochemical corrosion rate) of Type 304 SS and of titanium in deaerated 0.01 m HCl as a function of temperature at a pressure of 250 bar. The solid squares are the current noise for Type 304 SS and open squares are the current noise of titanium, respectively. As shown by the figure, the current noise for titanium increases with increasing temperature before the temperature reaches the critical area, then the current noise decreases with increasing temperature with a maximum, again, occurring at about 350°C. As before, the observed maximum can be explained

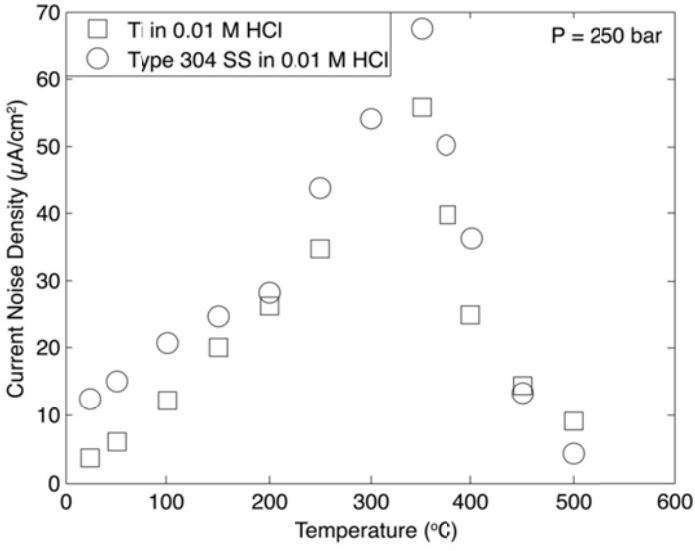

Figure 63. Comparison of electrochemical corrosion rates (standard deviations of current noise) of Type 304 SS and Ti in deaerated 0.01 m HCl as a function of temperature at 250 bar. Reprinted from Ref. 140, Copyright (2009) with the permission from NACE International.

by the electrochemical/chemical corrosion mechanisms discussed previously in this review. The electrochem-ical corrosion rate increases with increasing temperature before it reaches a maximum value at 350°C, because the corrosion process is dominated by the increase in the rate constant with increasing temperature, noting also that HCl is essentially completely dissociated at temperatures below 350°C. Then, the electrochemical corrosion rate decreases sharply in the high subcritical and supercritical region, because of the low degree of dissociation of aggressive electrolyte (HCl), the low dielectric constant of the system, and the decrease in the density. The graph shows that the titanium is more corrosion resistant than is Type 304 SS in 0.01 m HCl as the current noise of Type 304 SS is around 10-15% higher than the current noise for titanium. Botella et al.[141] reported that titanium and its alloys have relatively high corrosion resistance when they were exposed to

high subcritical and supercritical HCl solutions, which can be attributed to the formation of the protective passive film on the titanium surface. They also reported that the titanium corrosion rate increases with increasing temperature in subcritical temperature range and decreases with increasing temperature in the supercritical temperature range. These finding are consistent with the results presented in Fig. 63.

Figures 63 and 64 shows the current noise of Type 304 SS as a function of temperature in 0.01 m HCl and in 0.01 m H_2SO_4. The working pressure for both experiments was 250 bar. Both HCl and H_2SO_4 solutions in the figure were purged by oxygen. Similar to the 0.01 m HCl case, the electrochemical corrosion rate of Type 304 SS in 0.01 m H_2SO_4 increases with increasing temperature before reaching a maximum value at approximately 350°C. Then, the electrochemical current noise decreases sharply in the supercritical temperature region (T > 374.15°C), because of the decreasing dielectric constant and density of the supercritical medium as the temperature is raised. As demonstrated by the data in the figure, a relatively larger current noise was obtained in 0.01 m HCl than in 0.01 m H_2SO_4, which may be due to the presence of pitting corrosion in the chloride-containing solution or due to chloride-catalyzed dissolution of the passive film.

Figure 65 shows the response of the standard deviation of the noise in the coupling current of Type 304 SS in deaerated 0.01 m NaOH as a function of temperature. Again, the working pressure was 250 bar. The current noise is observed to increase to a maximum value as the temperature rises to 300°C, which is significantly lower than the 350°C observed in the case of HCl. Then, the current noise decreases sharply. This can be explained, again, by the chemical/electrochemical corrosion mechanisms theory, as outlined previously in this review. AS before, at low temperatures (T < 300°C), the corrosion process is dominated by the exponential (Arrhenius) dependence of the rate constant on increasing temperature. At temperatures higher than that at which the maximum corrosion rate occurs, the standard deviation of the current noise decreases sharply with increasing temperature, following the same behavior observed in other systems for the same reasons.

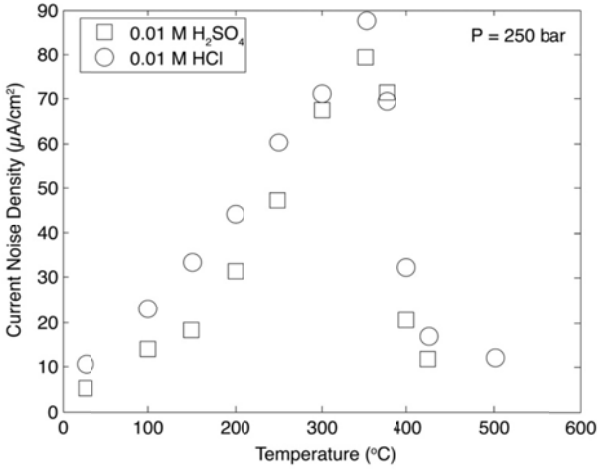

Figure 64. Comparison of electrochemical corrosion rates (standard deviations of the current noise) of Type 304 SS in 0.01 m H_2SO_4 purged by oxygen and in 0.01 m HCl purged by oxygen as a function of temperature at 250 bar. Reprinted from Ref. 140, Copyright (2009) with the permission from NACE International.

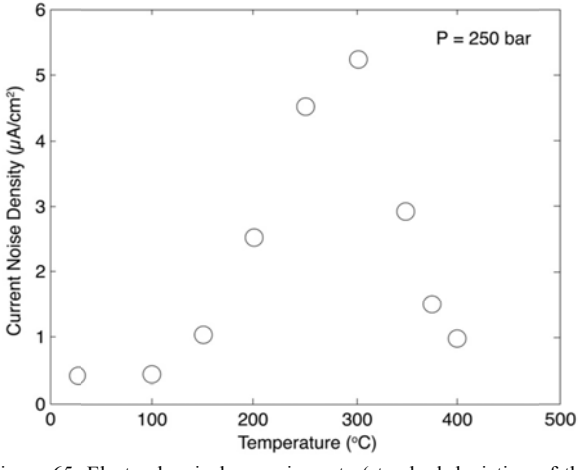

Figure 65. Electrochemical corrosion rate (standard deviation of the current noise) of Type 304 SS as a function of temperature at 250 bar in 0.01 m NaOH purged with nitrogen. Reprinted from Ref. 140, Copyright (2009) with the permission from NACE International.

Figure 66 compares electrochemical corrosion rates (standard deviation of current noise) of Type 304 SS in water, 0.01 m NaOH, and in 0.01 m HCl. The media in all three experiments were purged by N_2 and the working pressures were identical at 250 bar. The standard deviation in the noise of the coupling current for Type 304 SS in 0.01 m NaOH is around 5 times higher than that in water at 350°C. The current noise of Type 304 SS in 0.01 m HCl is much higher than those in 0.01 m NaOH and water as demonstrated by the figure. In fact, the standard deviation of the current noise from Type 304 SS in 0.01 m HCl is more than 20 times higher than that from the same alloy in 0.01 m NaOH at 350°C.

The corrosion rate of metals in deaerated acidic solutions can be expressed by,

$$R = k\left[C_{H^+}\right]^a\left[O_2\right]^b = km_{H^+}^a m_{O_2}^b \rho^{a+b} \tag{78}$$

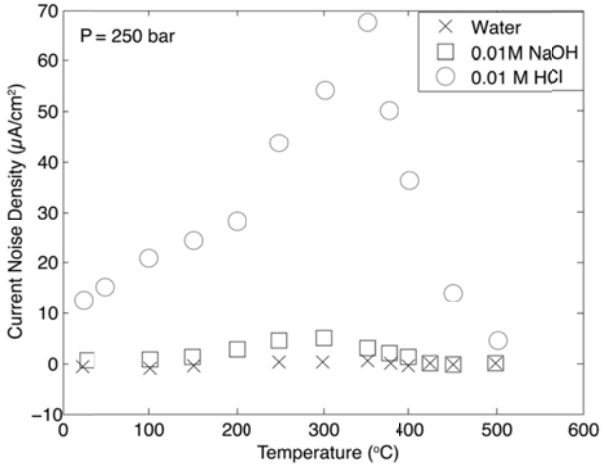

Figure 66. Comparison of electrochemical corrosion rates (standard deviations of the current noise) of Type 304 SS in deaerated water, in deaerated 0.01 m NaOH and in deaerated 0.01 m HCl at 250 bar as a function of temperature. Reprinted from Ref. 140, Copyright (2009) with the permission from NACE International.

where a and b are the reaction order with respect to H^+ and O_2, respectively. The standard Gibbs energy of activation ($\Delta G^{0,\neq}$), which may be determined by mass transfer or charge transfer processes, can be estimated by using Eq. (6). As there are no data available for the reaction order, α, of the electrochemical corrosion reactions of Type 304 SS in high temperature acidic solutions, we assume that the reaction orders with respect to both H^+ and O_2 are one half. Accordingly, $a = b = ½$ is used in this study. A value of $b = ½$ was previously found experimentally for the corrosion of carbon steel in supercritical aqueous solutions, as shown in Fig. 52.[128] The molal concentration of hydrogen ion (m_{H+}) was obtained by solving the speciation problem based on mass balance, charge balance, and mass action equations for the appropriate reaction set.[131] The density was taken as that for pure water from the NIST steam data, as the working solutions are dilute [NIST Steam Algorithm]. The relative corrosion rate R/R^0 was obtained experimentally by electrochemical noise analysis (ENA).

Figure 67 shows the energy of activation for electrochemical corrosion processes for Type 304 SS and titanium in deaerated 0.01 m HCl at the temperature range of 50–250°C. The solid squares in the figure are the energy of activation of Type 304 SS and the open squares are the energy of activation of titanium. As shown by the figure, the energy of activation for corrosion of Type 304 SS is lower than that for titanium. Although the corrosion resistance of stainless steel is lower than that of titanium in those environments, the rate of change of corrosion with increasing temperature is greater for titanium than for stainless steel. This observation is consistent with the results obtained previously, as presented by Fig. 63, in which the standard deviation of the coupling current noise for titanium is lower than that for Type 304 SS. As noted previously, the high corrosion resistance of titanium can be attributed to the formation of a protective passive film of TiO_2 on its surface. It is important to note that the above calculation of the activation energy is based on the assumptions that the electrochemical corrosion rate is proportional to the standard deviation in the coupling current noise, as measured by monitoring spontaneous current fluctuations between identical electrodes using a zero resistance ammeter (ZRA), and the corrosion reaction rate is a half

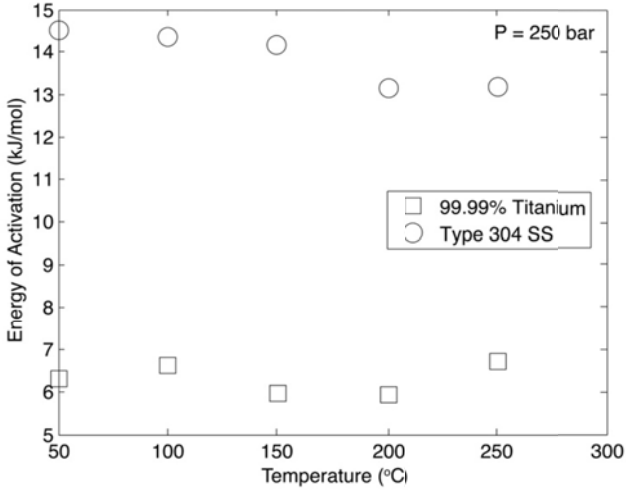

Figure 67. Comparison of energy of activation of electrochemical corrosion processes of Type 304 SS and Ti in deaerated 0.01 m HCl solution at 250 bar as a function of temperature. Reprinted from Ref. 140, Copyright (2009) with the permission from NACE International.

order with respect to both H^+ and O_2. At the current time, there is no theoretical and experimental support for the latter two assumptions, except for the observed half order of the corrosion rate of carbon steel in supercritical aqueous solutions with respect to oxygen.[128]

5. Effect of Pressure on Metal Corrosion Rate

Due to the unique properties of high subcritical and supercritical aqueous systems (SCAS), two corrosion mechanisms, i.e., *electrochemical oxidation* (*EO*) and *chemical oxidation* (*CO*), have been postulated to describe the corrosion of metals and alloys in high temperature media,[143] as outlined above. EO usually involves two or more coupled partial redox reactions at different sites on the corroding metal surfaces in relatively high-density SCAS. On the other hand, CO is postulated to occur through direct reaction of aggressive species with the metal in one act (but possibly in several elemental steps) on one site in low-density supercritical aqueous

solutions, without direct charge transfer between sites, due to the low degree of dissociation and low dielectric constants. Since the overall reaction form of a EO process (such as $M + 2\ H_2O \rightarrow MO_2 + 4\ H^+ + 4\ e^-$ and $O_2 + 4\ H^+ + 4\ e^- \rightarrow 2\ H_2O$ to give the overall reaction $M + O_2 \rightarrow MO_2$) is indistinguishable from that of a CO process ($M + O_2 \rightarrow MO_2$), the reaction rate of an electrochemical/chemical corrosion process in a deaerated, acidic, high subcritical and supercritical solution can be expressed by the following rate law,

$$R = k\left[C_{H^+}\right]^a \tag{79}$$

where k is the heterogeneous rate constant with $k = \kappa(k_B T/h)\exp(-\Delta G^{0,\neq}/RT)$, k_B is Boltzmann's constant, h is Planck's constant, T is the Kelvin temperature, $\Delta G^{0,\neq}$ is the change in standard Gibbs energy of activation, C_{H+} is the volumetric concentration of hydrogen ion, and a is the corresponding reaction orders with respect to H^+. It is postulated that either a chemical or an electrochemical mechanism is the dominant corrosion mechanism under any given set of temperature/pressure conditions. The activity of H^+ has been widely used to indicate the corrosion susceptibility in condensed liquid solutions (as indicated in a Pourbaix diagram). The dominant form of corrosion in high temperature acidic solution is acid attack. Consequently, corrosion in those solutions is an electrochemical oxidation (EO) dominated process in which the cathodic partial reaction is hydrogen evolution. Other species, such as Cl^-, may be aggressive and induce particular forms of corrosion, such as pitting, or may enhance the general corrosion rate by catalyzing the dissolution of the barrier oxide layer of the passive film, as noted previously. These species are not included in Eq. (71). The treatment of this topic presented below is essentially identical to than recently published by Guan and Macdonald.[129]

By taking the natural logarithm of Eq. (71) and differentiating with respect to pressure, the pressure dependence of the corrosion reaction rate in high temperature aqueous systems can be expressed as,

$$\left(\frac{\partial \ln R}{\partial P}\right)_T = \left(\frac{\partial \ln k}{\partial P}\right)_T + a\left(\frac{\partial \ln C_{H^+}}{\partial P}\right)_T \tag{80}$$

As illustrated by Eq. (80), the pressure effects on corrosion reaction rate can be attributed to the impact of pressure on the activation process and on volume concentration of the aggressive species.[144] The volumetric concentrations (mol/l of the solution) of the aggressive species, C_{H+}, in Eq. (80) is density-dependent and can be expressed in terms of the molal (mol/kg of solvent) concentration by

$$C = \frac{1000 m\rho}{1000 + mM_s} \tag{81}$$

where m is the molal concentration (mol/kg), M_s the molecular weight of dissolved species (g/mol), and ρ is the density of the solution (g/cm^3). For dilute solutions, we can approximate that $C \approx m\rho$ as $mM_s << 1000$. The pressure dependence of the molar concentration then becomes

$$\left[\frac{\partial \ln(C)}{\partial P}\right]_T = \left[\frac{\partial \ln(m)}{\partial P}\right]_T + \left[\frac{\partial \ln(\rho)}{\partial P}\right]_T = \left[\frac{\partial \ln(m)}{\partial P}\right]_T + \kappa_T \tag{82}$$

where $[\partial \ln(\rho)/\partial P]$ is defined as the isothermal compressibility (κ_T) of the system with $\kappa_T = \partial \ln(\rho)/\partial P = -(\partial V/\partial P)_T / V$. Since solutes, such as acids and bases, are only partially dissociated in low-density, high temperature water, the degree of dissociation of $\alpha = m/m^0$ is introduced to demonstrate the effect of pressure on the dissociation of aggressive species, where m is the molal concentration of the dissociated species such as Cl^- from HCl and m^0 is the stoichiometric concentration of the solute. Equation (82) becomes,

$$\left[\frac{\partial \ln(C)}{\partial P}\right]_T = \left[\frac{\partial \ln(\alpha)}{\partial P}\right]_T + \kappa_T \tag{83}$$

The pressure dependence of the corrosion reaction rate (Eq. 80) can be further modified by applying the above equations, such that

$$\left(\frac{\partial \ln R}{\partial P}\right)_T = \left(\frac{\partial \ln k}{\partial P}\right)_T + a\left(\frac{\partial \ln \alpha_{H^+}}{\partial P}\right)_T + a(\kappa_T) \tag{84}$$

As illustrated in Eq. (80), the effect of pressure on the rate of corrosion of metals in high temperature aqueous systems can be attributed to the activation process, to changes in the degree of dissociation of aggressive species, and to the system isothermal compressibility.

The effect of pressure on reaction rate constant k can be explained by the activated complex theory. The theory postulates that the elementary chemical reactions occur via a transition state, such as A + B ↔ $M^{\neq}$ → products, in which the reactants and transition state are assumed to be in equilibrium. The transition state (activated complex), $M^{\neq}$, is defined as the state of the maximum energy along the reaction path (*reaction coordinate*). The rate constant can be expressed as follows, based on the activated complex theory,[145]

$$k = \kappa \frac{k_B T}{h} \exp\left(\frac{-\Delta G^{\neq}}{R_g T}\right) \tag{85}$$

Where κ is the transmission coefficient, $\Delta G^{0,\neq}$ is the difference in standard Gibb's free energy between the reactants and the transition state, R_g is the universal gas constant. Based on activated complex theory, the standard volume of activation ($\Delta V^{0,\neq}$) of a reaction is related to the pressure dependence of the reaction rate constant as expressed by,

$$\Delta V^{0,\neq} = -RT(\partial \ln k / \partial P)_T = \overline{V}^{0,\neq} - \overline{V}_M^0 - \overline{V}_{H^+}^0 \tag{86}$$

where k is the rate constant, $\overline{V}^{0,\neq}$ is the standard partial molar volume of the transition state, and $\overline{V}_M^0$ and $\overline{V}_{H^+}^0$ are the standard

partial molar volumes of the reactants; metal M and H^+. It is recognized that the volume of activation includes volume changes due to solvent-solute electrostatic interaction as the reaction proceeds along the reaction coordinate toward the transition state.[146] The volume of activation for chemical reactions in liquid aqueous solutions is generally $\pm$ 50 cm^3/mol. On the other hand, a much larger volume of activation has been observed for chemical reactions in the highly compressible supercritical fluids.[128,146] For instance, the volume of activation for the uni-molecular decomposition of chlorobenzyl methyl ether in supercritical 1,1-difluoroethane is –6,000 cm^3/mol at 130°C and 50 bar and volume of activation for the uncatalyzed reaction of butyronitrile in high temperature water is around –362 cm^3/mol at 330°C and 128.5 bar.[128,133] This large volume of activation undoubtedly reflects the large magnitudes of the partial molar volumes of some species in highly compressible, supercritical fluids. Beside the electrostatic and compressibility effects, Wu et al[146] suggested that the phase-behavior and diffusional limitations effects also can affect the volumes of activation.

Based on the partial charge method, Macdonald[148] suggested that the reaction coordinate of corrosion processes of metals in deaerated acidic solutions can be expressed as follows:

$$M + 2H^+ \rightarrow [\delta\delta^{2+} + (1-\delta)M + \delta H_2 + 2(1-\delta)H^+]^{\neq} \rightarrow M^{2+} + H_2 \tag{87}$$

where *M* is the metal, the entity in square brackets is the transition state, and δ is the extent of charge development at the knoll in the reaction coordinate between the initial state and the final state (i.e., at the *transition state*). The value of the quantity δ is restricted to a range between 0 and 1. The volume of activation of this corrosion processes can be expressed as:

$$\Delta V^{0,\neq} = \overline{V}^{0,\neq} - \overline{V}_M^0 - 2\overline{V}_{H^+}^0 \tag{88}$$

where $\overline{V}^{0,\neq}$, $\overline{V}_M^0$ and $\overline{V}_{H^+}^0$ are the standard partial molar volumes of the transition state, the metal, and hydrogen ion, respectively. If the volume of activation and the partial molar volumes of the reactants are known, the standard partial molar volume of the transition

state $\overline{V}^{0,\neq}$ can be determined and the extent of the charge development in the transition state may be estimated by comparison with the partial molar volumes of model compounds, as has been done with solvolysis reactions at ambient or near ambient temperatures.[149] It is important to note that the corrosion reaction is being treated as elementary process in Eq. (78), even though the corrosion processes are typical complex, multi-step processes. However, this simplification does not compromise the present application of the partial charge method, since it is equally valid for multi-step reactions.[149]

As described before, corrosion reaction rates can be expressed in terms of the chemical reaction rate law for both chemical and electrochemical corrosion processes and the volume of activation can be expressed by Eq. (80). Applying Eq. (80) to Eq. (78) and integrating, Eq. (78) becomes,

$$\int_{P^0}^{P} \ln R dP = \left(-\frac{1}{RT}\right)\int_{P^0}^{P} \Delta V^* dP + a\int_{P^0}^{P} \ln[\alpha_{H^+}(P)]dP + a\int_{P^0}^{P} \kappa_T(P)dP \tag{89}$$

Where P^0 is the reference pressure. It is important to note that the isothermal compressibility of high temperature aqueous systems is pressure dependent. The relative corrosion reaction rate at pressure P and P^0 is expressed as,

$$\ln\left(\frac{R_P}{R_{P^0}}\right) = \left(-\frac{1}{RT}\right)\int_{P^0}^{P} \Delta V^* dP + a\ln\left(\frac{\alpha_{H^+}(P)}{\alpha_{H^+}(P^0)}\right) + a\int_{P^0}^{P} \kappa_T(P)dP \tag{90}$$

Where R_P/R_{P0} is the relative corrosion reaction rate. The first term in the right hand side of Eq. (84) is related to the activation process; the second term is the contribution from the dissociation of aggressive species; and the third term corresponds to the pressure dependence of the volumetric concentration of the aggressive species.

The experimental setup used in the study of Guan and Macdonald[126] comprised a closed, circulating loop system as illustrated in Fig. 60, within which the test solution was heated to the desired

temperatures (up to 500^{o}C) while being pumped into the reaction cell using a high pressure, positive displacement liquid chromatography pump. The internal pressure (up to 400 bar) was regulated by a check valve with a precision of ±15 bar. Heating of the cell was provided for by an OMEGA heating-band and the temperature was controlled by a temperature controller with a precision of ±1^{o}C.

The electrochemical noise sensors (ENS) used in this study comprised three identical 0.5 mm diameter Type 304 SS wires (annealed 99.98% nickel wires later). Two of the electrodes were used as *identical working electrodes* and the third was employed as the pseudo reference electrode. The three 0.5 mm diameter, identical wire electrodes were inserted into separate 1.0 mm diameter quartz tubes. The remaining space in the quartz tubes was filled with Zirconia (ZrO_2) cement to electrically insulate the electrodes from each other. The three quartz tubes were then inserted into a ceramic tube before inserting the ceramic tube into a stainless steel outer tube, which served as the pressure boundary. The ceramic and stainless steel outer tubes were sealed by Zirconia cement. The length of each wire was trimmed to 15 mm at one end, which was exposed to the high temperature test solution. The electrodes were separated from each other by a distance of 3-4 mm. The exposed wire was lightly polished and washed with acetone and de-ionized water before use. The other ends of the wires were inserted into a three-hole ceramic tube. A CONAX gland with Lava sealant was used to seal the EN sensor.

The corrosion current noise between the two identical working electrodes and the potential noise between the coupled working electrodes and the pseudo reference electrode were measured simultaneously using a Gamry PC 400 electrochemical system operating as a zero resistance ammeter. The data were collected at an acquisition rate of 2Hz and a high-frequency filter was used in this study to prevent aliasing. A ZRA maintains the two identical working electrodes at virtually the same potential via negative feedback, with the measured instantaneous coupling current being that put out by the control amplifier to maintain this condition. Furthermore, an electrometer was used to measure the potential noise, with both measurements being made simultaneously. The working solution was 0.01 M HCl.

The purpose of this study was to understand the effect of pressure on the rate of corrosion of a metal in high subcritical and supercritical aqueous systems (SCAS), with emphasis on the contributions from activation, system compressibility, and degree of dissociation of aggressive species. Since the amplitude of the electrochemical noise is postulated to be proportional to the electrochemical corrosion rate, the electrochemical corrosion rate can be estimated using electrochemical noise analysis (ENA). Note that, because the CO mechanism does not involve partial charge transfer processes, it is postulated not to produce electrochemical noise. Accordingly, measurement of the current noise and the weight loss over a period of time, and knowledge of the relationship between the current noise amplitude and the instantaneous corrosion rate, provides a means of delineating the EO and CO mechanisms. This was partially achieved by Liu et al.,[130] who measured the RMS of the noise in the coupling current between identical carbon steel electrodes in water at 450°C as a function of density and found that the noise disappeared at densities below 0.06 g/cm^3. Accordingly, we may conclude that at lower densities the dominant corrosion process is CO and at higher densities EO prevails.

As described above, the corrosion reaction rate in deaerated acidic solutions can be expressed by Eq. (72), in which the corrosion mechanism is electrochemical oxidation (EO) with H^+ being the principal corrodent. As there are no data available for the reaction order of the electrochemical corrosion of stainless steel in high temperature acidic solutions, we assume that the reaction is half order with respect to $[O_2]$, as noted above, and hence that a = ½. The relative corrosion reaction rate at pressure P with respect to that at pressure P^0 is then expressed as:

$$\ln\left(\frac{R_P}{R_{P^0}}\right)=\left(-\frac{1}{RT}\right)\int_{P^0}^{P}\Delta V^{\neq}dP+\frac{1}{2}\ln\left(\frac{\alpha_{H^+}(P)}{\alpha_{H^+}(P^0)}\right)+\frac{1}{2}\int_{P^0}^{P}\kappa_T(P)dP \tag{91}$$

where P^0 is the reference pressure, and R_P/R_{P0} is the relative corrosion reaction rate. The first term on the right hand side of Eq. (91) is due to activation; the second term corresponds to the change in the degree of dissociation of the aggressive species; and

the third term describes the pressure dependence of the volumetric concentration of aggressive species. The degree of dissociation of aggressive species (α_{H+}) in SCAS is pressure-dependent and it can be determined by modeling species dissociation equilibria based on mass balance, charge balance, and the law of mass action.[131] In this study, the compressibility of working solutions was estimated from steam data obtained from the NIST steam algorithm recognizing that 0.01 M HCl is a dilute solution.[149] The relative reaction rate of R_P/R_{P0} was measured by ENA. Consequently, the volume of activation was estimated as outlined above. Macdonald suggested that the volume of activation is only weakly dependent on pressure in liquid phases over relatively narrow pressure ranges.[137] However, the volume of activation is expected to change dramatically as the system transitions the critical temperature and is expected to display strong pressure dependence in super critical systems for the reasons discussed above. Thus, Johnson et al.[15] reported that the volume of activation of uni-molecular decomposition of chlorobenzyl methyl ether in supercritical 1,1-difluoroethane ranges from a negative few thousand cm^3/mol in the highly compressible, near-critical region to a negative few dozen cm^3/mol in the liquid state. As the compressibility of SCAS is high and hence the density of SCAS is highly pressure dependent, the volume of activation of corrosion processes in SCAS may also be highly pressure-dependent. In order to solve Eq. (90), the authors assumed that the volume of activation of a corrosion process in SCAS is constant between the two neighboring measured pressures as there are no data available for the differential relationship between the volume of activation of an electrochemical corrosion processes and pressure.

Figure 68 shows the standard deviation of the coupling current noise (postulated to be proportional to the electrochemical corrosion rate) of Type 304 stainless steel in deaerated 0.01 M HCl as a function of pressure at a high subcritical temperature ($T = 350^oC$). As demonstrated by the data, the electrochemical corrosion rate increases with increasing pressure, corresponding to negative value for the volume of activation. The figure illustrates that the current noise increases from 50.5 $\mu A/cm^2$ at 224 bar to 74.7 $\mu A/cm^2$ at 272 bar, and then to 85.8 $\mu A/cm^2$ at 317 bar. The increasing

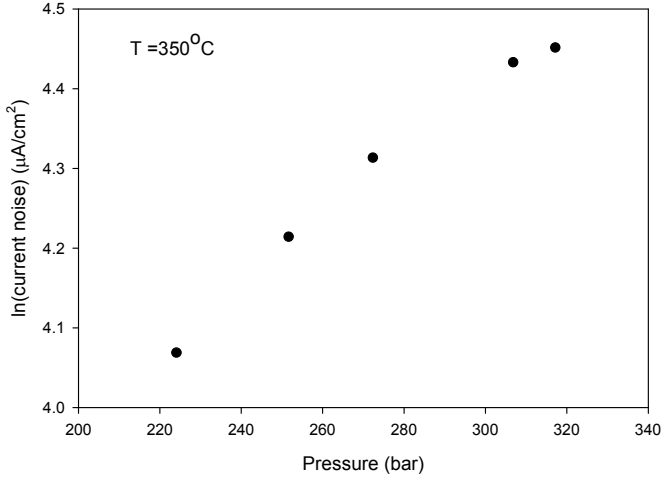

Figure 68. Electrochemical corrosion rate (standard deviation of the current noise) of Type 304 SS as a function of pressure at 350°C in deaerated 0.01 M. Reprinted from Ref. 142, Copyright (2009) with the permission from NACE International.

corrosion rates may be attributed to the effect of pressure on the solvent-solute interactions and on the degree of dissociation of the aggressive species.

Figure 69 presents the volume of activation of the electrochemical corrosion of Type 304 SS in 0.01 M HCl at 350°C as a function of pressure. In this study, the relative electrochemical corrosion rate is estimated as the ratio of the two neighboring measured standard deviations in the current noise, such as the current noise of 67.6 μA/cm^2 at 252 bar divided by the current noise of 50.5 μA/cm^2 at 224 bar. In addition, it was also assumed that the volume of activation is constant between the two neighboring measured pressures, such that the volume of activation is taken to be –210.8 cm^3/mol over the pressure range of 224 to 252 bar, –183.3 cm^3/mol over the pressure range of 252 to 272 bar, and –120.3 cm^3/mol over the pressure range of 272 to 306 bar, as explained above. As demonstrated by the data in the figure, a large, negative volume of activation (–210.8 cm^3/mol) is observed at the

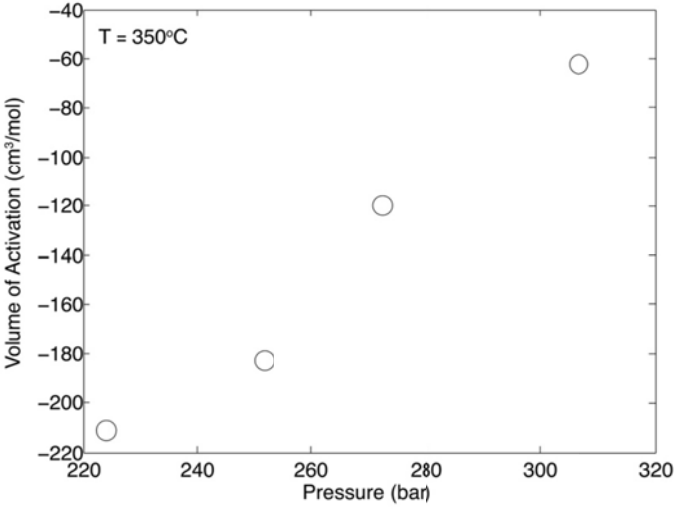

Figure 69. Volume of activation of corrosion reactions of Type 304 SS in deaerated 0.01 M HCl as a function of pressure at 350ºC. Reprinted from Ref. 142, Copyright (2009) with the permission from NACE International.

lowest pressure range of 224–252 bar and a relatively smaller, but still negative volume of activation (–63 cm^3/mol) is obtained at the highest pressure range of 306–317 bar. The negative value of the volume of activation can be attributed to electrostriction of the solvent as charge is developed and/or redistributed in the transition state. Because electrostriction is expected to result in a smaller negative volume change as the density increases, the volume of activation should become smaller as the pressure is increased, as observed.

The larger volume of activation at lower pressures may be due to the large effect of pressure on the compressibility of solvent and on the degree of dissociation of the aggressive species. So far, there are no other studies of the volume of activation of corrosion processes that could confirm or deny above position. Theoretically speaking, the postulate is reasonable, as the corrosion process presumably passes through a transition state of the type indicated in reaction (77). In forming the transition state, the charge is dispersed over a larger sphere than in the initial state, with the result

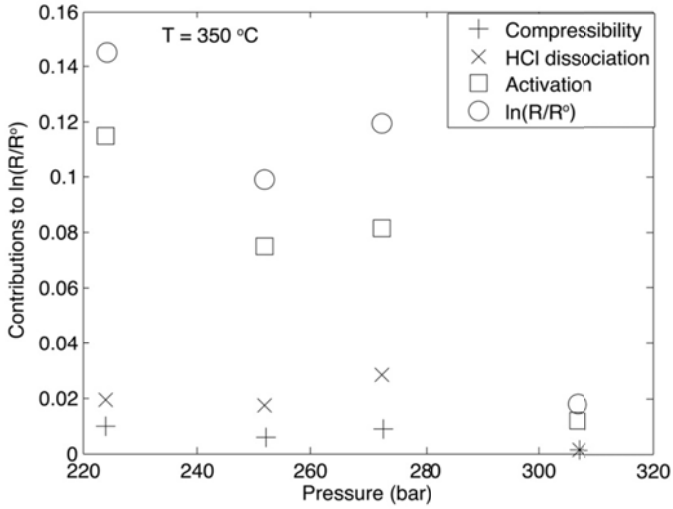

Figure 70. Contribution of activation, density, and HCl dissociation to corrosion rate of Type 304 SS as a function of pressure at 350°C in deaerated 0.01 M HCl solution. Reprinted from Ref. 142, Copyright (2009) with the permission from NACE International.

that solvent electrostriction is greater and hence the activation volume should be negative as the water is drawn into the transition state by ion-dipole interaction. Clearly, this issue needs to be explored in future work, possibly by molecular dynamics simulation.

The relative importance of the activation, compressibility, and degree of dissociation of HCl to the relative corrosion rate of Type 304 SS in deaerated 0.01 M HCl at of 350°C is illustrated in Fig. 70. As indicated by the figure, the contribution from the compressibility is much less important, compared with the contributions from the activation and HCl dissociation at high subcritical temperatures (350°C). This can be explained by the relatively small compressibility of the condensed *liquid* system. The figure also shows that the contribution from the volume of activation to the relative reaction rate is more important than the contribution from the degree of dissociation at high subcritical temperatures.

Figure 71 compares the electrochemical current noise of Type 304 SS in deaerated water and in deaerated 0.01 M HCl at 350°C

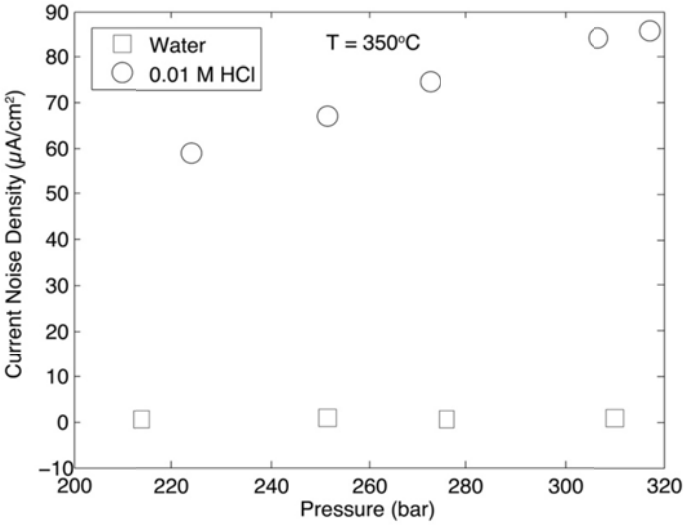

Figure 71. Comparison of electrochemical corrosion rates of Type 304 SS as a function of pressure in deaerated water in deaerated 0. 01 M HCl. Reprinted from Ref. 140, Copyright (2009) with the permission from NACE International.

as a function of pressure. The open squares in the graph represent the corrosion rate of the steel in the 0.01 HCl solution as a function of pressure, and the solid squares represent the corrosion rate in water under the identical conditions of temperature and pressure. Both solutions were deaerated by nitrogen gas. As shown by the figure, pressure has a more significant influence on the corrosion rate of Type 304 SS in 0.01 M HCl solution than it does in water. This may be attributed to the impact of pressure on the degree of dissociation of HCl, compared with that of H_2O, resulting in a much higher concentration of H^+ from HCl than from water.

Figure 72 displays the electrochemical current noise of Type 304 SS in deaerated 0.01 M HCl as a function of pressure at a supercritical temperature of 450°C. Similar to the pressure dependence of corrosion processes at subcritical temperatures (Fig. 50), the corrosion rate increases with increasing pressure yielding an apparently negative value for the activation volume. The current noise rises from 8.7 μA/cm^2 at 197 bar to 114.1 μA/cm^2 at 255 bar

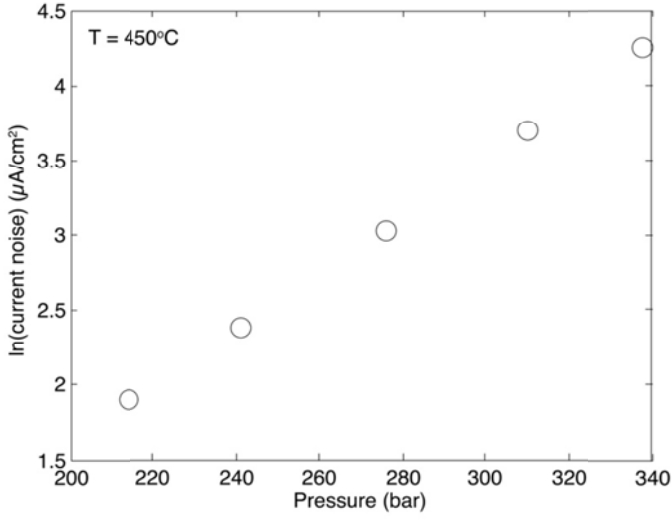

Figure 72. Electrochemical corrosion rate (standard deviation of the current noise) of Type 304 SS as a function of pressure at 450°C in deaerated 0.01 M HCl. Reprinted from Ref. 142, Copyright (2009) with the permission from NACE International.

and to 20.1 μA/cm^2 at 327 bar. However, in this case, the system is characterized by a very high compressibility, so that the effects of pressure on the activation process must be delineated from the other contributions before a rational discussion of the data can be undertaken.

Solutes, such as acids and bases, are not fully ionized under supercritical conditions, due to the low density and low dielectric constant of the solvent, as noted elsewhere in this review. For example, the density and dielectric constant of water at 450°C and 327 bar are 0.1757 g/cm^3 and 2.5, respectively, compared with that of 1 g/cm^3 and nearly 80 under ambient conditions. Additionally, a modest change in pressure of a supercritical aqueous system can strongly affect the degree of dissociation, due to the high compressibility of the systems. For instance, the degree of dissociation of 0.01 M HCl is calculated to be 1.62x10^{-7} at T = 450°C, P = 197 bar, but is 5.29x10^{-5} at T = 450°C, P = 327 bar.

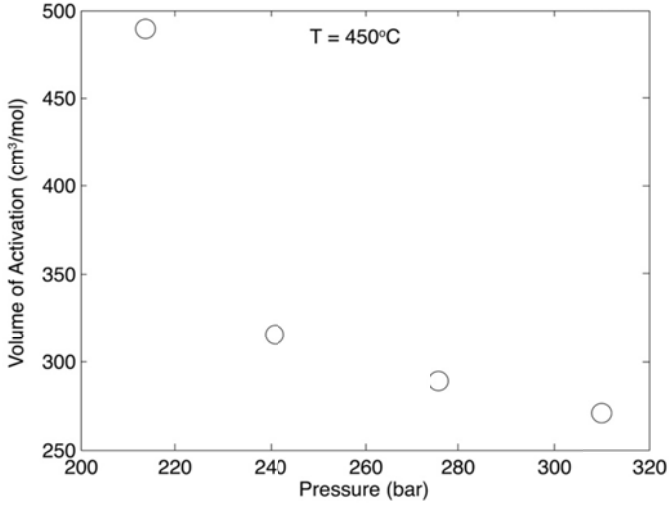

Figure 73. Volume of activation of corrosion reactions of Type 304 SS in deaerated 0.01 M HCl as a function of pressure at 450°C. Reprinted from Ref. 142, Copyright (2009) with the permission from NACE International.

Figure 73 shows the volume of activation of Type 304 SS in 0.01 M HCl at 450°C as a function of pressure after correction for the change in the volumetric concentration and the dissociation of HCl. In this case, the volume of activation is positive, rather than being negative as indicated by the raw data (Fig. 71). Similar to the corrosion processes at 350°C (Fig. 71), the magnitude of the volume of activation (but of opposite sign) decreases with increase- ing pressure (density), corresponding with the decreasing compressibility of the solvent. Fig. 74 demonstrates the contributions of activation, the degree of dissociation, and density (isothermal compressibility) to the relative corrosion rate of Type 304 SS in deaerated 0.01 M HCl at temperature 450°C. The figure shows that the contribution from the degree of dissociation dominates the pressure dependence of the relative reaction rate as the result of the significant pressure effect on the density and the degree of dissociation of systems. The contribution from compressibility is more significant at supercritical temperatures (450°C) than it is for subcritical temperatures (350°C), which is expected as the compressibility of the supercritical systems (a gas phase) is much

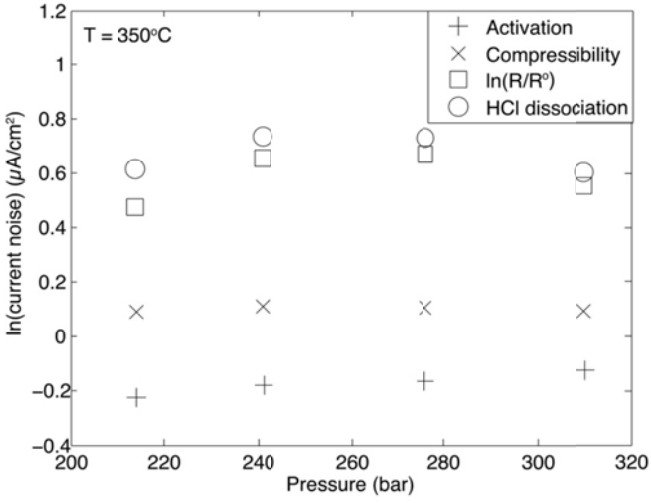

Figure 74. Contributions of activation, degree of dissociation, and compressibility to corrosion rate of Type 304 SS as a function of pressure at 450°C in deaerated 0.01 M HCl. Reprinted from Ref. 142, Copyright (2009) with the permission from NACE International.

larger than the compressibility of a subcritical systems (a condensed liquid phase).

Figure 75 illustrates the electrochemical current noise of Type 304 SS in deaerated 0.01 M HCl as a function of pressure at a supercritical temperature of 500°C. Similar to the pressure dependence of corrosion processes at 450°C (Fig.72), the corrosion rate increases with increasing pressure due to the increasing of degree of dissociation of HCl with increasing pressure. Figure 76 displays the volume of activation of Type 304 SS in 0.01 M HCl at 500°C as a function of pressure after correction for the change in the volumetric concentration and the dissociation of HCl. Similar to the pressure dependence of corrosion processes in 450°C the volume of activation is positive and the magnitude of the volume of activation decreases with increasing pressure (density), corresponding with the decreasing compressibility of the solvent.

Figure 77 demonstrates the contributions of activation, the degree of dissociation, and density (isothermal compressibility) to the relative corrosion rate of Type 304 SS in deaerated 0.01 M HCl

at a temperature 500°C. The figure shows that the contribution from the degree of dissociation and activation volume term dominates the pressure dependence of the relative reaction rate as the result of the significant pressure effect on the density and the degree of dissociation of systems, which is expected as the activation volume is higher in low-density supercritical aqueous systems than in subcritical systems.

Nickel is a very important component for many corrosion resistance alloys used in high temperature aqueous systems. Therefore, the effect of pressure on corrosion processes of nickel in high temperature acidic solutions has been analyzed. Similar to the Type 304 SS noise sensor, the nickel noise sensor comprises three identical nickel electrodes (0.5 mm annealed 99.98% nickel wire) and electrochemical noise was measured between two of the

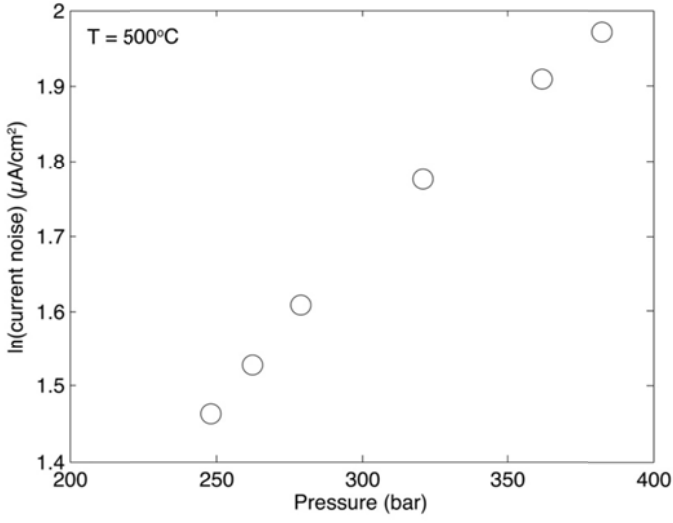

Figure 75. Electrochemical corrosion rate (standard deviation of the current noise) of Type 304 SS as a function of pressure at 500°C in deaerated 0.01 M HCl. Reprinted from Ref. 142, Copyright (2009) with the permission from NACE International.

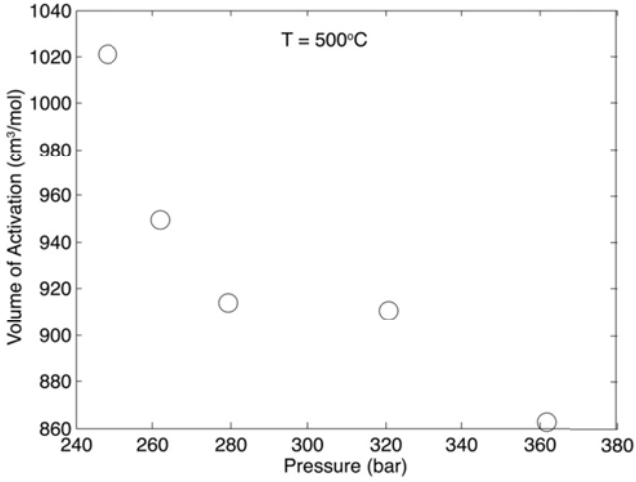

Figure 76. Volume of activation of corrosion reactions of Type 304 SS in deaerated 0.01 M HCl as a function of pressure at 500°C. Reprinted from Ref. 142, Copyright (2009) with the permission from NACE International.

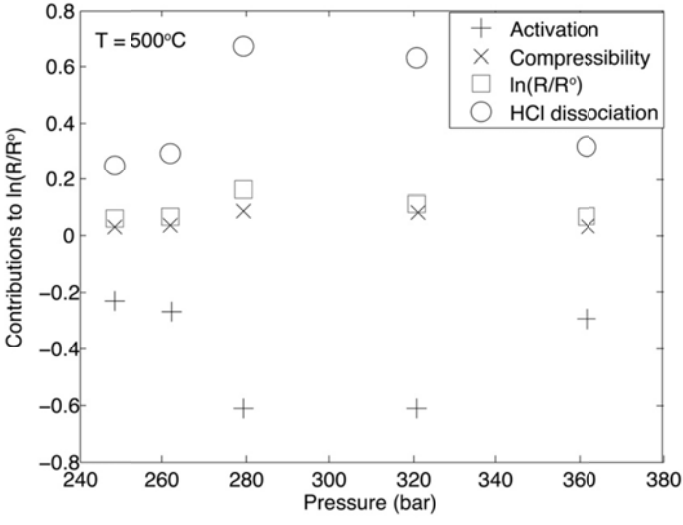

Figure 77. Contribution of activation term, degree of dissociation, and compressibility to corrosion rate of Type 304 SS as a function of pressure at 500°C in deaerated 0.01 M HCl solution. Reprinted from Ref. 142, Copyright (2009) with the permission from NACE International.

electrodes using a low noise zero resistance ammeter, while the third was employed as a pseudo reference electrode. It is important to note that the corrosion reaction rate law (Eq. 71) is a generic reaction for corrosion of metals in high temperature acidic solutions, therefore the reaction rate law and the following relative reaction rate equations should be valid for nickel (and other metals or alloys) corrosion processes in high temperature aqueous systems.

Figure 78 shows the electrochemical current noise (proportional to the electrochemical corrosion rate) of nickel in deaerated 0.01 M HCl as a function of pressure at 350°C. As illustrated by the figure, the corrosion rate increases with increasing pressure, corresponding to the increasing density and dielectric constant of the solvent.

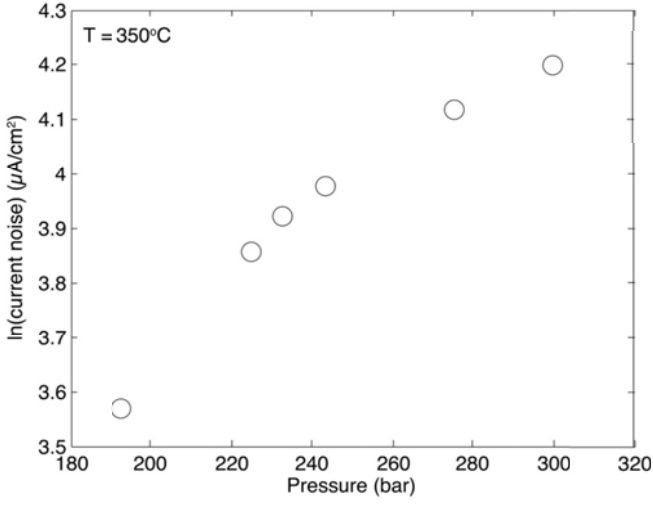

Figure 78. Electrochemical corrosion rate (standard deviation of the current noise) of Ni as a function of pressure at 350°C in deaerated 0.01 M HCl. Reprinted from Ref. 142, Copyright (2009) with the permission from NACE International.

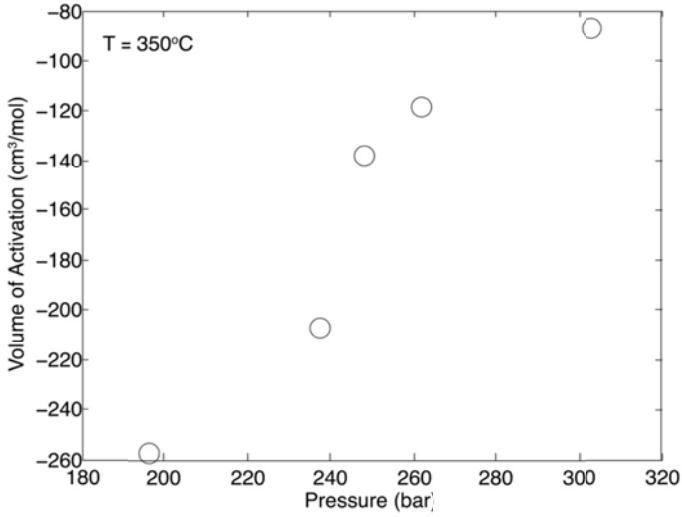

Figure 79. Volume of activation of corrosion reactions of Ni in deaerated 0.01 M HCl as a function of pressure at 350°C. Reprinted from Ref. 142, Copyright (2009) with the permission from NACE International.

Figure 79 displays the volume of activation of corrosion of nickel at 0.01 M HCl as a function of pressure at 350°C. Similar to the volume of activation of SS 304 in 0.01 M HCl at 350°C as a function of pressure, the magnitude of the volume of activation decreases with increasing pressure due to the pressure effect on the electrostriction of the solvent and on the solvent-solute interactions.

Figure 80 shows the contribution of the activation, system compressibility, and HCl dissociation to the relative corrosion rate of nickel in deaerated 0.01 M HCl at temperature of 350°C. As demonstrated by the figure, the contribution from activation term plays a dominant role on the relative corrosion rate, compared with

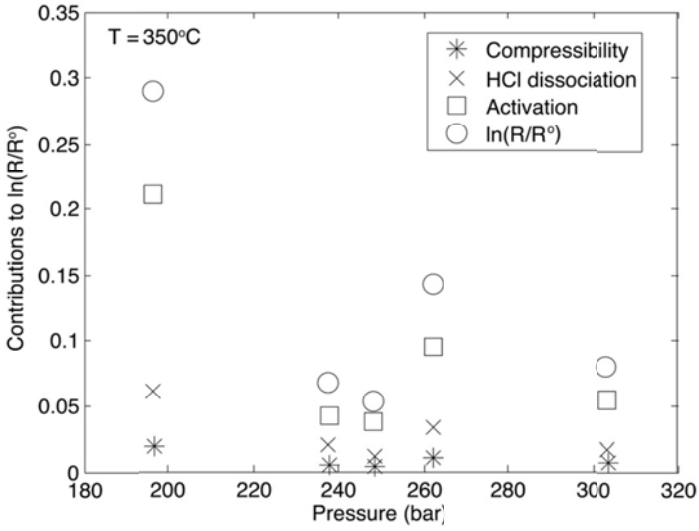

Figure 80. Contribution of activation, density, and HCl dissociation to corrosion rate of Ni as a function of pressure at 350°C in deaerated 0.01 M HCl. Reprinted from Ref. 142, Copyright (2009) with the permission from NACE International.

the contributions from the system compressibility and from HCl dissociation in high subcritical temperatures (350°C). At the same time, the contribution from the system compressibility is less importance than the contribution from the degree of dissociation as the solution is a condensed *liquid* phase and the compressibility of the system is small. The figure also shows that the contribution from the volume of activation to the relative reaction rate is more important than the contribution from the degree of dissociation at high subcritical temperatures.

6. Stress Corrosion Cracking

The extensive IGSCC (intergranular stress corrosion cracking) of sensitized Type 304 SS observed in Boiling Water Reactor (BWR) primary coolant circuits over the past three decades has prompted examination of the stress corrosion cracking of possible structural

alloys for Generation IV, Supercritical Water Nuclear Power Reactors (SCWNPRs). Just as much materials selection was simply transferred from subcritical fossil-fueled thermal power plants in designing BWRs, with disastrous results, concern has been expressed that a similar mistake may be being made in transferring materials technology from supercritical thermal (fossil fueled) power plants to supercritical nuclear systems by inadequately defining the properties of the environment or the response of an alloy when in contact with that environment. In the BWR case, when materials selection was affected, little was known of the electrochemical nature of IGSCC in sensitized Type 304 SS and in Type 316 SS. For example, in the 1960s it was not known that a critical potential for IGSCC (E_{IGSCC}) existed or that the critical potential was a sensitive function of temperature, crack length, degree of sensitization, or conductivity of the medium.[150] Also, it was not generally appreciated that the radiolysis of water in the reactor core produced oxidizing (e.g., O_2, H_2O_2, OH) and reducing (H_2, H, O_2^-) species that are electroactive (i.e., the species participate in redox reactions on the alloy surface) and that these species establish the redox potential of the environment and the corrosion potential of the steel. Over the past four decades a great deal has been learned of the electrochemical nature of IGSCC in austenitic stainless steels in subcritical systems, including the exponential dependence of crack growth rate on the electrochemical corrosion potential (ECP), as shown in Fig. 81.[151] Indeed, the evidence demonstrates that IGSCC in sensitized austenitic stainless steels is primarily an electrochemical phenomenon and not a mechanical process, although the bulk of the models that have been devised to account for the CGR are mechanical in nature (for example, see the model of Shoji, et.al.[152] The importance of electrochemistry in determining CGR underlies the current technology for mitigating IGSCC in operating BWRS (Hydrogen Water Chemistry, HWC) through the addition of hydrogen to the primary coolant in order to displace the potential in the negative direction thereby reducing the crack growth rate (Fig. 81) or in eliminating IGSCC altogether if the ECP is more negative than –0.23 V_{SHE}. This value is recognized by the Nuclear Regulatory Commission (NRC) as the

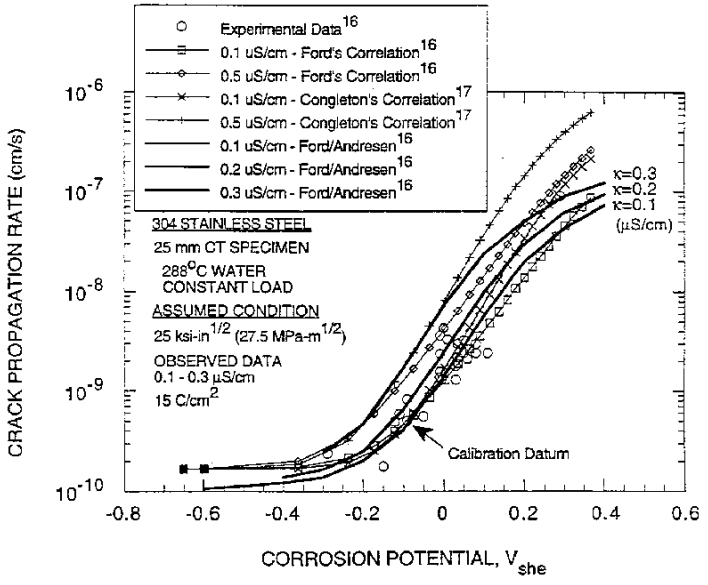

Figure 81. Measured and calculated (via the CEFM) crack growth rates for sensitized Type 304 SS in high temperature aqueous solutions as a function of ECP and conductivity. The solid lines correspond to predicted crack growth rate using the CEFM. The citations refer to references in the original source. Reprinted from Ref. 149, Copyright (1996), with permission from NACE International.

critical potential for IGSCC in sensitized Type 304 SS in BWR environment (pure water at 289°C), E_{IGSCC}, such that if the ECP is more negative the reactor operator may take credit for controlling IGSCC. This topic is revisited later in this section.

Because stress corrosion cracking is a localized corrosion process, involving the spatial separation of the local anode (in the crack) and the local cathode (on the external surfaces), the phenomenon of IGSCC is expected to fall under the theoretical umbrella of the Differential Aeration Hypothesis (DAH), as depicted in Fig. 82. The DAH, which was first postulated by Evans in the 1920s and which has since been recognized as the theoretical basis for essentially all localized corrosion phenomena requires that, in order to maintain the spatial separation between the local anode and local cathode, a positive ionic coupling current flows through

the solution from the crack to the external surface where it is annihilated by oxygen reduction on the crack external surfaces and by the equivalent electron current flowing through the metal, as depicted in Fig. 82. The magnitude and the distributions in the current and the potential from the crack tip to a point on the external surface that is remote from the crack mouth are such that charge is conserved in the system. Indeed, this condition determines the potential at the crack mouth, which is always more positive (i.e., the electrostatic potential in the solution) than that on the external surface remote from the crack mouth (negative of the corrosion potential).

The coupling current depicted in Fig. 82 is readily measured by mounting side cathodes on a compact toughness specimen whose surfaces (except for the crack) have been insulated from the solution and then measuring the electron current that flows from the specimen to the cathodes using a ZRA, as described by Manahan, et.al.[152] (Fig. 83). Under optimal conditions, and by using a suitably high data acquisition rate, the coupling current is found to comprise packages of 6 to 13 periodic oscillations that are separated by brief periods of intense current activity (Fig. 84). These oscillations arise from brittle microfracture events that occur at the crack tip and by determining their frequency (approx 2 s–1) and knowing the crack growth rate it is possible to estimate the size of the microfracture event at about 3 μm.[154] The size of the event does not appear to be consistent with the slip/dissolution model, where the dimension should be of the order of a few Burger's vectors (i.e., a few nanometers) corresponding to the dimension of a slip band. In this case the frequency of the events might be expected to be in the kHz range, in order to account for the known crack growth rate. Instead, the frequency and dimension of the microfracture event is more consistent with a hydrogen-induced cracking mechanism, even though the external environment is oxidizing. HIC is attributed to differential aeration displacing the potential of the metal at the crack tip below the hydrogen evolution line, thereby injecting hydrogen into the matrix ahead of the crack tip where it embrittles the grain boundary matrix, which

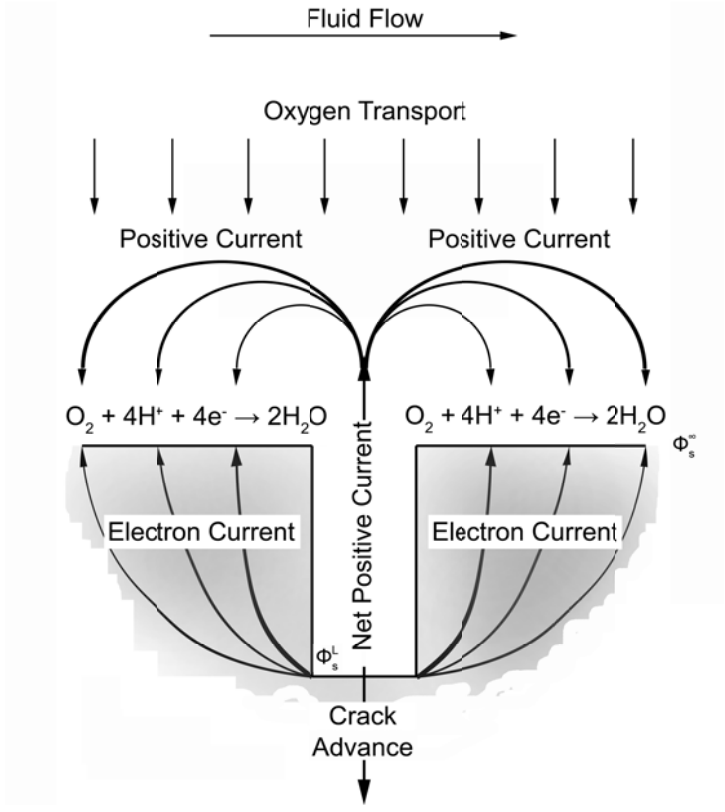

Figure 82. Depiction of the Differential Aeration Hypothesis (DAH) for localized corrosion showing the coupling currents (electronic through the metal, ionic through the solution) from the corrosion cavity to the external surface, where the two currents annihilate via a charge transfer reaction involving a cathodic depolarizer (e.g., reduction of oxygen). Reprinted from Corrosion Science, **32** (1991) 51, Copyright (1991), with permission from NACE International

may contain significant hydrogen-and strain-induced martensite, resulting in brittle, intergranular fracture.

The reader will note that the measured coupling current provides for the direct interrogation of events that occur at the crack tip as a function of various independent variables, such as the applied stress intensity factor (Fig. 83). The author knows of no other measurement that can be made that yields comparable information on the events that occur at the crack tip and it remains as a mystery, at least to the author, as to why this measurement, which is easy to make, is not used more extensively in the study of stress corrosion cracking. For example, it has been shown[154] that the crack growth rate is proportional to the average coupling current, which is expected from Faraday's law. Because current can be measured much more conveniently and to far greater accuracy than can crack growth rate, measurement of the coupling current might be an effective means of measuring CGR, particularly at very low rates. Additionally, there is no other method for the in situ determination of the dimension of the microfracture events, although the frequency can be ascertained using acoustic emission, but that technique has yet to be applied at high subcritical temperatures.

The role of radiolysis in establishing the ECP of stainless steels in determining IGSCC crack growth rate (CGR) is now well understood in terms of radiolysis models that predict the concentrations of electroactive radiolysis products around the coolant circuit of a BWR,[155] the mixed potential model for calculating the ECP,[156] and the Coupled Environment Fracture Model[152,128,157] for estimating the IGSCC CGR. These models have been assembled into codes (DAMAGE-PREDICTOR, ALERT, REMAIN, and FOCUS) for predicting the accumulation of damage due to IGSCC in BWR primary coolant circuits as a function of the operating history of the reactor. Figure 85, for example, shows the predicted ECP around the primary coolant circuit of the Leibstadt BWR in Swizerland operating under normal water chemistry protocol, in which no hydrogen is added to the reactor feed water. The ECP is predicted to vary from about 0 V_{SHE} in the recirculation piping

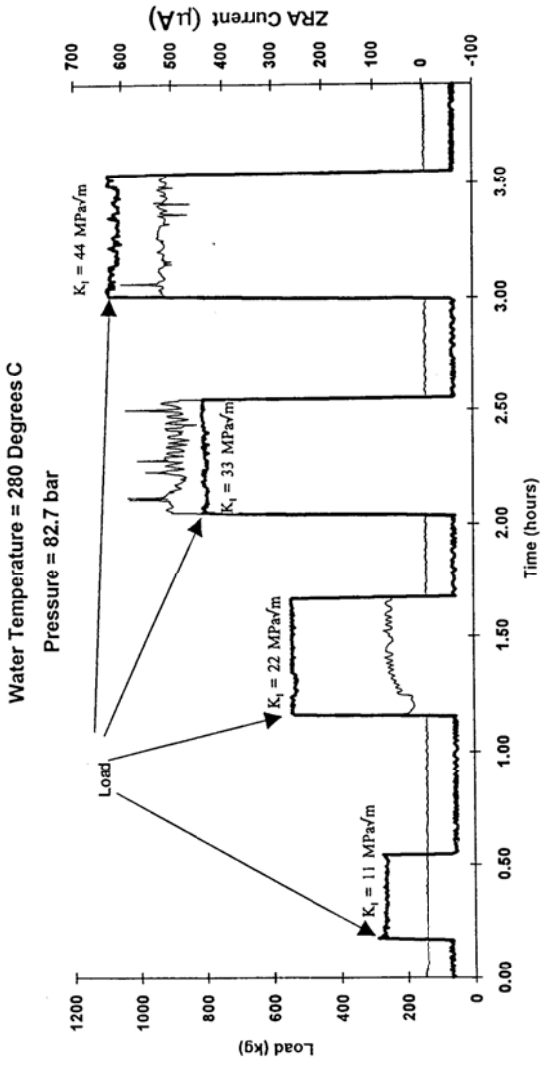

Figure 83. Coupling current and stress intensity versus time for Type 304 SS in simulated BWR coolant at 288°C. The specimen was equipped with one platinized nickel side cathode. Reprinted from Ref. 153, Copyright (2001), with permission from Elsevier.

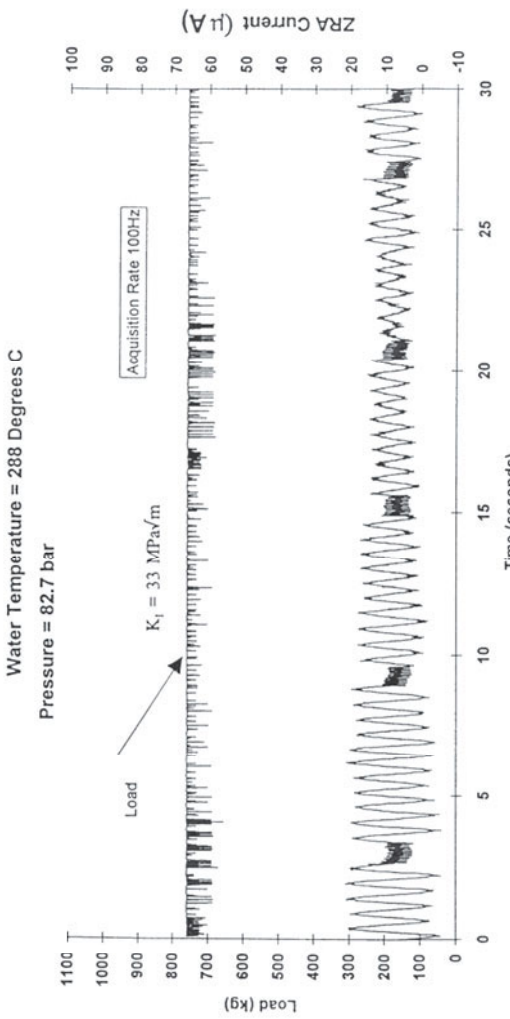

Figure 84. Noise in the coupling current generated by IGSCC in sensitized Type 304 SS in water at 288°C and at a stress intensity factor of 33 MPa.√m. Reprinted from Ref. 153, Copyright (2001), with permission from Elsevier.

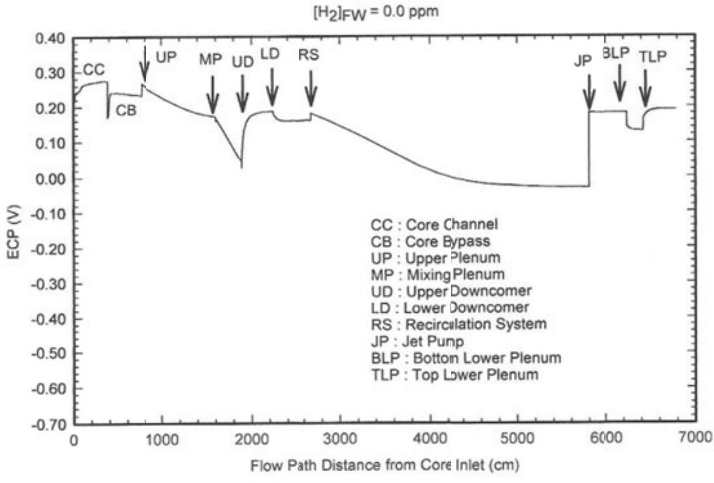

(a)

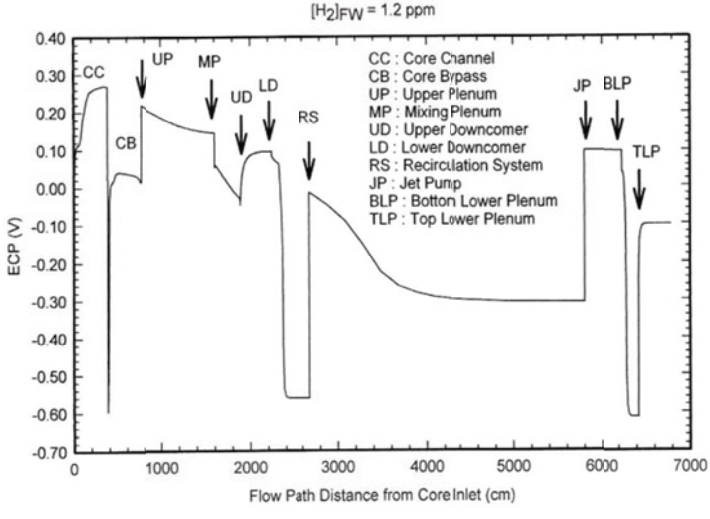

(b)

Figure 85. Predicted ECP around the primary coolant circuit of a BWR under (a) normal water chemistry (NWC) conditions (no hydrogen added to the feedwater) and (b) hydrogen water chemistry (1.2 ppm of H_2 added to the reactor feedwater. Reprinted from Ref. 9, Copyright (1995) with permission from Elsevier.

to about 0.3 V_{SHE} in the core channels, where radiolysis and the generation rate of H_2O_2 is most intense. On the other hand, H_2O_2 decomposes thermally in the recirculation piping, such that its concentration at the exit of the recirculation pipe is greatly reduced compared with that in the reaction core. Because the ECP is very dependent upon the concentration of hydrogen peroxide, because this is the most powerful oxidizing agent that is produced in a significant concentration by water radiolysis, the ECP reflects, to a large extent, the concentration of H_2O and, to a lesser extent, the concentration of oxygen.

Shown in Fig. 85, it is not surprising to find that the CGR around the coolant circuit, as shown in Fig. 86, closely resembles that for the ECP (Fig. 72). Thus the crack growth rate for a 0.5 cm long crack loaded to a stress intensity factor of 27 MPa.$m^{1/2}$ varies from about 10^{-9} cm/s at the exit of the recirculation piping system to about 5 x10^{-9} cm/s in the core channels. A crack growth rate of 10^{-9} cm/s corresponds to the lengthening of a crack by 0.3 mm over one year. This magnitude of CGR is tolerable during operation and according to the data plotted in Fig. 71 for low conductivity the corresponding potential is about –0.05 V_{SHE}. This is significantly more positive than the NRC-mandated critical value of -0.23 V_{SHE}, suggesting that the latter may be too conservative, as previously noted.[152] Also presented in Figs. 85 and 87 are plots of ECP and crack growth rate, respectively, for the reactor operating under hydrogen water chemistry (HWC) with the addition of 1.2 ppm of hydrogen to the reactor feedwater. These plots show that hydrogen significantly shifts the ECP in the negative direction and lowers the crack growth rate in many, but not all, regions of the primary coolant circuit. Thus, using the –0.05 $V_{SHE}/10^{-9}$ cm/s as the *protection* criteria, it is evident that HWC may protect much of the lower down comer and lower plenum [beneath the reactor core at the bottom of the reactor pressure vessel (RPV) containing the control rod drives (CRDs), and most of the recirculation piping system], but the core channels (containing the fuel), the core bypass (between the core and the inside of the core shroud), the upper plenum, the mixing plenum (both above the core and in contact with water exiting the core channels and the bypass and hence containing radiolytically- generated H_2O_2), and the jet pumps.

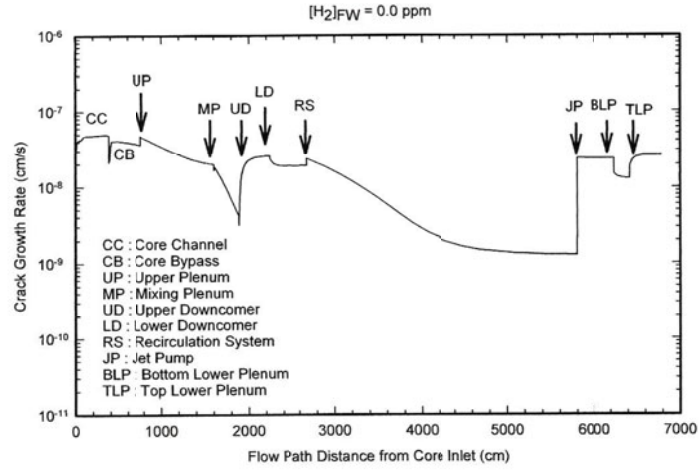

(a)

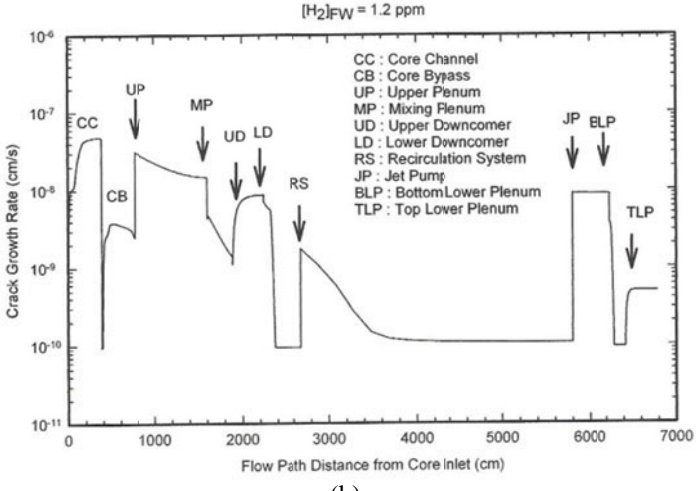

(b)

Figure 86. Predicted IGSCC CGR for a 0.5 cm long crack around the primary coolant circuit of a BWR under (a) normal water chemistry (NWC) conditions (no hydrogen added to the feedwater) and (b) hydrogen water chemistry (1.2 ppm of H_2 added to the reactor feedwater. Reprinted from Ref. 9, Copyright (1995), with permission from Elsevier.

The efficacy of HWC is significantly improved by depositing noble metal on the steel surfaces in a protocol termed *noble metal chemical addition* (NMCA), as offered to reactor operators by the vendor, General Electric Company.[158]

As noted above codes have been developed to predict the accumulation of damage by IGSCC in the primary coolant circuits of operating reactors as a function of the reactor operating history (start-ups, shut-downs, variation in power level, hydrogen additions, etc), which defines the *corrosion evolutionary path*. The predicted damage (length of a crack on the upper inner surface the core shroud adjacent to the H-3 weld) for three operating scenarios is shown in Fig. 87. Under NWC operating conditions (no added hydrogen), the crack is predicted to grow by about 2 cm over the ten year operating period, corresponding to an average crack growth rate of 1.3×10^{-8} cm/s, but if HWC had been initiated immediately upon start-up the crack is predicted to have advanced by a little more than 0.5 cm. On the other hand, had HWC been instituted after five years, the crack is predicted to have lengthened by about 1.7 cm, considerably more than half of the advance under NWC operating conditions. This *law of decreasing returns*, in this case, is a consequence of the parabolic form of the CGR versus time curve, which, in turn, reflects the fact that the CGR decreases as the crack length increases, due to the increase in the IR potential drop down the crack. In closing, the author notes that the predictions of the code (these calculations were performed using ALERT) are in excellent agreement with the observed damage due to IGSCC in the shroud, where comparisons between prediction and measurement can be made.

It is important to note that no comparable models have been developed for supercritical aqueous systems, so that similar calculations are not yet possible for supercritical water nuclear power plants (SCWNPPs). In the opinion of the author, the development of such a code would prove to be invaluable for selecting materials and for devising water chemistry and operating protocols for SCWNPPs. That radiolysis occurs in supercritical water to produce a variety of electroactive species is well established experimentally, particularly through the work of Bartels and coworkers[158] and of that by Katsumura.[159] The current situation with regard to

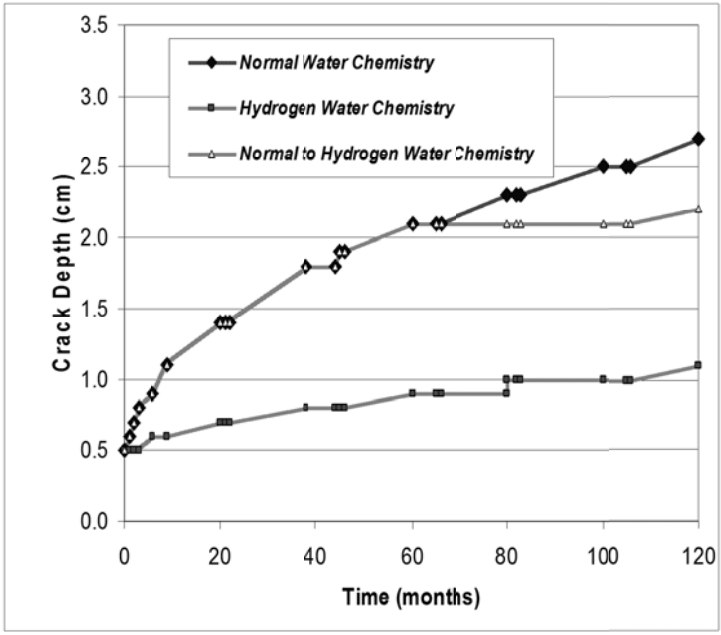

Figure 87. Predicted accumulated damage for IGSCC (crack length) in a Boiling Water Reactor as a function of the reactor operating history over ten years and as a function of the water chemistry protocols employed. Reprinted from Ref. 9, Copyright (1995) with permission from Elsevier.

predicting corrosion damage in SCWNPPs is entirely comparable to the situation that existed with regard to BWRs in the early 1960s; the phenomena (cracking) were known to occur, but only rudimentary knowledge was available with regard to mechanisms. Thus, our shortcomings include:

- No generally accepted model exists for the radiolysis of water and no consistent sets of radiolytic yield (g values) or rate constants are currently available. The availability of these data is a prerequisite for calculating the concentrations of electroactive radiolytic species in a reactor coolant circuit.
- We currently have no experimental data for the exchange current densities or Tafel constants for redox couples in-

volving those radiolytic species (e.g., H_2/H^+, O_2/H_2O, H_2O_2/H_2O) or for the species diffusivities, which are needed for estimating limiting currents. These data are a prerequisite for being able to calculate the ECP using the Mixed Potential Model.[156]

- No crack growth rate data under well controlled fracture mechanics and electrochemical conditions are currently available for any alloy in supercritical aqueous solutions. Indeed, it may well be that under conditions where the Chemical Oxidation (CO) mechanism dominates (low density) the electrochemistry may not be important, but that deeds to be demonstrated. At high density ($\rho > 0.06$ g/cm^3) general corrosion occurs via an Electrochemical Oxidation (EO) mechanism and it is likely that SCC also will be an electrochemical phenomenon.
- The experimental techniques required to measure the data have yet to be fully developed.

As noted above, various groups are working on determining G-values for the radiolysis products of water and some data are now becoming available. Most experiments employ pulse radiolysis with scavenging by an additive to the solution that produces a product that exhibits an absorption spectrum within the visible region of the electromagnetic spectrum. The concentration of the species of interest (e.g., hydrated electrons) is then readily determined from Beer's law and the measured absorbance.

An example of the type of study that is being carried out in this area is that reported by Ghandi and Percival[160] (Fig. 88). These workers, using radiolysis data in the literature explored various models for predicting rate constants for the reactions OH + OH → H_2O_2 (triangles, Fig. 88), OH + OOH → O_2 + H_2O (squares, Fig. 88) in water and (b) OH + nitrobenzene in water at temperatures ranging from ambient to 450°C. The two principal models employed were those based upon the Noyes equation

$$\frac{1}{k_{obs}} = \frac{1}{k_{diff}} + \frac{1}{k_{act}} \tag{92}$$

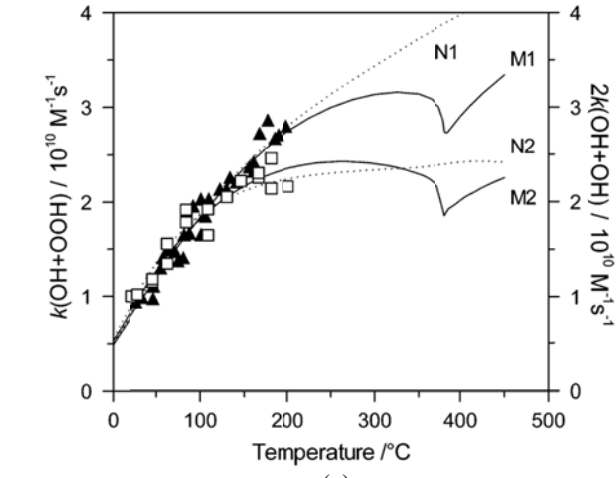

(a)

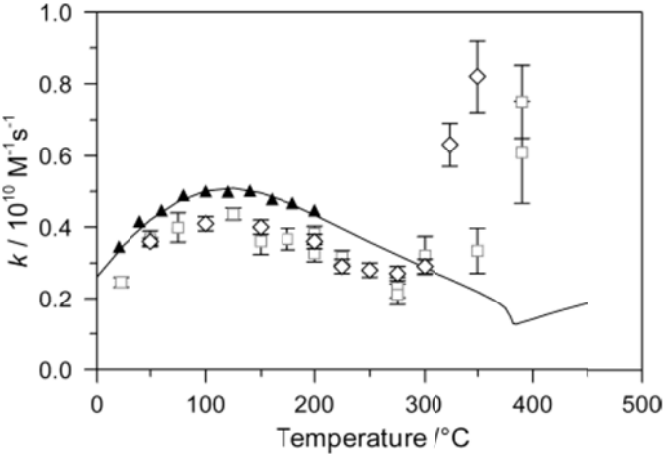

(b)

Figure 88. Temperature dependencies of the rate constants for: (a) the reaction OH + OH → H_2O_2 (triangles), OH + OOH → O_2 + H_2O (squares) in water and (b) OH + nitrobenzene in water at temperatures ranging from ambient to 450°C. N1, N2 in (a) are fits to and extrapolation of Elliot's data,[162] M1 and M2 are predictions of a *multiple collision* model, while the line in (b) is the prediction also by a *multiple collision* model. The experimental data indicated by squares in (b) are data from Notre Dame while the diamonds are data from the Argonne National Laboratory. Reprinted from Ref. 161, Copyright (2003), with permission of The American Chemical Society.

where k_{diff} is the diffusion-limited rate constant and k_{act} is the rate constant for the activated process. The diffusion limited rate constant, k_{diff}, is given by the Schmoluchowski equation

$$k_{diff} = 4000\pi\beta(D_1 + D_2)R_{eff}N_{Av} \tag{93}$$

where β is the spin statistical factor for reactions between radicals, D_1 and D_2 are the diffusivities of the two reacting species, R_{eff} is the mutual reaction diameter, and N_{Av} is Avogadro's number. The reader will note that, as predicted by Eq. (92) the smaller of the two rate constants, k_{diff} and k_{act}, controls the observed rate constant for a given reaction. Thus, in the radiolysis models that have been developed for subcritical temperatures.[152] The activation rate constant, k_{act}, is given by the Arrhenius equation as

$$k_{act} = Ae^{-E_a/RT} \tag{94}$$

where k_B is Boltzmann's constant, h is Planck's constant, and $\Delta G^{0,\neq}$ is the change in Gibbs energy of activation of the reaction. The second model employed by Ghandi and Percival[160] makes use of a modified form of Eq. (94) as

$$k_{react} = f_R Ae^{-E_a/RT} \tag{95}$$

where the efficiency factor, f_R, is given by

$$f_R = p_R q/(1 + p_R q) \tag{96}$$

which takes account of reactive orientation (described by p_R) and the number of collisions between the reactants over the duration of an encounter (q). The parameter q can be expressed as the ratio of the encounter lifetime (τ_{enc}) and the time between collisions (τ_{coll})

$$q = \tau_{enc}/\tau_{coll} \tag{97}$$

Methods are available for estimating both τ_{enc} and τ_{coll} (see Ghandi and Percival).[160] Importantly, q is found to change from

about 1000 for liquid water to about one (every collision being effective) for low density, supercritical water conditions, with the reaction efficiency falling from 100% per encounter to a lower value as the density decreases from that for subcritical liquid water.

It should be noted that, in the reaction mechanisms that are currently used for modeling the radiolysis of water in subcritical systems,[152] most of the bimolecular reactions are at the diffusion limit. Because the temperature dependence of an activation controlled reaction is normally greater than that of a diffusion controlled reaction, any reaction that is diffusion controlled at subcritical temperatures is almost certainly diffusion controlled at supercritical temperatures and many that are activation controlled at subcritical temperatures will become diffusion controlled at supercritical temperatures. Accordingly, the rate constants for many reactions between radiolytic species in any mechanism adopted for the radiolysis of water in supercritical water might be reasonably estimated. The challenge exists with the unimolecular reactions and those bimolecular reactions whose rates are below the diffusion limit. Nevertheless, the author's opinion is that a good chance exists that an acceptable set of rate constants for a reaction mechanism could be developed for use at supercritical temperatures.

As a second example, the rate constant for the scavenging of hydrated electrons by nitrobenzene in water at 380°C as a function of density, as reported by Marin, et al.,[162] is plotted in Fig. 89. For lower densities ($\rho < 0.4$ g/cm3), the rate constant decreases with increasing density, but at higher density the opposite trend is observed. There is no obvious property versus temperature correlation that can account for the density dependence of the rate constant.

The need to actual measure kinetic data, rather than extrapolating data from lower temperatures, is that the theoretical models are insufficiently sophisticated to accurately describe the transition from subcritical conditions to supercritical conditions, as is evident from the data plotted in Fig. 88. Thus, a simple Arrhenius extrapolation of Elliot's[161] subcritical data or by using a *multiple collision* model does not produce the data at all well in the

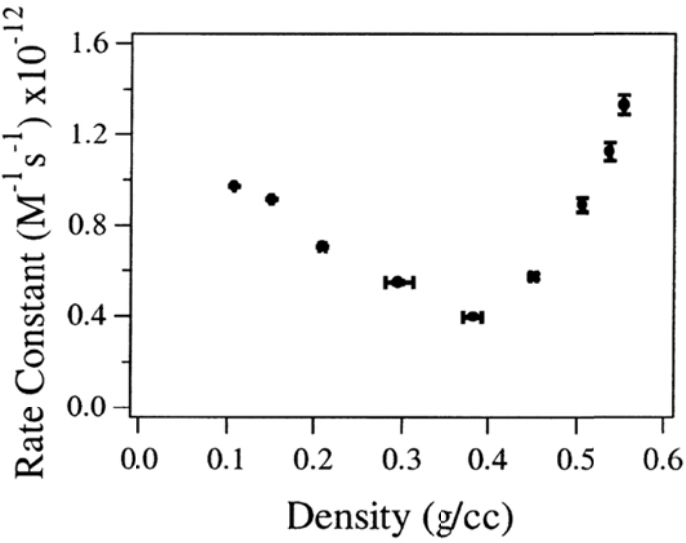

Figure 89. Effect of density on the rate constant for the scavenging of hydrated electrons by nitrobenzene at 380oC. Reprinted from Ref. 163, Copyright (2004) with permission from The American Chemical Society.

supercritical temperature region, demonstrating that there is something seriously amiss with reaction rate theory for these conditions. A similar discontinuity is in the radiolytic yield of the electron ($G(e^-)$, number of electrons produced/100 eV of energy absorbed) (Fig. 90).

The first study of the radiolysis of water at supercritical temperatures was apparently that of Burns and Marsh published in 1981.[164] These measurements were made at 400°C and the techniques employed were generally adopted by later workers in repeating and expanding upon this initial, pioneering work. (Fig. 91) The Burns and Marsh study produced a radiolysis mechanism and associated rate constants and activation energies that need to be verified or modified, as the case may be.

The other key parameter in any radiolysis study is the radiolytic yield for the various radiolytic products. Several studies have been reported in measuring this quantity for various reactions and some of the results are summarized below. Much of the work

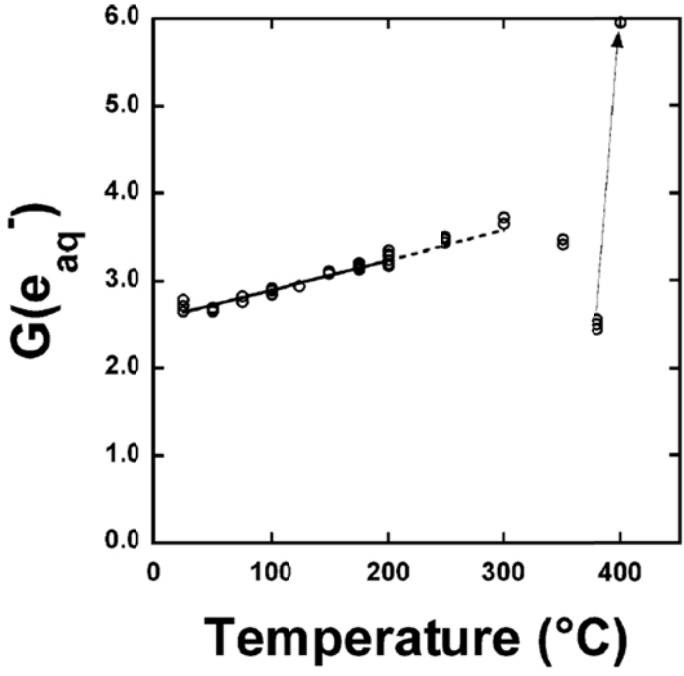

Figure 90. Plot of the radiolytic yield of electrons, G(e⁻), as a function of temperature from ambient to supercritical temperatures at a constant pressure of 25 MPa (250 bar). Reprinted from Ref. 164, Copyright (1981) with permission from The American Chemical Society.

reported to date has explored the radiolytic yield of hydrated electrons, with some of the data being summarized in Fig. 92. The radiolytic yields of other electroactive species need to be determines, in order that effective radiolysis models may be developed.

Returning now to stress corrosion cracking, it is evident that it is premature to expect calculation of the ECP in the coolant circuit. Of a SCWNPP, but it is possible to perform experiments under electrochemical control using the electrochemical techniques (reference electrodes, etc.) discussed above. However, none of the work reported to date has employed a reference electrode to moni-

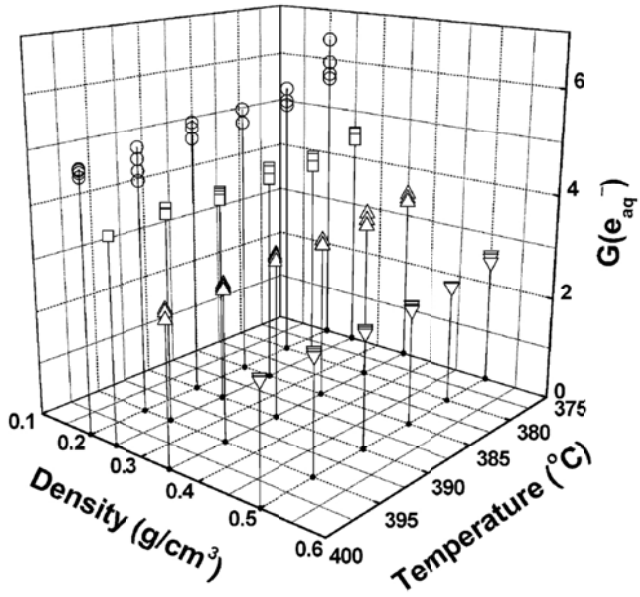

Figure 91. Three dimensional plot of $G(e^-)$ as a function of density and temperature in supercritical water. (o) 0.20 g/cm^3; (□) 0.25 g/cm^3; (Δ) 0.35 g/cm^3; (▼) 0.50 g/cm^3. Reprinted from Ref. 164, Copyright (1981) with permission from The American Chemical Society.

tor the potential and no attempts have been reported on controlling the potential of the specimen at a preselected value, although some data are available as a function of oxygen concentration. Teysseyre and Was[165] studied the stress corrosion cracking of four austenitic alloys (Type 304 SS, Type 316L SS, Alloy 690, and Alloy 625) in deaerated, supercritical water using constant extension rate tests (CERTs) and their stress-strain curves recorded at a constant extension rate of 3 x 10^{-7} s^{-1} are displayed in Fig. 93. These data show that the two stainless steels (Type 304 SS and Type 316L SS) generally fail at the lower strains indicating that they are most susceptible to SCC. However, none of the alloys displayed intergranular fracture at 400°C and Alloy 690 displayed only ductile fracture at 450°C. Upon increasing the temperature to 500°C, however, mixed mode, intergranular/ductile fracture was observed un-

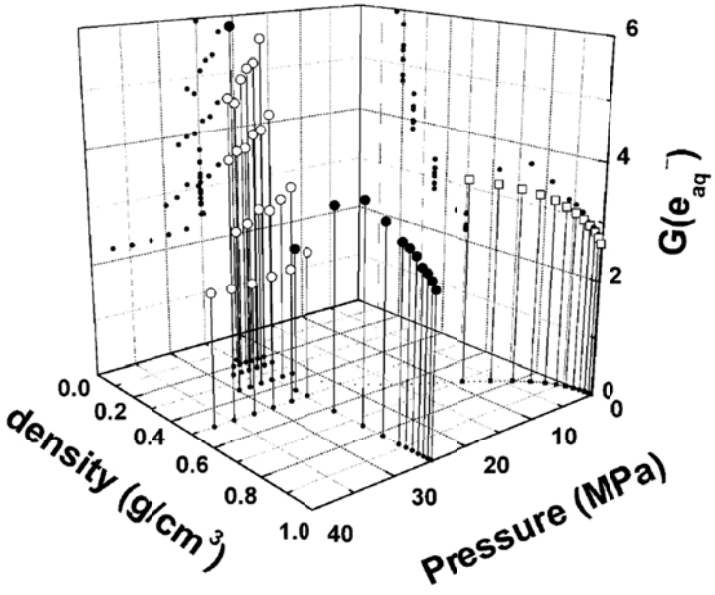

Figure 92. (a) Three dimensional plot of G(e-) as a function of density and pressure, Source of data is indicated in the paper of Lin, et al.[163] Reprinted from Ref. 164, Copyright (1981) with permission from The American Chemical Society.

der all conditions. Although the appearance of intergranular facets on the fracture surface strongly suggest the occurrence of ISCC, in the case of Type 304 SS, the strains to failure in deaerated and non-deaerated supercritical water were greater than that in argon gas; the quintessential non-SCC environment. However, intergranular cracks were observed on the fracture surfaces and on the side surfaces of the round tensile specimen and the statistics describing these cracks are summarized in Fig. 94. These data show that cracks are generally deeper for specimens exposed at higher temperature, particularly for those specimens exposed at 550°C, indicating that the cracks are thermally activated and hence follow an Arrhenius relationship.

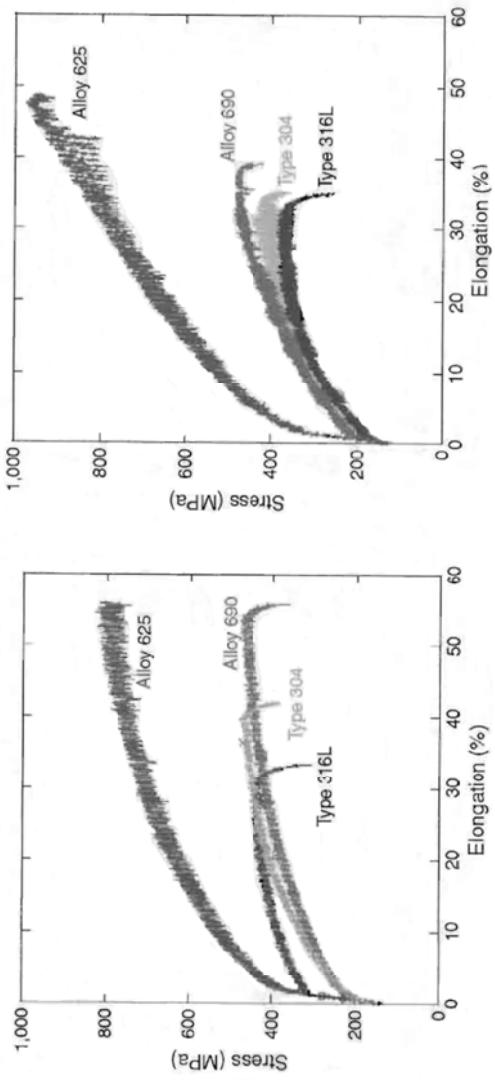

Figure 93. CERT stress-strain curves obtained for three alloys, Type 304 SS, Type 316L SS, Alloy 690, and Alloy 625 in de-aerated supercritical water at temperatures of: (a) 400°C, (b) 500°C, (c) 550°C, and (d) for Alloy 690 at 400°C, 450°C, 500°C, and 550°C and at a pressure of 25.5 MPa. Reprinted from Ref. 166, Copyright (1993) with permission from NACE International.

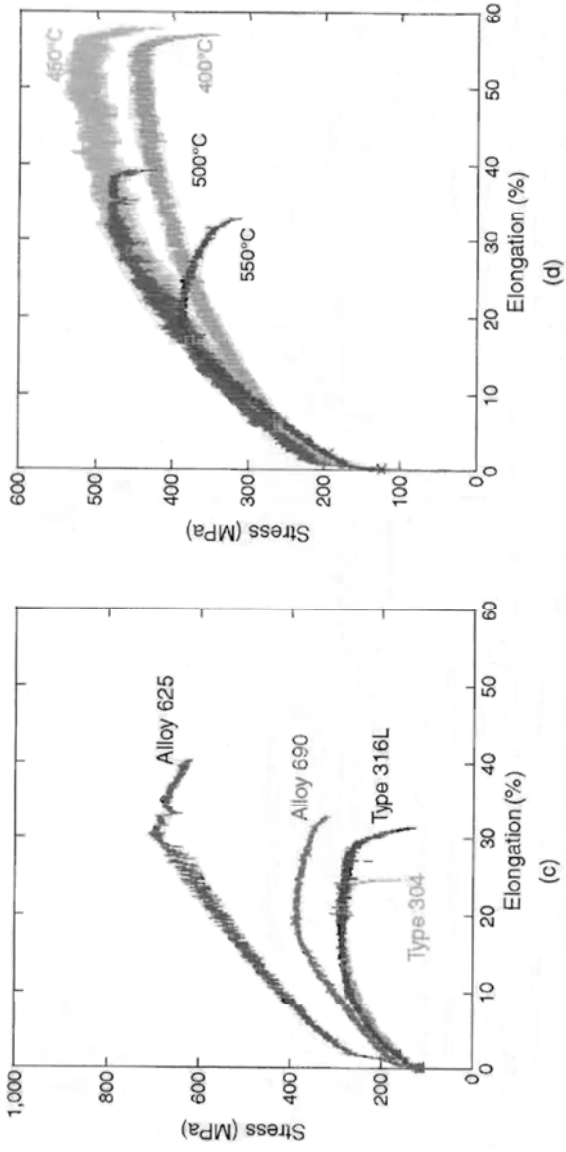

Figure 93. Continuation.

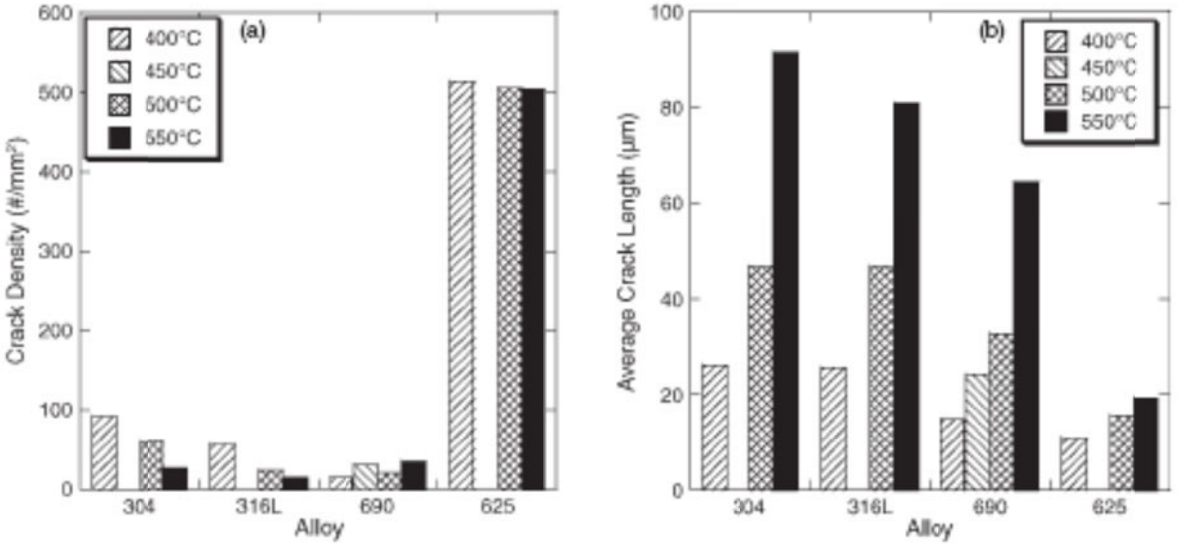

Figure 94. (a) crack density, (b) average crack depth, (c) crack depth per unit area, and (d) maximum crack depth observed after straining Type 304 SS, Type 316L SS, Alloy 690, and Alloy 625 in deaerated supercritical water at 400°C, 450°C, 500°C, and 550°C at a constant strain rate of 3 $x10^{-7}$ s^{-1} and at a pressure of 25.5 MPa. Reprinted from Ref. 166, Copyright (1993) with permission from NACE International.

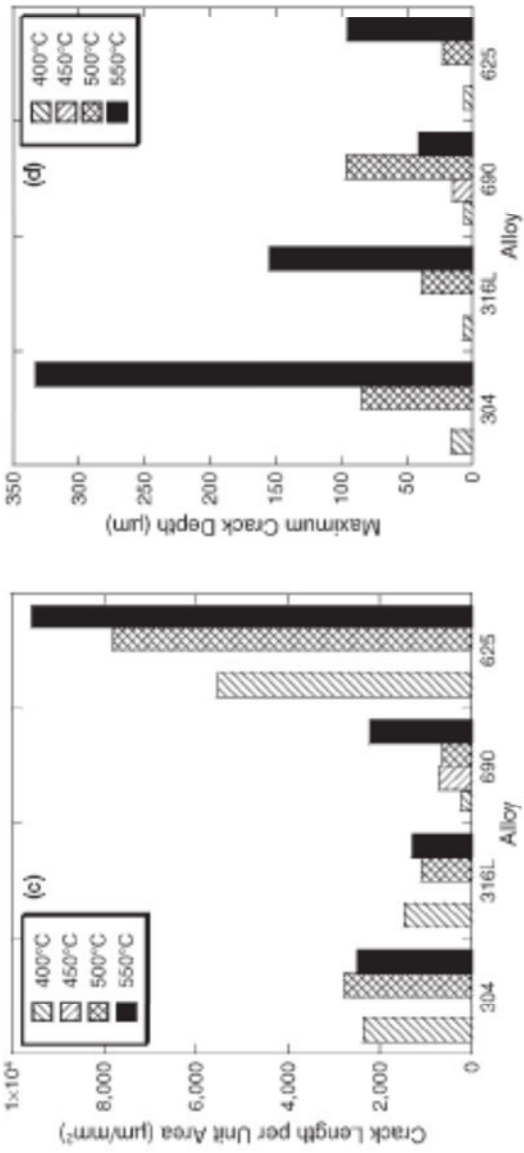

Figure 94. Continuation.

Cross-sectional micrographs of Alloy 690 specimens after exposure to deaerated supercritical water at (a) 400°C; (b) 450°C; (c) 500°C; and (d) 550°C and at a pressure of 25.5 MPa are displayed in Fig. 95. The cracks are clearly evident and it is also evident that many initiate at emergent grain boundaries, but others initiate intergranularly and penetrate transgranularly (Fig. 95c). In sensitized Type 304 SS, at BWR operating temperatures (288°C), cracks are often found to initiate at a surface discontinuity (e.g., a pit, which acts as a stress raiser) and then grow transgranularly across the first grain (Figs. 96 and 97) until intersecting a sensitized grain boundary, as found for Type 304 SS in chloride-containing solutions at 288°C.[165] Thereafter, the crack grows intergranularly. It appears, then, that there is little difference between crack initiation in subcritical and supercritical aqueous systems.

That crack growth in the four alloys is a thermally activated process is clearly shown by plotting the crack growth rate (Fig. 98a) in Arrhenius form (Fig. 98b). The activation energy is found to be of the order of 84–105 kJ/mol, which is a commonly observed range for a thermally activated process of this type. The crack growth rates were determined by dividing the depth of the deepest crack on the fracture surface of the failed CERT specimen by the time of straining from the yield point. This method has been extensively used in subcritical temperatures, but there are significant objections to its use, including:

(a) The mechanical state at the tip of a crack is poorly defined;
(b) data analysis is considerably complicated by the existence of multiple cracks propagating simultaneously on the failure surface and on the specimen side surfaces;
(c) the time at which the cracks nucleate, and hence the time over which the cracks grow, is uncertain; and
(d) the specimen is forced to fail regardless of the crack velocity, which does not reflect in service dynamics. Furthermore, where comparisons have been made, crack growth rates determined by CERTs are significantly higher than those measured using well-defined fracture mechanics specimens.

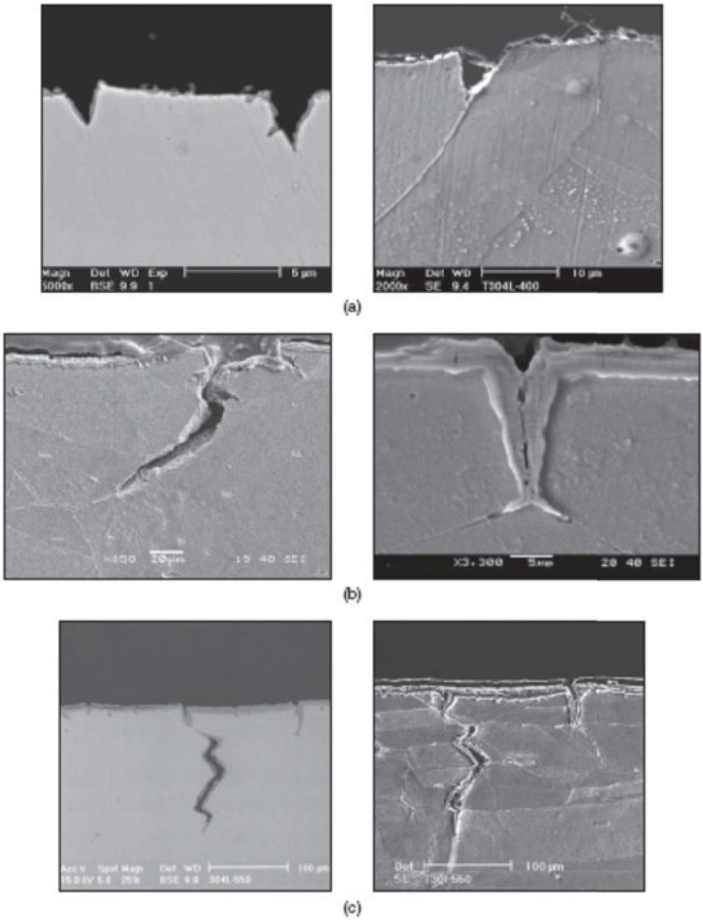

Figure 95. Cross sectional micrographs of Type 304 SS after exposure for about 300 hours in deaerated supercritical water at: (a) 400ºC; (b) 500ºC; and (c) 550ºC and at a pressure of 25.5 MPa. Note the intergranular nature of the cracks. Reprinted from Ref. 166, Copyright (1993) with permission from NACE International.

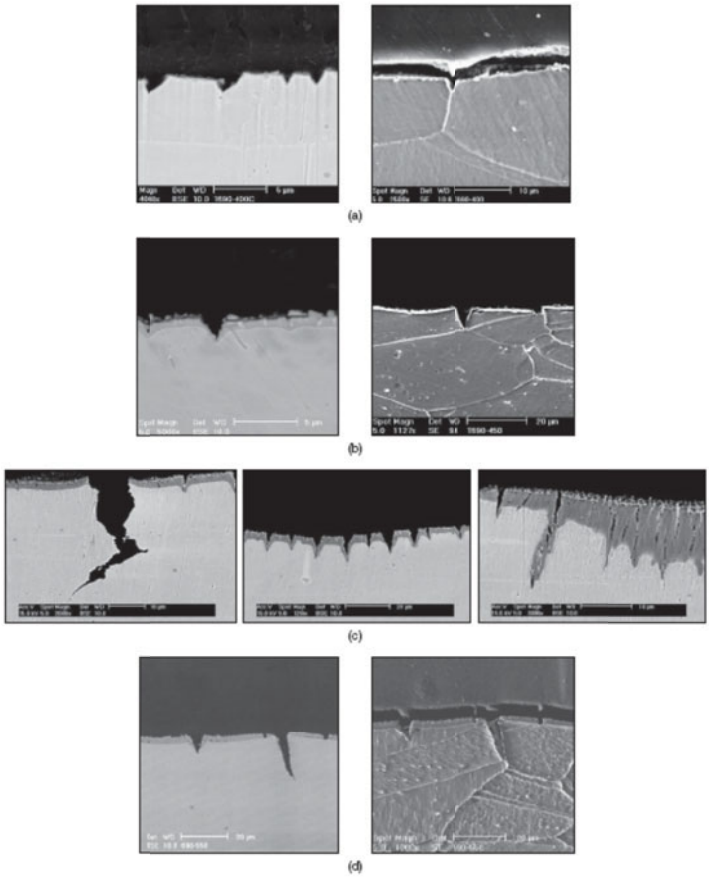

Figure 96. Cross sectional micrographs of Alloy 690 after exposure for about 300 hours in deaerated supercritical water at: (a) 400°C; (b) 450°C; (c) 500°C; and (d) 550°C and at a pressure of 25.5 MPa. Note the intergranular nature of the cracks and that the cracks appear to initiate at emergent grain boundaries. Reprinted from Ref. 166, Copyright (1993) with permission from NACE International.

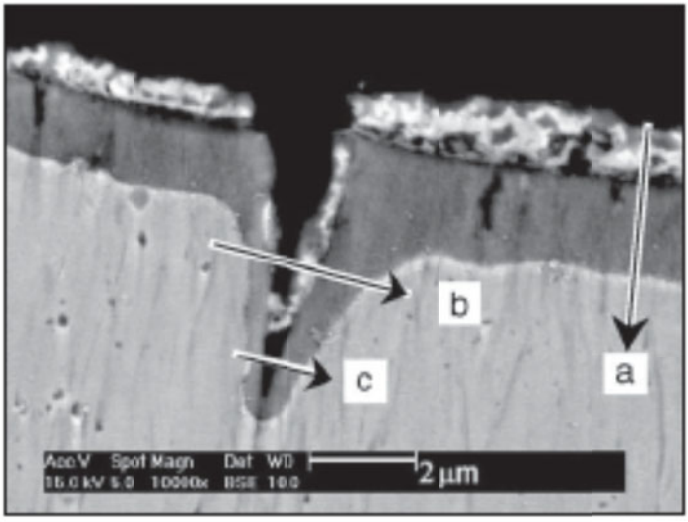

Figure 97. Transgranular crack in the surface of Alloy 690 exposed to deaerated supercritical water at 500°C and at a pressure of 25.5 MPa. The arrows indicate the tracks of EDS analyses. Reprinted from Ref. 166, Copyright (1993) with permission from NACE International.

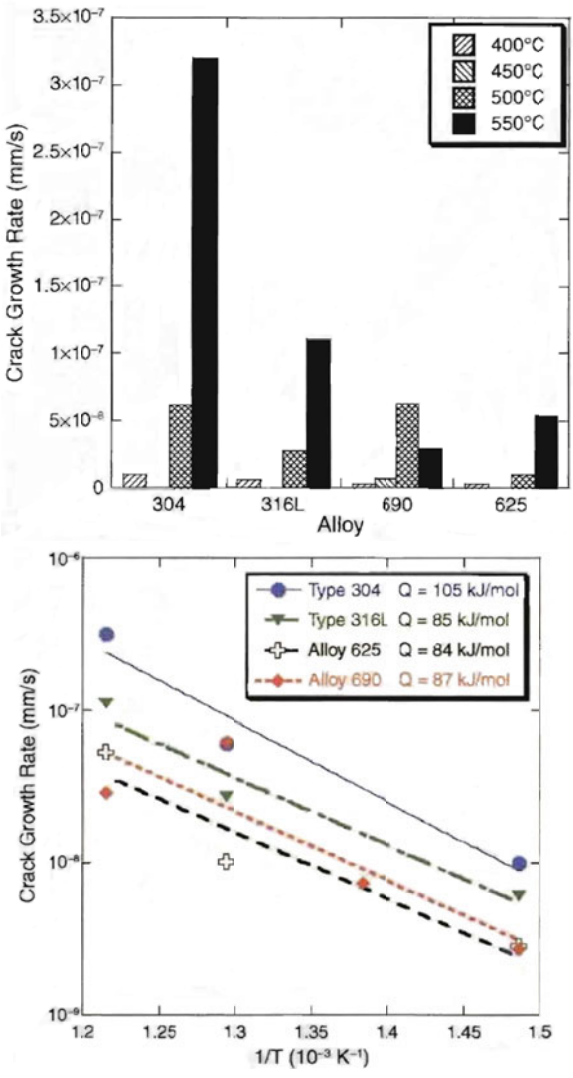

Figure 98. (a) Crack growth rate as a function of temperature for Types 304 SS, Type 316L SS, Alloy 690, and Alloy 625 (in deaerated water at 500°C) and at a pressure of 25.5 MPa. (b) Arrhenius plots for crack growth rate. Reprinted from Ref. 166, Copyright (1993) with permission from NACE International.

If we accept that the crack growth rate in these alloys in deaerated supercritical water is of the order of 10^{-7} mm/s at 550°C (roughly the proposed operating temperature of a SCWNPP) and noting that there are about $3x10^7$ seconds in a year, crack extension is calculated to be of the order of 3 mm per year. This is judged to be a little high in practical engineering terms, because it corresponds to the growth of a greater than one-inch deep crack in ten years. However, recognizing that crack growth rates measured using CERT experiments are likely to be high, by as much as an order of magnitude, a crack growth rate of 0.3 mm/year would be acceptable, corresponding to that observed under BWR coolant conditions. Clearly, the crack growth rate needs to be measured using well-defined (mechanically) fracture mechanics specimens.

Attention is now turned to examining the possible role of electrochemistry in SCC in supercritical aqueous systems. Thus, because oxygen is known to impact the corrosion potential (see above) and recognizing that the effect of oxygen on the fracture behavior of the austenitic alloys in supercritical water has yet to be studied systematically, some data suggest that high oxygen may exacerbate IGSCC. Thus, the data shown in Fig. 99 show that the extent of IGSCC on the fracture surfaces failed in CERT tests in high subcritical and at supercritical temperatures, which is associated with stress corrosion cracking, show that the extent of IGSCC decreases dramatically with increasing temperature in the supercritical region, possibly reflecting increasing dominance of the CO mechanism over the EO mechanism.

Finally, it is of interest to examine, briefly, the temperature dependence of IGSCC in sensitized Type 304 SS in pure water at subcritical temperatures. A plot of the available data from Andresen,[166] together with predictions from the Coupled Environment Fracture Model,[158] are shown in Fig. 100. The crack growth rate (CGR) is found to pass through a maximum at about 170°C. At higher temperatures, the crack growth rate is found to decrease dramatically with increasing temperature, such that at 300°C the CGR is about two orders in magnitude higher than the creep crack growth rate. Unfortunately, no CGR data appear to be available for the temperature range of 300°C to the critical temperature for this (or any other) steel, so that it is not possible

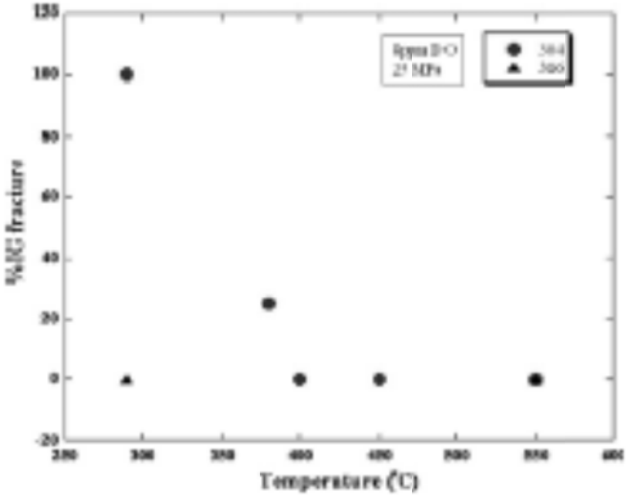

Figure 99. Percent intergranular cracking on the fracture surface of sensitized Type 304 SS as a function of temperature in high subcritical and supercritical water containing 8 ppm of oxygen. Reprinted from Ref. 114, Copyright (1999) with permission from Elsevier.

to ascertain how or whether the lower temperature data mesh with those measured at supercritical temperatures.

VII. POLARIZATION STUDIES

1. Effect of Temperature

The selection of materials for use in many industrial environments, including supercritical thermal power plants (SCTPPs) and Supercritical Water Oxidation (SCWO) systems requires a broad study of the forms and the rates of corrosion of various metals and alloys in supercritical (T > 374°C) aqueous environments. Nickel is an important component of many corrosion resistant alloys and is a classic model for corrosion studies. Extensive electrochemical polarization studies of this metal in

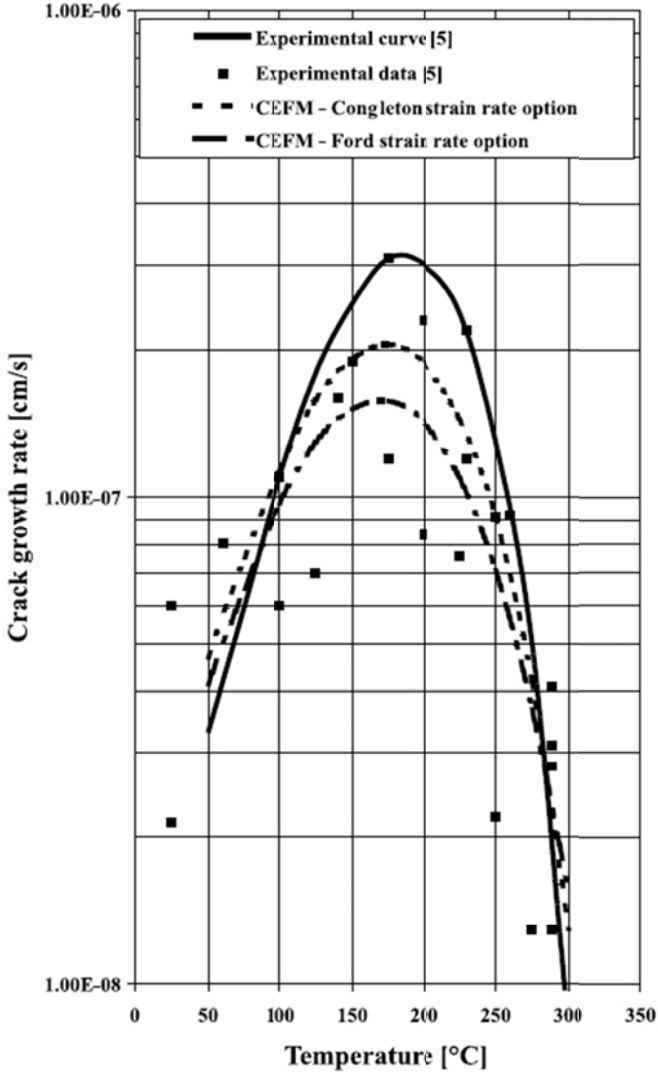

Figure 100. Crack growth rate in Type 304 SS in pure water as a function of temperature. Reprinted from Ref. 157, Copyright (2005) with permission from Elsevier.

subcritical systems have been reported, but few studies of this type apparently have been previously performed at supercritical temperatures.

A number of groups have developed experimental techniques for performing electrochemical polarization studies at high subcritical and at supercritical temperatures. The measurements are performed in a stainless steel, high temperature/high pressure test cell. In the studies performed by the author and his colleagues the working electrode (Ni) and counter electrode (Pt) were incorporated into an alumina holder with a cooled PTFE support and this assembly was then inserted into the test cell through which the electrolyte was slowly pumped (at a rate of 4-5 ml/minute) (e.g., Fig. 54). A silver/silver chloride external pressure balanced electrode was employed as the reference electrode. This system was used to measure polarization curves at temperatures over the range 20–430°C and at a pressure of 340 bar (5000 psi) in deaerated 0.01 m NaOH.

In Fig. 101 we present polarization curves obtained for nickel in 0.01 m NaOH over the temperature range from 20 to 400°C. The classic behavior of a passive metal is observed at temperatures up to 400°C, with the active dissolution *hump* being more pronounced when compared with the ambient temperature behavior. At 430°C and at higher temperatures (not shown), the conductivity of the solution is very low and polarization measurements have proven to be difficult to perform and interpret. However, the reproducibility of the measurements illustrated in Fig. 101 was good, including those at the highest temperatures.

With increasing of the temperature, the range of passivity shrinks considerably, as illustrated by Fig. 102. A strong dependence of the length of the passive region on temperature is observed, possibly because the overpotential for oxygen evolution and hydrogen evolution, which defines the practical stability range of water, become smaller as the temperature is increased. Furthermore, increasing temperature most likely shifts the potential at which transpassive dissolution occurs, which marks the upper boundary of the passive range to lower values. In any event, shrinkage of the passive range implies increased susceptibility to corrosion, particularly at highly positive and negative corrosion potentials.

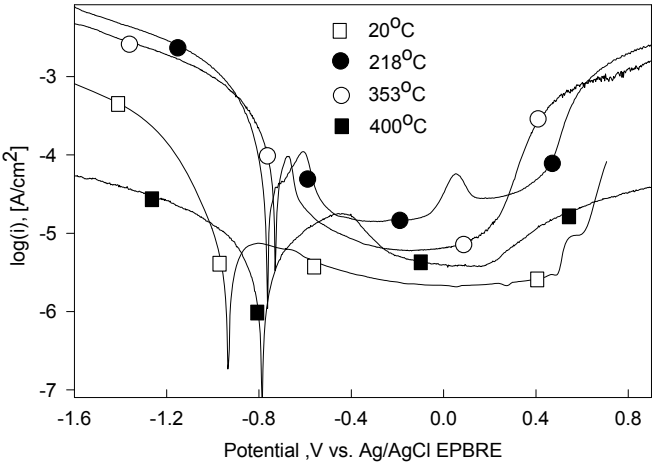

Figure 101. Polarization curves for nickel in 0.01 m NaOH at temperatures ranging from 20ºC to 400ºC. *P* = 340 bar. Reprinted from Ref. 5, Copyright (1997) with permission from Elsevier.

The value of the current in passive region is very important parameter for the prediction and modeling of the metallic corrosion. In Fig. 103 the current in the passive region is plotted as a function of temperature. It is noted that the passive current passes through a maximum at a temperature of around 300°C. The passive current is expected to increase with temperature, because it is partly determined by the transport of ions through the oxide film, a process that is temperature activated. However, the passive current is also determined by the rate of dissolution of the passive oxide film, which is sensitive to the chemical and physical properties of the environment. The Point Defect Model[168] for the growth and breakdown of passive films on metal surfaces gives the steady state current on nickel in terms of

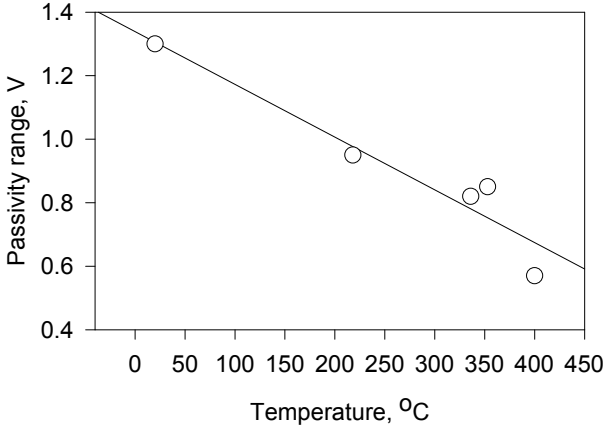

Figure 102. Length of the passive range for nickel in 0.01 m NaOH as a function of temperature at a pressure of 340 bar. Reprinted from Ref. 5, Copyright (1997) with permission from Elsevier.

$$i_{passive} = 2F[k_1^0 e^{aV} e^{-bL_{ss}} + k_s^0 (c_{H^+} / c_{H^+}^o)^n] \tag{98}$$

where a and b are constants, k_1^o and k_s^o are the standard rate constants for the injection of cations into cation vacancies at the metal/film interface and for the dissolution of the film, respectively, L_{ss} is the steady state film thickness, c_{H+} and $c_{H+}{}^o$ are the molar concentrations of H^+ in the solution and in the standard state, and n is the reaction order for the film dissolution reaction with respect to H^+. The steady state barrier layer thickness is given in explicit form as

$$L_{ss} = \left(\frac{1-\alpha}{\varepsilon}\right)V + \frac{1}{\varepsilon}\left\{\frac{2.303n}{\alpha_2 \chi \gamma} - \beta\right\} pH + \frac{1}{\alpha_2 \chi \gamma \varepsilon} \ln\left(\frac{k_2^o}{k_s^o}\right) \tag{99}$$

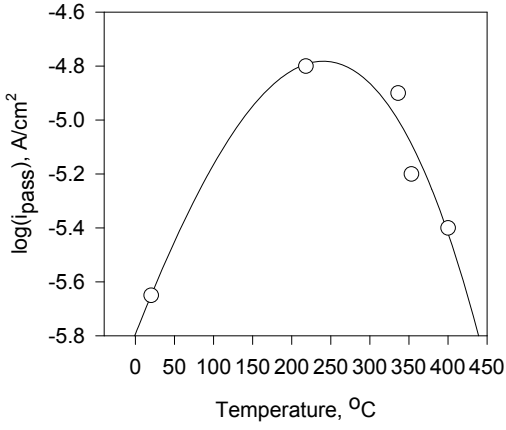

Figure 103. Dependence of the passive current density for nickel in 0.01 m NaOH on temperature at a pressure of 340 bar. Reprinted from Ref. 5, Copyright (1997) with permission from Elsevier.

where α is the polarizability of the film/solution interface, β is the dependence of the potential drop across the film/solution interface on pH, $\gamma = F/RT$, and α_2 and k_2^0 are the standard rate constant and transfer coefficient for the generation of oxygen vacancies at the metal/film interface and hence for generation of the film, ε is the electric field strength, and k_s^0 is the standard rate constant for film dissolution. Equations (71) and (72) have been derived for the case where no change occurs in the oxidation state of the cation upon ejection from the film into the environment. We have previously argued[169] that the rate of corrosion of a metal, which reflects the rate of dissolution of the passive film, because that controls the barrier layer thickness, passes through a maximum at a high subcritical temperature by virtue of competing effects of temperature on the rate constant and on the properties of the aqueous medium (density and hence molar concentration, acid dissociation, and dielectric constant), as shown in Fig. 104, which is taken from the work of Kriksunov and Macdonald.[10] Plotted in this figure is the relative rate of corrosion for two different stoichiometric HCl concentrations and for three different activation

energies. The existence of the maximum in the corrosion rate has been found experimentally using a variety of techniques,[170] including electrochemical emission spectroscopic (*electrochemical noise*) methods,[170,171] and it appears that the same factors extend to determining the passive current density (Fig. 103).

Returning now to Eq. (72), we see that, if the rate of dissolution of the passive film passes through a maximum (due to the competing effects of the second and third terms), then the steady state film thickness (L_{ss}) should pass through a minimum with increasing temperature. That being the case, then both terms on the right side of Eq. (71) will pass through coincident maxima (both terms are sensitive to the same dissolution phenomenon), thereby accounting for the observed maximum in the passive current.

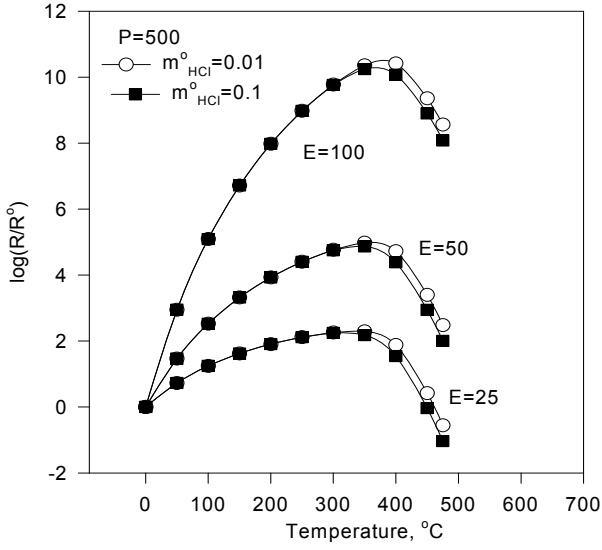

Figure 104. Relative rate of a corrosion reaction versus temperature plotted as a function of activation energy and stoichiometric HCl concentration. Reprinted from Ref. 5, Copyright (1997) with permission from Elsevier.

VIII. SUMMARY AND CONCLUSIONS

It has been argued in this review and elsewhere that a rational basis exists for defining pH in supercritical aqueous systems and sensors have been developed for measuring this parameter at temperatures well in excess of the critical temperature (374.15°C). The principal impediment to realizing the goal of making *research grade* pH measurements that are accurate to better than ± 0.05 is the lack of a viable reference electrode that can operate at temperatures above 500°C and which can provide a reference potential of that is accurate to ca ±5mV. This goal has not yet been realized for T > 500°C, although it has been achieved at low supercritical temperatures up to 400°C.[171] The development of a reference electrode that provides an accurate reference potential remains a pressing need in this field. However, for the specific purpose of monitoring pH in SCWO systems, the external pressure balanced reference electrode (EPBRE), which has now been used to measure potentials to better than ±5 mV in low subcritical systems (T < 300°C) and to about ±20 mV at high supercritical systems (T > 500°C), will probably remain the workhorse for routine potential measurements in high temperature aqueous solutions. Indeed, we believe that considerable room exists for improving the precision of the EPBRE, particularly for measurements in supercritical media.

One such strategy, which is currently being exploited[172] is to slowly pump the internal solution from an external reservoir through the electrode at a slow enough rate so as to maintain the temperature gradient along the non-isothermal bridge but at a high enough rate that the tendency for thermal diffusion to occur is effectively suppressed. This idea is not new, having been described by Danielson[172] about twenty years ago. Nevertheless, this electrode, when combined with a hydrogen electrode in a solution of accurately known hydrogen fugacity, has enabled the measurement of pH to ±0.05 at temperatures to 400°C. However, this reference electrode suffers from two problems that may or may not adversely impact its acceptability as a general tool for studying supercritical aqueous solutions. The first is that the pump that is required to slowly and precisely meter the internal solution into the electrode considerably complicates the system, to the point that, while such complexity may be acceptable in the research laboratory, it is unlikely to find acceptance in the field. The second issue is that the

reference potential, as measured against a hydrogen electrode, strongly depends on the flow rate of the solution through the internal reference electrode compartment, thereby requiring accurate control of the flow rate and calibration against a known standard. The extent to which calibration can be done accurately and conveniently over wide ranges of temperature, pressure, and solution type and composition remains to be determined.

We have also shown that it is possible to measure redox potential at high supercritical temperatures with a sensor that automatically compensates for changes in pH. The sensors that have been developed are rugged and respond rapidly to changes in the redox potential. In particular, the sensor that employs a W/WO_3 pH-sensitive element, is particularly promising, because of its all solid-state structure and exceptional ruggedness. These sensors, when combined with a suitable reference electrode, provide the means for measuring the two most important parameters defining the corrosion conditions that exist in SCWO reactors, namely potential and pH.

Finally, we have demonstrated that it is now possible to perform electrochemical polarization studies in high subcritical and supercritical aqueous systems, which suggests that the whole range of powerful electrochemical techniques, including transient methods and electrochemical impedance spectroscopy (EIS) can be brought to bear on the behavior of metals at the interface between *wet* and *dry* corrosive environments.

REFERENCES

[1] B. Mitton, *Supercritical Water – Materials Challenges*, 17th ICC Meeting, Las Vegas, NV, Oct. 7-11, 2008.

[2] G. Was, P. Ampornrat, G. Gupta, S. Teysseyre, E. A. West, T. Allen, K. Sridharan, L. Tan, Y. Chen, X. Ren, and C. Pister, *J. Nucl. Mat*., **371** (2007) 1.

[3] D. D. Macdonald and L. B. Kriksunov, Electrochim. Acta, **47**, (2001) 775.

[4] D. D. Macdonald, et al., "Supercritical Water Oxidation Studies: Understanding the Chemistry and Electrochemistry of SCWO Systems", Pennsylvania State University Final Report to the US Army Research Office, Grant Nos. DAAL 03-92-G-0397 and DAAH 04-93-G-0150, Feb. 1997.

[5] L. B. Kriksunov and D. D. Macdonald, Corrosion, 53 (1997) 605.

[6] D. D. Macdonald, B. G. Pound, and R. P. Singh "Extension of Potential-pH Diagrams to Concentrated Aqueous Solutions". Proc. Symp. on Equilib. Diagrams and Localized Corrosion. Proc. Honoring Prof. Marcel Pourbaix on his

Eightieth Birthday, 84-2: 69, edited by R. P. Frankenthal and J. Kruger. The Electrochemical Society, Inc., Pennington, N.J. Pennington, NJ, 1984.
[7] G. W. Morey, *Econ. Geol*., **52** (1957) 225.
[8] M. Hodes, P. A. Marrone, G. T. Hong, K. A. Smith, J. W. Tester, *J. Supercritical Fluids*, **29** (2004) 265.
[9] L. B. Kriksunov and D. D. Macdonald, "Measurement and Standardization of pH in Supercritical Aqueous Systems", *Proc. Symp. High Temp. Press. Soln. Chem.*, Int. Conf. Pacific Basin Chem. Socs., PACIFICHEM '95, Amer. Chem. Soc., Washington, DC, 1995.
[10] D. D. Macdonald and L. B. Kriksunov, "Critical Issues in the Supercritical Water Oxidation of Army Toxic Waste," *Proc. Symp. Emerging Technols. Hazardous Waste Manag. VII*, D. W. Tedder (Ed.), ACS Meeting, Atlanta, GA, 1995, (Amer. Chem. Soc., Washington, DC), pp. 1280–1283.
[11] S. N. Lvov, H. Gao, D. Kuznetsov, I Balachov and D. D. Macdonald, *Fluid Phase Equilibria*, **150-1** (1998) 515.
[12] S. N. Lvov, X. Y. Zhou, S. M. Ulyanov, and A. V. Bandura, *Chem. Geol.*, **167** (2000) 105.
[13] R. A. Robinson and R. H. Stokes, *Electrolyte Solutions*, Butterworths, London, 1959.
[14] J. D. Frantz and W. L. Marshall, *Amer. J. Sci*., **284** (1984) 651.
[15] J. W. Johnson, E. H.Oelkers, and H. C. Helgeson, *Computers & Geosciences*, **18** (1992) 899.
[16] NIST Properties of Water Software, National Institute of Science and Technology, Gaithersburg, MD, 1997.
[17] ASME Steam Tables, Thermodynamic and Transport Properties of Steam, 6th Edition, ASME, NY, 1993.
[18] D. D. Macdonald, L. B. Kriksunov. *Corrosion,* **34** (1978) 75.
[19] R. E. Mesmer, C. F. Baes, Jr. *Inorganic Chemistry* **10** (1971) 2290.
[20] R.E. Mesmer, C.F. Baes, Jr. and F.H. Sweeton. *Inorganic Chemistry,* **11** (1972) 537.
[21] R. E. Mesmer, C. F. Baes, Jr. *J. Soln. Chem.,* **3** (1974) 307.
[22] F. H. Sweeton, R. E. Mesmer, C. F. Baes, Jr. *J. Phys. E: Sci. Instrum.,* **6** (1973) 165.
[23] B. F. Hitch, R. E. Mesmer. *J. Soln. Chem.,* **5** (1976) 667.
[24] R. E. Mesmer, H. F. Holmes. *J. Soln. Chem.,* **21** (1992) 725.
[25] D. A. Palmer, D. J. Wesolowski. *Geochimica et Cosmochimica Acta,* **56** (1992) 1093.
[26] D. A. Palmer, D. J. Wesolowski. *Geochimica et Cosmochimica Acta,* **57** (1993) 2929.
[27] D. J. Wesolowshi, D. A. Palmer, R. E. Mesmer, *Water-Rock Interaction,* **51** (1995)
[28] P. Benezeth, D. A. Palmer, D. J. Wesolowski. *Geothermics,* **26** (1997) 465.
[29] P. C. Ho, D. A. Palmer, R. H. Wood. *J. Phys. Chem., B* **104** (2000) 12084.
[30] P. Benezeth, D. A. Palmer, D. J. Wesolowski. *J. Chem. Eng. Data,* **46** (2001) 202.
[31] P. Benezeth, D. J. Wesolowski D. A. Palmer. *J. Chem. Eng. Data,* **48** (2003) 171.
[32] D. D. Macdonald, P. Butler and D. Owen. *Can. J. Chem.,* **51** (1973) 2590.
[33] D. D. Macdonald, P. Butler,and D. Owen. *J. Phys. Chem.,* **77** (1973) 2474.
[34] D. D. Macdonald, D. Owen. *Can. J. Chem.,***51** (1973) 2747.

[35] D. W. Shoesmith, L. Woon. *Can. J. Chem.,* **54** (1976) 3553.
[36] G. Giasson, P. H. Tewari. *Can. J. Chem.,* **56** (1978) 435.
[37] Y. Matsushima, A. Matsunaga, K. Sakai, A. Okuwaki. *Bull. Chem. Soc. Japan.,* **61** (1988) 4259.
[38] B. A. Bilal, E. Mueller. *Z. Naturforsch.,* **48A** (1993) 1073.
[39] L. W. Niedrach. *J. Electrochem. Soc.,* **127** (1980) 2122.
[40] T. Tsuruta, D. D. Macdonald. *J. Electrochem. Soc.,* **129** (1982) 1202.
[41] M. J. Danielson, O. H. Koski, J. Meyers. *J. Electrochem. Soc.,* **132** (1985) 296.
[42] M. J. Danielson, O. H. Koski, J. Meyers. *J. Electrochem. Soc.,* **132** (1985) 2037.
[43] W. L. Bourcier, G. C. Ulmer, H. L. Barnes. *Hydrothermal Experimental Techniques,* Wiley-Interscience, New York, 1987, p. 157.
[44] L. W. Niedrach. *Science,* **207** (1980) 1200.
[45] L. W. Niedrach. *Patent Number,* 4264424 (General Electric, 1981).
[46] L. W. Niedrach. *J. Electrochem. Soc.,* **212** (1982) 672.
[47] L. W. Niedrach. *Adv. Ceram. Sciences,* **12** (1984) 672.
[48] D. D. Macdonald, S. Hettiarachchi, S. J. Lenhart. *J. Solut. Chem.,* **17** (1988) 719.
[49] S. Hettiarachchi, D. D. Macdonald. *J. Electrochem. Soc.,* **131** (1984) 2206.
[50] D. D. Macdonald, S. Hettiarachchi, H. Song, K. Makela, R. Emerson, M. Haim. *J. Solut. Chem.,* **21** (1992) 849.
[51] S. Hettiarachchi, K. Makela, H. Song, D. D. Macdonald. *J. Electrochem. Soc.,* **139** (1992) L3-L4.
[52] L. B. Kriksunov, D. D. Macdonald. *ASME Heat Transfer Div Publ HTD,* Vol. 317-2, ASME Heat Transfer Division, 1995, p. 271.
[53] S. N. Lvov, G. Perboni, M. Broglia. *Physical Chemistry of Aqueous Systems*, Begell House, New York, 1995, p. 441.
[54] D. D. Macdonald, L. B. Kriksunov. in *Proc. Symp. Emerging Technols. Hazardous Waste Manaf. VII,* Ed. by. D.W. Tedder, Atlanta, GA, 1995, p. 1280.
[55] L. B. Kriksunov, D. D. Macdonald. in *Proc. Symp. High Temp. Press. Soln. Chem., Int. Conf. Pacific Basin Chem. Socs., PACIFICHEM '95*, Washington D. C., 1995.
[56] S. N. Lvov, G. Perboni, M. Broglia, *Physical Chemistry of Aqueous Systems 441* (Begell House, New York, 1995).
[57] D. D. Macdonald, L. B. Kriksunov, in *Proc. Symp. Emerging Technols. Hazardous Waste Manuf. VII*, Ed. by D. W. Tedder, Atlanta, GA, 1995, p. 1280.
[58] L. B. Kriksunov and D. D. Macdonald, in *Proc. Symp. High Temp. Press. Soln. Chem., Int. Conf. Pacific Basin Chem. Socs., PACIFICHEM'95*, Washington, D.C., 1995.
[59] K. Ding, W.E. Seyfried, Jr., *Geochimica et Cosmochimica Acta,* **59** (1995) 4769.
[60] K. Eklund, S. N. Lvov, D.D. Macdonald. *J. Electroa. Chem.,* **437** (1997) 99.
[61] R. Fernandez-Prini, R. Crovetto. *J. Phys. Chem. Ref. Data,* **18** (1989) 1231.
[62] N. Kishima, H. Sakai. *Earth Planetary Sci. Lett.,* **67** (1984) 79.
[63] K. Ding, W. E. Seyfried, Jr. *J. Soln. Chem.,* **25** (1996) 421.
[64] S. N. Lvov, H. Gao, D. D. Macdonald. in *Proc. Fifth Int. Symp. Hydrothermal Reacts.*, Ed. by D. A. Palmer and D. Wesolowski, ORNL, U.S. Dept. of Energy, Gatlinburg, TN, 1997, p. 146.
[65] S. N. Lvov, H. Gao, D. D. Macdonald. *J. Electroa. Chem.,* **443** (1998) 186.
[66] S. N. Lvov, X. Y. Zhou, D. D. Macdonald. *J. Electroanal. Chem.,* **463** (1999) 146.

[67] K. Sue, M. Uchida, T. Usami, T. Adschiri, K. Arai. *J. Supercritical Fluids,* **28** (2004) 287; K. Sue, M. Uchida, T. Adschiri, K. Arai. *J. Supercritical Fluids,* **31** (2004) 295.
[68] M. H. Lietzke. *J. Amer. Chem. Soc.,* **77** (1955) 1344.
[69] R. S. Greeley, W. T. Smith, R. W. Stoughton, M. H. Lietzke. *J. Phys. Chem.,* **64** (1960) 652.
[70] R. S. Greeley, W. T. Smith, M. H. Lietzke, and R. W. Sroughton. *J. Phys. Chem.,* **61** (1960) 1445.
[71] M. H. Lietzke, H. B. Hupf, R. W. Stoughton. *J. Phys. Chem.,* **69** (1965) 2395.
[72] D. D. Macdonald. in *Modern Aspects of Electrochemistry*, Ed. by J. O'M. Bockris and B. E. Conway, Plenum, NY, 1975, p. 141.
[73] ????
[74] B. Case, G. J. Bignold. *J. Appl. Electrochem.,* **1** (1971) 141.
[75] K. Ding., W. E. Seyfried, Jr., *Science,* **272** (1996) 1634.
[76] K. Ding, W. E. Seyfried, Jr., *Geochim. Cosmochim. Acta,* **56** (1992) 3681.
[77] G. B. Naumov, B. N. Ryzhenko, I. L. Khodakovsky. *Handbook of Thermodynamic Data,* Ed. by I. Barnes and V. Speltz, U.S. Geological Survey, Menlo Park, CA, 1974.
[78] J. C. Tanger IV, H. C. Helgeson. *Am. J. Sci.,* **288** (1988) 19.
[79] D. A. Sverjensky, J. J. Hemley, W. M. D'Angelo. *Geochim. Cosmochim. Acta,* **55** (1991) 988.
[80] E.L. Shock, E. H. Oelkers, J. W. Johnson, D. A. Sverjensky, H. C. Helgeson. *J. Chem. Soc. Faraday Tran.,* **88** (1992) 803.
[81] J. V. Dobson, M. N. Dagless, H. R. Thirsk. *J. Chem. Soc., Faraday Trans. i.,* **68** (1972) 739.
[82] J. V. Dobson, M. N. Dagless, and H. R. Thirsk. *J. Chem. Soc., Faraday Trans.i* **68** (1972) 764.
[83] J. V. Dobson, B. R. Chapman, and H. R. Thirsk, in *International Conference on High Temperature High Pressure Electrochemistry in Aqueous Solutions(NACE)*, University of Survey, 1973.
[84] D. D. Macdonald, P. R. Wentrcek, A. C. Scott. *J. Electrochem. Soc.,* **127** (1980) 1745.
[85] Z. Nagy, R. M. Yonco. *J. Electrochem. Soc.,* **133** (1986) 2232.
[86] S. Hettiarachchi, D. D. Macdonald. *J. Electrochem. Soc.,* **134** (1987) 1307.
[87] P Jayaweera, T. O. Passell, and P. J. Millett, USA Patent 5425871.
[88] D. de Jones, H. C. Mastrson. *Adv. Corr. Sci. Tech.,* **1** (1970) 1.
[89] D. D. Macdonald, D. Owen. *J. Electrochem. Soc.,* **120** (1973) 317.
[90] D. D. Macdonald, A. C. Scott, P. Wentrcek. *J. Electrochem. Soc. Electrochemical Science and Technology,* **126** (1979) 908.
[91] D. D. Macdonald, S. Hettiarachchi, S. J. Lenhart, in Proc. 1987 Symposium on Chemistry in High Temperature Water, EPRI Report NP-6005, Brigham Young University, Provo, Utah, 1990.
[92] S. Hettiarachchi, S. J. Lenhart, D. D. Macdonald, in *Proc. 3rd Int'l. Symp. Envir. Degrad. Mat. Nucl. Power Systs. -Water Reactors* Ed. by G. J. Theus and J. R. Weeks, Met. Soc. AIME, Warrendale, PA, 1988, p. 165.
[93] D. D. Macdonald, S. Hettiarachchi, R. Emerson, K. Makela, H. Song, M. B. Haim. in Proc. Symp. on Chemistry in HIgh-Temperature Aqueous Solutions, Brigham Young University, Provo, UT, 1991, C3a-1.
[94] M. J. Danielson, *Corrosion* **39** (1983) 202.
[95] S. N. Lvov, X.Y. Zhou, *Mineralogical Magazine,* **62A** (1998) 929.

[96] A. J. Bard, L.R. Faulkner in *Electrochemical Methods Fundamentals and Applications,* 2nd Edition, John Wiley & Sons, Inc., 2000, p. 63.
[97] T. Tsuruta, D. D. Macdonald. *J. Electrochem. Soc.,* **129** (1982) 1221.
[98] H. W. Harper. *J. Phys. Chem.,* **89** (1985) 1659.
[99] R. Haase, *Thermodynamics of Irreversible Processes,* Addison-Wesley, Reading, MA, 1969.
[100] S. N. Lvov, D. D. Macdonald, *J. Electroanal. Chem.,* **403** (1996) 25.
[101] G. R. Engelhardt, S. N. Lvov, D. D. Macdonald, *J. Electroanal. Chem.,* **429** (1997) 193.
[102] D. D. Macdonald, A. C. Scott, and P. R. Wentrcek, *J. Electrochem. Soc.,* **126** (1979) 1618.
[103] L. S. Hwang, A. Boateng, and D. D. Macdonald, in Proc. Symp. Corr. Batteries and Fuel Cells and Corr. Solar Energy Systs, Ed. by C. J. Johnson and S. L. Pohlman, The Electrochemical Society, Inc., Pennington,NJ, 1983, p. 492.
[104] N. Akinfiev, S.N. Lvov, D.D. Macdonald. *Comput. Geosci.* (in press).
[105] A. S. Quist, W. L. Marshall, *J. Phy. Chem.,***69** (1965) 2984.
[106] Y. D. Rakhmilevich, I. A. Dibrov, S. N. Lvov. *Russ. J. Phys. Chem.,* **61** (1987) 2391.
[107] S. N. Lvov, A. Marcomini, M. M. Suprun, in Proc. 4th Int. Sym. On Hydrothermal Reactions, Ed. by M. Cuney and M. Cathelineau, Nancy, 1993, p. 135.
[108] S. N. Lvov, X. Y. Zhou, G. C. Ulmer, H. L. Barnes, D. D. Macdonald, S. M. Ulyanov, L. G. Benning, D. E. Grandstaff, M. Manna, and E. Vicenzi. *Chemical Geology,* **198** (2003) 141.
[109] K. Sue, K. Murata, Y. Matsuura, M. Tsukagoshi, T. Adschiri, K. Arai. *Rev. Sci. Instrum.,* **72** (2001) 4442.
[110] K. Sue, K. Murata, Y. Matsuura, M. Tsukagoshi, T. Adschiri, K. Arai. *Fluid Phase Equilib.,* **194-197** (2002) 1097.
[111] D. D. Macdonald, S. Hettiarachchi, H. Song, K. Makela, R. Emerson and M. Ben-Haim, *J. Soln. Chem*., **21**(1992) 849.
[112] M. J. Danielson, O. H. Koski and J.Myero, *J. Electrochem. Soc*., **132** (1985) 296; **132** (1985) 2037.
[113] S. N. Lvov, X. Y. Zhou, S. M. Ulyanov, H. Gao and D. D. Macdonald, "Potentiometric Measurement of Association Constant and pH in HCL(aq) High Temperature Solutions", in *Steam, Water, and Hydrothermal Systems: Physics and Chemistry Meeting the Needs of Industry*, Ed. by P. R. Tremaine, P. G. Hill, D. E. Irish, and P. V. Palakrishnan, NRC Press, Ottawa, 2000, pp. 653-660.
[114] D. D. Macdonald, I. Balachov and G. R. Engelhardt, *Power Plant Chemistry*, **1** (1999) 9.
[115] L. B. Kriksunov, C. Liu and D.D. Macdonald. "Oxygen, Hydrogen and Redox Potential Combination Sensors for Supercritical Aqueous Systems," Proc. 1st Int'l. Workshop Supercritical Water Oxidation, Amelia Island Plantation, FL, February, 1995.
[116] L. B. Kriksunov, D. D .Macdonald and P. J.Millett, *J. Electrochem. Soc*., **141** (1994) 3002.
[117] G. S. Was, S. Teysseyre and Z. Jiao, "Corrosion of Austenitic Alloys in Supercritical Water," *Corrosion Science Section*, Vol. 26, No. 11, (2006).
[118] D. D. Macdonald, *J. Electrochem. Soc*., **139** (1992) 3434
[119] E. C. Potter and G. M. W. Mann, "Oxidation of Mild Steel in High Temperature Aqueous Systems," Proc. 1st Int. Congr. Met. Corros., Butterworths, London, Int. Union Pure Appl. Chem., 1961, p. 417.

[120] A. G. Crouch and J. Robertson, *Acta Metall. Mater.*, **38** (1990) 2567
[121] J. Davenport, L. J. Oblonsky, M. P. Ryan, and M. F. Toney, "The Structure of the Passive Film That Forms on iron in Aqueous Environments," *J.Electrochem. Soc.*. **147** (2000) 2162.
[122] P. Ampornrat and G. S. Was, "Oxidation of ferritic-martensitic alloys T91, HCM12A, and HT-9 in supercritical water", *Journal of Nuclear Materials* **371** (2007) 1.
[123] Y. Chen, K. Sridharan, T. R. Allen, S. Ukai, "Microstructural examination of oxide layers formed on an oxide dispersion strengthened ferritic steel exposed to supercritical water," *Journal of Nuclear Materials* **359** (2006) 50-58.
[124] A. T. Motta, A. D. Siwy, J.M. Kunkle, J. B. Bischoff, R. J. Comstock, Y. Chen, and T. R. Allen, "Microbeam Synchrotron Radiation Diffraction and Fluorescence Study of Oxide Layers Formed on 9Cr ODS Steel in Supercritical Water'.
[125] A. Yilmazbayhan, Marcelo Gomes da Silva, Arthur Motta, Hyun-Gil Kim, Yong Hwan Jeong, Jeong-Yong Park, Robert Comstock, Barry Lai, Zhoughou Cai, "Characterization of Oxides Formed on Model Zirconium Alloys in 360ºC Water Using Micro-Beam Synchrotron Radiation", (2005)
[126] Q. Peng, E. Gartner, J. T. Busby, A. T.Motta, and G. S. Was, "Corrosion Behavior of Model Zirconium Alloys in Deaerated Supercritical Water at 500ºC," *Corrosion Science Section*, **63** (6) (2007) .
[127] Y. H. Jeong, J. Y. Park, H. G. Kim, J. T. Busby, E. Gartner, M. Atzmon, G. S. Was, R. J. Comstock, Y. S. Chu, M. Gomes da Silva, A. Yilmazbayhan and A. T. Motta, "Corrosion of Zirconium-Based Fuel Cladding Alloys in Supercritical Water", (2005).
[128] A. T. Motta, A. D. Siwy, J. K. Kunkle, J. M. Bischoff, R. J. Comstock, Y. Chen, and T. R. Allen, "Microbeam Synchrotron Radiation Diffraction and Fluorescence Study of Oxide Layers Formed on 9Cr ODS Steel in Supercritical Water", 17th ICC Meeting, Las Vegas, NV, Oct. 7-11, 2008.
[129] X. Y. Guan, T. Zhu, D. D. Macdonald, "Application of electrochemical noise analysis in high subcritical and supercritical aqueous systems", *NACE* paper No. 06449 (2006).
[130] C. Liu, D. D. Macdonald, E. Medina, J. J. Villa and J. M. Bueno, "Probing Corrosion Activity in High Subcritical and Supercritical Water through Electrochemical Noise Analysis," *Corrosion*, **50** (1994) 687.
[131] K. Wagner, W. Traud, Z. *Elektrochem* **44** (1938) 391.
[132] N. Akiya, P. E. Savage, *Chem. Rev*. **102** (2002) 2725.
[133] L. B. Kriksunov, D. D. Macdonald; "Corrosion in Supercritical Water Oxidation Systems: A Phenomenological Analysis," *J. Electrochem. Soc***. 142**, 1995, 4069.
[134] X.Y. Zhou, S.N. Lvov, X.J. Wei, L.G. Benning, D.D. Macdonald, "Quantitative Evaluation of General Corrosion of Type 304 Stainless Steel in Subcritical and Supercritical Aqueous Solutions via Electrochemical Noise Analysis", *Corrosion Science,* **44** (2002) 841.
[135] W. P. Iverson, *J. Electrochem. Soc*., **115** (1968) 617.
[136] J. L. Dawson, "Electrochemical Noise Measurement for Corrosion Applications," ASTM Publication Code Number (PCN) 04-012770-27, p.3-35
[137] R. A. Cottis, "Interpretation of Electrochemical Noise Data", *Corrosion*, **57** (2001) 265.
[138] F. Mansfeld and H. Xiao, "Electrochemical Noise Analysis of Iron Exposed to NaCl Solutions of Different Corrosivity", *J. Electrochem. Soc*., **140** (1993) 2205.
[139] D. D. Macdonald and L. Chen, unpublished data (1982).

[140] X.-Y. Guan and D. D. Macdonald, *Corrosion* **65** (2009) 376
[141] P. Botella, C. Frayret, T. Jaszay, and M. H. Delville; "Experimental study, via current-potential curves, of the anodic behavior of Alloy C-276 and T60 titanium in chlorinated and oxygenated aqueous media under sub- to supercritical conditions" *J. of Supercritical Fluids*, **25** (2003) 269.
[142] X.-Y. Guan and D. D. Macdonald, Corrosion 65 (2009) 427.
[143] K. J. Laidlaw, *Chemical Kinetics*, Harper & Row, NY, 3rd Ed., 1987.
[144] D. D Macdonald, "Effect of Pressure on the Rate of Corrosion of Metals in High Subcritical and Supercritical Aqueous Systems" *J. Supercritical Fluids*, 3**0** (2004) 375.
[145] S. D. Iyer, and M. T. Klein, "Effect of pressure on the rate of butyronitrile hydrolysis in high-temperature water" *J. Supercritical Fluids*, **10** (1997) 191.
[146] B. Wu, M. T. Klein, and S. I. Sandler, "Solvent effects on reactions in supercritical fluids" *Ind. Eng. Chem. Res*., **30** (1991) 822.
[147] D. D. Macdonald and J. B. Hyne. "The Pressure Dependence of Benzyl Chloride Solvolysis in Aqueous Acetone and Aqueous DimethylSulfoxide." *Can. J. Chem.*, **48** (16) (1970) 2494.
[148] ???
[149] D. D. Macdonald, D. D., P. C. Lu, M. Urquidi-Macdonald, and T. K. Yeh, "Theoretical Estimation of Crack Growth Rates in Type 304 Stainless Steel in BWR Coolant Environments." *Corrosion*, **52**(10), 768-785 (1996).
[150] D. D. Macdonald and G. Cragnolino, "The Critical Potential for the IGSCC of Sensitized Type 304 SS in High Temperature Aqueous Systems". Proc. 2nd Int'l. Symp. Env. Deg. Mat. Nucl. Power Syst. - Water Reactors. Monterey, CA, September 9-12, 1985.
[151] Q. J. Peng, J. Kwon, and T. Shoji, "Development of a fundamental crack tip strain rate equation and its application to quantitative prediction of stress corrosion cracking of stainless steels in high temperature oxygenated water," *J. Nuc. Mat.* **324** (2004) 52.
[152] M. P. Manahan, Sr., D. D. Macdonald and A. J. Peterson, Jr., *Corros. Sci*., **37** (1995) 189.
[153] A. Wuensche and D. D. Macdonald, Corrosion 2001, Paper No. 01236, Houston, TX, 2001.
[154] D. D. Macdonald and M. Urquidi-Macdonald, "The Electrochemistry of Nuclear Reactor Coolant Circuits," Encyclopedia of Electrochemistry, Ed. by A.J. Bard and M. Stratmann, Vol. 5; "Electrochemical Engineering," Ed. by Digby D. Macdonald and Patrik Schmuki, Wiley-VCH Verlag GmbH & Co. KGaA, Weinheim, 2007, pp. 665-720.
[155] D. D. Macdonald, "Viability of Hydrogen Water Chemistry for Protecting In-Vessel Components of Boiling Water Reactors," *Corrosion*, **48**(3) (1992) 194.
[156] M. Vankeerbergen and D. D. Macdonald, *Corros. Sci*., **44** (2002) 1425.
[157] S. Hettiarachchi, "BWR SCC mitigation experiences with hydrogen water chemistry," Proceedings of the Twelfth International Conference on Environmental Degradation of Materials in Nuclear Power Systems-Water Reactors, 2005, Proceedings of the Twelfth International Conference on Environmental Degradation of Materials in Nuclear Power Systems-Water Reactors., NACE International, Houston, TX, 2005, p 685-701.
[158] D. M. Bartels, K. Takahashi, J. A. Cline, T. W. Marin and C. D. Jonah, "Pulse Radiolysis of Supercritical Water. 3. Spectrum and Thermodynamics of the Hydrated Electron", *J. Phys. Chem. A*, **109** (2004) 1299-1307.

[159] G. Wu, Y. Katsumura, Y. Muroya, X. Li, Y. Terada, "Pulse radiolysis of high temperature and supercritical water: experimental setup and e-observation" *Radiation Physics and Chemistry*, **60** (2001) 395-398.
[160] K. Ghandi and P.W. Percival, "Prediction of Rate Constants of Reactions of the Hydroxyl Radical in Water at High Temperatures and Pressures," *The Journal of Physical Chemistry A*, **107(**17) (2003).
[161] J. Elliot, "Rate Constants and G-Values for the Simulation of the Radiolysis of Light Water Over the Range 0-300 ^{o}C", Atomic Energy of Canada Ltd (AECL) Report No. 11073, Oct., 1994.
[162] T. W. Marin, J. A. Cline, K. Takahashi D. M. Bartels and C. D. Jonah, "Pulse Radiolysis of Supercritical Water. 2. Reaction of Nitrobenzene with Hydrated Electrons and Hydroxyl Radicals," *J. Phys. Chem. A*, **106** (2002) 12270.
[163] M. Lin, Y. Katsumura, Y. Muroya, H. He, G. Wu, Z. Han, T. Miyazaki and H. Kudo, "Pulse Radiolysis Study on the Estimation of Radiolytic Yields of Water Decomposition Products in High-Tembperature and Supercritical Water: Use of Methyl Viologen as a Scavenger," *J. Phys. Chem. A*, **108** (2004) 8287-8295.
[164] W. G. Burns and W. R. Marsh, "Radiation Chemistry of High Temperature (300 – 400^{o}C) Water", *J. Chem. Soc. Faraday*, 1 **77** (1981) 197.
[165] S. Teysseyre and G. S. Was, "Stress Corrosion Cracking of Austenitic Alloys in Supercritical Water", *Corrosion Science Section,* (2006).
[166] P. Andresen, *Corrosion*, **49** (1993) 714.
[167] D. D. Macdonald, *Pure Appl. Chem*., **71** (1999) 951.
[168] L. B. Kriksunov and D. D. Macdonald, *J. Electrochem. Soc*., **142** (1995) 4069.
[169] C. Liu, D. D. Macdonald, E. Medina, J. Villa, and J. Bueno, *Corrosion*, **50**(9) (1994) 687.
[170] X. Y. Zhou, S. N. Lvov, X. J. Wei, L. G. Benning, and D. D. Macdonald, "Measuring Corrosion Rate of Type 304 SS in Subcritical and Supercritical Aqueous Solutions via Electrochemical Noise Analysis", *Corrosion*, in preparation (2000).
[171] S. N. Lvov, X. Y. Zhou, and D. D. Macdonald, *J. Electroanal. Chem.*, **463** (1999) 146.
[172] M. J. Danielson, *Corrosion*, **39** (1983) 202.

2

Passive Oxide Films on Iron by In-Situ Detection of Optical Techniques

Toshiaki Ohtsuka

Division of Materials Science, Graduate School of Engineering, Hokkaido University, Kita13 Nishi 8, Kita-ku, Sapporo 060-8628 Japan

I. INTRODUCTION

Passivity of metals was initially stated by Faraday[1] and Schœnbein[2] over 150 years ago. The origin of the passivity was argued and at the present the passivity is thought to be the formation of three dimensional oxide films. It is stably formed in aqueous solution. The passive oxides are extremely thin (usually a few nm), so it is very difficult to detect them analytical techniques. For the quantitative description, electrochemistry is a key technology, because the oxidation state of the metal surface can be precisely controlled by electrochemical apparatus. Since the electrochemical control is restricted into solution phase, the passivated surface should be characterized in the same phase. To overcome the difficulty for characterization, several optical techniques have been applied.

The presence of the thin oxide film on iron was confirmed by Freundlich[3] and Tronstadt[4] by using an optical technique of ellipsometry. The ellipsometry is one of the most sensitive techniques

S.-I. Pyun and J.-W. Lee (eds.), *Progress in Corrosion Science and Engineering II*, Modern Aspects of Electrochemistry 47, DOI 10.1007/978-1-4419-5578-4_2,

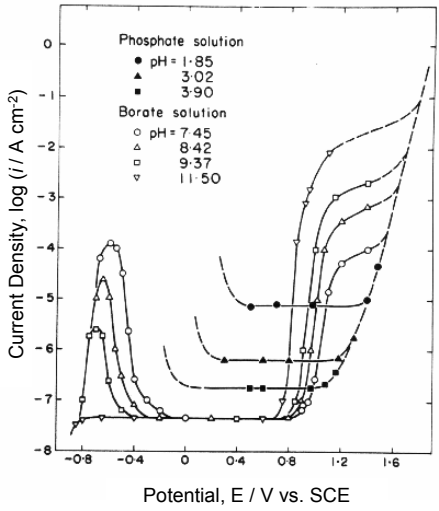

Figure. 1. Potential-current density (*cd*) relation of iron electrode in borate and phosphate solutions at various pH values. The *cd* is taken after 1 h at each potential. Reprinted from N. Sato, T. Noda, and K. Kudo, "Thickness and Structure of Passive Films on Iron in Acidic and Basic Solutions", *Electrochim. Acta*, **19** (1974) 471, Copyright ©1974 with permission from Elsevier Science.

to detect a thin layer on metals and has been applied to the study of surface oxide film by many authors. The advantage of ellipsometry is that it can be used in an aqueous environment. Electronic spectroscopy such as XPS, AES etc., electron diffraction, mass spectroscopy such as SIMS have been conducted to determine the structure and composition of the passive oxide. For the ex-situ techniques under vacuum, since the electrodes are removed from electrolyte, the film may be altered through crystallization and/or dehydration. To avoid the alteration, the following in-situ techniques by which the oxide film is measured in the environment where it was formed have been used; Mössbauer spectroscopy, Raman spectroscopy including surface enhanced Raman spectroscopy, and X-ray adsorption techniques such as XANES and EXAFS.

First, a typical potential-current relation is shown in Fig. 1 where the potential was plotted against saturated calomel electrode (SCE).[5] The iron electrode exhibits four potential regions: the active dissolution, active-passive transition, the passive and the oxygen evolution. In the passive potential region, the steady current density (*cd*) is not dependent on the potential, but changes with solution pH values. The *cd*s plotted in Fig. 1 were taken after 1 h polarization under the constant potential control. They reach a steady *cd* in the solution at pH lower than four in 1 h. The *cd* in neutral and slightly alkaline solutions does not, however, reach the steady-state value and continues to decay even after 1 h polarization. The steady *cd* means that the passive oxide is under the stationary state in which the passive oxide remains unchanged as time goes on. In this chapter, the discussion is mainly focused on the passive oxide under the stationary state.

In this chapter we first introduce optical techniques combined with electrochemistry for study of the passive oxide and then we focus on the growth mechanism, composition, and nature of the passive oxide on iron and steels, which were detected by the optical techniques of ellipsometry, Raman spectroscopy, potential modulation reflectance, and photo-electrochemistry combined with electrochemistry.

II. OPTICAL TECHNIQUES

1. Ellipsometry

Ellipsometry is an optical technique in which the change in ellipsoidal shape of the polarized light is measured between the incident and reflected polarized lights. Since the change is related to the complex refractive indices of the solid surface and the surface film, and the thickness of the film, the ellipsometry characterizes the surface film in thickness at sub-nanometer scale. Since the ellipsometry operates with visible light with a constant wavelength and the corrosion environment (i.e., air and electrolyte) is transparent in that light region, in-situ application to the study of corroded metal surfaces could be easily achieved. The basics and application of ellipsometry are described in detail in the book published by Azzum and Bashara.[6]

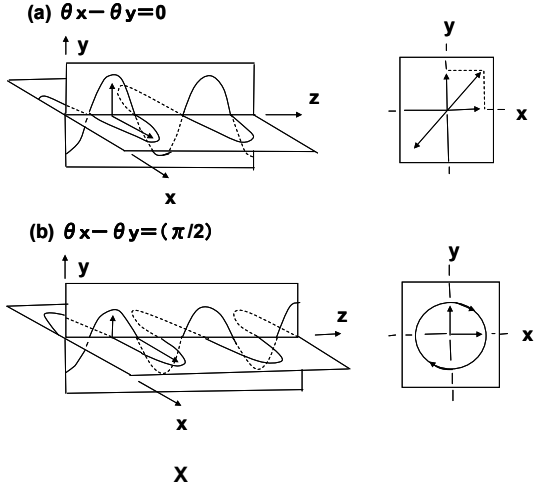

Figure 2. Loci combined by two vectors at vibrated on x plane and on y plane. (a) In the case that the phase shift between the two vectors is zero, and (b) the phase shift is (π/2) radian.

(*i*) *Polarized Light*

The polarized light can be divided into plane-polarized and ellipsoidal-polarized lights. The polarized light is described by two basic plane-polarized lights, the electric vector of which meets at right angle with each other. When the propagation direction is z, and vibration directions of the vectors of the two basic polarized lights are x and y, the vibration of electric vectors are described as follows:

$$\boldsymbol{E}_x = E_x \exp\left[j(\omega t - kz + \theta_x)\right] \tag{1}$$

$$\boldsymbol{E}_y = E_y \exp\left[j(\omega t - kz + \theta_y)\right] \tag{2}$$

where $j = (-1)^{1/2}$ and $\boldsymbol{E}_x$ and $\boldsymbol{E}_y$ are complex number. When the phase shifts, θ_x and θ_y, are same as each other ($\theta_x = \theta_y$), the loci of the summation of two vectors reveals a vector propagating on the plane slanting against the x axis with the angle of arctan (E_y/E_x) (Fig. 2a). When the phase shift between the two vectors is ($\pi/2$)

radian, the shape of the loci in the x-y plane becomes an ellipsoid (Fig. 2b), depending on the amplitude ratio of (E_y/E_x). The shapes of the ellipsoid shown in Fig. 1 are the special cases and in general it is seen that the shape changes with the amplitude ratio of (E_y/E_x) and the phase shift of ($\theta_x - \theta_y$).

(*ii*) *Reflection of Polarized Light at Solid Surface*

Let's consider light reflection on a solid surface at an incidence angle of ϕ_1, where the incidence angle is defined at an angle between the incidence light beam and the normal direction on the surface (Fig. 3). For the light reflection, the two basic plane-polarized lights are selected as follows; one is a plane-polarized light which vibrates on a plane including incident and reflected light beams (the incidence plane) and the other vibrates on the plane normal to the incidence plane. The former is designated as parallel (p-) polarized light and the latter as parpendicular (s-) polarized light. The shape of the ellipsoidal polarized light propagating is a function of the amplitude ratio of E_p/E_s and the phase shift of $\theta_p - \theta_s$.

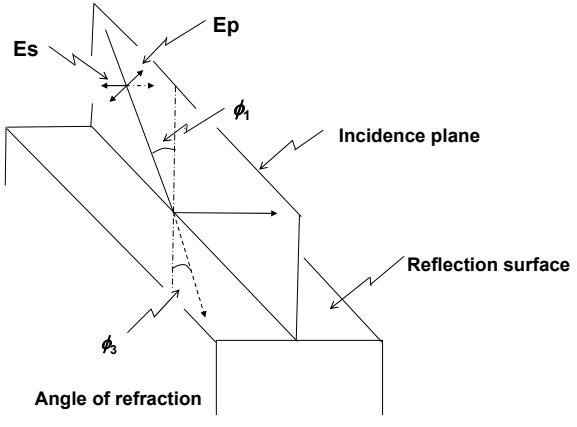

Figure 3. Incidence of polarized light at angle of incidence ϕ_1, refraction at angle of refraction ϕ_3, and reflection. $\mathbf{E}_P$ is electric vector which vibrates on the incidence place and Es on the place normal to the incidence plane.

When a plane-polarized light reflects on a solid surface, phase retardation occurs as well as amplitude reduction. The ratio of the reflected light to the incident light can be described as the following reflection coefficients for the p- and s- polarized light.

$$\boldsymbol{r}^{p} = \boldsymbol{E}^{p}(r) / \boldsymbol{E}^{p}(i) = r^{p} \exp [j(\Delta^{p}(r - i))] \tag{3}$$

$$\boldsymbol{r}^{s} = \boldsymbol{E}^{s}(r) / \boldsymbol{E}^{s}(i) = r^{s} \exp [j(\Delta^{s}(r - i))] \tag{4}$$

where p and s represent the reflection of p- and s-polarized light, respectively, and (r) and (i) reflected and incident lights, respectively. $\Delta^{p}(r - i)$ and $\Delta^{s}(r - i)$ is phase retardation at the reflection for the individual lights.

The change in ellipsoidal shape between the incident and reflected lights is determined by a ratio of $\boldsymbol{r}^{p}$ to $\boldsymbol{r}^{s}$ described in Eqs. (3) and (4). The change is described by the following relative reflection ratio:

$$\boldsymbol{r} = \boldsymbol{r}^{p} / \boldsymbol{r}^{s} = \tan \Psi \exp \Delta \tag{5}$$

where

$$\tan \Psi = r^{p} / r^{s} \tag{6}$$

$$\Delta = \Delta^{p}(r - i) - \Delta^{s}(r - i) \tag{7}$$

and tan Ψ represents a relative amplitude ratio and Δ a relative phase retardation. For the ellipsometric experiment, Ψ and Δ become measurable parameters and compared with the values theoretically calculated from the reflection equations.

(*iii*) *Reflection Coefficient*

The reflection coefficient shown in Eqs. (4)-(6), i.e., the change of the reflected light against the incident light is theoretically derived from the usual reflection equations. In this calculation, refractive indices are expressed as complex numbers (complex refractive index),

$$\boldsymbol{N} = n - jk \tag{8}$$

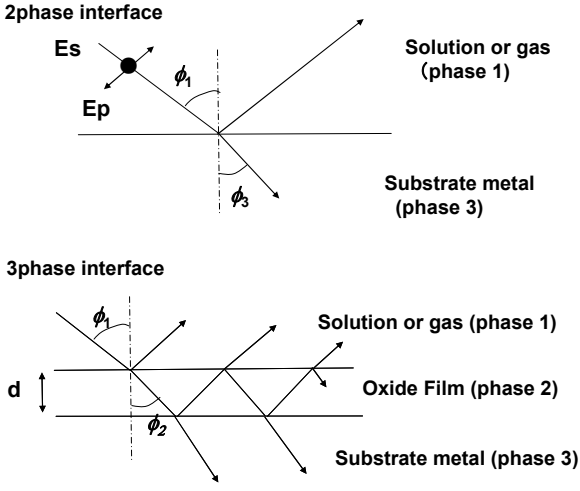

Figure 4. Reflection of the light at two-phase interface and the three-phase interface. In the three-phase interface, thin film is formed between the initial two phases.

where n is an usual refractive index and k an extinction coefficient which indicates the degree of decay in magnitude of propagating light in a medium.

The refection coefficients for the p- and s- polarized lights at the interface between the solution or gas (phase 1) and the substrate (phase 3), as shown in Fig. 4, are described as the following Fresnel's equations,

$$r^{p}_{13} = (N_3\cos\phi_1 - N_1\cos\phi_3) / (N_3\cos\phi_1 + N_1\cos\phi_3) \quad (9)$$

$$r^{s}_{13} = (N_1\cos\phi_1 - N_3\cos\phi_3) / (N_1\cos\phi_1 + N_3\cos\phi_3) \quad (10)$$

where the ϕ_3 is an angel of refraction derived from the Snell's law,

$$N_3\sin\phi_3 = N_1\sin\phi_1 \quad (11)$$

Since the N_3 is a complex number, $\sin\phi_3$ is becomes a complex number.

When the surface film (phase 2) is formed between the phase 1 and phase 3, the reflection coefficient for the three phases is changed according to the following Drude's equation with consideration of the multiple reflection in the film:

$$\boldsymbol{r}^{p}_{123} = (\boldsymbol{r}^{p}_{12} + \boldsymbol{r}^{p}_{23}\exp(-j\boldsymbol{D})/\,[1 + \boldsymbol{r}^{p}_{12}\boldsymbol{r}^{p}_{23}\exp(-j\boldsymbol{D})] \tag{12}$$

$$\boldsymbol{r}^{s}_{123} = (\boldsymbol{r}^{s}_{12} + \boldsymbol{r}^{s}_{23}\exp(-j\boldsymbol{D})/\,[1 + \boldsymbol{r}^{s}_{12}\boldsymbol{r}^{s}_{23}\exp(-j\boldsymbol{D})] \tag{13}$$

where $\boldsymbol{r}^{p}_{12}$ and $\boldsymbol{r}^{s}_{12}$ are the Fresnel's reflection coefficients at the interface between the phase 1 and phase 2 (metal/film interface), and $\boldsymbol{r}^{p}_{23}$ and $\boldsymbol{r}^{p}_{23}$ are those between the phase 2 and phase 2 (film/solution or gas)interface. $\boldsymbol{D}$ is a function of thickness (d) of the film and wavelength of light (λ), indicating the phase retardation by the multi-reflection in the film,

$$\boldsymbol{D} = 4\pi\boldsymbol{n}_2(\cos\phi_2)d/\lambda \tag{14}$$

Experimentally Ψ and Δ are measurable with ellipsometry and theoretically one can evaluate those values from the reflection coefficients described in Eqs. (9)-(13),

$$\boldsymbol{\rho} = \boldsymbol{r}^{p}_{i}/\boldsymbol{r}^{s}_{i} = \tan\Psi_l \exp j\Delta_l \tag{15}$$

where i = 13 indicates a system without the film and i =123 a system with the film.

(*iv*) *Apparatus*

Various types of ellipsometers have been developed. Classically nulling method has been adopted, and recently the photometric ellipsometers have been used.

Figure 5 shows a typical arrangement of ellipsomteter which consists of a light source, polarizer (P), phase compensator (C), reflection surface (S), analyzer (A), and photo-detector. In the nulling method, azimuths of the three optical elements (polarizer, compensator, and analyzer) are adjusted for the light intensity of the photo-detector to be zero or minimum. For example, when one fixes the azimuths of the compensator at $C = (\pi/4)$ or $-(\pi/4)$ and its

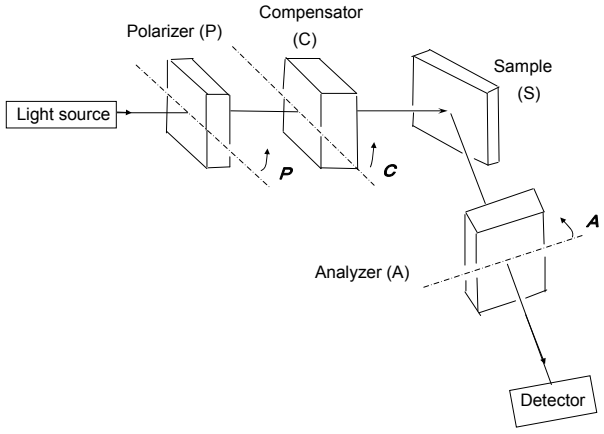

Figure 5. Basic arrangement of optical elements for ellipsometry.

phase shift at $\delta_c = (\pi/2)$, the parameters of Ψ and Δ are determined by the azimuths of polarizer (P) and analyzer (A) at the zero intensity,

$$\Psi = A, \qquad \Delta = 2P + (1/2)\pi \tag{16}$$

or

$$\Psi = -A, \qquad \Delta = -2P + (1/2)\pi \tag{17}$$

where the azimuths are measured in reference to the plane of incidence. Since the polarization state is the same in case that each of P and A is rotated by π radian, eight sets of P and A are possible at the zero intensity.

A typical photometric ellipsometer is a rotating analyzer apparatus. When the analyzer rotates, the light intensity is modulated,

$$I = I_0 [1 + \alpha\cos(2A) + \beta\sin(2A)] \tag{18}$$

For the arrangement of P-C-S-A, Ψ and Δ are calculated from the following equation:

$$\tan\Psi \exp j\Delta = \frac{1+\alpha}{\beta \pm j\left(1-\alpha^2-\beta^2\right)^{1/2}} \frac{\tan C + \rho_c \tan(P-C)}{1-\rho_c \tan C \tan(P-C)} \tag{19}$$

where $\boldsymbol{\rho_c}$ is the complex transmittance of the compensator,

$$\boldsymbol{\rho_c} = \rho_c \exp j\delta_c \tag{20}$$

Usually, for the quarter wave compensator, $\boldsymbol{\rho_c} = \exp j(\pi/2) = j$. For the rotating ellipsometer, during continuous rotation of the analyzer, the Fourier coefficients, a and b, are monitored and converted to the ellipsometric parameters, Ψ and Δ.

(*v*) *3-Parameter Ellipsometry*

For the thin surface oxide film which absorbs light, the estimation of three unknown parameters are required which are a real part (refractive index, n_2) of complex refractive index, $\boldsymbol{N}_2 = n_2 - jk_2$, an imaginary part (extinction coefficient, k_2), and thickness of the film (d). From the usual ellipsometry, one obtains two parameters, Ψ and Δ. The three unknown parameters will thus be not solved mathematically from the two measurable values. For the calculation, simply, one parameter is first assumed, and the other two parameters are solved with a computer program for the reflection equations (Eqs. 9-15).

To overcome this difficulty, several methods are proposed for obtaining the three unknowns without assumptions. First, one has to measure reflectance, R, in addition to Ψ and Δ.[7–11] During the oxide film formation, the reflectance change, ΔR, is measured with the changes of Ψ and Δ. Since I_0 in Eq. (18) corresponds to the reflection intensity from the sample surface, the photometric ellipsometer can easily be modified to the simultaneous measurement of reflectance. For the nulling ellipsometer, however, it is difficult to simultaneously measure the reflectance with Ψ and Δ. From the three parameters of Ψ, Δ, and R, one can calculate the three unknowns, n_2, k_2, and d with help of computer program.

For the other technique for the estimation, multiple-incidence angles method has been applied.[12-14] The Ψ and Δ are measured by several angles of incidence (ϕ_1) and the optimal values of n_2. k_2, and d were calculated by the sets of Ψ_i and Δ_i at each angle, $\phi_{1,i}$.

2. Raman Spectroscopy

Raman scattering originates from an interaction between molecular vibration and electromagnetic light wave.[15] In infra-red spectroscopy, absorption is measured by which the frequency or energy of the incident radiation of light matches that of a molecular vibration so that the molecules is promoted to a vibrational excited state. In Raman spectroscopy, scattering light from the molecules is detected. The incident photon interacts with the molecule and distorts (polarizes) the cloud of electrons around the nuclei to form a short-lived state. This state is not stable and the photon is quickly re-radiated. When the nuclear motion is induced during the scattering process, energy is transferred from the incident photon to the molecule or from the molecule to the scattered photon. The energy of the scattered photon is thus different from that of the incident light. The scattering light is very weak so that incident light with high energy density from laser and highly sensitive detection may be required.

Figure 6 shows the basic process which occurs for the scattering from a molecule. In addition of the Rayleigh scattering which is elastic radiation, two scattering processes occur, one of which is Stokes scattering where the photon with the energy less than the incident photon by the vibration energy of the molecule is scattered,

$$\Delta\nu = \nu_0 - \nu \tag{21}$$

and the other anti-Stokes scattering with energy higher than the incident photon,

$$\Delta\nu' = \nu - \nu_0 \tag{22}$$

where ν is wave-number of Raman scattering light, ν_0 wave number of incident light, and $\Delta\nu$ and $\Delta\nu'$ are Raman shifts. The Stokes

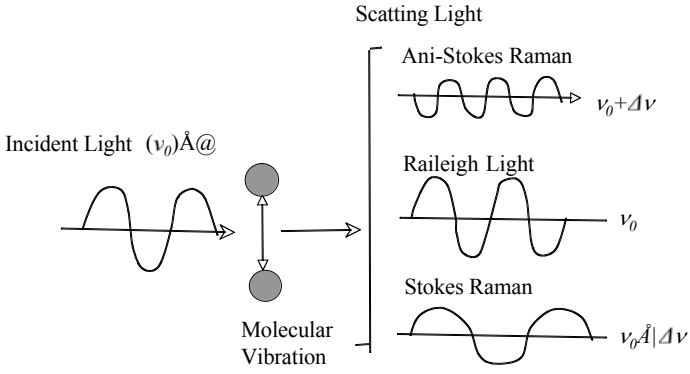

Figure 6. Interaction between electromagnetic wave and molecular vibration. The three scattering lights are radiated from the interaction.

Raman scattering light is usually measured, because intensity of the anti-Stoles Raman scattering is relatively very weak.

For the measurement of Raman scattering, laser as excitation source and spectrometer equipped with high efficient detector are required. In the earlier stage, double- or triple-monochromator was used to effectively reject the Rayleigh scattering light, intensity of which will be much stronger than the Raman scattering. However, filter technology has been improved and at present effective notch and edge filters can reject the Rayleigh scattering so that a combination of notch or edge filter, single monochromator, and multi-channel detector of CCD are adopted for recent measurement.

For the measurement of the passive film on metals under the in-situ condition, the scattering light from the aqueous phase surrounding the surface oxide blocks the measurement of the passive film, because of the much larger scattering from the aqueous phase. To reject the scattering light from the aqueous phase, confocal optical path for the collection of scattering light will be effective. A small pinhole is located at the confocal point to pass the scattering light from the electrode surface and to remove the scattering light from the electrolyte surrounding the electrode. However, since the scattering light from the aqueous phase will be still one hundred times more than that from the passive oxide a few nm thick, the accumulation of the signal on CCD over a thousand seconds may

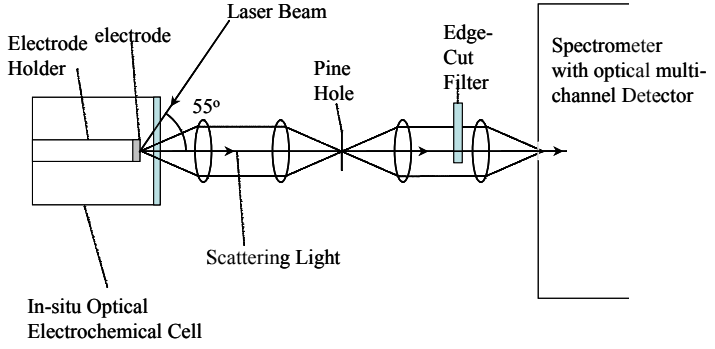

Figure 7. Optical confocal system for collection of scattering light from electrode surface.

be necessary. In Fig. 7, an example for the apparatus with the confocal optical path is shown, in which a pinhole with 50 mm diameter was inserted at the confocal point between the sample electrode and the entrance slit of the spectrometer. The scattering light from the electrolyte around the electrode surface can be considerably omitted.[16]

3. AC Technique

AC impedance technique is also effective to study the passive oxide. The passive oxide may have semiconductive property, so that the AC potential application will induce the charge modulation in the oxide film. [16, 17] For example, when we consider n-type semiconductive oxide film under positive bias, i.e., under reverse bias condition, as shown in Fig. 8, a depression layer is formed in the oxide film. In the depression layer, space charge is extended.

The AC potential applied to the electrode covered by the oxide modulates the width of the space charge which may be estimated by the differential capacitance. Since the width of space charge layer is greatly dependent on the DC potential applied to the oxide-covered electrode, one can characterize the type of the semiconductive oxide from the relation between the space charge capacitance, C_{sc}, and the potential applied. The relation is described

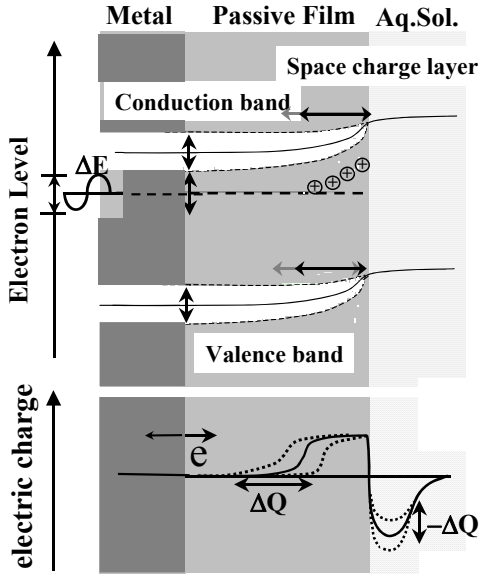

Figure 8. Modulation of space charge by AC potential applied to electrode covered by n-type semiconductive passive oxide under positive bias relative to the flat band potential.

by the following Mott-Schottky approximation for the n-type oxide under the positive bias relative to the flat-band potential, E_{FB},

$$(1/C_{sc})^2 = (2/F\varepsilon\varepsilon_0 N_D)(E - E_{FB} - RT/F) \quad (23)$$

and for the p-type oxide under the negative bias relative to the flat-Band potential,

$$(1/C_{sc})^2 = (2/F\varepsilon\varepsilon_0 N_A)[-(E - E_{FB}) - RT/F] \quad (24)$$

where F is Faraday constant, ε dielectric constant of the oxide, ε_0 vacuum permittivity, N_D donor density and N_A acceptor density.

From the AC impedance, the capacitance was estimated which include the capacitance of the ,electric double layer, ,C_{DL}, ,in addi-

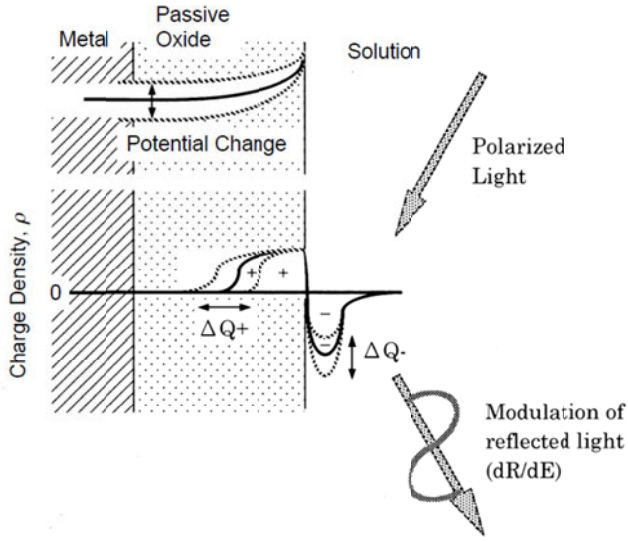

Figure 9. Modulation of reflectance induced by space charge. The space charge is modulated by AC potential applied to electrode covered by n-type semiconductive passive oxide under positive bias relative to the flat band potential.

tion to the capacitance of the space charge. For usual semiconductive electrodes, since the capacitance of the electric double layer is much larger than that of the space charge, it may be neglected, i.e., $(1/C_{DL}) << (1/C_{sc})$. Since the oxide film with a few nm thickness includes a large number of N_D or N_A, C_{sc} may be comparable to C_{DL}, so that some approximations may be necessary for the estimation of C_{sc} from the AC impedance.

The space charge layer can also be detected the potential modulation reflectance by which the modulation of the reflectance from the oxide-covered electrode is induced by AC potential. The model is shown in Figure 9, where the reflectance is assumed to be a function of charge accumulated in the space charge of the oxide film and $R = R(Q_{sc})$.

When the AC potential is applied to the electrode, the space charge layer and the amount of charge are harmonically changed with the potential and thus the reflectance is also changed,

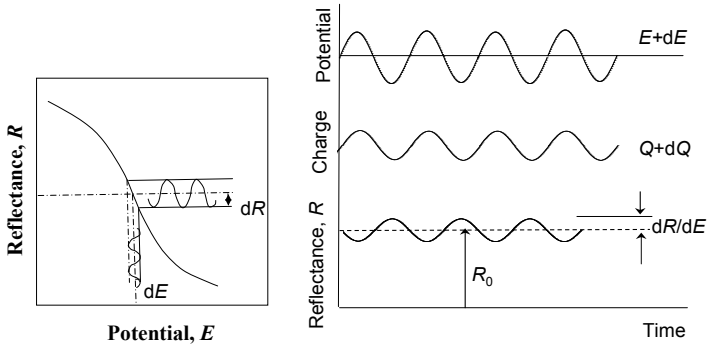

Figure 10. Modulation of reflectance induced by AC potential applied to the electrode covered by passive oxide. The AC potential also induces the modulation of space charge.

$$E = E_0 + \Delta E \exp j\omega t \tag{25}$$

$$R = R_0 + \Delta R \exp (j\omega t + \theta) \tag{26}$$

The model is shown in Fig. 10.

Where E_0 is DC potential superimposed by AC potential with the amplitude ΔE, and R_0 is DC reflectance on which a modulation signal induced by AC potential is superimposed with the magnitude, ΔR and the phase shift, θ. The modulated reflectance is usually normalized by R_0, so that,

$$(dR/dE)(1/R_0) = (1/R_0)(dR/dE) \exp(-j\theta) \tag{27}$$

Figure 11 is an example of the apparatus of the potential modulation reflectance.[19] The modulation of the reflectance, ΔR, induced by AC potential is taken by a two-phase lock-in amplifier or a frequency response analyzer referred to the AC potential and DC reflectance is taken through a low-pass filter.

If the linear combination between dQ_{sc}/dE (= C_{sc}) and dR/dE is assumed, dR/dE is proportional to C_{sc} and thus the formation of the space charge can be discussed from the modulation reflectance.

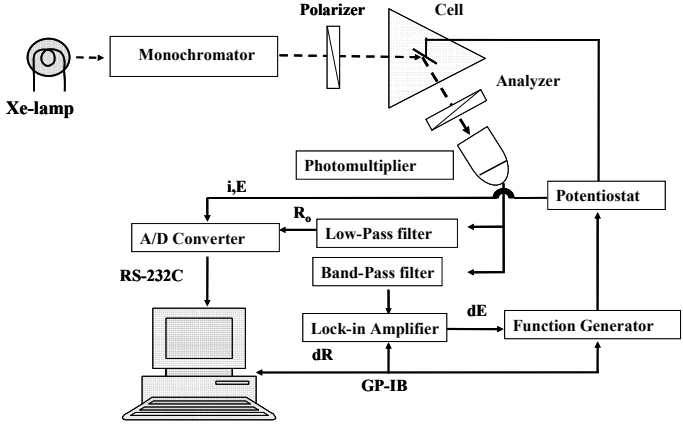

Figure 11. A scheme for the apparatus of potential modulation reflectance.

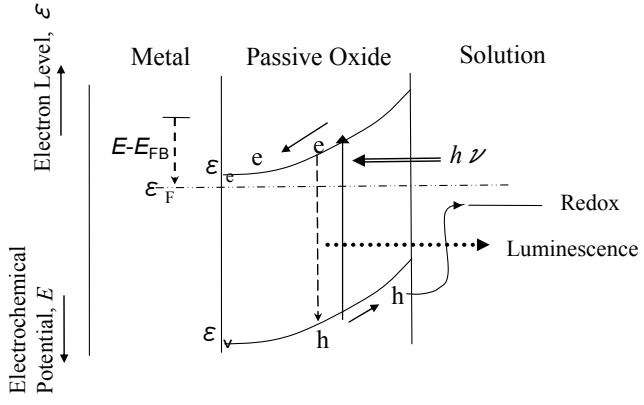

Figure 12. Photo-excitation process of n-type semiconductive passive oxide under positive bias condition. Electrons in the valence band are excited by photon irradiated higher than the band gap energy to leave positive holes in the conduction band. The electron-hole pair thus formed is separated by the potential bias in the depression layer or is recombined with each other to radiate luminescence light.

4. Photo-Excitation

For study of the semiconductive electrode, the photo-excitation with incidence energy higher than the Band gap energy, ε_{BG}, of the semiconductor has been utilized. Figure 12 shows a model in which the light is incident into an electrode covered by an n-type semiconductive oxide and biased by positive potential relative to the flat band potential. The incidence light with the energy $h\nu > \varepsilon_{BG}$, excites electrons from the valence band to the conduction band and therefore makes pairs of free electron in the valence band and positive hole in the conduction band. Due to potential gradient in the space charge, the electron and hole are moved to the separated direction, electron moving to the metal side and the hole to the solution side. The separation of electron and hole is measured by the outer circuit as photo-excited current. The photo-excited current is a function of the potential applied (E) and the incident photon energy ($h\nu$) of light. From the dependence of E and $h\nu$, the semiconductive properties of the oxide film can be discussed.

The pair of electron and hole undergoes another process in which the electrons in the conduction band are recombined with the positive holes in the valence band to radiate the energy. A part of the energy is emitted as a luminescence light. Since the recombination process preferentially occurs under the reverse bias, the potential is applied of the negative or zero bias for the n-type semiconductor and of the positive or zero-bias condition for the p-type. Since spectra of the photo-excited luminescence include the information on the band gap energy and mid gap levels, the energy levels of the oxide film can be discussed.[20]

III. PASSIVE OXIDE FILM ON IRON

1. Thickness of Passive Films on Iron at the Stationary State

The thickness of passive oxide on various metals has been reported. In the first, the results are limited only under the stationary state or nearly stationary state. Figure 13 shows oxide thickness as a function of potential in the pH 8.4 borate solution and the pH 3.1 phosphate solution.[21] The film thickness was obtained after 1-h oxidation at constant potential and assumed to be under nearly

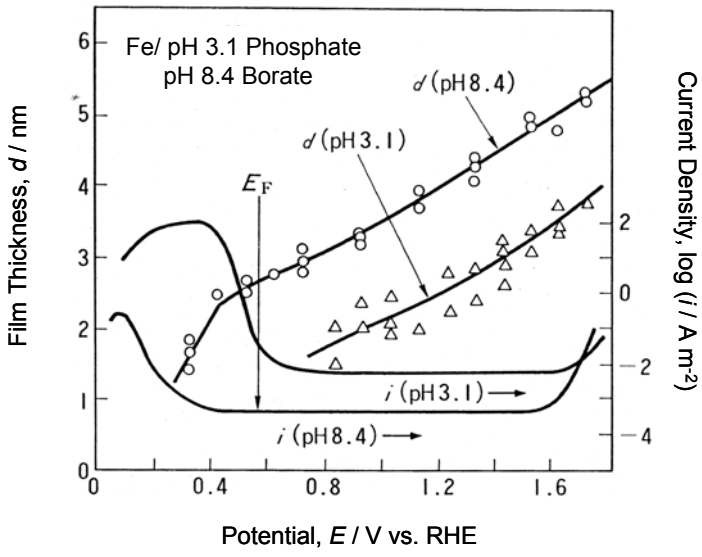

Figure 13. Thickness of the passive oxide and current density (*cd*) as a function of potential in pH 8.4 borate solution and pH 3.1 phosphate solution. The *cd* was taken after 1 h oxidation at each potential. Reprinted from K. Azumi, T. Ohtsuka, and N. Sato, "pH dependence of Thickness of Passive Films on Iron; Measurement by three Parameter Reflectrometry", *Denki Kagaku*, 53 (1985) 700, Copyright ©1985 with permission from The Electrochemical Soc. of Japan.

stationary state. The linear relation between the thickness and potential applied was reported by several authors.[22-26] In Fig. 13 the current density (*cd*) was also plotted, which was taken after 1 h oxidation. It is seen that the passive oxide grows with anodic potentials and the *cd* remains constant in the passive potential region, regardless of the potential value, and, however, it is dependent on the solution pH. The pH dependence of the stationary state *cd* was reported in the pH lower than five to be [28,29]

$$\mathrm{d} \log i / \mathrm{d}\, \mathrm{pH} = -0.84 \qquad (28)$$

Such a linear increase of the thickness was reported in other pH solutions by various authors,[24-26] except for an alkaline solution in which the much thicker film was reported.[29]

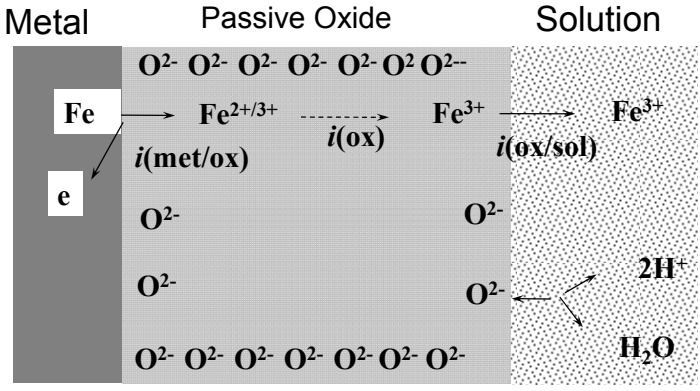

Figure 14. Ionic compound model of the passive oxide. The iron ions formed at the metal/oxide interface migrates in the passive oxide and then dissolves into the electrolyte solution. O^{2-} in the oxide matrix is related to H_2O in the electrolyte with the reaction of $O^{2-}_{(ox)} + 2H^{+}_{(aq)} = H_2O_{(aq)}$.

The linear increase of the film with potential was assumed to follow the mechanism suggested by Vetter[30,31] and Sato[27] with a model of the high-field assisted ionic migration[32,33]. According to the model, the ionic compound is assumed for the passive oxide consisting of Fe^{3+} and O^{2-} (see Fig. 14). Fe^{3+} in the oxide reacts with Fe atoms in the metal substrate and with Fe^{3+} in the electrolyte,

$$Fe^{0}(met) = Fe^{3+}(ox) + 3e(met) \quad (29)$$

$$Fe^{3+}(ox) = Fe^{3+}(sol) \quad (30)$$

O^{2-} in the oxide reacts with H_2O in the electrolyte under deaerated condition,

$$O^{2-}(ox) + 2H^{+}(sol) = H_2O(sol) \quad (31)$$

Since the interfacial reactions are accompanied by charge transfer, their rates depend on the interfacial potential difference. For reaction (31), the rate described in current density, $i_{O(ox/sol)}$, is ex-

pressed as a function of the potential difference at the oxide/solution interface, $\phi_{(ox/sol)}$,

$$i_{O(ox/sol)} = i^0_{O(ox/sol)} \{\exp[\beta nF/RT(\phi_{(ox/sol)} - \phi^0_{(ox/sol)})] - \exp[(1-\beta)nF/RT(\phi^0_{(ox/sol)}) - \phi_{(ox/sol)})]\} \quad (32)$$

where β and n are the transfer coefficient and the valence of transferred ion respectively. Since the amount of O^{2-} is constant under the stationary state, O^{2-} is assumed to be in equilibrium with H_2O in the electrolyte in reaction (31),

$$i_{O(ox/sol)} = 0 \quad (33)$$

Under the stationary state, the interfacial potential difference at the oxide/solution interface is determined by the equilibrium of reaction (31), so $\phi_{(ox/sol)} = \phi^0_{(ox/sol)}$ and thus it will be a function of pH of the solution,

$$\phi_{(ox/sol)} = \phi^0_{(ox/sol)} = \phi^0_{(ox/sol)(pH=0)} - (RT/F)(2.303pH) \quad (34)$$

where $\phi^0_{(ox/sol)(pH=0)}$ is the potential difference at pH = 0. The ionic transfer of Fe ions is determined by the reactions (29) and (30), and the ionic migration rate in the oxide film. For the reaction (29), the rate, $i_{(met/ox)}$, is expressed as a function of the potential drop at the metal/oxide interface, $\phi_{(met/ox)}$,

$$i_{Fe\ (met/ox)} = i^0_{Fe(met/ox)} \{\exp[(\alpha_1 nF/RT)(\phi_{(met/ox)} - \phi^0_{(met/ox)}) - \exp[(1-\alpha_1)nF/RT(\phi^0_{(met/ox)} - \phi_{(met/ox)})]\} \quad (35)$$

where $\phi^0_{(met/ox)}$ indicates the interfacial potential difference in equilibrium. For the reaction (30), the rate is

$$i_{Fe(ox/sol)} = i^0_{Fe(ox/son)} \exp[(\alpha nF/RT)\phi_{(ox/sol)}] \quad (36)$$

where α_1 and α are transfer coefficients for the individual reactions.

Under the stationary state, $\phi_{(ox/sol)} = \phi^0_{(ox/sol)}$, thus the dissolution rate of Fe^{3+} becomes a function of solution pH,

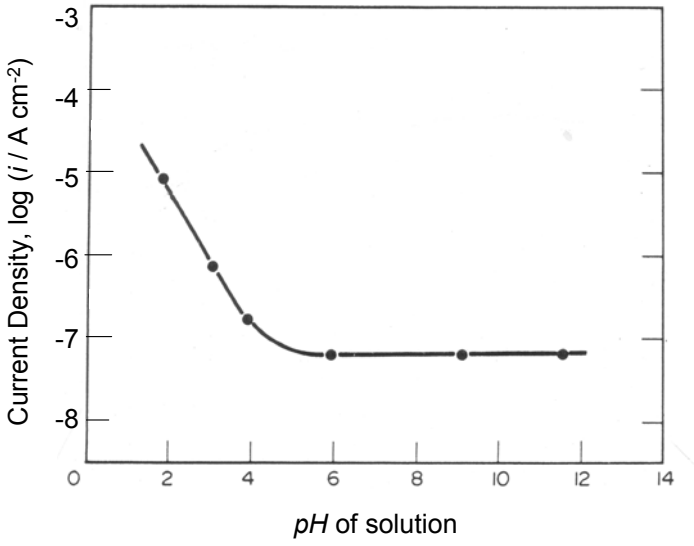

Figure 15. Steady current density in the passive potential region as a function of solution pH. The *cd* reached the stationary value in the solution at pH lower than 5 in 1 h oxidation at each potential, however, it does not reach at pH higher than 5 in which the *cd* was plotted after 1h oxidation. Reprint from N. Sato and T. Noda, "Ion Migration in Anodic Barrier Oxide Films on Iron in Acidic Phosphate Solutions", *Electrochim. Acta*, 22 (1977) 839, Copyright ©1977 with permission from Elsevier Science.

$$i_{\mathrm{Fe(ox/sol)}} = \mathrm{i}^{0}_{\mathrm{Fe(ox/son)}} \exp[(\alpha n\mathrm{F/RT})\phi_{\mathrm{(ox/sol)(pH=0)}} - \alpha n(2.303)\mathrm{pH}] \quad (37)$$

The anodic current measured by the outer circuit (i_a) corresponds to the reaction rate described in current density of reaction (29)

and under the stationary state, the ionic transfer of Fe ion at the interfaces and in the oxide film are kept same as each another,

$$i_a = i_{\mathrm{Fe(met/ox)}} = i_{\mathrm{Fe(ox)}} = \mathrm{i}_{\mathrm{Fe(ox/sol)}} \quad (38)$$

The stationary state *cd* represented by a logarithmic scale, therefore, is a linear function of pH according to Eq. (28) and the pH dependence can be described as follows:

$$\mathrm{d}\log i / \mathrm{d}\,\mathrm{pH} = -\alpha n \tag{39}$$

From the result by Sato and Noda,[27] and Vetter,[34] the stationary *cd* was found to depend on the solution pH as shown in Fig. 15 with d log *i* / d pH = –0.84 in solutions at pH lower than five. From $\alpha n = 0.84$, the transfer ions has been thought to be a complex ions of Fe^{3+} coordinated by OH^- anion or others.[34]

The ionic migration of Fe ions, $i_{Fe(ox),}$ through the oxide film is assumed to follow by the high-field assisted migration mechanism,

$$\ln i_{Fe(ox)} = \ln i^0_{Fe(ox)} + (zaF/RT)(d\phi_{(ox)}/dx) \tag{40}$$

where $i_{Fe(ox)}$ is migration *cd* of Fe(III) ions through the oxide film, $d\phi_{(ox)}/dx$ electric field intensity in the film, $i^0_{Fe(ox)}$ an exchange *cd* at $d\phi_{(ox)}/dx = 0$, *z* the valence of the migration ion, and *a* the half jump distance or activation distance. If one assumes for $d\phi_{(ox)}/dx$ the average electric field, $\Delta\phi/d$, where *d* is the film thickness and $\Delta\phi$ the potential drop in the oxide film, the ionic *cd* can be related to the film thickness,

$$\ln i_{Fe(ox)} = \ln i^0_{Fe(ox)} + (zaF/RT)(\Delta\phi_{(ox)}/d) \tag{41}$$

Since the ionic migration *cd* is equal to the ionic transfer *cd* at the metal/oxide interface and at the oxide/solution interface under the stationary state (Eq. 38), the thickness measured can be combined with the solution pH and the potential difference,

$$d = \Delta\phi_{(ox)}(zaF/RT)\ \{\ln(i^0_{Fe(ox/sol)}/i^0_{Fe(ox)}) - 2.303pH + \alpha F\phi_{(ox/sol)(pH=0)}/RT\}^{-1} \tag{42}$$

Equation (42) indicates that

1) the film thickness increases linearly with the potential drop in the oxide film, $\Delta\phi_{(ox)}$, at constant pH, and

2) the inverse of the thickness, d^{-1}, decreases with the increase of solution pH at constant $\Delta\phi_{(ox)}$. The prediction is in agreement with the results shown in Figures 13 and 15.

In the solution at pH higher than five, the stationary state *cd* does not easily reach in the experimental time period because it is extremely low *cd* and very long time period is required to reach the stationary state. Figure 16 shows an example in borate solution

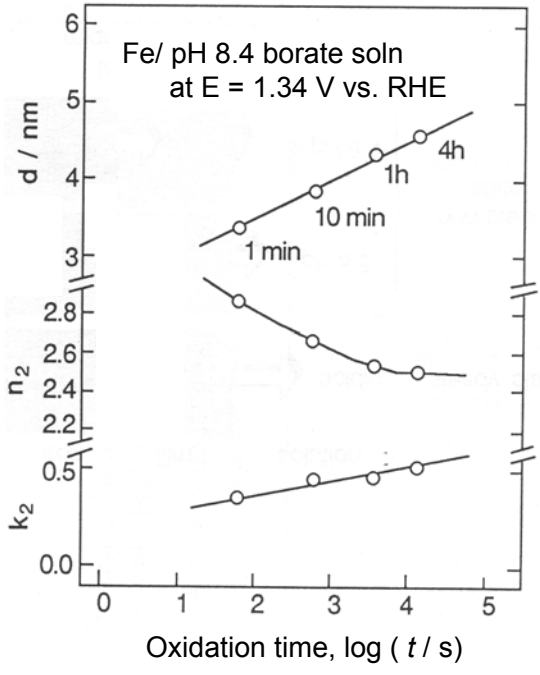

Figure 16. Change of film thickness of passive oxide formed in pH 8.4 borate solution as a function of time. The refractive index (n_2) and extinctio index (k_2) of the film which was simultaneously estimated from the 3-parameter ellipsometry was also plotted. Reprinted from K. Azumi, T. Ohtsuka, and N. Sato, "pH dependence of Thickness of Passive Films on Iron; Measurement by three Parameter Reflectrometry", *Denki Kagaku*, 53 (1985) 700, Copyright ©1985 with permission from The Electrochemical Soc. of Japan.

at pH 8.4, in which the film thickness continues to increase after the constant oxidation for 10^4 s.[35] During the slow increase of the thickness, the *cd* in the order of 10^{-8} A cm^{-2} gradually decreases with time. In the solution at pH higher than five, the stationary state *cd* will be lower than the *cd* plotted in Figure 15 which was taken after 1 h. In the solution, since there is a difference between the solubility of ferric and ferrous ions, the anodic deposition from the ferrous ions in the electrolyte onto the passive oxide occurs, as discussed later.

2. Non-Stationary Growth of the Passive Oxide on Iron

In the non-stationary state, the thickness changes with time. For the film growth, since the amount of O^{2-} and Fe^{3+} in the film increases with time, $i_{0(ox/sol)}$ in Eq. (32) is,

$$i_{O(ox/sol)} > 0 \tag{43}$$

and since the accumulation rate of Fe(III) in the film is given by the difference between $i_{Fe(met/ox)}$ in Eq. (35) and $i_{Fe(ox/son)}$ in Eq. (36),

$$i_{Fe(met/ox)} - i_{Fe(ox/sol)} > 0 \tag{44}$$

and for keeping neutrality,

$$i_{O(ox/sol)} = i_{Fe(met/ox)} - i_{Fe(ox/sol)} \tag{45}$$

Since $i_a = i_{Fe(met/ox)}$,

$$i_a = i_{O(ox/sol)} + i_{Fe(ox/sol)} \tag{46}$$

Vetter and Gorn evaluated the partial currents of $i_{O(ox/sol)}$ and $i_{Fe(ox/sol)}$ during the oxide film growth by constant *cd* in 0.5 M sulfuric acid solution.[37] They estimated the dissolution *cd* of Fe, $i_{Fe(ox/sol)}$, from the quantitative analysis of Fe^{3+} as a function of time and, and calculated the *cd* of oxide ions, $i_{o(ox/sol)}$, as $i_{o(ox/sol)} = i_a - i_{Fe(ox/sol)}$. The result is given in Figure 17, where the $\log(i_{o(ox/sol)})$ is plotted against $\log(i_{Fe(ox/sol)})$. In Figure 17, the interfacial potential difference, $\phi_{(ox/sol)}$, was calculated from Eq. (28) with $\alpha n = 0.84$

and plotted in the upper scale. The similar result was reported by Heusler by using the rotating ring-disc electrode,[36] where the $i_{Fe(ox/sol)}$ was estimated from the ring current instead of the analysis of Fe^{3+} dissolved.

Ohtsuka and Ohta measured the non-stationary oxide growth of the passive oxide on iron during anodic potential sweep in pH 8.4 borate solution.[37] Figure 18 shows the result, in which changes of Ψ, Δ, and R was measured during the potential sweep from 0.0 V vs. Ag/ AgCl/ Sat. KCl to 0.90 V at a sweep rate of 2.0×10^{-3} Vs^{-1} following the potentiostatic oxidation at 0.0 V for 10^3 s. The reflectance was converted to $\Delta R/R_0 = [R(d) - R_0]/R_0$, where $R(d)$ is reflectance of the electrode covered by the passive oxide and R_0 a reflectance of the reduced electrode which is free from the oxide.

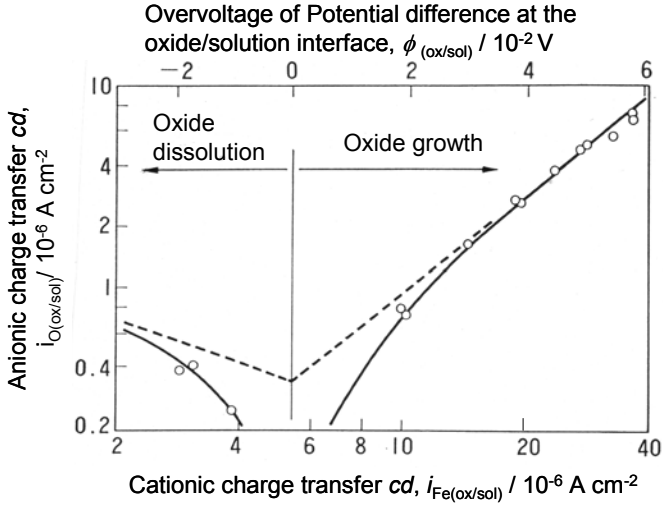

Figure 17. Relation between the two partial cds of cationic and anionic charge transfer. The overvotage of interfacial potential difference was estimated from $i_{Fe(ox/sol)}/i^0_{Fe(ox/sol)}$ in Eq. (36) or $i_{O(ox/sol)}/i^0_{O(ox/sol)}$) in Eq. (32). Reprint from K. J. Vetter and F. Gorn, "Kinetics of Layer Formation and Corrosion Processes of passive Iron in Acid Solutins", *Electrochim. Acta*, 18 (1973) 321, Copyright ©1973 with permission from Elsevier Science.

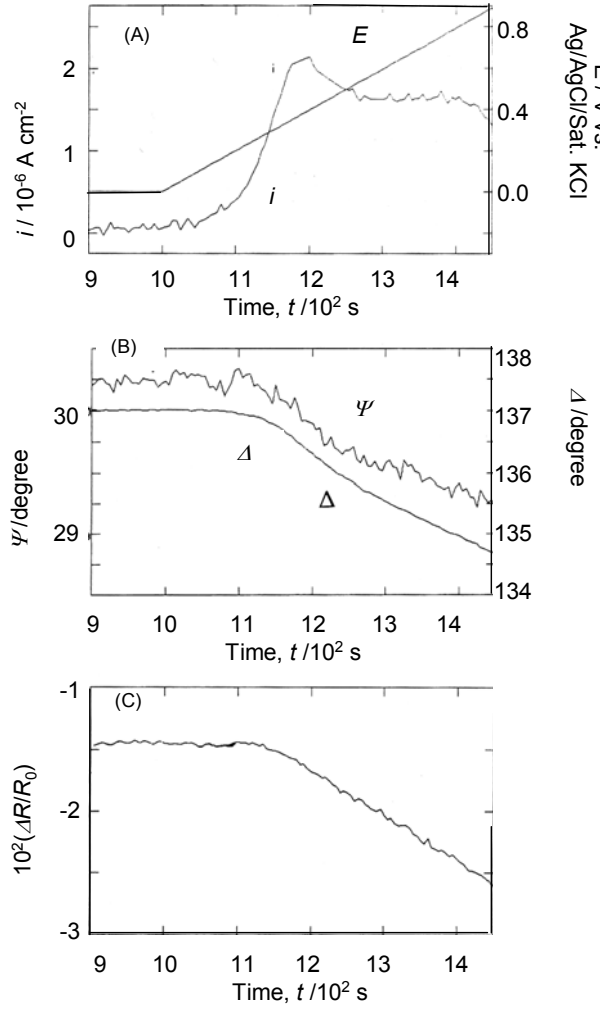

Figure 18. Change of (a) potential E and current density i, (B) ellipsometric parameters, Ψ and Δ, and reflectance, $\Delta R/R_0 = (R(\mathrm{f})\text{-}R_0)/R_0$, during the potential sweep from 0.00 V vs. Ag/AgCl/Sat. KCl to 0.90 V at sweep rate 2×10^{-3} V s^{-1}. The passive oxide was formed at 0.00 V for 10^3 s before the potential sweep. Reprinted from T. Ohstuka and A. Ohta, "Growth of a passive film on iron in a Neutral Borate Solution by Three-parameter Ellipsometry", *Materials Sci. and Eng.* A,198 (1995) 169, Copyright ©1974 with permission from Elsevier Science.

The initial film at 0.0 V before the sweep was 2.4 nm thick. The changes of those parameters during the sweep do not starts immediately after onset of the potential sweep, and the beginning of the changes requires some delay. The change of *cd* exhibits a similar behavior. The changes of the three parameters were converted to the thickness and complex refractive index of the growing oxide film. One example of the growing oxide film is given in Fig. 19, where the film thickness growth was plotted against time as well as *cd* during the potential sweep at a rate 5.0×10^{-3} Vs^{-1}. In Fig. 19, the film growth process during the potential sweep can be divided into two processes, in which at the initial stage no film growth takes place in spite of the potential increase and at the second stage the steady growth of the oxide with the increase of potential.

In Fig. 20, a model of potential distribution during the linear increase of potential is given. In Fig. 20(a), the film electrode is under the stationary sate by potentiostatic control. When the additional potential is applied, it first appears as the increase of the interfacial potential difference denoted by $\phi_{(ox/sol)}$ without any growth of the oxide (Fig. 20b). With the increase of the interfacial potential difference, the potential gradient i.e., electric field, in the oxide gradually increases. The interfacial ionic transfers and the ionic migration in the oxide at the process can increase with the potential increase. From the condition free from the growth of the oxide, the following relations can be derived:

$$i_{Fe(met/ox)} - i_{Fe(ox/sol)} = 0 \tag{47}$$

$$i_{O(ox/sol)} = 0 \tag{48}$$

In Fig. 20(c), after reaching the enough large electric field in the oxide, the ionic migration equal to the interfacial ionic transfer at the metal/ oxide interface is larger than the cationic transfer at the oxide/solution interface,

$$i_{Fe(met/ox)} - i_{Fe(ox/sol)} > 0 \tag{49}$$

and since $i_{Fe(met/ox)} - i_{Fe(ox/son)} = i_{O(ox/sol)}$ from the neutrality condition,

$$i_{O(ox/sol)} > 0 \tag{50}$$

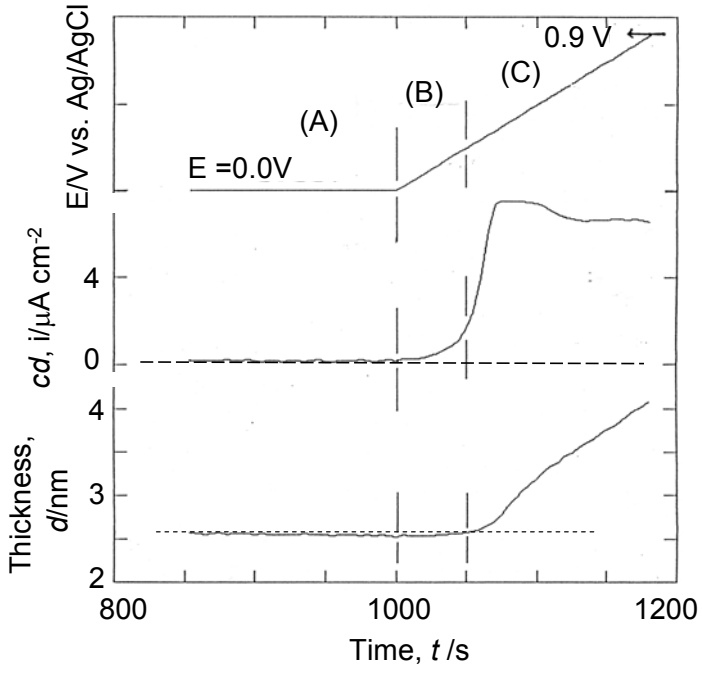

Figure 19. Non-stationary growth of the passive oxide in pH 8.4 borate solution during anodic sweep of potential at rate of 2×10^{-3} Vs^{-1} following the potentiostatic oxidation at 0.0 V vs. Ag/AgCl/Sat. KCl for 10^3 s. Reprinted from T. Ohstuka and A. Ohta, "Growth of a passive film on iron in a Neutral Borate Solution by Three-parameter Ellipsometry", *Materials Sci. and Eng*. A,198 (1995) 169, Copyright ©1974 with permission from Elsevier Science.

Since the interfacial anionic transfer is assumed to be constant from the steady growth,

$$i_{\mathrm{Fe(met/ox)}} - i_{\mathrm{Fe(ox/son)}} = i_{\mathrm{O(ox/sol)}} = \text{constant} \tag{51}$$

the interfacial potential difference ($\phi_{(\mathrm{ox/sol})}$) at the oxide/solution will be constant and the potential drop in the oxide film increases with keeping the electric field constant in the film. Under the situation, the anionic transfer in reaction (31) and the cationic transfer

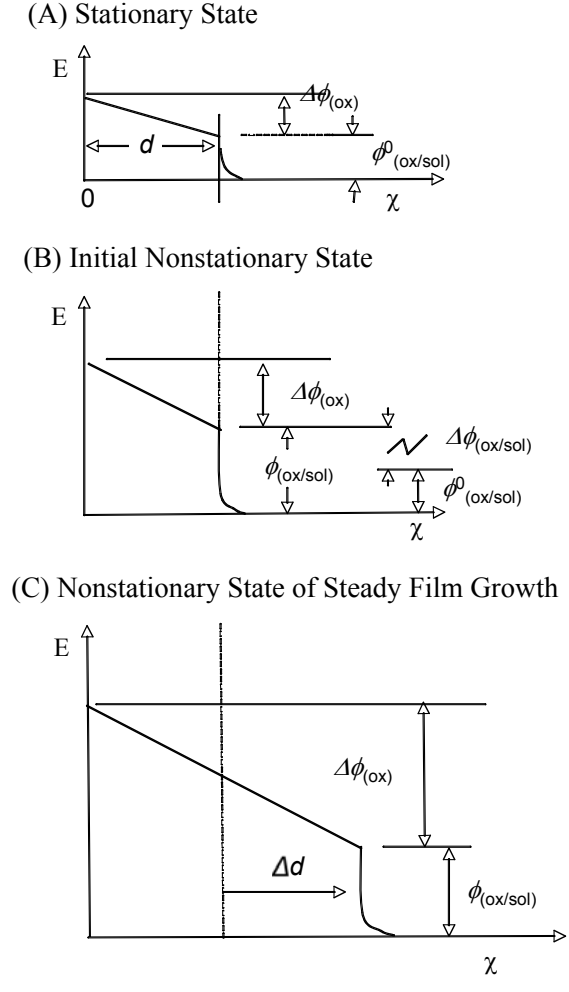

Figure 20. Schematic representation of potential distribution under nonstationary growth of the passive oxide during anodic potential sweep. Reprinted from T. Ohstuka and A. Ohta, "Growth of a passive film on iron in a Neutral Borate Solution by Three-parameter Ellipsometry", *Materials Sci. and Eng. A*,198 (1995) 169, Copyright ©1974 with permission from Elsevier Science.

in reaction (30) at the oxide/solution interface simultaneously proceed. This indicates that the oxide film grows, accompanying the iron dissolution.

3. Outer Hydrous Layer on the Passive Oxide Film

In neutral solution, Fe^{2+} dissolved in the electrolyte can be anodically deposited on the electrode to form a hydrous layer [38-43]. When iron electrode is passivated after the passage of active dissolution, the ferrous ions dissolved in the active potential region are deposited in the passive potential region to form the relatively thick hydrous layer. [38-45]

Ohtsuka et al. measured the oxide film growth during potentiostatic oxidation in neutral borate solution at pH 8.4 containing the Fe^{2+} ions by ellipsometry with 632.8 nm wavelength light and 60.0 deg for incidence angle.[46] Figure 21 shows current decay at a potential of 0.8 V vs. Ag/ AgCl/ Sat. KCl in the borate solution containing Fe^{2+} ions at concentrations of 0.0, 0.25, and 0.50 mM.

Monotonous decay of anodic *cd* is observed in the solution without Fe^{2+} and, however, the higher anodic *cd* is seen after the initial 10 s in the solution containing Fe^{2+}. The larger film growth was observed for the higher *cd*. Figure 22 shows the loci of Ψ vs. Δ during the film growth. The loci move to the directions of the smaller values of Ψ and Δ at the initial period and almost stop in the solution without Fe^{2+}. The loci, however, change in the direction to the higher value of Ψ at the latter stage of the oxidation in the solution containing Fe^{2+}. The change of the direction of the loci indicates that the film growing in the initial stage is different in optical property from that growing in the latter stage. From this loci, the complex refractive index was evaluated to be $\boldsymbol{N}_2 = 2.3 - j(0.38 - 0.50)$ for the inner layer initially growing and $\boldsymbol{N}_2 = 1.8 - j(0.045 - 0.096)$ for the outer layer growing at the latter stage. The smaller refractive index for the outer layer may correspond to an optically lower density and to more hydrated oxide film. From the loci during the oxidation, the thickness of the oxide film was calculated, which is given in Fig. 23. Without Fe^{2+} the film growth mainly occurs at the initial 50 s and the thickness is kept almost constant at 5 nm for the latter period. In the solution containing Fe^{2+}, the thickness increases almost linearly with the

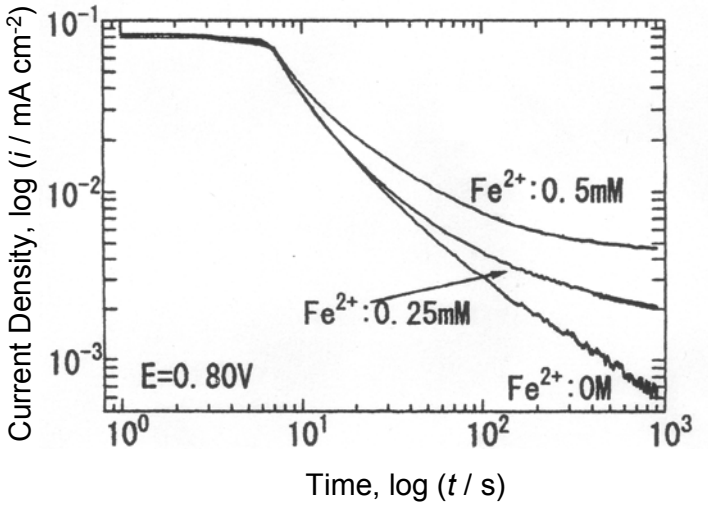

Figure 21. Decay of carrent density during potetiostatic oxidation at 0.80 V vs. Ag/AgCl/Sat. KCl in pH 8.4 borate solution containing Fe^{2+} at 0.0, 0.25, and 0.50 mM. Reprint from T. Ohtsuka and H. Yamada, "Effect of Ferrous Ion in Solution on the Formation of Anodic Oxide Film on Iron", *Corrosion Sci*., 40 (1998) 1131, Copyright ©1998 with permission from Elsevier Science.

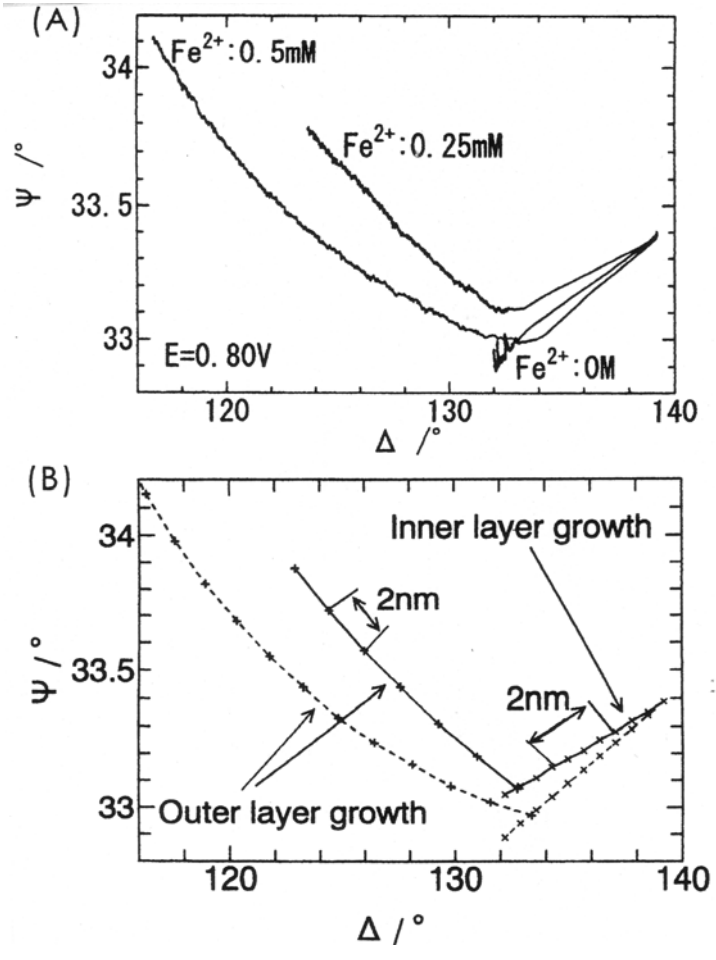

Figure 22. Comparison between Ψ-Δ relations (A) experimentally obtained and (B) theoretically calculated from bi-layerd model for the film at 0.80 V in pH 8.4 borate solution containing 0.0, 0.25, and 0.50 mM Fe^{2+} ions. Reprint from T. Ohtsuka and H. Yamada, "Effect of Ferrous Ion in Solution on the Formation of Anodic Oxide Film on Iron", *Corrosion Sci*., 40 (1998) 1131,

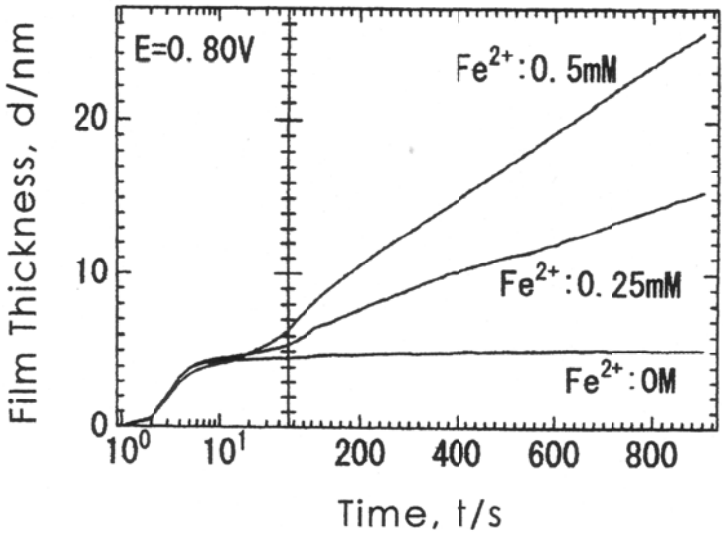

Figure 23. Thickness vs. time during the passive oxide growth for 900 s at 0.80 V vs. Ag/AgCk/ Sat. KCl in pH 8.4 borate solution containing Fe^{2+} ions at concentration of 0.0, 0.25 and 0.50 mM. Reprint from T. Ohtsuka and H. Yamada, "Effect of Ferrous Ion in Solution on the Formation of Anodic Oxide Film on Iron", *Corrosion Sci*., 40 (1998) 1131, Copyright ©1998 with permission from Elsevier Science.

oxidation time. The thickness increase is proportional to the concentration of Fe^{2+} in the solution and independent of the oxidation potential. The growth rate may be limited by diffusion of Fe^{2+} in the electrolyte. The similar ellipsometric measurement for the anodic deposition of ferrous ions was reported by Ord and DeSmet.[47]

This effect of Fe^{2+} concentration indicates that when iron is passivated by an anodic potential sweep from the active potential region, the thick hydrous oxide layer would be formed by the anodic deposition of Fe^{2+} dissolved from the iron in the active potentials. Much thicker oxide films on iron have been reported by various authors in neutral solutions. The origin of the thick films may be Fe^{2+} accumulated in the solutions.

Since the anodic deposition from Fe^{2+} does not take place in acidic solution, the thickness is independent of the concentration of Fe^{2+} ions in solution at pH lower than four.

The composition of the anodic deposition layer was studied by using ex-situ reflection electron diffraction by Cohen et al.[41] They found γ-FeOOH for the deposited film formed on platinum from perchlorate solution containing Fe^{2+}. Ohtsuka et al. estimated the composition from Raman spectroscopy as well as in-situ EQCM and ellipsometry to be amorphous FeOOH-H_2O (i.e., $Fe(OH)_3$).[43]

4. Spectroscopic Property of the Passive Oxide

The multi-wavelength ellipsometry (i.e., spectroscopic ellipsometry) can characterize spectroscopic property of the passive oxide. Figure 24 indicates spectra of the complex refractive index, $N_2 = n_2 - jk_2$, of the passive oxide formed on iron at 1.43 V vs. reversible hydrogen electrode at the same solution (RHE) in pH 8.4 borate solution and in pH 3.1 phosphate solution for 1 h.[49-51] In Fig. 24, the thickness of the passive oxide was estimated at each wavelength of incident light. The measurement and estimation were made by the 3-parameter method. Similar results were also reported by Cahan et al.[24, 52]

The extinction coefficient, k_2, in Fig. 24 is seen to increase with decrease of wavelength. The k_2 value can be converted to the light absorption coefficient, α, of the passive oxide by the following equation,

$$\alpha = 2\pi k_2/\lambda \tag{52}$$

The light absorption at the neighbor of the absorption edge (i.e., the Band gap energy) is approximately described as the following equation,

$$\alpha = (A/h\nu)(h\nu - \varepsilon_{AE})^n \tag{53}$$

where $h\nu$ is photon energy of incident light and ε_{AE} absorption edge energy. When one assumes that the incidence photon energy is close to the absorption edge, Eq. (53) can be approximated as follows:

$$\alpha = A'(h\nu - \varepsilon_{AE})^n \tag{54}$$

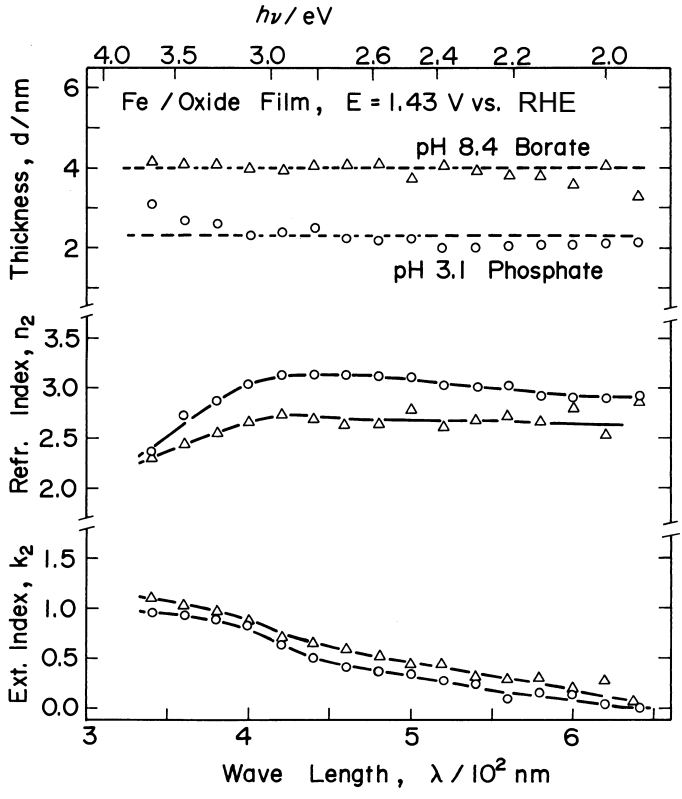

Figure 24. Spectra of complex refractive index, $N_2 = n_2 - jk_2$ for the passive oxide formed at 1.43 V vs. RHE in pH 8.4 borate and pH 3.1 phosphate solution for 1 h. The N_2 was calculated from multi-wavelength ellipsometry with the film thickness. Reprint from T. Ohtsuka, K. Azumi, and N. Sato", A spectroscopic Property of the Passive Film on Iron by 3-parameter Reflectometry", *Denki Kagaku*, 51 (1983) 155, Copyright ©1983 with permission from The Electrochemical Soc. of Japan.

where n = (1/2) for the direct transition of excitation process of electrons from the valence to the conduction band and n = 2 for the indirect transition. When one assumes the direct transition for electron excitation process, one can plotted α^2 vs. $h\nu$. The intercept of the plot may correspond to the absorption edge energy and thus to the band-gap energy, ε_g, of the passive oxide. The plot is shown in Fig. 25 for the passive oxide formed in pH 8.4 borate solution at 0.50 V, 1.00 V, and 1.60 V vs. RHE.

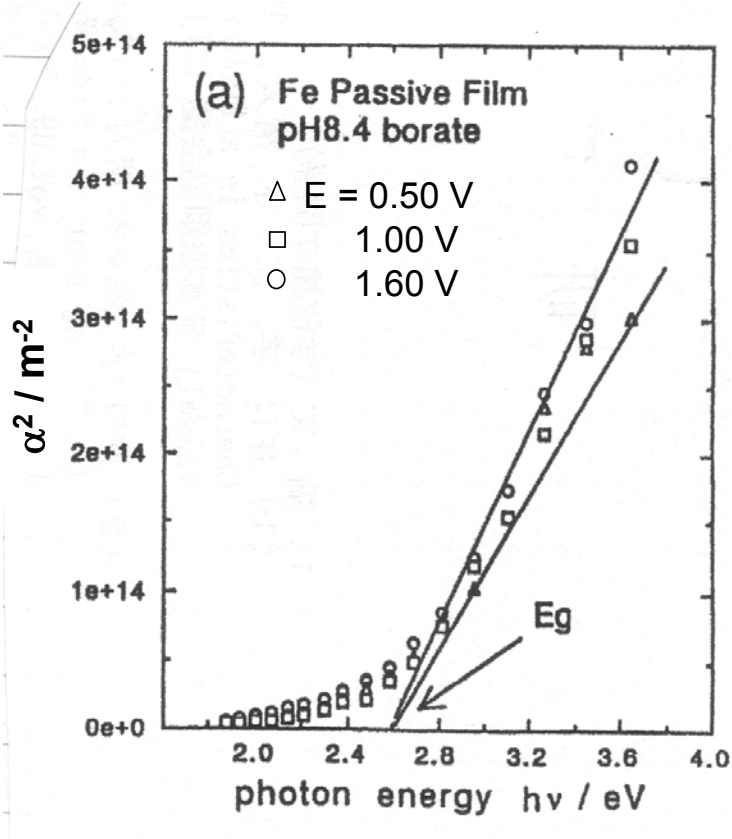

Figure 25. α^2 vs. photon energy, $h\nu$, for the passive oxide formed at 0.50, 1.00, and 1.60 V for 1 h in pH 8.4 borate solution.

From the intercept the ε_g is estimated to be 2.6 eV. Searson et al. replotted the absorption coefficient estimated from the data in Fig. 24 in $(\alpha h\nu)^{0.5} = A^{0.5} (h\nu - \varepsilon_{AE})$ to evaluate the band gap energy of 1.75 eV for the indirect transition.[52] Such band gap energy has been evaluated from the photo-excited *cd* measured as a function of photon energy under an assumption that the *cd* was proportional to the absorption coefficient.[55] The absorption edge was estimated from the photo-excited *cd* to be a range from 2 to 3 eV.[54-56] The photo-excited current will be discussed in the following section.

5. Composition from Raman Spectroscopy

Raman spectroscopy is a promising technique for in-situ detection of the electrode surface. However, large scattering of light from aqueous electrolyte surrounding the electrode interferes the detection of electrode surface. To detect the thin passive film, the surface enhanced Raman scattering (SERS) was applied in which the fine silver particles was cathodically deposited on the iron surface before the anodic passivation, or the thin iron film present on the roughening silver surface.[58-64] The enhancement of Raman scattering from the electrode surface may overcome the scattering from the electrolyte. When one applies to the electrode the potential high enough for passivation of iron, the silver particles or silver substrate are, however, oxidized and the electrode loses the property of the Raman enhancement. The potential range for the SERS detection, therefore, is restricted to the low potential region from the active to the initial passive potential region. Further, the deposition of the silver particles on the surface may possibly introduce an unexpected influence on the passive oxide film. The detection of the passive oxide by normal Raman scattering is probably desired.

Recently, Ohtsuka and Taneda applied Raman spectroscopy without any enhancement to the detection of the passive oxide on iron.[16] The measurement was done with a confocal collection system to reduce light scattering from the electrolyte surrounding the passivated iron electrode.[16] The relatively large background scattering light from the electrolyte was observed, even though the confocal system was used. Figure 26 shows the result, in which Raman spectra of the passive oxides formed on iron in pH 8.4 bo-

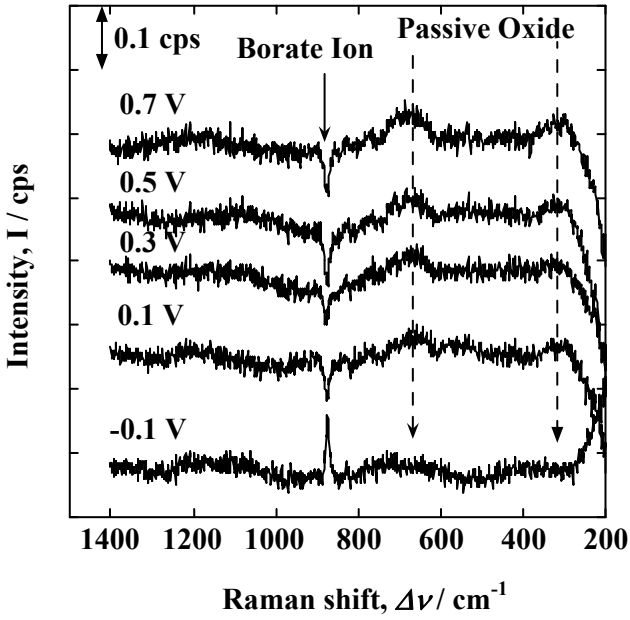

Figure 26. Raman spectra of the passive oxide on iron formed at –0.1 V to 0.7 V vs. Ag/AgCl/sat. KCl in pH 8.4 borate solution. The spectra were obtained from subtraction of a spectrum of bare ion surface reduced from those of the iron covered by passive oxides.

rate solution at various potentials for 1 h was plotted.[16] The spectra were determined by a difference between a spectrum measured for the electrode with cathodically reduced bare surface and a spectrum for the passivated electrode. The original Raman spectra include a large background in the higher intensity 100 times than the spectra from the oxide film. The subtracted spectra reveal Raman peaks about 670 cm^{-1} and 320 cm^{-1}. Figure 27 shows an ex-situ Raman spectra of the passive oxide measured in air after removal from electrolyte.[16]

The Raman peak is more clearly seen than the in-situ spectra and the peak wavelengths are same to those of the in-situ spectra. The Raman spectra of the passive oxide were compared with the

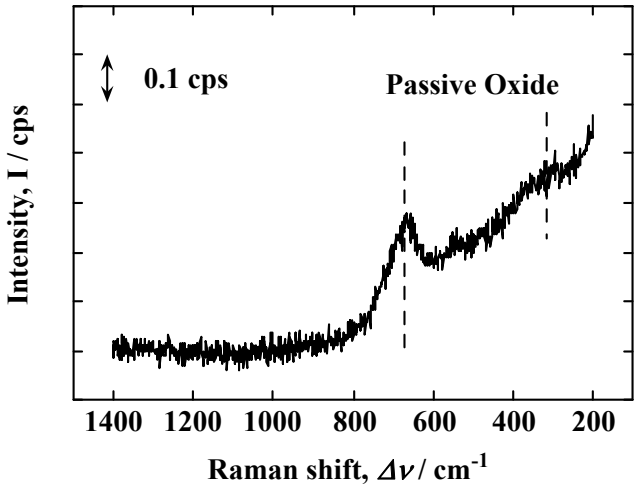

Figure 27. Ex-situ Raman soectrum of the passive oxide on iron formed at 0.70 V vs. Ag/AgCl/sat. KCl in pH 8.4 borate solution. The Raman spectrum was measured immediately after removal from the electrolyte.

reference spectra of various iron oxides and oxyhydroxides, which are given in Fig. 28.[64]

Although the spectra measured are broad and do not exhibit clear peaks, the passive oxide may be basically considered an amorphous-like Fe(III) oxide and oxyhydroxide. In the Raman spectra of iron oxides and oxyhydroxides, Fe_3O_4, γ-Fe_2O_3, and δ-FeOOH possess the strongest peak at a Raman shift of about 600-700 cm^{-1} on the individual Raman spectra; for example, the strongest peak of Fe_3O_4 is 670 cm^{-1}, γ-Fe_2O_3 is 680 cm^{-1}, and δ-FeOOH is 700 cm^{-1}.[62,64-66] From the second peak at 300-400 cm^{-1} observed under the ex-situ condition as well as the in-situ condition, one can select the compounds of Fe_3O_4 and γ-Fe_2O_3 as candidates for the passive oxide. The assignment is in agreement with the presumption derived by many authors.[66-76] They assumed that the passive oxide film was composed of Fe_3O_4 in the neighbor at the oxide/metal interface and γ-Fe_2O_3 at the oxide/solution interface.[67,68]

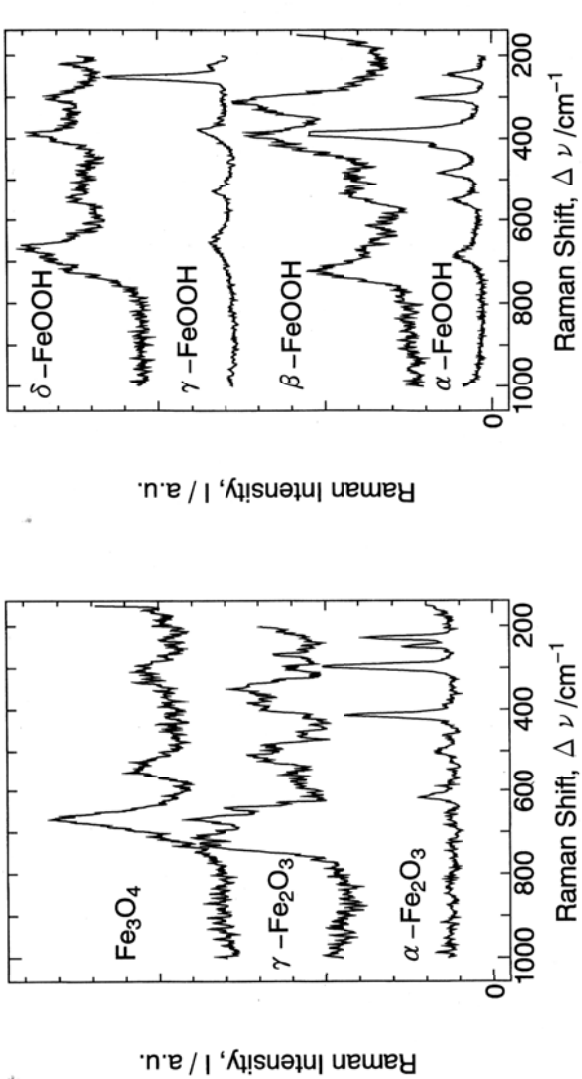

Figure 28. Raman spectra of Fe oxides and oxyhyroxides. Reprint from T. Ohtsuka, "Raman Spectra of Passive Films of Iron in Neutral Borate Solution", *Materials Transaction Japan Inst. Metals*, 37 (1996) 67, Copyright ©1996 with permission from Japan Institute of Metals.

For the composition of the passive oxide on iron, many authors have applied in-situ techniques such as Mössbauer spectroscopy, X-ray diffraction, X-ray spectroscopy, and probe techniques of STM and AFM as well as ex-situ techniques such as XPS, SIMS, AES, electron diffraction, etc. The electron diffraction in vacuum indicated that the passive oxide revealed a cubic structure of O^{2-} lattice which may be assigned to be γ-Fe_2O_3 and Fe_3O_4[41,69-72]. From the Mössbauer spectroscopy, O'Grady[72] and Berett et al.[73] estimated a hydrated Fe(III) oxy-hydroxide with a polymeric structure containing OH bridges and the passive oxide changed to γ-Fe_2O_3 after it was removed from electrolyte and dried. Kruger et al.[74] and Dabenport et al.[75] applied X ray absorption to the passive oxide on iron to conclude the presence of hydrated Fe(III) oxide which may have amorphous structure. The work of X-ray diffraction by Toney et al. indicated the diffraction was in coincident with a modified γ-Fe_2O_3 under the in-situ condition as well as the ex-situ.[76] XPS measurement also showed a presence of Fe(III) compound.[77]

In the SERS studies, a large peak at about 550–600 cm^{-1} was reported and assumed to be a Raman peak of the passive oxide.[58-63] The peak was observed in the relatively low potential corresponding to the active to the transient region and continued to the passive potential region. For the SERS measurement, the potential is restricted in the initial of passivation, because silver causing the enhancement of Raman scattering is oxidized to silver oxide in the passive potential region of iron electrode and thus loses the enhancement effect. Among iron oxides, oxyhydroxides, and hydroxides, only $Fe(OH)_2$ exhibits a main Raman peak at about 500-600 cm^{-1}.[62] However, many authors in the previous paper did not estimate presence of $Fe(OH)_2$ in the passive potential region, because the Fe(II) compounds did not stably form from the viewpoint of thermodynamic. In the SERS studies, the Raman scattering of Fe^{2+} ions, $Fe(OH)_2$ or its oxidized hydrated compound, may be enhanced by the effects of the silver particles or silver substrates in the active and initially passive potential regions. In the earlier section, we described that Fe^{2+} ions in electrolyte solution are deposited on the passive oxide film as an outer hydrated layer, resulting in growth of the oxide film much thicker than the original passive oxide.[43,46,47] When one polarizes the iron electrode at the active potential region in neutral pH solution, Fe^{2+} is dissolved into

the electrolyte solution. Then, when one changes the potential in the passive region, in addition to the thin passive oxide film, the thick outer hydrated layer can be formed by the anodic deposition from Fe^{2+} that was dissolved into the electrolyte solution at the previous active potential. It is conceivable that the Raman peak at 550–600 cm^{-1} observed by the SERS studies does not correspond to that of the passive oxide film, but to a hydrate layer deposited from Fe^{2+} in the electrolyte solution.

6. AC Response for Characterization as n-Type Semiconductor

Dielectric and semiconductive properties of the passive oxide was estimated by capacitance measurement from the AC impedance. When the film capacitance is measured during step-wise increase of potential, the inverse of capacitance increases with increase of potential. The result is given in Fig. 29.[78] In Fig. 29, (1/*C*) is plotted with the film thickness against potential for the passive oxide formed in pH 6.4 borate solution. Such a linear increase of (1/*C*) was also reported by Ord and Bartlett,[79] and Moshtev.[80] With the linear increase of (1/*C*), the thickness of the passive oxide is increased with potential, as shown in Fig. 29. However, at the potential at which (1/*C*) is extrapolated to zero, the film has a definite thickness. It is conceivable that the whole oxide film does not work as a dielectric layer, but some part of the oxide film has a conductive property. If the (1/*C*) represents the thickness of the dielectric layer, the passive film can be assumed to consist of the inner conductive layer with a constant thickness and the outer dielectric layer, which linearly grows with potential. For the inner conductive layer, for example, a Fe_3O_4 or incomplete γ-Fe_2O_3 (i.e., γ-$Fe_{2-x}O_3$, x = 0-1/3) may be possibly assigned to the layer. From the linear relation between (1/*C*) and the thickness, the dielectric constant was estimated to be 40.[78] At potentials near the region of oxygen evolution, the value of (1/*C*) starts to decrease. This decrease of (1/*C*) or increase of the capacitance may be caused by the oxidation reaction from H_2O to O_2 at the oxide/ solution interface. In the passive region, the positive charge accumulates in the space charge layer in the n-type semiconductive passive oxide, and, however, due to adsorption intermediate on the oxide surface in the oxidation reaction of H_2O, the site of the

charge accumulation changes to the oxide/ solution interface in the potentials in which oxygen evolution can take place. The charge density at the interface is much higher than the space charge in the passive oxide, the capacitance at the potentials of oxygen evolution may reveal much larger value.

In the case that the capacitance was measured with potential decrease after formation of the passive oxide at a relatively high potential, the capacitance can represent the dielectric layer thinning with potential decrease in the oxide film whose thickness remains constant. For the n-type semiconductor oxide, the dielec-

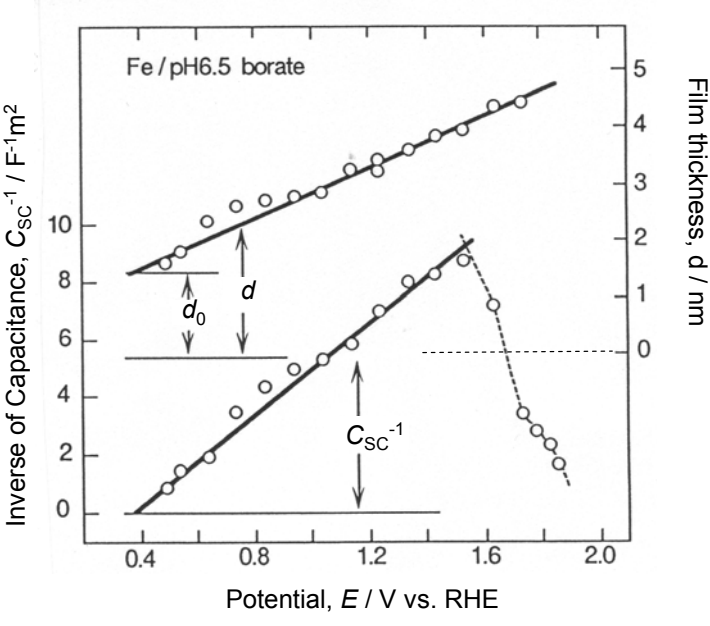

Figure 29. Inverse of Capacitance, 1/C, of iron electrode covered by the passive oxides. The passive oxide was formed during step-wise increase of potential form 0.5 V to 1.9 V vs. RHE and the capacitance was measured at each potential after keeping for 1 h at individual potentials. The thickness is also plotted for comparison. Reprint from K. Azumi, T. Ohtsuka, N. Sato, "Impedance of Iron Electrode Passivated in Borate and Phosphate Solutions", *Transaction Japan Inst. Metals*, 27 (1986) 382. Copyright ©1986 with permission from Japan Institute of Metals.

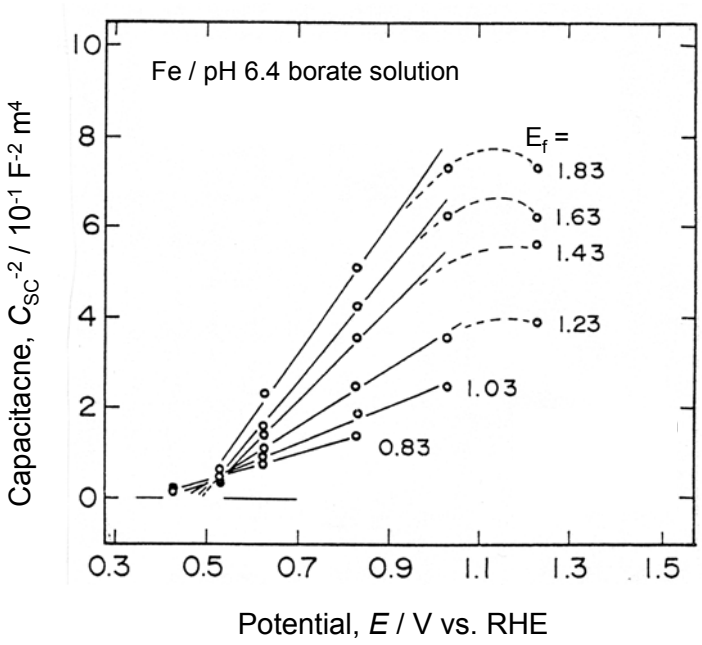

Figure 30. C_{sc}^{-2} vs. potential plot for the iron covered by the passive oxide in pH 6.4 borate solution. The capacitance was measured by step-wise decrease of potential form the formation potentials, E_f, at which the passive oxide was formed by poentiostatic oxidation for 1 h. Reprint from K. Azumi, T. Ohtsuka, and N. Sato, "Mott-Schottky Plot of the Passive Film Formed on Iron in Neutral Borate and Phosphate Solutions", *J. Electrochem. Soc.*, 134 (1987) 1352, Copyright ©1987 with permission from The Electrochemical Soc.

tric layer corresponds to a space charge layer, at which the potential drop in the passive film appears. For the thickness of the space charge layer thinning with potentials, the Mott-Schottky approximation is formulated on the relation between the capacitance and potential,

$$(1/C_{sc})^2 = (2/F\varepsilon\varepsilon_0 N_D)(E - E_{FB} - RT/F) \quad (54)$$

The plot of C^{-2} vs. E for the passive oxide is shown in Fig. 30, in which the oxide film was first formed in pH 6.5 borate solution at

potentials from 0.83 V to 2.03 V vs. RHE and then the AC impedance was measured during the step-wise potential decrease.[82] The capacitance was calculated from a relation between log (Z) and log (f) in the frequency range from 10 mHz to 10 kHz, where Z is impedance of the passivated iron and f frequency. From the intersept and the slope in Fig. 30, a flat band potential and the product of $\varepsilon\varepsilon_0 N_D$ are respectively determined. The flat band potential is estimated from Fig. 27 to be 0.50 V vs. RHE in pH 8.4 solution. The donor density, N_D, is a range of $1 - 10\text{x}10^{26}$ m^{-3}. The same order of the density was reported by other authors.[55,56,81] The N_D value means that one donor site is present in every 1-10 nm^3 volume. The semiconductor with such large concentration of N_D may not be classified into the crystalline semiconductors, but into the amorphous semiconductors. The average distance between the neighboring donors is about 1-2 nm. Since the electrons trapped on the donor site can tunnel over the distance, the electrons can migrate through the donor sites. In this case, for the electron conduction, the migration gap between the donor level and the acceptor level or the valence band edge may have a more important meaning than the band gap between the conduction and valence bands. The electrochemistry of the amorphous semiconductors is not enough established and thus introduction of new theories will be expected.

The potential modulation reflectance can give the same evaluation of the capacitance. One can consider that the modulation in reflectance of the oxide-covered electrodes induced by AC potential will be caused by change of concentration of various type of charge; change of electron concentration in the metal substrate, change of ionic charge in the electric double layer, change of charge in dielectric films, and change of space charge in semiconductive oxides. When one considered the oxide film with a space charge corresponding to the passive oxide of iron under the positive bias, the modulation of the space charge is thought to cause the reflectance change. When one converts the AC impedance, $Z = \mathrm{d}E/\mathrm{d}i$, and the charge modulation, $\mathrm{d}Q/\mathrm{d}E$, becomes:

$$\mathrm{d}Q/\mathrm{d}E = (1/\mathrm{j}\omega)(\mathrm{d}i/\mathrm{d}E) = (1/\mathrm{j}\omega)(1/Z) \tag{55}$$

We can define complex capacitance, Θ, for $(\mathrm{d}Q/\mathrm{d}E)$. When the reflectance is harmonically modulated with the charge in the electrode system, the modulation reflectance, $\mathrm{d}R/\mathrm{d}E$, may reveal the

same complex response. Figure 31 shows a complex response of $(dR/dE)(1/R_0)$ as well as Θ, in which the amplitude in logarithmic scale and phase is plotted against log (f).[83] Although the signal of dR/dE is so small that the phase is not correctly detected in the high frequencies, the complex response is almost same between $(dR/dE)(1/R_0)$ and Θ. The reflectance modulation is thus assumed to be thus responsible to the space charge in the passive oxide similarly as the capacitance.

The potential modulation reflectance is thought to be followed by the Mott-Schttoky type plot as well as the capacitance. Such type of the plot is shown in Fig. 32 with the original plot for the capacitance for the passive oxide formed at 1.55 V vs. RHE in pH 9.6 borate solution.[53] The intercepts on the abscissa, which is corresponding to (E_F – RT/F), are in coincident with each other. From the intercept the flat band potential can be estimated to be E_F = 0.35 V vs. RHE.

7. Photo-Excitation Current

In the Mott-Schottky plot of the capacitance, the passive oxide is classified to n-type semiconductor. When the passive oxide is situated under the electron depression state in the passive potential region, the space charge layer is formed in the passive oxide. Under the condition, irradiation of photon whose energy is higher than the band gap energy excites electrons in the valence band to free electrons in the conduction band to leave positive holes in the valence band. The electrons in the conduction band are driven to the metal/oxide interface according to the potential gradient formed in the depression layer. Since the potential gradient moves the positive holes in the valence band to another direction. The excited electron-hole pairs are effectively separated in the depression layer. If the holes moving to the oxide surface can transfer to redox pairs in the electrolyte, the steady current flow can be observed by an outer circuit. If the transfer of the holes at the interface does not occur, the separated electrons and holes may cause a change of charge distribution and potential profile in the depression layer.

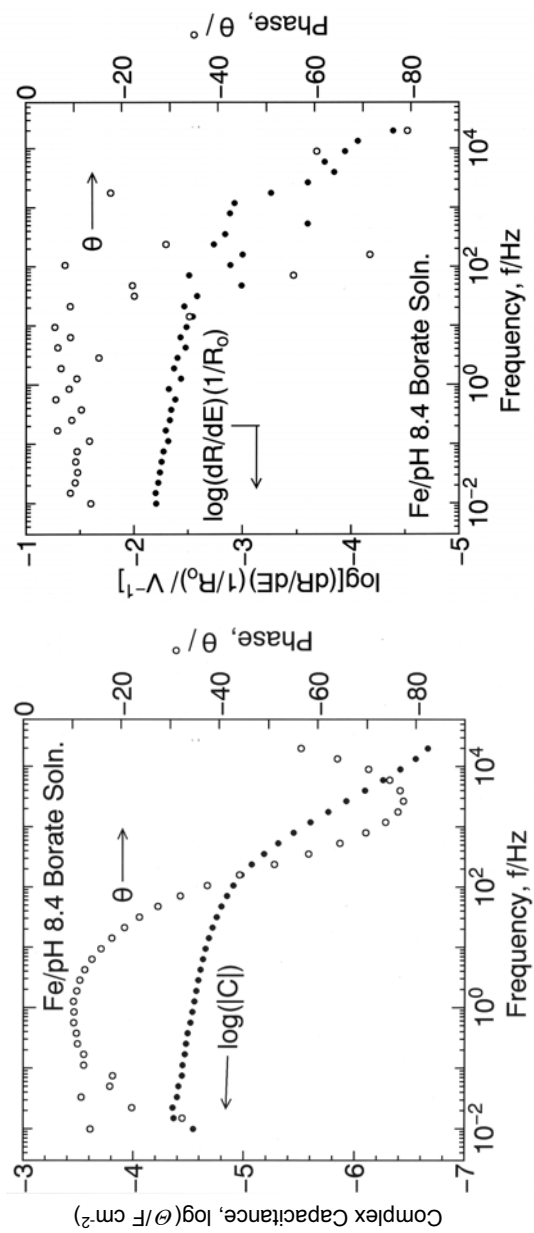

Figure 31. Complex capacitance, Θ, and potential modulation reflectance, $(dR/dE)(1/R_0)$, against frequency, f, for the iron electrode covered by the passive oxide formed at 0.86 V vs. Ag/AgCl/Sat. KCl in pH 8.4 borate solution. Reprint from T. Ohtsuka, "Potential Modulation Reflectance", *Denki Kagaku*, 65 (1997) 735, Copyright ©1987 with permission from The Electrochemical Soc. of Japan.

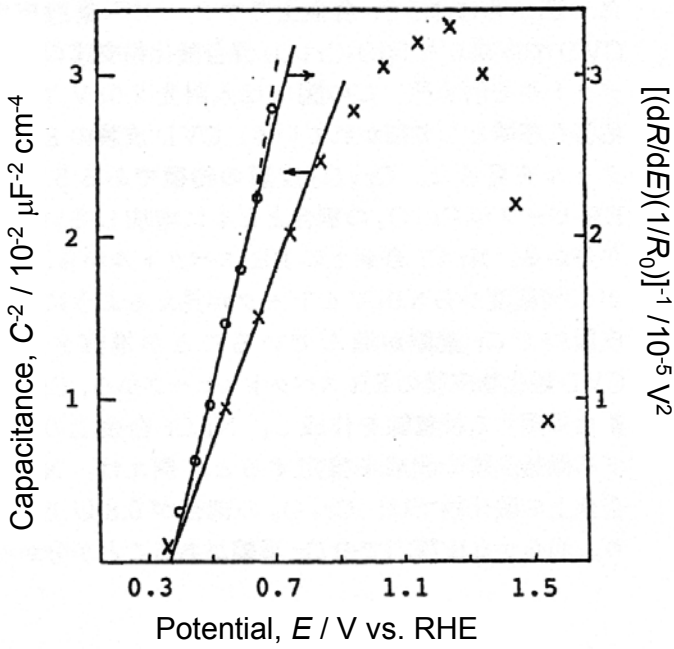

Figure 32. The Mott-Schottky type plot of capacitance (C^{-2} vs. E) and potential modulation reflectance (PMR), $[(dR/dE)(1/R_0)]$ vs. E for the iron electrode covered by passive oxide formed at 1.55 V vs. RHE. The PMR measurement was done at frequency of 500 Hz by light wavelength for 350 nm. Reprint from D. J. Wheeler, B. D. Cahan, C. T. Chen, and E. Yeager, "Optical Study of the Passivation of Iron", in *Passivity of Metals*, Ed. by R. P. Frankenthal and J. Kruger, The Electrochem. Soc. Inc., Pronceton, 1978, p. 546, Copyright ©1978 with permission from The Electrochemical Soc.

The transient change of photo-excitation current is shown in Fig. 33, where light from Xe lamp is irradiated for 17 ms onto the iron electrode passivated at various potentials for 1h in pH 6.5 borate solution.[84,85] The current initially reveals a sharp peak and then decays with time. The steady photo-current which is evaluated from the end current of the 17 ms irradiation is almost zero at the potentials lower than 1.1 V vs. RHE and the appreciable current is observable at the higher potentials. The steady photo-current is assumed to be the transfer of the holes from the va-

lence band edge on the oxide surface to the redox of H_2O/O_2 in the electrolyte to form oxygen molecule due to water oxidation. Since the oxygen evolution is appreciable at potential higher than 1.6 V vs. RHE in the dark condition, the photon irradiation assists the water oxidation, decreasing the potential for water oxidation by 0.5 V.

The similar photo-excited current was measured for the film first oxidized at 2.03 V to form a passive oxide 5 nm thick. The photo-current of the oxide film was measured as a function of decreasing potentials (Fig. 34).[84] Due to the thicker oxide film, the photo current is larger than that shown in Fig. 33. The steady pho-

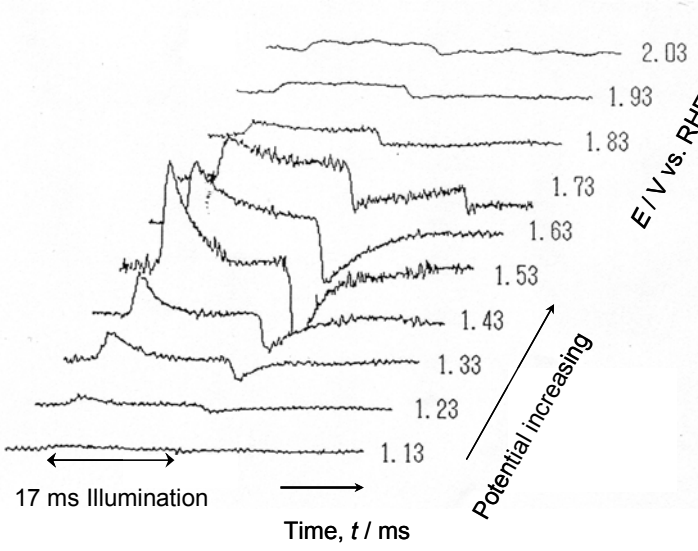

Figure 33. Response of photo-excited current to 17 ms illumination for the iron electrode covered by the passive oxide in pH 6.5 borate solution. The passive oxide was formed by step-wise increase of potential and the photo-current was measured after 1.8ks oxidation at the respective potentials. Reprint from K. Azumi, T. Ohtsuka and N. Sato, "Analysis of Transient Photocurrent in Passivated Iron Electrode in Neutral Borate Solution", *Nippon Kinzoku Gakai-shi* (*Bulletin of JIM*), 53 (1989) 479, Copyright ©1973 with permission from Japan Inst. Metals.

to-current is almost zero at the potentials lower than 0.6 V and is observable in the higher potentials. The similar decay of photo-curent was reported by Riefer and Plieth,[86] and P. C. Searson et al.,[52] although the time scales for the measurement are much different between each other.

In the potentials lower than 1.1 V for the forward (positive) potential step and 0.6 V for the backward (negative) potential step, although the hole generated by photon migrates to the oxide/solution interface, the transfer of the holes does not occur probably because the position of energy level of the adsorption

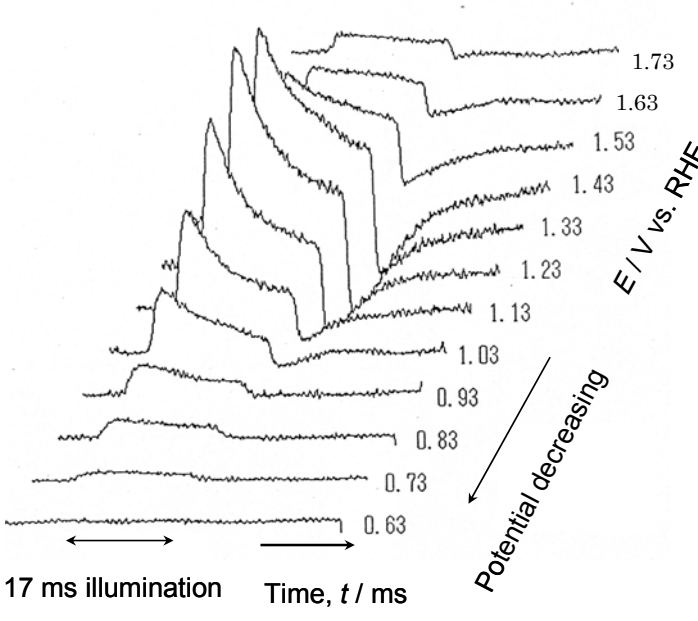

Figure 34. Response of photo-excited current to 17 ms illumination for the iron electrode covered by the passive oxide in pH 6.5 borate solution. The passive oxide was first formed at 2.03 V following step-wise decrease of potential. The photo-current was measured during the decreasing potential after 1.8ks polarization at the respective potentials. Reprint from K. Azumi, T. Ohtsuka and N. Sato, "Analysis of Transient Photocurrent in Passivated Iron Electrode in Neutral Borate Solution", *Nippon Kinzoku Gakai-shi* (*Bulletin of JIM*), 53 (1989) 479, Copyright ©1973 with permission from Japan Inst. Metals..

intermediate species for the water oxidation is lower than the Fermi level of the iron/ oxide system. Figure 35 shows a model which is assumed for the band diagram of the passive oxide. In Fig. 35, a surface state of the adsorbed species of O^{-}/O^{2-} is assumed which locates in the mid gap region. The state may work as an intermediate to transfer holes from the valence band edge to H_2O/O_2 redox couple in the electrolyte. In the case that the electron level (ε) of the state is enough lower than the Fermi level (ε_F) of the oxide, the

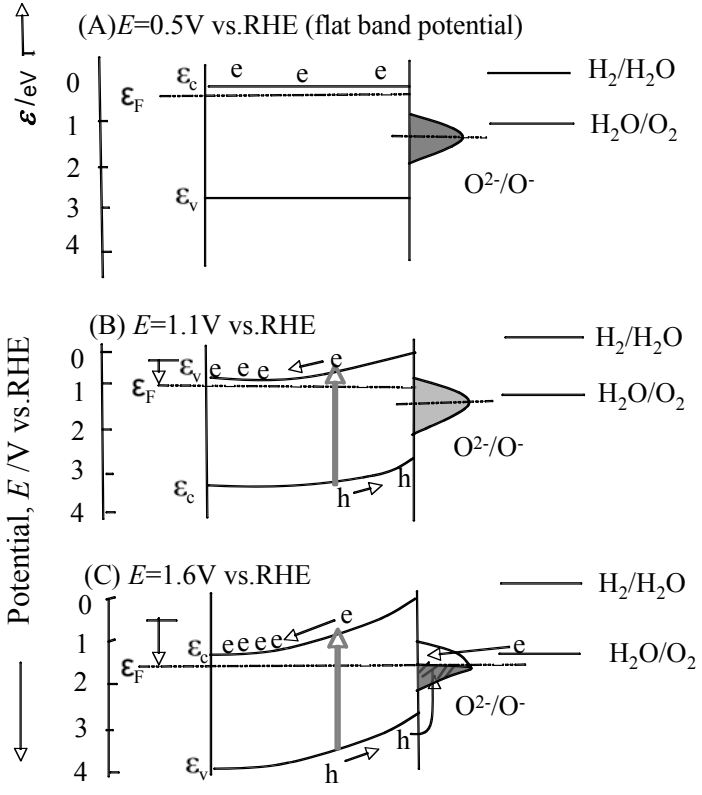

Figure 35. Schematic model of the band level of the passive oxide under positive bias and photo-excitation in the passive oxide.

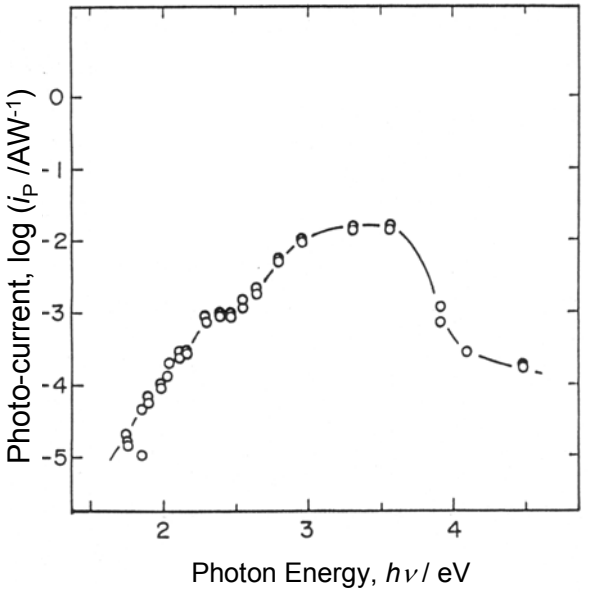

Figure 36. Spectra of photo-excited current per normalized power of incidence light. The passive film was formed at 1.60 V in pH 8.4 borate solution for 1 h. The photo-excited current was measured at the same potential. Reprint from K. Azumi, T. Ohtsuka and N. Sato, "Spectroscopic Photoresponse of the Passive Film Formed on Iron", *J. Electrochem. Soc*., 133 (1986) 1326, Copyright ©1986 with permission from The Electrochemical Soc.

state is occupied by electrons and the electron transfer from the H_2O/O_2 redox level to the state is inhibited. In that case, the holes excited by photon are accumulated at the oxide surface region. The current decay in Figs. 34 and 35 will be the accumulation process. In the higher potential, the surface state will change to partially occupied state and can accept the electron from the H_2O/O_2 redox, resulting in observation of the steady photo-current (Fig. 35c).

Action spectrum of the photo excited current, which was measured by lock-in technique with chopped light at 830 Hz by monochromated light, is shown in Fig. 36 in which the photo-current normalized by 1W incidence power is plotted by loga-

rithmic scale for the passive oxide formed at 1.6 V for 1h in pH 8.4 borate solution.[48] In the photon energy lower than the bang gap energy at 2.6 eV for the direct transition process of photo excitation, the photo current is lower than 10^{-3} A cm^{-2} $(W\ cm^{-2})^{-1}$ and in

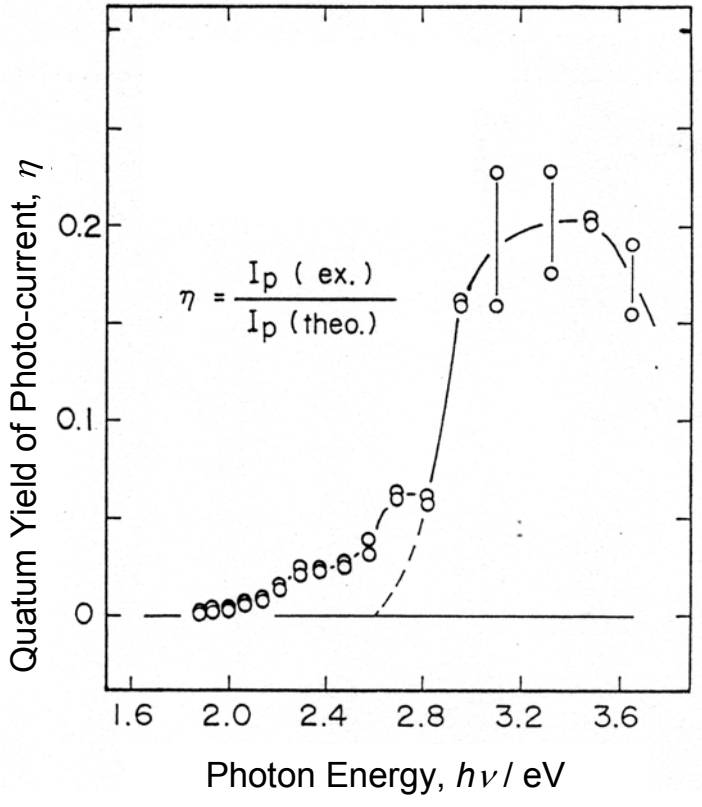

Figure 37. Quantum yield of photo-excited current as a function of photon energy incident to the iron electrode covered by the passive oxide. The passive oxide was formed at 1.60 V in pH 8.4 borate solution for 1h an the photocurrent was measured at the same potential. Reprint from K. Azumi, T. Ohtsuka and N. Sato, "Spectroscopic Photoresponse of the Passive Film Formed on Iron", *J. Electrochem. Soc.*, 133 (1986) 1326, Copyright ©1986 with permission from The Electrochemical Society.

the higher photon energy, the photo current increased to 10^{-2} A W^{-1}. From the comparison between the action spectra in Fig. 36, the absorption spectra calculated from the extinction index in Fig. 24, and the oxide thickness, the quantum yield of the conversion from absorbed photon to photo-current was calculated. The result is given in Fig. 37. The yield reveals a sharp increase to about 0.2 in the photon energy higher than the band gap energy of 2.6 eV for the direct transition process.

The band gap energy has been discussed from the photo-current action spectrum. The band gap energy estimated from the photo-current spectra is about 2 eV for the assumption for the indirect photo excitation process.[86-89] We can illustrate a model of the band diagram of n-type semiconductive passive oxide for the photo-induced process in Fig. 38. The indirect transition may pos-

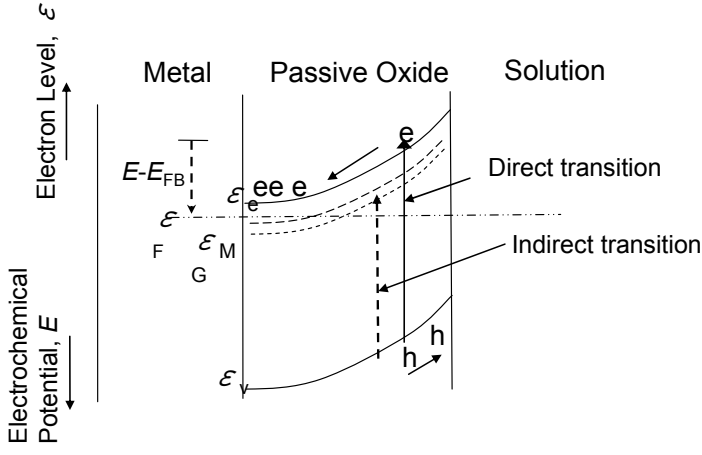

Figure 38. Model of the band diagram of the passive oxide on iron for photo excitation process. The flat band is about 0.35 V vs. RHE and the band gap between the valence and conduction band edges is about 2.6 eV. The direct transition may take place over this band gap energy. The indirect transition may take place via excitation from the valence band to the mid gap level i.e. the ionized donor sites with the excitation energy at about 2 eV.

sibly occur from electrons in the valence band to ionized donor sites and the electrons in the donor sites are migrated through the neighbor donor sites. The transition relating with the donor sites is not supposed to be high efficiency. However, the direct transition with the edge at about 2.6 eV may be an excitation of electrons from the valence to the conduction band and the separation of free electrons and positive holes would occur at relatively high efficiency.

IV. CONCLUSIONS

The passive oxide of iron was characterized by in-situ optical techniques such as ellipsometry, Raman scattering spectroscopy, photo-excitaed current and AC modulation combined with electrochemistry. It may be summarized as follows:

1) The thickness-potential relation may be followed by the ionic migration under high electric field and the equilibrium potential difference at the oxide/solution interface. The thickness is linearly increases with potential applied and the passive steady current is pH dependent.
2) The passive oxide on iron is probably composed of spinel type oxides of Fe_3O_4 and γ-Fe_2O_3 or those slightly modified. From thermodynamic, Fe_3O_4 may exist in the metal side and γ-Fe_2O_3 in the solution side.
3) In neutral solution, the outer hydrated layer is formed, in the case that ferrous ions exists in electrolyte.
4) The passive oxide works as a semiconductor of n-type with high concentration of donor density as large as 10^{26} m^{-3}.
5) The band gap of the n-type semiconductive oxide is about 2 eV for the indirect transition process and 2.6 eV for the direct transition. The conversion ratio of the photon to photo-current by the indirect transition is much smaller than that by the direct transition. The band diagram can be illustrated as Fig. 38.

REFERENCE

[1] M. Faraday, *Philos. Mag*., **9** (1836) 57.
[2] C. T. Schœnbein, *Philos. Mag*, **9** (1836) 53.
[3] H. Freundlich, G. Patscheke, and H. Zocher, *Z. Phys. Chem*., **238** (1927) 321.
[4] L. Tronstadt and C. W. Borgmann, *Trans. Rafaday Soc*., **30** (1934) 349.
[5] N. Sato, T. Noda, and K. Kudo, *Electrochim. Acta*, **19** (1974) 471.
[6] R. M. A. Azzum and N. M. Basshra, *Ellipsometry and Polarized Light*, North Holland-Elesevier Sci. Publ., Amsterdam, 1977.
[7] W. -K. Paik and J. O'M. Bockris, *Surf. Sci*., **28** (1971) 61.
[8] B. D. Cahan, J. Horkans, and E. Yeager, *Surf. Sci*., **37** (1973) 559.
[9] J. M. M. Droog and G. A. Bootsma, *J. Electroanal. Chem*., **105** (1979) 261.
[10] T. Ohtsuka and K. E. Heusler, *J. Electroanal. Chem*., **100** (1979) 319.
[11] T. Ohtsuka, *Denki Kagaku*, **60** (1992) 1123.
[12] R. M. A. Azzam, *Optica Acta*, **30** (1983) 1113.
[13] J. A. Johnson and N. M. Bashara, *J. Opt. Aoc. Am*., **61** (1971) 457.
[14] F. K. Urban III, Appl. *Surf. Sci*., **33/34** (1988) 934,
[15] E. Smith and G. Dent, *Modern Raman Spectroscopy- A Practical Approach*, John Wiley & Sons, The Atrium, 2005.
[16] T. Ohtsuka and K. Taneda, to be published.
[17] S. R. Morrison, *Electrochemistry at Semiconductor and Oxidized Metal Electrodes*, Prenum Press, New York and London, 1980.
[18] K. Uosaki and H. Kita, in *Modern Aspects of Electrochemistry*, No. 18, Ed. by P. E. White, J. O'M. Bockris and B. E. Conway, Plenum Press, New York and London, 1986, p. 1.
[19] T. Ohtsuka and Y. Sasaki, to be published.
[20] M. Ueda and T. Ohtsuka, *Corrosion Sci*., **44** (2001) 1633.
[21] K. Azumi, T. Ohtsuka, and N. Sato, *Denki Kagaku*, **53** (1985) 700.
[22] N. Sato and K. Kudo, *Electrochim. Acta*, **16** (1971) 447.
[23] Z. Szklarska-Smialowska and W. Kozlowski, *J. Electrochem. Soc*., **136** (1984) 234.
[24] Y-T. Chin and B. D. Cahan, *J. Electrochem. Soc*., **139** (1992) 2432.
[25] K. Azumi, T. Ohtsuka, and N. Sato, *Denki Kagaku*, **51** (1983) 155
[26] P. Soutiworth, A. Hamnett, A. M. Riley, and M. Sykes, *Corros. Sci*., **28** (1988) 1139.
[27] N. Sato and T. Noda, *Electrochim. Acta*, **22** (1977) 839.
[28] K. J. Vetter, Z. Elektrochem. *Ber. Bunsenges. Phys. Chem*., **59** (1955) 67.
[29] Z. Q. Huang and J. L. Ord, *J. Electrochem. Soc*., **132** (1985) 24.
[30] K. J. Vetter, Z. Elektrochem. *Ber. Bunsenges. Phys. Chem*., **60** (1962) 577.
[31] K. J. Vetter, *J. Electrochem. Soc*., **110** (1963) 597.
[32] N. F. Mott, *Trans. Faraday Soc*., **36** (1940) 472.
[33] H. Cabrera and N. F. Mott, *Rep. Progr. Phys*., **12** (1949) 163.
[34] K. J. Vetter and F. Gorn, *Electrochim. Acta*, **18** (1973) 321.
[35] K. Azumi, T. Ohtsuka, and N. Sato, *Denki-Kagaku*, 53 (1985) 700.
[36] K. E. Heusler, *Ber. Bunsenges. Phys. Chem*., **72** (1968) 1197.
[37] T. Ohstuka and A. Ohta, *Mat. Sci. and Eng. A*, **198** (1995) 169.

[38] V. Markovac and M. Cohen, *J. Electrochem. Soc*., **114** (1967) 678.
[39] J. L. Leibenguth and M. Cohen, *J. Electrochem. Soc*., **119** (1972) 987.
[40] K. Hashimoto and M. Cohen, *J. Electrochem. Soc*., **121** (1974) 37.
[41] M. Cohen, D. Mitchel and K. Hashimoto, *J. Electrochem. Soc*., **126** (1979) 442.
[42] J. W. Schultze, M. Mohr, and M. M. Lohrengel, *J. Electroanal. Chem.*, **154** (1983) 57.
[43] T. Ohtsuka, J.-C. Ju, S. Ito, and I. Einaga, *Corros. Sci.*, **36** (1994) 1257.
[44] M. Nagayama and M. Cohen, *J. Electrochem. Soc*., **110** (1963) 670.
[45] V. Markovac and M. Cohen, *J. Electrochem. Soc*., **114** (1967) 674.
[46] T. Ohtsuka and H. Yamada, *Corros. Sci*., **40** (1998) 1131.
[47] J. L. Ord and J. DeSmet, *J. Electrochem, Soc*., **118** (1971) 206.
[48] K. Azumi, T. Ohtsuka and N. Sato, *J. Electrochem. Soc*., **133** (1986) 1326.
[49] T. Ohtsuka, K. Azumi, and N. Sato, *Denki Kagaku*, **51** (1983) 155.
[50] T. Ohtsuka, K. Azumi, and N. Sato, *J. De Physique*, **C10** (1983) 191.
[51] C.-T. Chen and B. D. Cahan, *J. Electrochem. Soc*., **129** (1982) 17.
[52] P. C. Searson, P. M. Latanision, and U. Stimming, *J. Electrochem. Soc*., **135** (1988) 1358.
[53] D. J. Wheeler, B. D. Cahan, C. T. Chen, and E. Yeager, in *Passivity of Metals*, Ed. by R. P. Frankenthal and J. Kruger, The Electrochem. Soc. Inc., Pronceton, 1978, p. 546.
[54] S. M. Wilhelm and N. Hackerman, *J. Electrochem. Soc*., **128** (1981) 1668.
[55] S. M. Wilhelm, K. S. Yun, L. W. Ballenger, and N. Hackerman, *J. Electrochem. Soc*., **126** (1979) 419.
[56] U. Stimming and J. W. Schultze, *Ber. Bunsenges. Phys. Chem*., **80**, (1976) 1297.
[57] J. C. Rubim and J. Dunnwald, *J. Electroanal. Chem*., **258** (1989) 327.
[58] J. Gui and T. M. Devine, *Corrosion Sci*., **32** (1991) 1105.
[59] J. Gui and T. M. Devine, *Corrosion Sci*., **36** (1994) 441
[60] J. Gui and T. M. Devine, *Corrosion Sci*., **37** (1995) 1177.
[61] L. J. Oblonsky, S. Virtanen, V. Schroeder and T. M. Devine, *J. Electrochem. Sci*., **144** (1997) 1604.
[62] N. Boucherit, A. Hugot-Le Goff and S. Joiret, *Corrosion Sci*., **32** (1991) 497.
[63] W.-C Beek, T. Kang, H.-J. Sohn, and Y. T. Kho. *Electrochim. Acta*, **46** (20010 2321.
[64] T. Ohtsuka, *Materials Transaction*, **37** (1996) 67-69.
[65] T. Ohtsuka, K. Kubo, and N. Sato, *Corrosion*, **42** (1986) 476.
[66] R. J. Thibeau, C. W. Brown, and R. H. Heidersbach, *Appl. Spectrosc*., **32** (1978) 532.
[67] R. Goetz, D. F. Mitchell, B. MacDougall, and M. J. Graham, *J. Electrochem. Soc.*, **134** (1987) 535.
[68] J. A. Bordwell, B. MacDougall, and M. J. Graham, *J. Electrochem. Soc.*, **135** (1988) 413.
[69] M. Nagayama and M. Cohen, *J. Electrochem. Soc*. **109** (1962) 781.
[70] C. L. Foley, J. Kruger, and C. J. Bechtold, *J. Electrochem. Soc*. **114** (1967) 994.
[71] K. Kuroda, B. D. Cahan, Gh. Nazri, E. Yeager, and T. E. Mitchel, *J. Electrochem. Soc*. **129** (1982) 2163.
[72] W. E. O'Grady, *J. Electrochem. Soc*. **127** (1980) 555.

[73] M. E. Brett, K. M. Parkin, and M. J. Graham, *J. Electrochem. Soc*. **133** (1986) 2031.
[74] J. Kruger, *Corrosion Sci*. **29** (1989) 149.
[75] A. J. Davenport, J. A., Bardwell, H. S. Isaacs, and B. MacDougall, in *Modification of Passive Films*, Ed. by P. Maucus, B. Bauoux, and M. Keddam, The Institute of Materials, London, 1994, 57.
[76] M. F. Toney, A. J. Davenport, J. Oblonsky, M. P. Ryan, and C. M. Vitus, *Phys. Rev. Lettt*. **79** (1997) 4282.
[77] T. Konno and M. Nagayama, in *Passivity of Metals*, Ed. by R. P. Frankelthal and J. Kruger, The Electrochemical Soc., Inc., Princeton, NJ, 1978, p. 585.
[78] K. Azumi, T. Ohtsuka, N. Sato, *Transact. Jpn Inst. Metals* **27** (1986) 382.
[79] J. L. Ord and J. H. Bartlett, *J. Electrochem. Soc*. **112** (1965) 160.
[80] R. V. Moshtev, Ber. Bunsenges. *Phys. Chem*. **72** (1968) 452.
[81] E. M. A. Mattine and I. L. Muller, *Corrosion Sci*. **42** (2000) 443.
[82] K. Azumi, T. Ohtsuka, and N. Sato, *J. Electrochem. Soc*. **134** (1987) 1352.
[83] T. Ohtsuka, *Denki Kagaku* **65** (1997) 735.
[84] K. Azumi, T. Ohtsuka and N. Sato, *Corrosion Sci*. **31** (1990) 715.
[85] K. Azumi, T. Ohtsuka and N. Sato, *Nippon Kinzoku Gakai-shi* (*Bulletin of JIM*), **53** (1989) 479.
[86] H. J. Rieger and W. J. Plieth, *Werkstoffe und Korrosion* **39** (1988) 603.
[87] P. C. Searson, R. M. Latanision, and U. Stimming, *J. Electrochem. Soc*. **135** (1988) 1358.
[88] R. Schmuki, M. Buchler, S. Virtanen, H. Bohni, R. Muller, and L. J. Gauckler, *J. Electrochem. Soc*. **142** (1995) 3336.
[89] U. Stimming, in *Passivity of Metals and Simiconductors*, Ed. by M. Froment, Elsevier Science Publ., Amesterdam, 1983, p. 477.

3

Probing and Modelling of Galvanic Coupling Phenomena in Localized Corrosion

Roland Oltra and Bruno Vuillemin

Institut Carnot de Bourgogne, UMR 5209 CNRS - Université de Bourgogne, Electrochimie Interfaciale - Corrosion (EIC/IRM) 9 Av. A. Savary, BP 47 870 F-21078 DIJON Cedex, France

I. INTRODUCTION

The basic driving force of localized corrosion or corrosion protection in numerous cases is the galvanic coupling of which the dimensional aspect is fixed by a combination of *scales* regarding interfacial processes or properties. At the electrolyte–metal interface, it is necessary to consider the microstructure (including all real-time modification induced for example by applied stresses), the possible chemical changes at the surface of the material, and the electrolyte conductivity contribution, among others factors.

The galvanic corrosion is sometimes defined as bimetallic corrosion and described mainly for engineering structures as they are fabricated from dissimilar materials, which are in electrical contact with a conductive electrolyte. The galvanic phenomena are considered in these latter cases at the macroscopic scale. The galvanic series (widely reported for example in seawater) which report the

S.-I. Pyun and J.-W. Lee (eds.), *Progress in Corrosion Science and Engineering II*, Modern Aspects of Electrochemistry 47, DOI 10.1007/978-1-4419-5578-4_3,

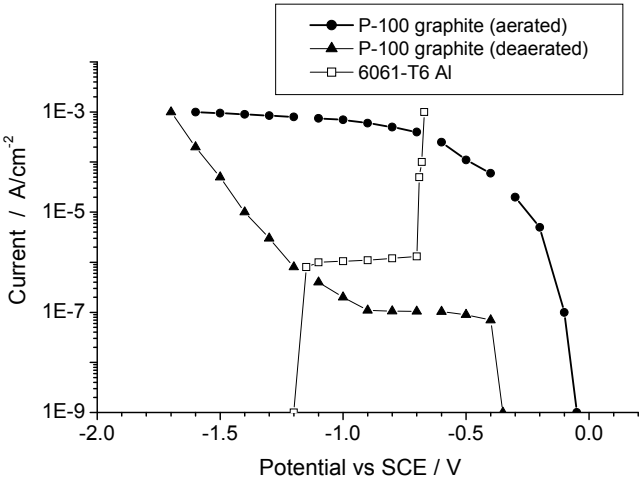

Figure 1. Evans diagram for estimating the galvanic current density. The bimetallic electrode consists of a carbon fibre embedded in a 6061 aluminium alloy (metal matrix composites). Two galvanic regimes can be reached as function of the aeration of the corrosive media. This analysis does not take into account the spatial distribution of the carbon fibers in the metallic matrix (see Fig. 12). Reprinted with permission from *International Materials Reviews*, **39** (1994) 245.Copyright ©1994 Maney Publishing .

ranking of the corrosion potentials for various pure metals or alloys is used to define the driving force between the elements of the couple. Regarding the rate of the galvanic corrosion, in a first approach Evans diagrams can be used (Fig. 1).[1]

From the experimental point of view the conventional measurement of the galvanic current is based on the Zero Resistance Ammeter (ZRA). But these approaches do not describe the real situation which is controlled basically by the current and potential distribution at the surface of the electrodes constituting the couple and in the solution as schematically illustrated in Fig. 2.

For reasons due to either the metallic material and /or the corrosive medium it is known that anodic and cathodic zones may take individual characteristics at the metal-solution interface and thus initiate localized corrosion phenomena. Localized corrosion

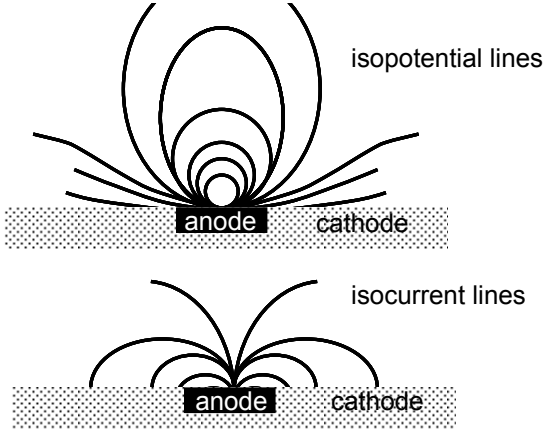

Figure 2. Schematic description of the potential and current distribution for a bimetallic electrode.

of metallic materials at macroscopic scale (crevice corrosion, welded junctions, etc.) and microscopic (pitting corrosion, intergranular corrosion, etc.) depends on the distribution of anode and cathode sites on a metal surface. The theory of current distribution in the vicinity of a corroding electrode couple has been worked out largely by Wagner[2] and Waber[3] in a series of papers published in the 1950's.

Their theoretical description is both stationary and coplanar. The nature of galvanic coupling in the case of localized corrosion of passivating metals (light alloys, stainless steels) takes on properties that differ depending on whether initiation (transient) or propagation phenomena (stationary) are under consideration. On the other hand, in real case of corrosion, and depending on the measurement techniques employed, description should take into account the dependence of these relations with time or frequency and should consider the dimensional aspect of current and potential distributions as well.

The dimensional aspects of the electrochemical polarization during galvanic coupling can be summarized as follows. The effect of the ohmic drop stabilizes processes of localized corrosion. In

terms of electrochemical kinetics, this means that the ohmic drop becomes part of the electrochemical polarization of the system. Their analysis of this situation was performed taking into account:

(a) the Laplace ‘s equation :

$$\nabla^2 \Phi = 0 \tag{1}$$

(b) the relation between the current density (j) and potential (E) on each electrode (cathode and anode)

The current density (j) is related to the potential by:

(a) Ohm’s law:

$$J = \frac{1}{\rho} \nabla \phi \tag{2}$$

where ρ is the electrolyte resistivity, valid in all the electrochemical cell; and

(b) by the electrochemical polarization:

$$j = f(E_{surf}) \tag{3}$$

Wagner has introduced a parameter L, which takes into account the fact that a knowledge of the two reactions (anodic and cathodic) but it is not sufficient for determining the coupling current of the two electrodes:

$$L = \kappa \left| \frac{\partial \Delta E}{\partial j} \right| \tag{4}$$

As illustrated in Fig. 3, it is possible to define the characteristic length of the coupling (λ) between anodic and cathodic zones. The nature of coupling changes as a function of the ratio between λ and L and therefore depends on a scale factor.

The main physical parameter which determines this scale factor for metallic materials is the metallurgical microstructure or the

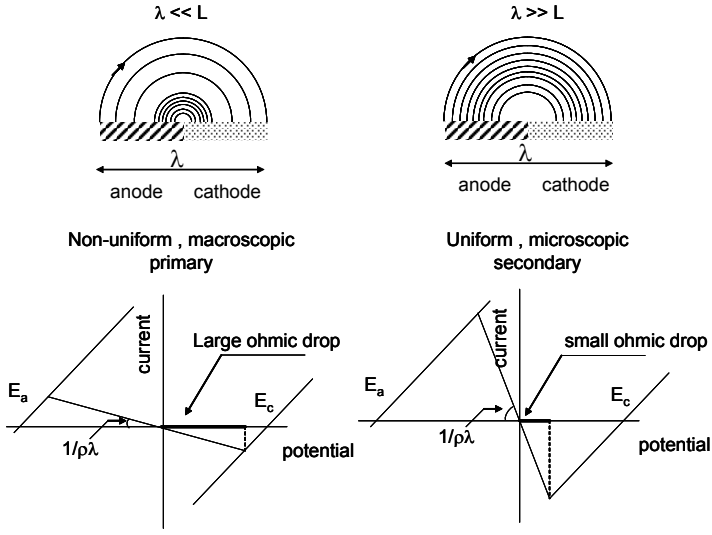

Figure 3. Concept of the Wagner's parameter. If λ is a characteristic dimension of the cell (anode-cathode) it can be compared to the Wagner's length L. It means that as a function of the relation between λ and L (depending of the electrolyte conductivity and the polarization) the ohmic drop between the anode and the cathode will affect the polarization of the anode and cathode.

metallurgical process. Regarding the metallurgical microstructure, it is largely demonstrated that the localized corrosion starts in mainly cases at small heterogeneities such as precipitates, inclusions, cracks that can be micrometer or submicrometer scale.[4] The basic chemical composition contrast, which is at the basis of the microstructural effect on galvanic corrosion, can be enhanced by metallurgical treatments or even during the early stages of local attack by aggressive solutions. This can be illustrated by local depletion of noble elements like chromium (well know case of intergranular corrosion of stainless steels) or by the local change in surface composition due to precipitation of dissolved species coming for example from inclusion dissolution.[5]

This latter chemical point illustrates the complexity of the microscopic description of the galvanic coupling. The chemical gradient is consequently an important parameter which can be also at the origin of the characteristic length of the time evolution of the

localized corrosion kinetics. It has been clearly illustrated for example by Smyrl on aluminium alloys[6] showing that the critical length for galvanic coupling is controlled by pH evolution around non-metallic precipitates.

Regarding the metallurgical process one of the most studied case is the corrosion of cut-edges of coated steels[7,8,9] In the case of galvanized steels, the critical size of the corrosion cell is fixed by the ration of the thicknesses of the zinc or zinc-alloyed coating versus the thickness of the steel plate. The corrosion of such a system is also a good example for illustrating the role of the conductivity change and thickness of the electrolyte layer. It is of interest to note that corrosion in presence of a thin layer of electrolyte has been largely investigated as it represents the conditions encountered during atmospheric corrosion.

From this brief review it appears that all these affecting parameters are not only metallurgical parameters and clearly demonstrate the need to develop or to apply local probes to reach an in-situ and a real time monitoring of the dimensional aspect of the localized corrosion (Fig. 4). On the other hand the Fig. 4 indicates that very close to the surface the solution chemistry changes can be significant so that the conductivity may be unknown (depends on supporting electrolyte concentration) and also some of the current is carried by diffusion. Thus, as indicated there will be limita-

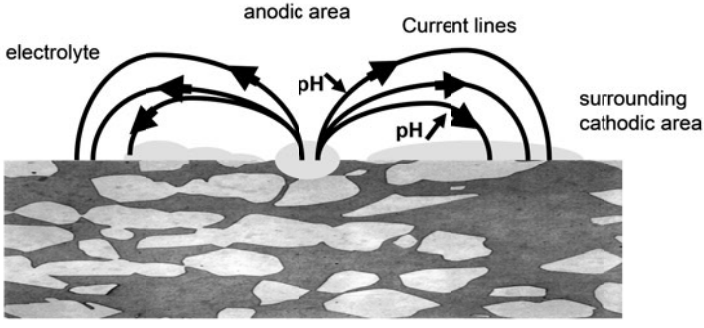

Figure 4. Electrical and chemical aspects of the galvanic coupling for a localized corrosion site in a real metallic microstructure. Acidification is related to the anodic dissolution and alkalinisation is associated to the surrounding cathodic reaction.

tions/uncertainties in use of the Laplace's equation and it will be necessary to use others governing laws as for example the Nernst-Planck's equation for refined modelling.

II. EXPERIMENTAL DATA FOR NUMERICAL SIMULATION AND MODEL VALIDATION

From the experimental point of view, it is necessary to adapt the chemical and electrochemical probe techniques for collecting entry data for predictive numerical simulation. The same objective must be reached for validating experimentally the results of the simulations.

A large number of physical and chemical parameters are of importance but in a first microstructural based approach, the whole microstructure can be described by an elementary cell representing the basic galvanic coupling at a reduced scale as demonstrated by Morris and Smyrl.[10] Following the introductive remarks related to the interfacial processes or properties, it can be proposed that the following parameters must be selected to describe for example the galvanic coupling between a phase and its surrounding matrix:

- The electromotive force related to their relative values in a specific *galvanic series*.
- Their individual electrochemical kinetics.
- The chemical evolution of the above electrolyte (conductive media) controlled by the mass transport of the species emitted at the anode and at the cathode.

Even if specific probe techniques allow obtaining separately the values of these parameters, the validation by measuring for example the galvanic current distribution inside the electrolyte by in situ techniques is not an easy task.

1. How to Evaluate the Galvanic Series for Elementary Microstructure Components: Scanning Kelvin Probe Force Microscopy

Kelvin Probe Force Microscopy (KPFM or SKPFM) was derived from the development of the atomic force microscope (AFM) al-

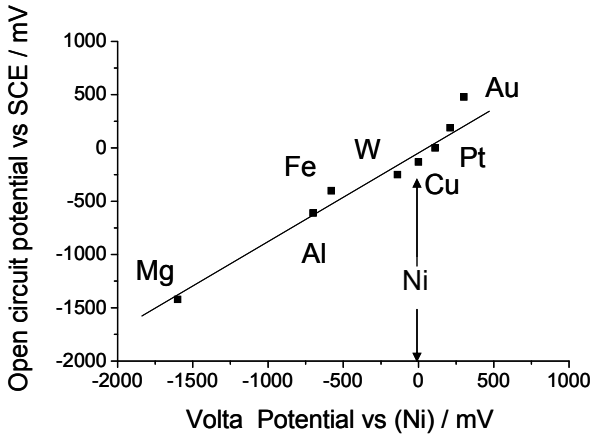

Figure 5. Relation between the potential measured in air by SKPFM with open-circuit potentials measured in dionized water for different metals (same trend has been found in 0.5 M NaCl) assuming the surface potential of pure Ni as the reference - Reprinted with permission from *J. Electrochem. Soc*., **145** (1998) 2285 Copyright ©1998, The Electrochemical Society.

lowing to probe the surface properties of sub-micron structures. KFM, developed on the basis of the Kelvin method in 1991,[11] was applied for example to explain the electrical properties of the metal/semiconductor interface in ultra high vacuum or in ambient conditions.[12,13] This technique seems capable of distinguishing constituents of a metal through their work-function differences. Application to localized corrosion was promoted about ten years ago by P. Schmutz and J. Frankel.[14] The authors mapped the Volta potential of various metals and the most interesting point was the linear relation found between the Volta potential measured in air and the corrosion potential in aqueous solution indicating that this potential is a measurement of the practical nobility of the surface (Fig. 5). They applied this approach to study the Volta potential of intermetallic particles in AA2024-T3 and the matrix phase. They concluded that all intermetallic particles, including the Mg-containing S-phase particles, had a Volta potential nobler to that of the matrix.

It is clear that the ability to map the potential on a sub-micron scale is extremely useful in studies of localized corrosion of alloys which contain heterogeneities on the micrometric scale. From a qualitative point of view a large amount of rough data are available in the literature on KPFM analysis. For example, they concern the practical nobility of phases versus matrix on aluminium alloys after careful surface preparation (ultramicrotomy),[15] the characterization of selective dissolution of intermetallics[16] or their role during the chemical conversion of an aluminium surface.[17] All these measurements give interesting starting point for discussing the galvanic coupling but mainly on a phenomenological point of view.

Nevertheless, strong discussions can be found in the literature concerning the origin of the surface potential measured through the KPFM. KPFM measurements are highly influenced by the structure, composition, and thickness of the oxide film covering the surface, surface charge distribution, and adsorbed species at the surface.[18] On the other hand recently, work of Rohwerder et al., demonstrated that the correlation between the KPFM potential measurement in ambient conditions and the corrosion potential is not of general validity.[19] In this paper the authors proposed an interesting discussion on the basics of SKPFM measurements compared to the more conventional Kelvin Probe. From this paper it appears that no direct relationship can be established between the work function measured on a freshly polished metal and its possible corrosion behaviour, as corrosion depends sensitively on the environment (pH, kind of ions, etc.) and is also determined by the kinetics of the involved reactions. It is in contradiction with the results presented in Fig. 5.

Nevertheless, the introduction of SKPFM measurements reveals the need to establish galvanic series for microstructures or elements of galvanic couples involved in localized corrosion at the micrometer scale. But the introduction of SKPFM data on numerical simulation seems to be not possible as a large doubt always exists. It justifies the interest to focus on in-situ local microelectrochemical studies for investigating the current-potential relation in an aqueous solution, i.e., the electrochemical kinetic at the scale of the microstructure.

2. How to Measure the Electrochemical Kinetics for the Elementary Microstructure Components: Microelectrochemical Probes

Microcapillary electrochemical cells are widely used in biology for local potential measurements at a very reduced size. In corrosion, pioneering work was performed for promoting the Scanning Reference Electrode Technique (SRET): in this case the microcapillary is immersed in the bulk electrolyte and local potential[20] or local electrochemical polarization or local electrochemical impedance[21] has been measured.

In the last 20 years capillary based cells not immersed in bulk electrolyte but delimiting a very restricted area of the metallic electrodes in contact with the electrolyte were developed in parallel by Böhni and Suter.[22]

The basic of these techniques, microcapillary electrochemical cells (MEC), consists in pulling a glass capillary in order to reach a tip diameter in the range of few micrometers (10 to 100 μm) which will be stick to the metallic area of interest (MAOI) by a silicone gasket deposited at the tip (Fig. 6a). As function of the size of the tip it is possible to investigate the electrochemical behaviour of multi-phases system or only one phase (Fig. 6b). Regarding the modelling of galvanic phenomena in localized corrosion the interest of MEC is to be appropriate for obtaining entry data on the anodic and cathodic reaction kinetics on the real phases involved in the galvanic process.

For the reactions occurring on the anode, i.e., dissolution, one can expect some limitations due to the acidification and the precipitation of solid phases in case of saturation of the electrolyte near the tip of the capillary. To avoid this, Lohrengel et al.[23,24] proposed a derived set-up consisting of a theta-capillary, i.e., capillaries with two channels separated by a partition wall where an electrolyte flows. In this configuration, reaction products like gases (bubbles of O_2 or H_2) or precipitates cannot block the capillary. (Fig. 6c).

If the MEC is used for elucidating the cathodic behaviour of the cathode one can expect same physical troubles, i.e., bubbles generation in acidic media which can interrupt the electrical conduction inside the capillary whereas chemical changes can also

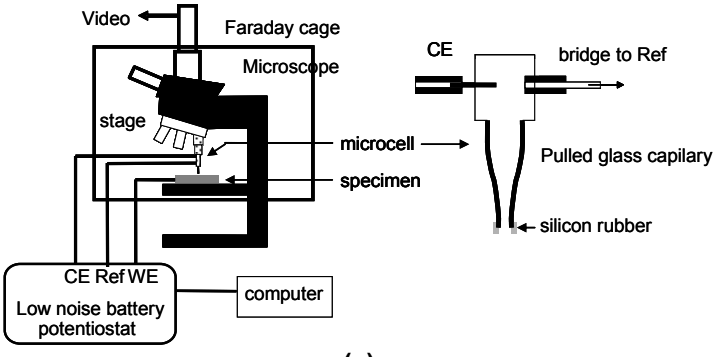

(a)

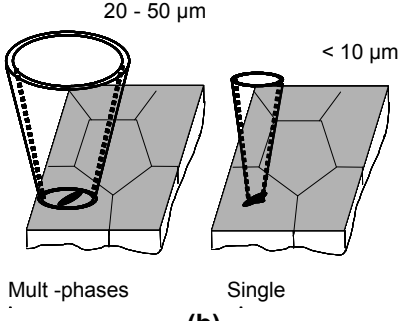

(b)

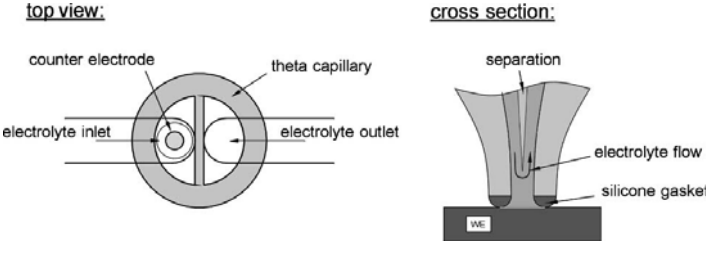

(c)

Figure 6. (a) Schematic description of the microcapillary electrochemical cell equipment, (b) typical analysis of the electrochemical behavior on a microstructure which can be performed with MEC equipment, and (c) design of a microcapillary tip for circulating. Reprinted with permission from *Electrochim. Act.,* **49** (2004), 2863 Copyright © 2004 , Elsevier Science.

arise as there will be alcalinization from inside the capillary due to the mass transport limitation.

Regarding the Section 3(*iii*) of this chapter, related to the modelling of the galvanic coupling on aluminium alloys, specific attention must be paid to the use of MEC for investigating the cathodic reduction occurring on a phase of reduced size in a neutral solution. In this case the reduction is due to the reduction of the oxygen dissolved inside the capillary in contact through the silicone gasket with the selected phase. It was demonstrated that in the case of cathodic polarization, the limiting current density (for oxygen reduction reaction - ORR) varies according to the capillary diameter used.[25] Nevertheless the dependence of cathodic current (limiting current) upon the diameter of the capillary was not explained.

On the basis of similarities of the design of MEC and electrochemical oxygen micro sensors,[26] Oltra et al.[27] discussed the possible role of the silicone gasket which can acts as a non-permeable membrane for oxygen. It was demonstrated controlling the surrounding gaseous environment by argon gas shielding (Fig. 7a) that oxygen reduction, which is of importance in neutral media, can be enhanced as function of the size of the capillary tip inducing for example non expected pH changes (alcalinization) at the MAOI interface.

This membrane effect strongly increases the oxygen reduction reaction (ORR) inside the capillary masking diffusion control which would be always observed considering the same metallic area, i.e., a microelectrode of the same diameter than the capillary tip but in bulk conditions (Fig. 7b). This remark is important and highlights the difficulty to interpret and apply microelectrochemical measurements when ORR is the controlling step. This would explain the strategy chosen for modelling in Section III.3 of this chapter.

To control the pH inside the capillary it was proposed also to perform microelectrochemical tests using buffered solutions[28] but it is not demonstrated that the interfacial pH is really controlled.

MAOI studied by MEC were mainly related to the role of the microstructure on stainless steels, e.g., role of manganese sulphide inclusions[29] or on aluminium alloys, e.g., electrochemical behaviour of intermetallics.[30]

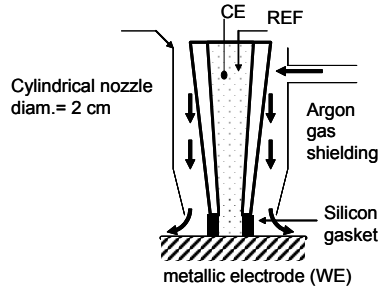

(a)

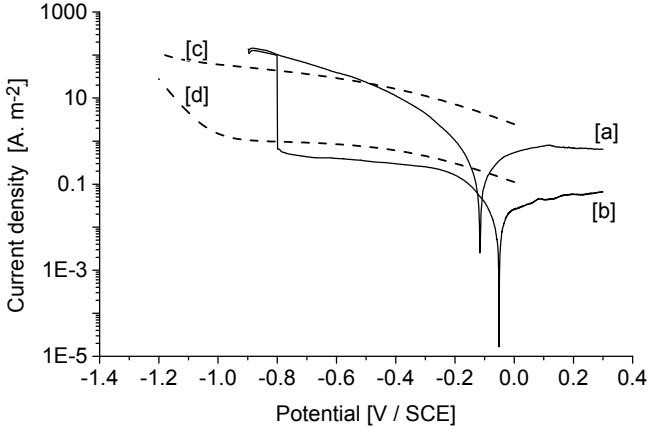

(b)

Figure 7. (a) Schematic description of the modified set-up of the MEC for reducing the role of the silicone gasket on ORR. An argon gas shielding is continuously applied during the polarization experiment. In this configuration only the oxygen is coming from inside the capillary (dissolved oxygen solubility can be assumed to be 0.26 mol m^{-3}). It corresponds to the real bulk conditions observed on the selected metallic spot surrounded by a macroscopic matrix. Reprinted with permission from *Electrochem. Comm.,* **10** (2008) 848, Copyright © 2008, Elsevier Science. (b) Effect of argon shielding on the cathodic reduction reactions in a NaCl (0.5 M) neutral solution on a platinum electrode for a microcapillary of 50 μm in diameter. Experimental polarization curves: from – 0.9 V to 0.4 V vs. SCE (solid lines); [a] scan in absence of gas shielding, and [b] during this scan, the argon shielding was turned on after –0.8 V vs. SCE. FEM simulation (dashed lines); [c] simulation in absence of argon shielding and [d] simulation in presence of argon shielding. Reprinted with permission from *Electrochem. Comm*., **10** (2008) 848, Copyright © 2008, Elsevier Science.

MEC measurements allowed to clarify the corrosion mechanism on manganese sulphide: local measurements confirmed the effect of sulphur species spreading due to the dissolution of manganese dissolution in a well defined range of potential. Interest of MEC was demonstrated in the study of the role of the shape of the inclusions upon the susceptibility for pitting of the alloy as it was easily possible to select only one inclusion and its surrounding matrix at a reduced size.[31] But a less amount of MEC studies were performed for investigating the elementary electrochemical kinetics on an individual metallic phase, like intermetallics or surrounding matrix to precipitates. Work of Buchheit et al. can be mentioned for the wide scope of investigation on intermetallics in aluminium alloys.[30,32] Nevertheless the results were only used to define the *galvanic series* of a large number of synthetic intermetallics and the kinetics were not used to model the galvanic coupling between intermetallics and aluminium based surrounding matrix.

3. How to Define the Chemical Composition Gradients: Electrochemical and Optical Sensors

In corrosion domain, pH gradients are the most studied as local acidification or alcalinization are directly related to local electrochemical reactions as shown in Fig. 4. These pH changes control the nature of the species emitted, the homogeneous reactions at the vicinity of the surface. These reactions can induce precipitation, gaseous bubbling which can be modelled using a stationary approach (see part on modelling).

(*i*) *Amperometric Sensors for Solution Chemistry Mapping*

Among amperometric sensors, the Scanning Electrochemical Microscope (SECM) is probably the most attractive but the less applied, even if SECM is a scanned probe microscope (SPM) that has proven to be a powerful instrument for the quantitative investigation of a wide range of processes that occur at interfaces.[33] The probe tip in SECM is an ultramicroelectrode (UME), which typically has a characteristic dimension in the 0.1–10 μm range. The amperometric, or potentiometric response of the tip UME is recorded as the probe is scanned either normal to the interface of interest (tip approach measurements) or over the interface typically

at some fixed height (for imaging purposes) or is held in a fixed position with respect to the substrate (for time-dependent measurements). SECM is mainly used in two modes: feedback or generation collection using a redox mediator in solution in order to characterize the species to be analyzed: this is an analytical technique.

SECM applications have been reported for localized corrosion studies. Still and Wipf[34] published work investigating the localized corrosion of a passivated iron sample using SECM in generation and collection modes of SECM separately, to firstly induce local generation of aggressive ion and secondly to collect after initiation the dissolution current issuing form the dissolving pit. They described experiments in which an iron sample was immersed in a solution of 30-mM trichloroacetic acid solution in phosphate/citrate buffer at pH 6, and passivated at fixed potential for a given period of time. A gold microdisc electrode initially at a potential of 0 V (versus a mercurous sulfate electrode (MSE)) was positioned close to the surface (within 1 tip radius). The potential of the tip electrode was then adjusted to –1.6 V to generate chloride ions by the reduction of the trichloroacetic acid. The equation given for this reaction is

$$Cl_3CCOO^- + H_2O + 2e^- \rightarrow Cl_2CHCOO^- + OH^- + Cl^- \quad (5)$$

Current fluctuations at the substrate were observed within a few seconds, indicating pitting corrosion. In addition, the tip current also fluctuated, and correlated well with the sharp changes in current observed at the substrate. This behaviour was attributed to the release of iron species by the sample during the corrosion process, which was then reduced at the tip.

On the other hand and in relation with the role of manganese sulphide in pitting of stainless steels already mentioned, R.C Alkire,[35] performed SECM experiments to demonstrate the role of adsorbed sulphur species near sulphide inclusions like a driving force for pitting of Nickel.

From an experimental point of view, electrochemical current-voltage measurements on microscopic parts of the electrodes were carried out with capillaries of 20–100 microns manipulated so as to cover specific sulphide inclusions, previously characterized by SEM/EDX measurements.

The active part of scanning electrochemical microscopy apparatus consisted of a carbon fiber tip. The solution used for SECM measurements was 10 mM KI + 0.1 M NaCl. The Ni and C fiber electrodes were independently controlled by two separate potentiostatic circuits. The SECM tip potential (E_{tip}) was held at 0.6 V to reduce I_2 to triiodide (Fig. 8).

In solution, the sulphur species emitted during dissolution of MnS inclusions can react with the I^{3-}/I redox system:

$$I^{3-} + 2\ S_2O_3^{2-} \rightarrow 3\ I^- + S_4O_6^{2-} \quad (6)$$

or

$$I^{3-} + HS^- \rightarrow 3\ I^- + H^+ + S \quad (7)$$

The reaction of dissolution of the MnS can be follow using the positive-feedback of the SECM:

$$3\ I^- \rightarrow I^{3-} + 2\ e^- \quad (8)$$

It was then possible to confirm a dissolution mechanism leading to the formation of thiosulfates:

$$2\ MnS + 3\ H_2O \rightarrow 2\ Mn^{2+} + S_2O_3^{2-} + 6\ H^+ + 8\ e^- \quad (9)$$

confirming the role of poisoning of the sulphur species by dismutation of thiosulfates as shown in reaction (6):

$$S_2O_3^{2-} + H_2O \rightarrow S_{ads} + SO_4^{2-} + 2\ H^+ + 2\ e^- \quad (10)$$

(*ii*) *Potentiometric Sensors for Solution Chemistry Mapping*

Ion selective microsensors can be designed using ultra microelectrodes to follow the changes of ion concentrations of selected species during galvanic corrosion experiments. Concentration maps can be obtained using liquid membrane glass capillary electrodes, home made from pulled glass capillaries filled with an ionophore having a functional detection range for the selected species. If a large number of papers are related to biosensors, in corro-

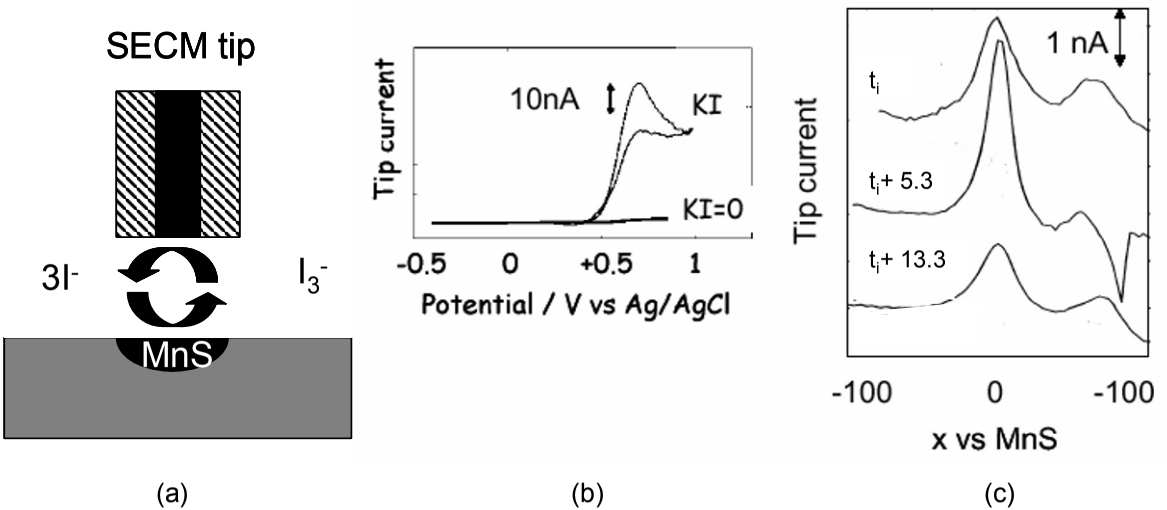

Figure 8. (a) Schematic diagram of the SECM detection of $S_2O_3^{2-}$ and/or H_2S above MnS inclusions in stainless steels (303 or 304). (b) The cyclic voltammogram responses of the SECM tip in a 0.1 M solution containing or not the chemical mediator (KI) showing the oxidation of I^- above a MnS inclusion (tip at 5µm above the inclusion). (c) SECM line scans measured at different times over an electroactive site on a 304 electrode in 10 mM KI in 0.1 M NaCl (the 304 electrode is polarized above the pitting potential during the time ti (40 mn) and the tip is polarized at +0.6V vs Ag/AgCl). Reprinted with permission from *J. Electrochem. Soc.*, **147** (2000) 4120, Copyright © 2000, The Electrochemical Society.

sion a more reduced number of examples can be found for detecting like Zn^{++},[36] Mg^{++},[37] and Cu^{++}.[38]

Potentiometric pH sensors are probably the most employed in corrosion studies. The simplest design is based on the introduction of the selected ionophore after silanization of the tip of the pulled capillary in which a silver chlorinated wire is immersed to serve as the internal reference electrode. This kind of microelectrodes can be mounted on the X-Y-Z positioning system to control the position and program the sweeping of the microelectrode.[39,40,41]

For example, pH mapping has been performed above galvanic cell representing the galvanic coupling for a 6061-aluminium alloys. In this case the basic galvanic cell consists in Al_3Fe intermetallic which acts as cathode versus the surrounding matrix.[42] pH scanning with a lateral resolution of 2 μm shown an increase of the pH (alcalinization) above a massive Al_3Fe electrode electrically coupled to a sheet of 6061 alloy.

The same kind of pH microelectrode can be designed using a working electrode made up a tungsten microelectrode inserted in one channel of a theta capillary (the other channel is similar to the previous sensor and consists in Ag/AgCl reference electrode) (Fig. 9).

A typical calibration curve obtained with the probe in 0.03 M NaCl solution, whose pH is modified by addition of concentrated hydrochloric acid and sodium hydroxide solutions is shown in Fig. 9. The interest of such pH mapping for validation of modelling will be illustrated in the second part of this chapter.

(*iii*) *Optical Sensors*

In-situ pH mapping can be also performed using optical sensors based on fluorescence or pH indicators. Fluorescence is largely used to measure concentrations of chemical species in fields of analytical chemistry, biology, and physiology. Fluorescent compounds can be added in the electrolyte directly: in this case the activity can be followed by confocal laser scanning microscopy (CLSM).[43] On the other hand fluorescent species can be trapped in polymer at the tip of optical fibers (Fiber Optic Chemical Sensors – FOCS)[44] Typical FOCS are constructed using one or more chemically sensitive fluorescent species or fluorophores immobilized on the tip of a single optical fiber or of a multi-fiber bundle. An

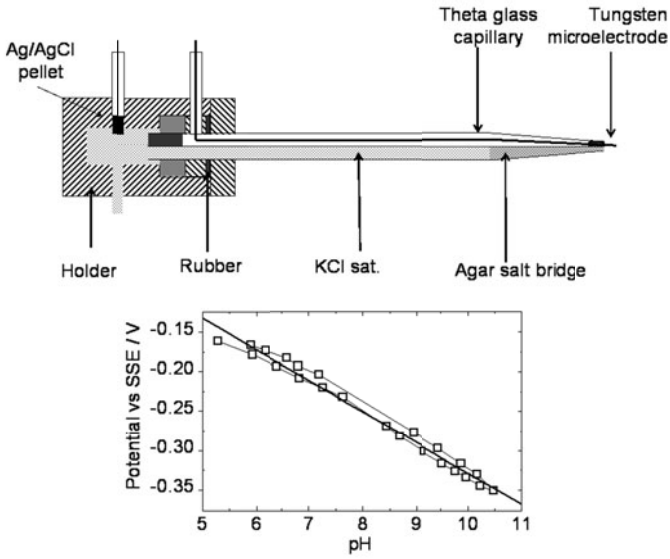

Figure 9. (a) Example of a metallic pH probe and (b) its calibration curve in 0.03 M NaCl. In this case a thin wire of W of which the tip (150μm in diameter) is oxidized.

initial excitation light is transmitted through the optical fiber to the fluorescent species or fluorophore at the distal tip of the fiber. The fluorophore's subsequent chemically dependent fluorescent response is transmitted back through the optical fiber to the proximal end where the fluorescence emission is monitored using a photonic sensor. The specific chemical concentration of a species can then be monitored at any point where the fiber tip is placed within a chemically reactive environment.

In corrosion applications, pH gradients have been tentatively measured using fluoresceine or fluoresceinamine. For fluoresceine excitation is at 488nm and emission is at 515nm.

CLSM[45] and Near-Field Scanning Optical Microscopy[46] has been used by R.W Smyrl to map the fluorescence during corrosion of 2024 and 6061 aluminium alloys. It has been shown that on 6061 alloy fluorescence is emitted from the Al-Mg-Si intermetallics. The fluorescence is in fact trapped by the corrosion products (Fig. 9a) due to the selective dissolution of Mg: it is an indirect

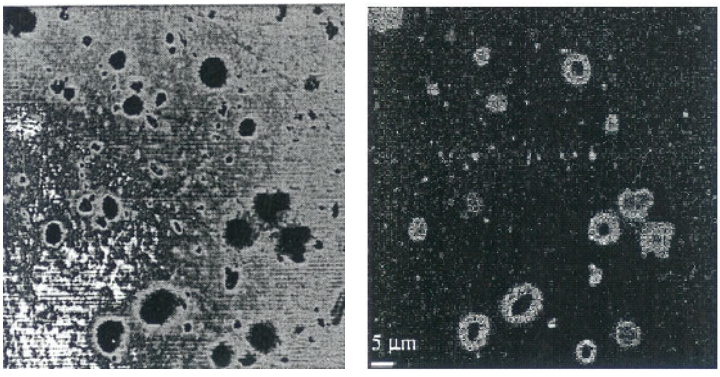

Figure 10. The CLSM reflectance image of a Al2024 after 10 mn of exposure in 0.1 M KCl solution (a). The corresponding fluorescence image due to the presence of 0.1 mM fluorescine in the test solution (b). Reprinted with permission from *J. Electrochem. Soc*., **145** (1998) 1571, Copyright © 1998, The Electrochemical Society.

measurement of the alcalinization demonstrating the cathodic behaviour of this kind of intermetallics (Fig. 10b). In the same paper a model based on simple diffusion is proposed for calculating the pH gradient above and around the particle. It will be discussed in the second part of this chapter.

FOCS (fiber bundle) was used by S.Szunerits et D.Walt[47] to image the concentration of Al^{3+} cations during localized dissolution of pure aluminium: in this case the fluorescent molecule was morin (excitation 310nm – emission 510 nm) which allowed the in situ visualization of the corrosion processes by monitoring the release of Al^{3+}. Nevertheless, application of FOCS for corrosion mechanisms has not been deeply investigated in the mentioned work but this kind of sensor represents a promising tool which could be applied.

At a larger scale (millimetre range), for investigating the galvanic coupling on assembled structures, e.g., welded structures, indicators can be used to determine the location and mechanisms of corrosion.[48] Broad-range of pH indicators can be trapped in electrolyte agar gels to study the change in pH related to acidification at dissolving parts and alcalinization on cathodic areas. This

approach remains qualitative and cannot be used for supporting modelling. It has been applied, for example, to characterize the galvanic coupling on aluminium sheets welded by friction stir welding (FSW).

4. How to Image In-Situ the Galvanic Current Distribution: Scanning Vibrating Electrode Technique

Galvanic corrosion is controlled by the local potential distribution above the metallic surface. The potential gradients can be imaged directly using a microcapillary cell containing the reference electrode (Scanning Reference Electrode Technique). This technique was more applied for detecting localized corrosion initiation[49] than to describe isopotential contour maps on a bimetallic electrode.[50,51] Pioneering work at a rather macroscopic scale has been conducted by Doig and Flewitt[52] and McCafferty[53] on modelling experimental systems like Cu-Zn and Fe-Zn. Nevertheless these studies were limited to validation of Laplace's equation.

As mentioned in the introduction the current distribution is the most useful parameter to quantify the local kinetics in a galvanic coupling arrangement. From this local analysis of the currents the local damage can be theoretically predicted. The most efficient in-situ current probing is the Scanning Vibrating Electrode (SVET) which allows to measure the local current potential gradients from which the current density is deduced applying the Ohm's law. This technique initially developed in biological domain for extracellular current measurement[54] was transferred to corrosion studies by pioneering work of H. Isaacs in 70's.[55] This technique is based on the ohmic measurement in electrolyte between two virtual points defined by the vibration of Pt-Ir microelectrodes which is black platinised.[56] The diameter of the sphere of the black platinum deposit was 15 µm, corresponding to a capacitance of about 10 nF (Fig. 11b). The amplitude of vibration was typically 20 µm, with a frequency around 600 and 200 Hz respectively parallel and normal to the sample surface.

The potential drop measured by the microelectrode is converted with the Ohm's law into a current density value after amplification. The displacement of the microelectrode is performed using a motorized and computer controlled XYZ micromanipulator (see Fig. 11a). To improve the application in case of localized cor-

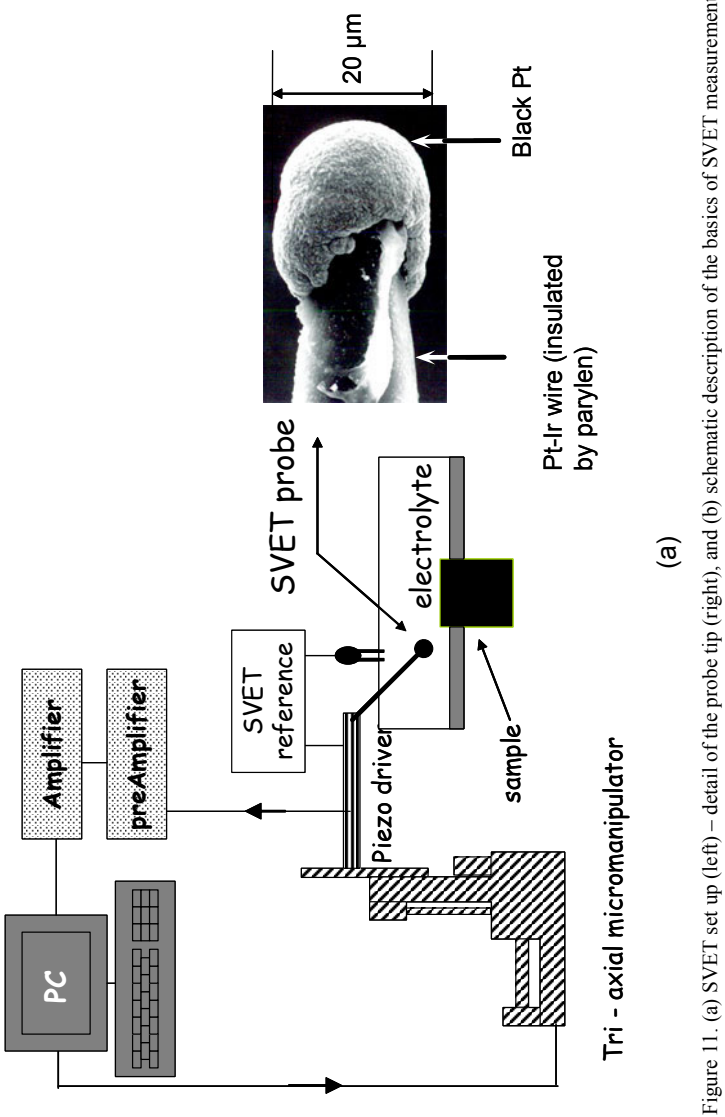

Figure 11. (a) SVET set up (left) – detail of the probe tip (right), and (b) schematic description of the basics of SVET measurement.

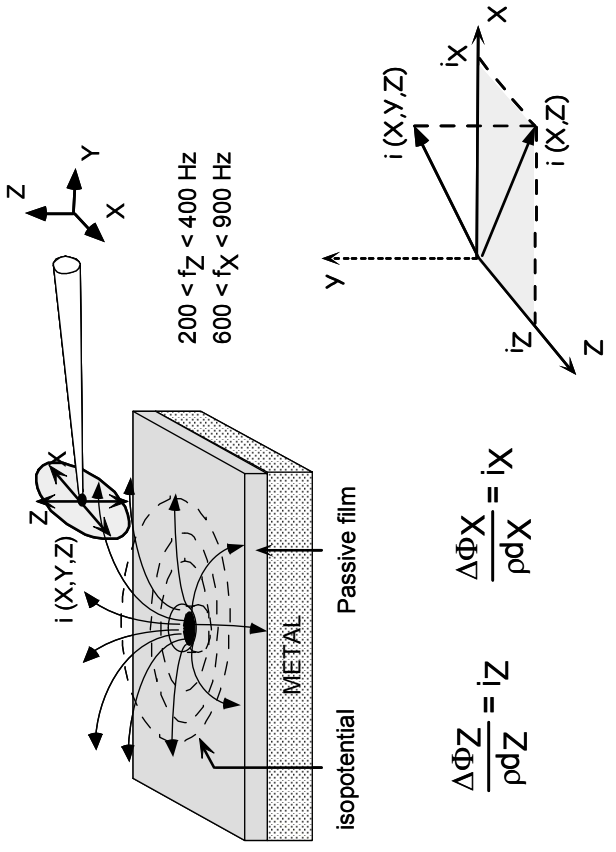

(b)

Figure 11. Continuation.

rosion this set-up was combined with a capillary technique in order to be able to follow a well defined site of corrosion which is generated by a local injection of aggressive solution in a buffered solution.[57] During pitting it is difficult to stabilize the galvanic coupling between the pitting area and the surrounding passive surface, whereas in case of localized corrosion on geometrically stable galvanic coupling, i.e., when the anodic and the cathodic areas are not changing of location, scanning (2-D or 3-D) is possible.

Application of SVET was clearly highlighted in the work of Kasper R.G and Crowe C.R. on a modelling Fe-Cu couple of relatively large size.[58] They demonstrated that ionic current density in the near field of the corroding Fe-Cu galvanic couple can be compared with the predictions of a finite element model that calculated near field potential and current density distributions. In the second part of this chapter it will be illustrated that SVET measurements can also be used to detect the change of surface activity during galvanic coupling as it was experimentally investigated by Ogle et al.[59]

III. SIMULATION OF LOCALIZED GALVANIC CORROSION

1. Basic Equations

Local probe techniques are available to measure the spatial distribution of potential, current, chemical species concentration and to quantify the corrosion rate.

Modelling is mainly based on the solution of partial differential equations obtained in most cases by numerical methods like Finite Difference Method (FDM),[60] Finite Element Method (FEM) [58] or Boundary Element Method (BEM)[61,62,63] describing always a bimetallic corrosion situation at various scales combining current and potential distribution (Laplace's equation) with the mass transport of reactive species (Nernst-Planck 's equation).

Modelling of galvanic corrosion, whatever the scale of the electrodes, can be solved considering the elementary cell characterizing the coupling length defined by Wagner and Waber[2,3] as shown in the first part of this chapter. For galvanic corrosion related to the microstructure of materials this was clearly demon-

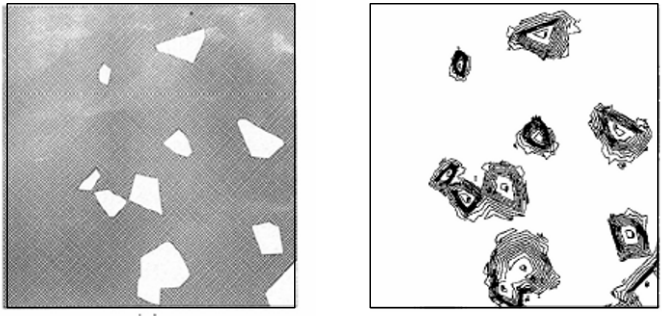

Figure 12. Simulated microstructure (on left) and corresponding isocurrent lines calculated solving the Laplace's equation. It is assumed that the cathodic reaction is located on the particles (white phase in left diagram), Reprinted with permission from *J. Electrochem. Soc.*, **136** (1989) 3237, Copyright © 1989, The Electrochemical Society.

strated by Smyrl and Morris.[64,10] In this work the authors considered only the current distribution ignoring the chemical gradients related to the anodic or cathodic reactions occurring at the scale of the microstructure. In fact the same authors have described the chemical contribution in another work related to the corrosion on 2024 aluminium alloy (see the Ref.[45] already mentioned), but they have not combined the two.

For example, in this latter case, the cathodic reduction of dissolved oxygen occurring on the IM phase is limited by the mass transfer and the alcalinization can contribute simultaneously to the dissolution of the surrounding aluminium matrix in addition to the pure galvanic coupling, e.g., the current density typically increased at the boundary between IM and matrix (Fig. 12).

It remains an open question recently discussed[65] on the basis of numerous experimental results. Aluminium alloys are an interesting system as the alcalinization related to oxygen reduction is affecting the dissolution of aluminum.[66] Considering various experimental works conducted on a large scale of model electrodes representing tentatively the galvanic corrosion between IM and matrix on 2xxx aluminium alloys[58,20,67] it can be noticed that this multi-physics approach, i.e., coupling of galvanic interaction and

chemical change, has not been considered. This is probably due to the fact that with aluminium alloys steady state cannot be reached preventing any validation of the numerical simulation. A bimetallic system exhibiting a stationary galvanic coupling will be chosen in this chapter to illustrate the combined effects of ionic current distribution and the chemical gradients on the galvanic corrosion damage.

For modelling corrosion damages induced by galvanic process, numerical resolution can be based on various mathematical approaches: one of the most applied, especially for taking into account the coupling of current distribution with the mass transport control, is the finite element method. It exists now powerful general-purpose finite element packages with which one can construct a 1-D, 2-D or quasi 3-D models with capabilities that exceed those of home-made codes. This then allows corrosion specialists to concentrate on the much more difficult task of obtaining the consistent experimental boundary conditions and defining valid models of the polarization behaviour of the electrodes.

From a general point of view, in electrochemistry (in corrosion) modelling allows to solve the equations solving the current and potential distributions in the electrolyte coupled with the chemical processes occurring homogeneously (in the solution bulk: chemical reaction) or heterogeneously (i.e., at the electrode surface: electrochemical reaction). Fluxes of each chemical species are described by transport equations including diffusion, convection and migration components. In modelling of galvanic corrosion related to local electrochemical sites (precipitates, intermetallics, inclusions, defects in coating, etc.) local probe techniques described in the previous part can be used to obtain quantitative data on the interfacial reactions and current and or potential distribution.

Simulations of galvanic coupling have been mainly limited to resolution of the Laplace's equation[58,67,68] to define the electrostatic potential in the solution Φ. This electrostatic approach, largely spread for solving large scale galvanic coupling, can be generalized to all involved species by solving the general Nernst-Planck's equation as followed assuming as negligible the effect of convection on the concentration of involved species:[69,70]

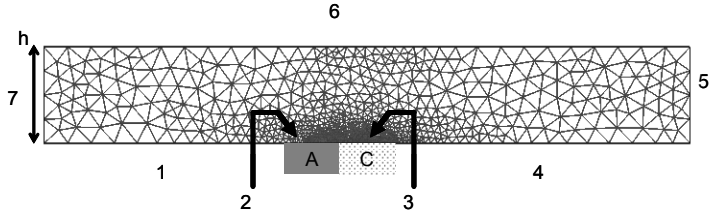

Figure 13. Typical FEM meshing for a galvanic cell (2D simulation).

$$D_i[\nabla^2 C_i + \frac{z_i F}{RT}\nabla(C_i \nabla\Phi)] + R_i = \frac{\partial C_i}{\partial t} \tag{11}$$

where C_i the concentration of species i inside the cell (mol.m^{-3}), D_i the diffusion coefficient of species i (for i = 1 ... n) (m^2/s), R the gas constant, T the temperature, F the Faraday number, z_i the charge of species i.

The term R_i for production/consumption depends on the homogeneous chemical reactions taken into account in the cell, and on the electrochemical reactions on the surface of the electrodes.

On the other hand, the electroneutrality is assumed everywhere in the cell

$$\sum_i z_i C_i = 0 \tag{12}$$

It is then necessary to set-up the boundary conditions which can be expressed as follows on the basis of indexes on Fig. 13 (assuming corrosion phenomena controlled by the oxygen reduction in neutral pH conditions):

- Boundaries 1, 4, 5, 7: electrical insulation for ionic current and oxygen flux.
- Boundaries 2 et 3: polarization behaviours which can be if possible described by the well-known Butler-Volmer relation or by empirical laws deduced from local probe techniques.
- Boundary 6: at the air/solution interface there is an insulating condition for the potential and an oxygen flux corre-

sponding to its dissolution rate in solution). The thickness h is an important parameter which is directly related to the nature of environmental conditions (corrosion in confined media, atmospheric corrosion, bulk electrolyte, etc.).

The meshing is always refined at the boundaries of both electrodes due to the localization of the current distributions and chemical perturbations.

The current distribution is obtained by solving the Laplace's equation if the concentration variations can be neglected and is called primary or secondary, depending on the nature of the boundary conditions on the electrodes.[71] It can be noticed that for solving Laplace's equation various numerical methods can be used, especially the boundary elements method (BEM) which has been largely promoted by the group of Brebbia.[72,73]

From an experimental point of view, various modelling approaches based on solution of Laplace's equation have been validated by measuring the profile of the induced damage which follows the anodic current profile. As shown in different works where the mass transport of species were controlled: galvanic coupling between pure aluminium and a Cu containing solid solution in a flowing electrolyte[68] or galvanic corrosion on two parts of a welded pipe made of stainless steel and low-alloy steel[74] (Fig. 14) is supported by the numerical modelling.

But it exist only few studies where the numerical simulation on well-defined bimetallic electrodes has been validated by in-situ current probe techniques: SVET for current distribution and/or pH probes for proton concentration. The work of Crowe et al.[58] already mentioned is probably one of the most advanced. The authors used FEM to fit SVET measurements above a galvanic iron-copper couple using polarization curves for each metal carried out in bulk solution.

Concerning the modelling of the corrosion damage itself, work of Oltra et al.[75] on bimetallic electrode obtained by casting of an aluminium Al-4% Cu alloy around a rectangular section bar of pure aluminium (AA 1199) tested in a 0.2 M NaCl + 0.3% H_20_2 solution in a specially designed corrosion cell can be mentioned. As shown in Fig. 15a, controlled electrolyte circulation was achieved using a peristaltic pump which allowed a sufficient renewal rate without causing hydrodynamic corrosion phenomena.

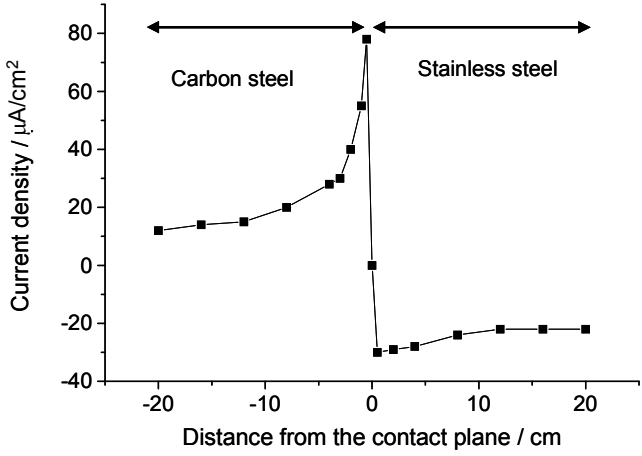

Figure 14. Current density distribution calculated from BEM modelling showing the localization of current densities at the interface between the anode (carbon steel) and the cathode (stainless steel). Reprinted with permission from *Corrosion*, **40** (1984) 628, Copyright © 1984, NACE

The renewal of liquid has been realized to avoid local chemistry problems and to evacuate corrosion products in order to model the corrosion damage solving the Laplace's equation by M-BEM method (Moving Boundary Elements Method). After exposure to the corrosive solution for periods of 6-72 hours the heterogeneous electrode was cleaned in an ultrasonic bath to remove the corrosion products from the surface of the sample.

The local attack was then characterized by laser profilometry and depth profiles have been compared with theoretical predictions obtained using M-BEM (Fig. 15b).

A good agreement was found between the numerical model and the evolution of the geometry of the junction between the anode (Al) and cathode (Al-4% Cu) as function of time.

One metallurgical way which can be chosen to explore a large range of size ratio between the anode and the cathode is to work on the cut-edge of coated metallic sheets. The coating can be performed for example by ion sputtering or hot metal dipping. In the following parts the modelling and validation of ionic current dis-

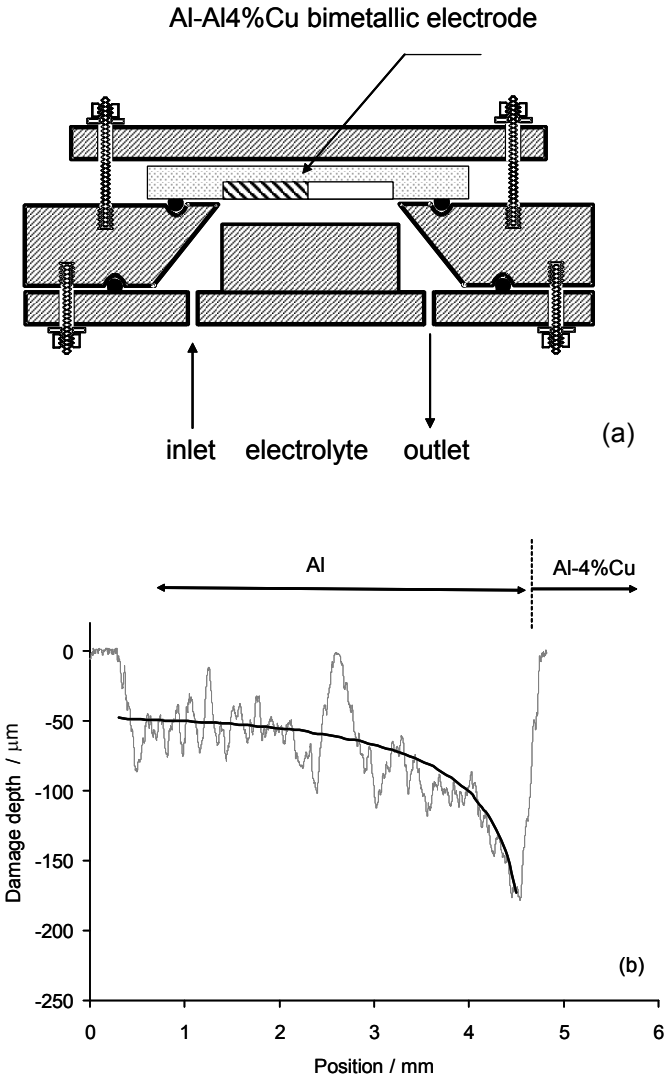

Figure 15. Galvanic corrosion experiments on a Al-Al%Cu model electrode. (a) Schematic view of the test cell consisting in a channel flow cell (gap = 1 mm). (b) Corrosion profile of the Al (anode)/Al-4% Cu (cathode) electrode obtained by laser profilometry after 48 h exposure in NaCl N/5 + 0.3% H_2O_2.

tribution will be illustrated on iron-zinc couple. After this, discussions will be focused on the transfer of such an approach on the galvanic behaviour which can be at the basis of the localized dissolution for a real microstructure.

In the following, application of the Nernst-Planck's equation will be described for such a system consisting in a cut-edge of galvanized steel. This example allows illustrating the role of concentration variations on the corrosion process itself and also on the in-situ probes limitations. Discussion on the use of in-situ electrochemical data for validating the results and for defining the entering data in the model will be proposed.

2. Resolution of the Nernst-Planck's Equation in the Case of a Bimetallic Couple of Well-Defined Geometry

This example described the behaviour of a galvanized low alloy carbon steel sheets. The galvanic corrosion between Fe (cathode) and Zn (anode) in contact with dilute NaCl solution (low conductivity media) is considered. Details of such an experiment has been widely described in literature.[59,76,77]

(*i*) *Set-Up of the Model*

The objective of the modelling is to describe the ionic current distribution which corresponds to the motion of charge carriers in solution through the flux of species by solving the Nernst-Planck's equation (the convection term can be neglected in a first approximation):

$$N_i = -D_i \nabla C_i - z_i \frac{D_i}{RT} F C_i \nabla \phi \tag{13}$$

The flux of a species is defined as the summation of a term of diffusion and a term of electromigration. The mass balance relation in a stationary mode for each species *i* is given by

$$-\nabla \cdot \left(-D_i \nabla C_i - z_i \frac{D_i}{RT} F C_i \nabla \phi \right) = R_i \tag{14}$$

where R_i is the production term of the species. Seven homogeneous chemical reactions have been considered. Their respective equilibrium constants are summarized in Table 1. In this example, considered species are Na^+, Cl^-, H^+, OH^-, O_2, Zn^{2+}, $ZnOH^+$, $Zn(OH)_{2(aq)}$, $ZnOH_3^-$, CO_2, HCO_3^-, CO_3^{2-}, $ZnCO_{3(aq)}$.

Finally, the electroneutrality condition,

$$\sum_i z_i C_i = 0 \tag{12}$$

which leads to the equation

$$\nabla \cdot \left(\sum_i - z_i F D_i \nabla C_i - z_i^2 \frac{D_i}{RT} F^2 C_i \nabla \phi \right) = 0 \tag{15}$$

completes the model in imposing an additional equation for variables.

Table 1
Listing of Homogeneous Chemical Reactions and their Respective Equilibrium Constants.

Homogeneous Chemical Reactions	Equilibrium Constant	Reference
$H^+ + OH^- \leftrightarrows H_2O$	10^{14}	
$Zn^{2+} + OH^- \leftrightarrows ZnOH^+$	$10^{5.04}$	[78]
$ZnOH^+ + OH^- \leftrightarrows Zn(OH)_{2(aq)}$	$10^{6.06}$	[8]
$Zn(OH)_{2(aq)} + OH^- \leftrightarrows Zn(OH)_3^-$	$10^{2.5}$	[78]
$CO_2 + OH^- \leftrightarrows HCO_3^-$	$10^{7.65}$	[79]
$HCO_3^- + OH^- \leftrightarrows CO_3^{2-} + H_2O$	$10^{3.67}$	[79]
$Zn^{2+} + CO_3^{2-} \leftrightarrows ZnCO_{3(aq)}$	$10^{5.3}$	[80]

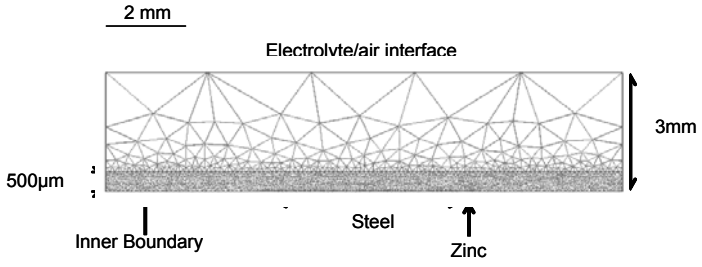

Figure 16. FEM meshing for the Nernst-Planck's model. Compared to Fig. 10 an interfacial domain has been introduced to mimic pseudo-diffusion layer, where both diffusion and migration of species are possible.

(*a*) *Model geometry*

Figure 16 shows the 2D-geometry and the corresponding meshing. The low alloy steel is in contact with a thin sheet of zinc, both surrounded by two walls corresponding to the mounting. The upper boundary is the air/solution where oxygen dissolution occurs. The cell domain is divided in two parts. One next to the electrodes surfaces behaves as a pseudo-diffusion layer, where both diffusion and migration of species are possible.

The other subdomain behaves as a bulk solution, where only migration exits inside, thanks to the specific boundary conditions imposed to the interior boundary. The position of this boundary at 500 µm above the electrodes surfaces has been estimated from the potential evolution measured by a pH sensor in the solution. This value is closed from the data proposed by Rosenfeld using a specific electrochemical cell.[78] Meshing is refined in the vicinity of the boundaries between the electrodes (steel and zinc where the highest fluctuations for variables are expected.

(*b*) *Heterogeneous reactions*

As shown in Fig. 17 electrochemical reactions on zinc and iron sheet are considered: the reduction of the oxygen by a four electrons transfer in one step, the oxidation of zinc and the oxidation of iron. Their respective rates are:

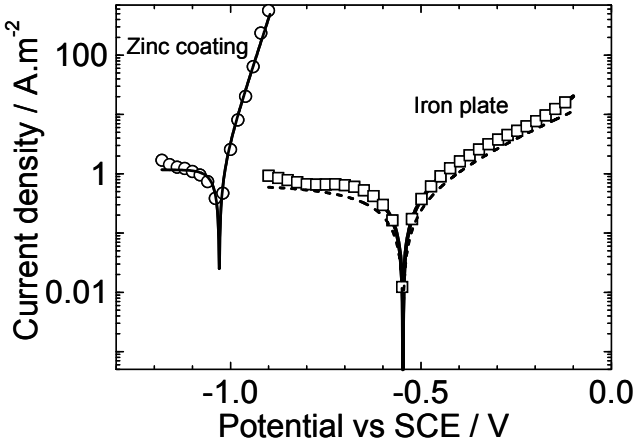

Figure 17. Polarization curves in 0.03 M NaCl of a (○) zinc and (□) steel electrodes. Corresponding calculated curves are also plotted (solid and dash curves).

$$J_{Zn} = 2Fk_{Zn} \exp\left(\frac{E - E^0_{Zn}}{a_{Zn}}\right) \tag{16}$$

$$J_{O_2} = -4Fk_{O_2} c_{O_2,s} \exp\left(-\frac{E - E^0_{O_2}}{b_{O_2}}\right) \tag{17}$$

$$J_{Fe} = 2Fk_{Fe} \exp\left(\frac{E - E^0_{Fe}}{a_{Fe}}\right) \tag{18}$$

where k_{O2}, k_{Zn} and k_{Fe} are interfacial rate constants; $E°_{O2}$, $E°_{Zn}$ and $E°_{Fe}$ are standard potentials and b_{O2}, a_{Zn} and a_{Fe} are Tafel parameters; and $C_{O2,s}$ is the activity of O_2. Data are indicated in Table 2. E, the local electrode potential, is defined as the difference of potential between the metal and the solution just outside the double layer (at the boundary). The values of the metal potentials for the

Table 2
Constants Used in the Model.

Constant name	Value	Reference
C_{bNa+}	0.03 mol/L	
C_{bCl-}	0.03 mol/L	
C_{bH+}	$10^{-5.6}$ mol/L	
C_{bOH-}	$10^{-8.4}$ mol/L	
C_{bO2}	0.26×10^{-3} mol/L	[82]
C_{bCO2}	1.31×10^{-5} mol/L	[83]
C_{bHCO3-}	2.33×10^{-6} mol/L	
C_{bCO32-}	4.3×10^{-11} mol/L	
C_{bZn2+}, Cb_{ZnOH+}, $C_{bZn(OH)2(aq)}$, $C_{bZn(OH)3-}$, $C_{bZnCO3(aq)}$	0 mol/L	
D_{Na+}	1.3×10^{-9} m²/s	[83]
D_{Cl-}	2×10^{-9} m²/s	[83]
D_{H+}	9.3×10^{-9} m²/s	[83]
D_{OH-}	5.3×10^{-9} m²/s	[83]
D_{O2}	2.4×10^{-9} m²/s	[83]
D_{Zn2+}	0.7×10^{-9} m²/s	[83]
D_{CO2}	1.91×10^{-9} m²/s	[83]
D_{HCO3-}	1.19×10^{-9} m²/s	[83]
D_{CO32-}	0.923×10^{-9} m²/s	[83]
D_{ZnOH+}, $D_{Zn(OH)2(aq)}$, $D_{Zn(OH)3-}$, $D_{ZnCO3(aq)}$	10^{-9} m²/s	Assumed
k_{O2}	10^{-5} m/s	
k_{Zn}	2.32×10^{-5} mol/m²/s	
k_{Fe}	1.45×10^{-6} mol/m²/s	
β_{O2}	0.05 V	[84]
α_{Zn}	0.022 V	
α_{Fe}	0.154 V	
N_{maxO2}	3.5×10^{-5} mol/m²/s	[85]

zinc and steel are supposed to be identical. For each reaction, a flux of species is associated to the current density in according to the Faraday's law.

(*c*) *Boundary conditions*

Heterogeneous kinetics expressions and associated species flux are the conditions for electrodes boundaries. Bulk concentrations for all species C_{bi} (see Table 2) are imposed at the inner

boundary with a condition of continuity for current. Those conditions permit to confine concentration gradients at proximity of electrodes boundaries and to force the transition between a current prevailed by diffusion to a current prevailed by migration.

(*d*) *Precipitation of solid phases*

Formation of five precipitates is considered in post-calculation in according to reactions:

$$Zn(OH)_{2(aq)} \leftrightarrows Zn(OH)_{2(S)} \quad (19)$$

$$Zn(OH)_{2(aq)} \leftrightarrows ZnO_{(S)} + 2\,H_2O \quad (20)$$

$$ZnCO_{3(aq)} \leftrightarrows ZnCO_{3(S)} \quad (21)$$

$$4\,Zn(OH)_{2(aq)} + Zn^{2+} + 2\,Cl^{-} \leftrightarrows Zn_5Cl_2(OH)_{8(S)} \quad (22)$$

$$3\,Zn(OH)_{2(aq)} + 2\,Zn^{2+} + 2\,CO_3^{2-} \leftrightarrows Zn_5(CO_3)_2(OH)_{6(S)} \quad (23)$$

Those precipitates are generally found in zinc corroded layers[79] and thermodynamic data are available. Domains of existence for those solid phases are areas where solution is supersaturated. Table 3 gives values of solubility products of the solid phases described above. Thanks to the use of a pseudo-diffusion layer an accurate stationary model is defined for chemical species concentration whereas precipitation is necessarily a non-stationary prob-

Table 3
Solubility Product of Precipitated Solid Phases.

Corrosion products	Solubility product, K_S	Reference
$Zn(OH)_{2(s)}$	$10^{-4.45}$	[78]
$ZnO_{(s)}$	$10^{-5.59}$	[78]
$ZnCO_{3(s)}$	$10^{-4.7}$	[80]
$Zn_5(OH)_8Cl_{2(s)}$	$10^{-29.1}$	[87]
$Zn_5(OH)_6(CO_3)_{2(s)}$	$10^{-41.01}$	[88]

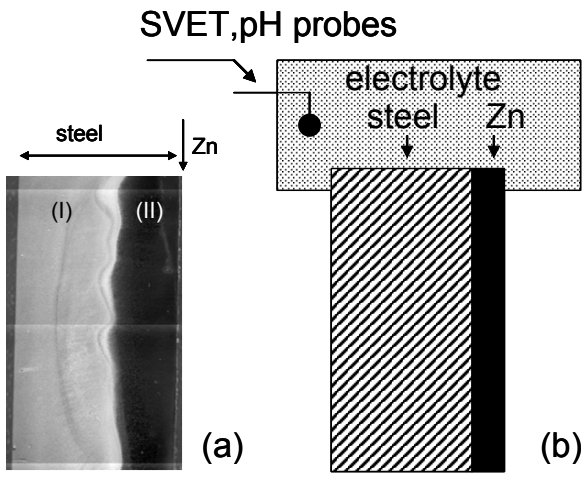

Figure 18. (a) In-situ image of the surface of the galvanic cell after 5 h of immersion in 0.03 M NaCl solution (top view), and (b) schematic view of the cut-edge (side view).

lem with accumulation of precipitates with time. Thus, a post-calculation procedure is used to simulate precipitation in the domain.

(*ii*) *Modelling Results*

(*a*) *Simulation of galvanic current distribution*

As heterogeneous and homogeneous reactions are taken into account some complex changes in the solution and at the surface of the electrodes can occur. It is why the basic modelling must be completed by the analysis of the corrosion feature.

In this example, after few minutes of immersion of the sample in the electrolyte, precipitation of mainly zinc dihydroxides occurs and settles on steel forming a white line almost parallel to the cut-edge length, as it can be seen in Fig. 18. Thereafter, these precipitates accumulate without changing in a considerable way theirs

distribution on the cut-edge. Between the line and the coating, there are almost no visible corrosion products. The steel electrode can be split in two zones: a zone beyond the line, where zinc based white precipitates are observed (mark I); and a zone close to the coating, where almost no white corrosion products are visible (mark II).

Consequently these phenomena must be integrated in the model. At this time of modelling set-up, it is difficult to ignore the current distribution analysis performed by SVET, which can be used here as an indirect entry data, as it allows to assume that the region II is a region where the cathodic reduction of oxygen is completely inhibited as shown in Fig. 18. It illustrates the importance of in-situ probe techniques to be used in close relation with the modelling. In the following, all the simulations have been performed assuming on a part of one of the electrode, the steel (i.e., the cathode), the reaction of the reduction of oxygen is inhibited by a surface oxide film.[80]

Normal ionic current profiles has been modelled on a galvanic couple using the Laplace's equation as it was proposed by Crowe and Kasper,[58] but without taking into account the effect of mass transport of species in solution. Considering the total current, i.e., migrative and diffusive components, a good fit is obtained between the experimental (Fig. 19a) and simulated (Fig. 20) profiles verifying the Nernst-Planck's equation (Eq. 13).

From an experimental point of view, the SVET measurements show it exits a stationary state of the galvanic cell itself. The motion of the solution is confined in the vicinity of the tip and limited in time (short scanning duration) and consequently the homogenous and heterogeneous reactions involved in the self-healing of the steel sheet considered in the Nernst-Planck's model are not disturbed.

(*b*) *Simulation of pH profiles*

Nernst-Planck's equation which accounts for the acido-basic equilibriums susceptible to occur in the solution allows to validate the experimental pH profile over the cut-edge. Figure 21 shows such an experimental profile performed 150 µm above the sample surface and the corresponding simulated profile with or without the cathodic inhibition on 1900 µm of steel.

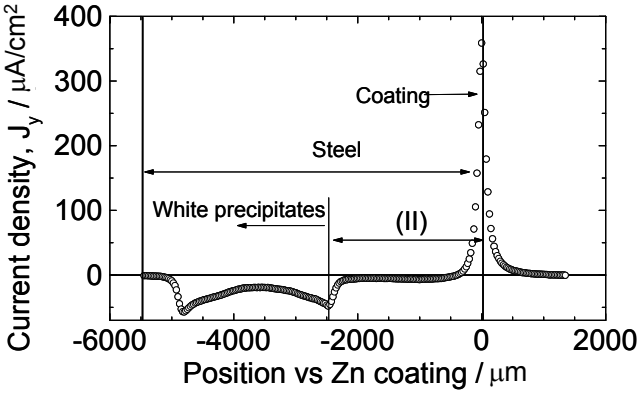

(a)

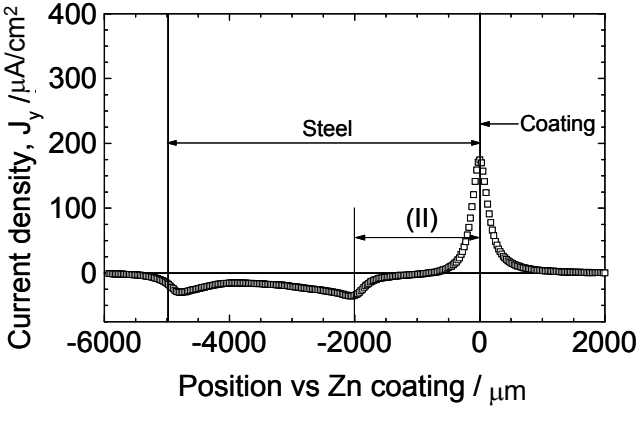

(b)

Figure 19. (a) Normal current density at 150 μm over the sample after 40 min of immersion in 0.03 M NaCl (SVET measurement), and (b) normal current density at 50 μm over the sample after 40 min of immersion in 0.03 M NaCl (SVET measurement).

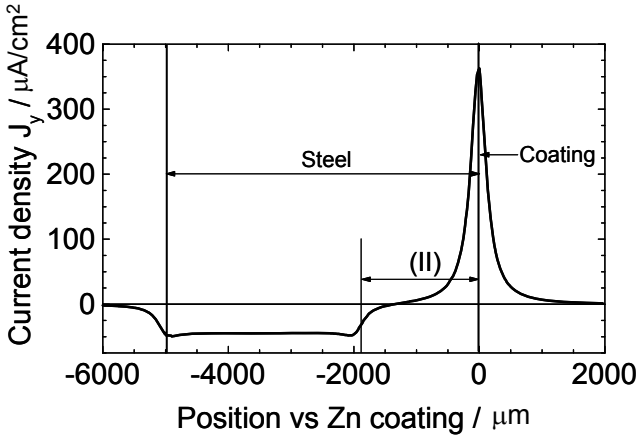

Figure 20. Simulated SVET profile (Solution of the Nernst-Planck equation). ORR is assumed to be inhibited on zone (II). The current density is the sum of the migrative and diffusive current densities.

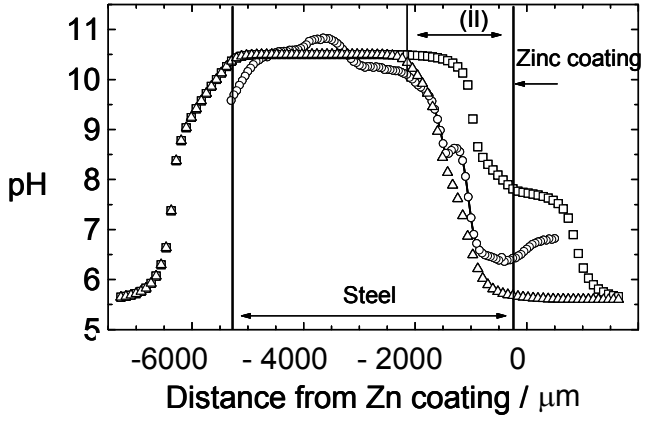

Figure 21. pH distribution at 150 μm above the cut-edge at 3 h of immersion in 0.03 M NaCl: (□) experimental data, (○) simulated distribution, (△) simulated distribution with oxygen reduction inhibition on a part of steel (size of area II is fixed to 1900 μm on steel).

It validates the necessary assumption in the definition of the geometry of the electrode boundaries: when a cathodic inhibition is assumed, simulated pH in solution above the coating and the inhibited area of steel is lower. Although SVET measurements give direct information on the surface reactivity and the cathodic inhibition on a part of steel, pH measurements need the numerical model to be interpreted in term of protective inhibition.

(*c*) *Simulation of interfacial chemical reactions induced by the galvanic coupling*

With the same numerical model, domains of stability of precipitated solid phases can be Domains of supersaturation are delimited by iso-lines corresponding to equality between reaction quotient and solubility product defined as the area where the solution is supersaturated (Fig. 22).

A comparison can be made with optical observations of the corrosion products distribution on cut-edge (see Fig. 18a) showing a good agreement. This kind of simulation also highlighted the contribution of CO_2 diffusion on the formation of carbonated species [81] which have been previously mentioned as important species in atmospheric corrosion of such metallic systems.[82]

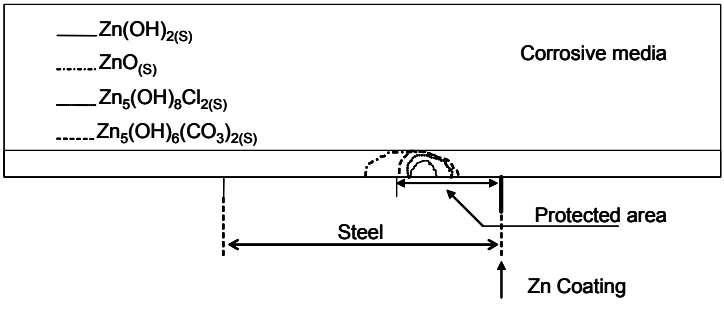

Figure 22. Thermodynamic domains of existence of precipitated solid phase.

3. Resolution of the Nernst-Planck's Equation in the Case of a Localized Galvanic Cell on a Real Microstructure

(*i*) *From Phenomenology to Model*

Compared to the previous example, galvanic coupling at the scale of the microstructure is not theoretically different as the same governing equations can be applied to model the corrosion behaviour. Nevertheless, only few modelling approach can be found in literature. It exits probably some difficulties in adapting numerical (mass-transport) models for simulating electrochemical reactions at the micrometer scale for local and selective corrosion. The works of Smyrl et al.[10,45,64] already mentioned are probably the most advanced in this domain. Modelling in relation with microstructure has been also performed to validate the microelectrochemical characterizations of pitting on MnS sulphide in stainless steels by Suter et al.[83] In this work a 1-dimensional mass transport model was applied to describe the corrosion in the vicinity of the inclusion-matrix interface where a local microcrevice crevice can be generated trapping aggressive chemical species. The results of the simulations confirmed that the pitting can be triggered by a critical solution chemistry mechanism due to sulphur species enrichment in a chloride environment in the confined media at the matrix-inclusion interface.

On the other hand the localized corrosion and more specially the role of galvanic coupling is largely discussed for aluminium alloys. In these alloys, microstructural corrosion e.g. pitting or intergranular corrosion (IGC) can be initiated at the interface between constituent intermetallic (IM) particles and the matrix. Most of the constituent particles contained in structural alloys have a simple cathodic behavior towards the matrix and support reduction. This reduction can be considered, in a simple way, as a four-electron process:

$$O_2 + 4\ e^- + 2\ H_2O \rightarrow 4\ OH^- \qquad (24)$$

The morphological characteristic of a simple cathodic IM/anodic matrix system after corrosion is the formation of a groove or trench around the almost unattacked particle due to the matrix dissolution. This has been shown on iron rich particles in

6XXX matrix[84,85,86,87] or on IM particles contained in 2024 (i.e., AlCuFeMn(Mg) or AlCu particles).[88,89,90]

In near-neutral, unbuffered, low-chloride solutions, it is supposed to be related to the destabilization of the oxide layer over the surrounding matrix due to local alcalinization.[99,91,6] It can be considered, according to the results of several authors,[92,93] that the driving force of the localized corrosion that occurs at the interface between constituent cathodic IM particles and the matrix of aluminium alloys is the galvanic coupling between the particles and the matrix. If a lot of experimental data obtained more and more by in-situ local probe techniques are available the question of application of general modelling remains an open question. Some models based on the resolution of second Fick's law for oxygen concentration allowed to illustrate the pH profile above and around a *cathodic* IM.[94,45]

In the work of Alodan and Smyrl,[45] the pH profiles over the particle were simulated by assuming a diffusion-controlled oxygen reduction reaction at the cathode and by setting a limiting diffusion current density of 0.1 mA cm^{-2}, calculated for a diffusion layer thickness of 20 μm and O_2 concentration of 0.26 mol m^{-3}.

Hydrolysis of Al into $AlOH_3$ at the anode was taken into account. The proton gradient at the anode is controlled by the oxygen reduction limit current density. For an initial pH equal to 7, the maximum pH was around 10 (Fig. 23a). In the studies,[90,45] modelling was based on the resolution of second Fick's law but the boundary current densities were set by experimental macroscopic passive dissolution current density measurements. No hydrolysis was considered at the anode. The pH profiles show that alcalinization up to pH = 9.5 is predicted for an initial pH of 6.

Even if the discussion on the role of alcalinization is always open, the question of the possible convolution of this pH profile with the effect of pH on dissolution of aluminium seems never asked even if surrounding trench around cathodic IM has been reported as shown in Fig. 24. It is obvious that the alkalinization clearly concerns the surrounding matrix and not only the IM (Fig. 23a), of which the size is fixed to 10 μm, whereas from the calculation the pH is higher than eight for a critical distance of about 25 micrometers which could correspond to the grooving observed sometimes.

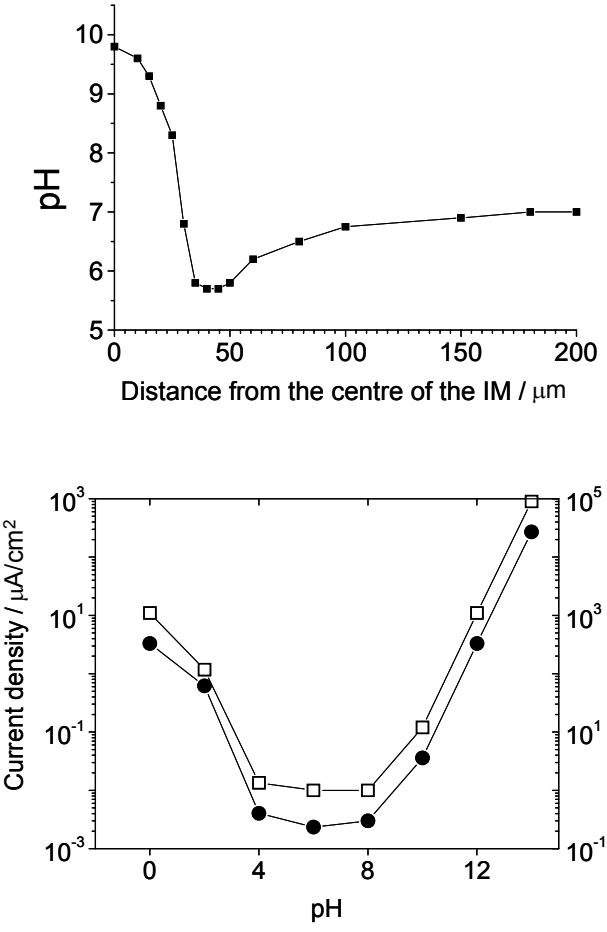

Figure 23. (a) pH profile along the plane in the radial direction and 1μm above from the centre of a disk (IM) of 10 μm in diameter for a bulk pH of 7. Reprinted with permission from *J. Electrochem. Soc*., **145** (1998) 1571, Copyright © 1998, The Electrochemical Society. (b) Influence of pH on the dissolution rate of pure aluminium. The curve is based on the mass loss rate measurement (circles) which has been converted in dissolution rate (squares) applying the Faraday's law assuming $Al \rightarrow Al^{3+} + 3\ e^-$. Reprinted with permission from *J. Electrochem. Soc.,* **105** (1958) 629, Copyright © 1958 The Electrochemical Society.

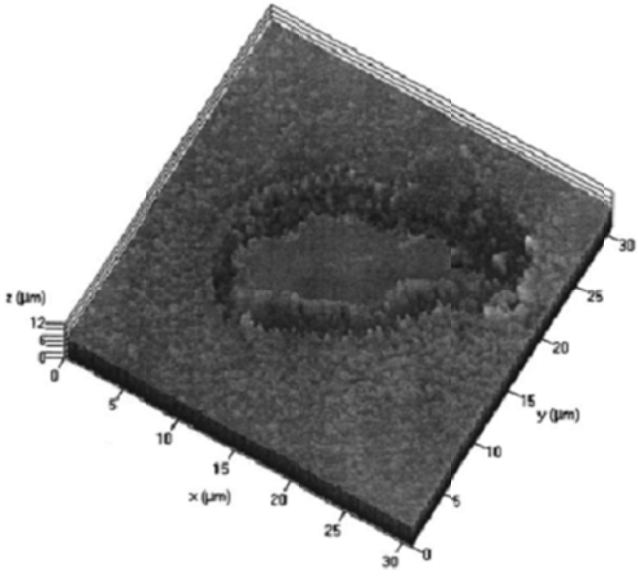

Figure 24. Example of trench formation observed by Confocal Scanning Microscopy. Trench formation is observed after 1 day immersion in pH 6 chloride containing solution. The depth of the trench was about 3 µm. Reprinted with permission from *J. Electrochem. Soc.*, **151** (2004) B465, Copyright © 2004 The Electrochemical Society.

(*ii*) *Set-Up of the Model*

Following the concept of *elementary galvanic cell* developed by Morris and Smyrl[10] it is nevertheless possible to define a *theoretical* galvanic cell consisting of a circular IM in contact with an aluminium matrix surrounded by an insulator as shown in Fig. 25. This configuration mimics a real microstructure as it can be seen in Fig. 26. Compared to the previous geometry (galvanized steel example), it illustrates the fact that simulation allows to focus on the more sensitive parameters. The geometry for the real system geometry must resemble an IM embedded in its matrix. Setting a symmetry axis (boundary 2), only the half of a *IM/matrix elementary cell* is considered. The size (length in 2D) of the cathodic IM is 10 µm (boundary 4), the anodic IM Matrix is 50 µm (boundary

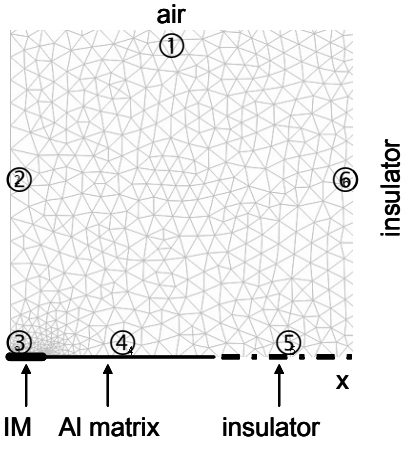

Figure 25. FEM meshing for simulation on a cathodic IM/anodic matrix system microstructure. Height of electrolyte : 0.1 mm ; cathodic IM at boundary 3 : 10 µm ; anodic alloy matrix at boundary 4 : 50 µm; resin at boundary 5 : 40 µm. Boundary 2 is a symmetry axis.

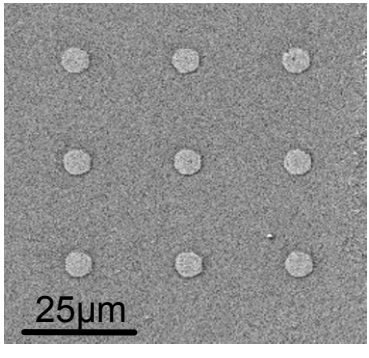

Figure 26. Arrays of Cu islands patterned using photolithography and deposited by electron beam evaporation (10 nm height) on a thin films of Al (200 nm) evaporated onto Si substrates. Reprinted with permission from *Journal of Metals*, **53** (2001) 34, Copyright © 2001 The Minerals, Metals & Materials Society (TMS), Warrendale.

5) and the resin is 40 μm (boundary 6). The thickness of electrolyte (boundaries 2 and 3) is 100 μm. The length of each boundary must be in the same order of magnitude so that the calculation can converge. The mesh is refined around the interface between the anode and the cathode and between the cathode and the symmetry axis.

This approach could also fit the experiments conducted by Missert et al.[95] To simplify the study of the galvanic corrosion between IM and aluminium matrix in Al-Cu alloys, N. Missert proposed to simulate the IM by copper islands evaporated on the surface of a pure aluminium substrate.[104]

It avoids considering the selective dissolution of the IM which in fact will lead to the increase in copper concentration: it explains the choice of the deposition of copper islands. The authors verified by fluorescence measurements with a confocal scanning laser microscope that pH is increasing above the individual copper islands. Unfortunately they did not observe local dissolution around Cu islands (Fig. 26) which could be used for validating the proposed simulation.

Comparing to the iron-zinc couple largely described in the previous part, there is not a large amount of data concerning the anodic reaction which will govern the dissolution rate of the aluminium matrix which is mainly related to:

$$Al \rightarrow Al^{3+} + 3e^{-} \qquad (25)$$

On the other hand, in the aluminium system, the most difficult is to express the relation between the interfacial and homogeneous reactions. It exists different ways for modelling the anodic dissolution of the aluminium matrix as follows.

As in Ref.[96] it can be considered that hydroxide ions are dissolving the oxide film, that is composed of, for the sake of simplicity, $Al(OH)_3$.

The dissolution reaction is :

$$Al(OH)_3 + OH^{-} \rightarrow Al(OH)_4^{-} \ (\text{or } AlO_2^{-} + 2\ H_2O) \qquad (26)$$

One mole of Al^{3+}, obtained by Al dissolution, is replacing one mole of dissolved $Al(OH)_3$.[99] Hence the overall reaction can be written as following :

$$Al + 4\ OH^- \rightarrow Al(OH)_4^- + 3\ e^- \quad (27)$$

Following the example of Alodan and Smyrl,[45] a hydrolysis reaction can be taken into account as follows:

$$Al + 3\ H_2O \rightarrow Al(OH)_3 + 3\ H^+ + 3\ e^- \quad (28)$$

Concerning the boundary conditions, the electrochemical polarizations could be defined theoretically from MEC measurements as illustrated in Fig. 27.

These MEC experiment were performed in absence of aeration control and it is difficult to define the cathodic reaction from this curve. Nevertheless the curve corresponding to the MAOI containing an IM particle confirms that the cathodic reaction is mainly distributed on the IM particle for such an aluminium alloy (6xxx). The IM particle represents 6 % of the capillary area and the cathodic current is more than 50 times higher, but does not exhibit a mass transfer control which is probably due to the non-controlled aeration of the capillary (see Fig. 6b).

Consequently, to simplify the choice of the boundary condition, for the IM it could be defined by imposing the oxygen concentration to zero at the surface of the IM and considering that the

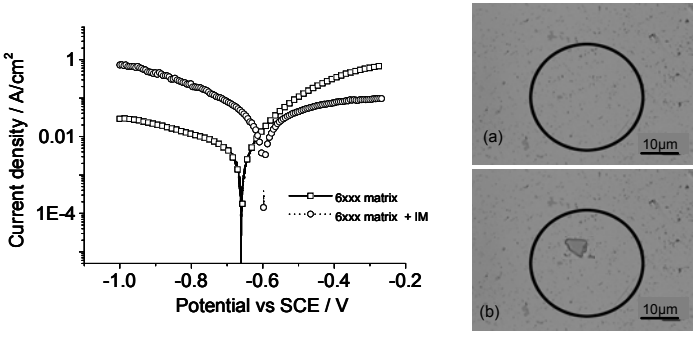

Figure 27. MEC experiment on a 6xxx aluminium alloy. Two MAOI are selected: representing the matrix (a) or a IM surrounded by a matrix (b). the surface ratio between the IM and the matrix is around 6%. The tip of the capillary was in the range of 30 µm. Polarization curves are represented on the left part highlighting the location of the cathodic reaction upon the IM. In this case the capillary was not under argon shielding (see Fig. 7a).

resulting dioxygen diffusion flow governs the cathodic current. Considering a bulk O_2 concentration of 0.26 mol m^{-3}, the condition $C_{O2} = 0$ is imposed as a boundary condition on the IM. The source of O_2 is the boundary called *air* at which is set an O_2 concentration equal to the bulk concentration.

The cathodic current density is proportional to the resulting diffusive O_2 flux:

$$j_C = 4\,F J_{O2} \tag{29}$$

and the OH^- flux is equal to $4J_{O2}$. Whereas the anodic current can be related to the electrochemical potential via a Butler-Volmer law for dissolution of the matrix using the anodic part of the MEC experiment for the matrix.

(*iii*) *Modelling Results*

Following this, it is possible to evaluate the balance between the damage related to the galvanic contribution estimated from the Faraday's law applied to the calculated surface current density distribution and the damage related to the dissolution related to the pH change relation.

The latter is directly defined through the pH profile which was found very close from the results obtained by Alodan and Smyrl[45] as shown in Fig. 28. It confirms that there is a critical distance larger than the radius of the IM for which the pH is above the threshold value for the aluminium dissolution.

To define the pH contribution to the total damage (Al dissolution), the dissolution depth associated with the pH is calculated from the radial pH distribution defined on Fig. 28 and by using the experimental law obtained by Pryor and Keir[66] already mentioned in Fig. 23. It gives the dissolution profiles presented in Fig. 29a. On the other hand the global current density distribution obtained by the Nernst-Planck's equation resolution, considering a mass transfer control of the galvanic coupling, can be used to estimate the damage applying the Faraday's law. As shown in Fig. 29b the galvanic contribution can be expressed in terms of an anodic dissolution depth.

Comparing the two contributions, it can be seen that the dissolution depth related to the pH is about 200 times less important

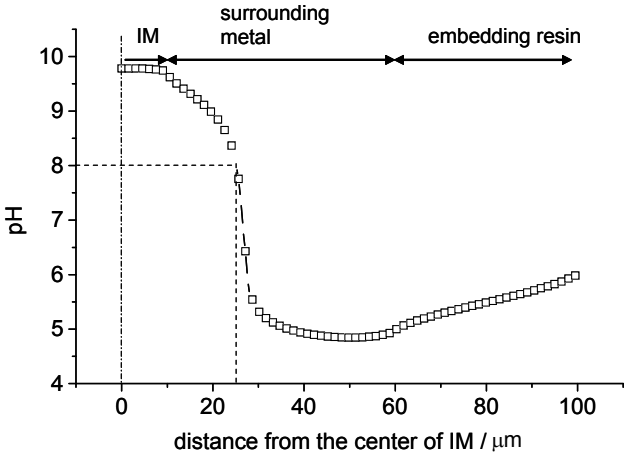

Figure 28. pH profile 1μm above the surface of the electrode calculated considering an oxygen diffusion limited cathodic reaction on the IM The hydrolysis reaction is considered to take place at the Al matrix. Axisymetrical FEM simulation (see Fig. 23).

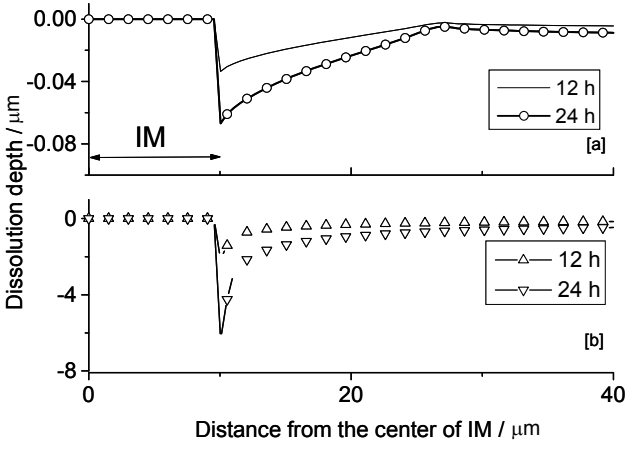

Figure 29. Calculation of the dissolution depth at the boundary between the IM particle and the Al matrix. (a) Damage related to the dissolution estimated by using mass loss versus pH change (see Fig. 23b) applied to the calculated pH distribution. (b) Damage related to the galvanic contribution estimated from Faraday's law applied to the calculated surface current density distribution.

than what the galvanic contribution. Indeed, dissolution depth obtained with the calculated current is equal, after 24 h to around 4 µm whereas for the same time the pH contribution is about 0.07 µm. Unfortunately, this result needs to be experimentally validated. Consequently the question of the role of alcalinization in localized corrosion processes at a *cathodic IM*/ Aluminium matrix interface remains an open question.

IV. CONCLUSIONS

In the first part of this chapter, experimental results illustrate how local probe techniques (SVET, microcapillary cell, pH probe) can be applied to quantify the corrosion on local electrochemical sites such precipitates, inclusions, intermetallics or defects on coated materials where galvanic coupling is the driving force.

In the second part, the purpose is focused on the application of numerical simulations for analysing galvanic coupling of localized corrosion sites. Discussions are proposed on the interest of simulations for validating the results of local probing and for predicting the localized corrosion behaviour (corrosion rate or corrosion protection). This second part confirms that modelling is important to clarify the complementary role of current and potential distribution and homogeneous and heterogeneous chemical processes occurring during localized corrosion. The modelling approach an especially the validation needs a careful design or control of the metallurgical microstructure.

ACKNOWLEDGEMENTS

The authors would like to thank the following PhD students: Philippe Bucaille, Florian Thebault and Nicolas Murer, for their contributions. This work was partly funded by ALCAN CRV, ARCELOR MITTAL. Furthermore this work was supported by the Agence Nationale de la Recherche (ANR 05-RMNP SICORAL) and the Conseil Régional de Bourgogne.

REFERENCES

[1] L. H. Hihara and R.M. Latanision, *International Materials Reviews*, **39** (1994) 245.
[2] C. Wagner, *J. Electrochem. Soc.*, **98** (1951)116; C. Wagner, *J. Electrochem. Soc*., **104** (1957) 129.
[3] J. T. Waber, *J. Electrochem. Soc*., **101** (1954) 271; J. T. Waber and M. Rosenbluth, *J. Electrochem. Soc*.,**102** (1955) 344; J. T. Waber, *J. Electrochem. Soc*.,**102** (1955) 420; J. T. Waber and B. Fagan, *J. Electrochem. Soc*., **103** (1956) 64; J. T. Waber, J. Mobrissey and J. Ruth , *J. Electrochem. Soc.,* **103** (1956) 138; J. T. Waber, *J. Electrochem. Soc*., **103** (1956) 567.
[4] R. C. Alkire and M. Verhoff, *Electrochim. Acta*, **43** (1998) 2733.
[5] B. Vuillemin, X. Philippe, R. Oltra, V. Vignal, L. Coudreuse, L. C. Dufour and E. Finot, *Corros. Sci*, **45** (2003) 1143.
[6] M. A. Alodan and W. H. Smyrl, *J. Electrochem. Soc*., **144** (1997) L282.
[7] K. Ogle, V. Baudu, L. Garrigues, X. Philippe, *J. Electrochem. Soc*., **147** (2000) 3654.
[8] H. N. McMurray, *Corrosion*, **57** (2001) 313.
[9] D. A. Worsley, J. Elvins and J. A. Spittle, in *Local Probe Techniques for Corrosion Research (EFC 45)*, Ed. by R. Oltra, V. Maurice, R. Akid, P. Marcus, Woodhead Publishing, (2007), p. 33.
[10] R. Morris and W. Smyrl, *J. Electrochem. Soc.*, **136** (1989) 3237.
[11] M. Nonnenmacher, M. P. O'Boyle, and H. K. Wickramasinghe, *Appl. Phys. Lett,* **58** (1991) 2921.
[12] Y. Rosenwaks, R. Shikler, Th. Glatzel and S. Sadewasser, *Physical Review B: Condensed Matter and Materials Physics*, **70** (2004) 085320/1.
[13] O. Vatel and M. Tanimoto, *J. Appl. Phys*., **77** (1995) 2358.
[14] P. Schmutz and G. S. Frankel, G. S., *J. Electrochem. Soc*., **145** (1998) 2285.
[15] B.S. Tanem, O. Lunder, O.Oe Knudsen, in *Local Probe Techniques for Corrosion Research (EFC 45)*, Ed. by R.Oltra, V. Maurice, R. Akid, P. Marcus, Woodhead Publishing, 2007, p. 99.
[16] L. Lacroix, L. Ressier, C. Blanc, G. Mankowski , *J. Electrochem. Soc*., **155** (2008) C8.
[17] F. Andreatta, A. Turco, I. De Graeve, H. Terryn, J. H. W. de Wit and L. Fedrizzi, *Surface and Coatings Technology*, **201** (2007) 7668.
[18] T. H. Muster and A. E. Hughes, *J. Electrochem. Soc*., **153** (2006) B474.
[19] M. Rohwerder and F. Turcu, *Electrochim. Acta*, **53** (2007) 290.
[20] C. D. S. Tuck, *Corr. Sci*., **23** (1983) 379.
[21] H. S. Isaacs, M.W. Kending, *Corrosion,* **36** (1980) 269.
[22] Boehni, H.; Suter, T.; Schreyer, A. *Electrochim. Acta*, **40** (1995) 1361.
[23] M. M Lohrengel, C. Rosenkranz, I. Kluppel, A. Moehring, H. Bettermann, B. Van den Bossche and J.Deconinck, *Electrochim. Act.,* **49** (2004), 2863.
[24] M. M. Lohrengel, *Electrochim. Acta*., **42** (1997) 3265.
[25] N. Birbilis, B. N. Padgett, R. G. Buchheit, *Electrochim. Acta*, **50** (2005) 3536.
[26] N. P. Revsbech, *Limnology and Oceanography,* **34** (1989) 474.
[27] R. Oltra, B. Vuillemin, F. Thebault, F. Rechou, *Electrochem. Comm.,* **10** (2008) 848.
[28] N. Birbilis and R. G. Buchheit, *J. Electrochem. Soc*, **155** (2008) C117.
[29] T. Suter and H. Bohni, *Electrochim. Acta*, **42** (1997) 3275.

[30] N. Birbilis and R. G. Buchheit, *J. Electrochem. Soc* , **152** (2005) B140.
[31] E. G. Webb, T. Suter and R. C. Alkire, *J. Electrochem. Soc*, **148** (2001) B186.
[32] N. Birbilis and R. G. Buchheit, *J. Electrochem. Soc*, **155** (2008) C117.
[33] A. J. Bard and M. V. Mirkin, *Scanning Electrochemical Microscopy*, New York, John Wiley & Sons, 2001.
[34] J. W. Still and D. O. Wipf, *J. Electrochem. Soc*., **144** (1997) 2657.
[35] C. H Paik, H. S. White and R. C. Alkire*, J. Electrochem. Soc*., **147** (2000) 4120.
[36] E. Tada, S. Satoh and H. Kaneko, *Electrochim. Acta* , **49** (2004) 2279.
[37] S. V. Lamaka, O. V. Karavai, A. C. Bastos, M. L. Zheludkevich, M. G. S. Ferreira, *Electrochem. Comm*., **10** (2008) 259.
[38] R. De Marco, *Anal. Chem*, **66** (1994) 3202.
[39] E. Klusmann and J. W. Schultze, *Electrochim. Acta*., **42** (1997) 3123.
[40] H. Ding and L. H. Hihara, *J. Electrochem. Soc*., **155** (2008) C226.
[41] K. T. Brown and D. G. Flaming, *Neuroseience*, **2** (1977) 813.
[42] J. O. Park, C. Paik, and R. C. Alkire, *J. Electrochem. Soc*., **143** (1996) L174.
[43] N. C. Rud, S. Cannan, E. Bitziou, I. Ciani, A. L. Whitwoth, P. Unwin, *Anal Chem*., **77** (2005) 6205.
[44] P. Pantano and David R. Walt, *Anal. Chem*, **67** (1995) 481A .
[45] M. A. Alodan and W. H. Smyrl, *J. Electrochem. Soc*., **145** (1998) 1571.
[46] M. Buchler, J. Kerimo, F. Guillaume, and W. H. Smyrl, *J. Electrochem. Soc.,* **147** (2000) 3691.
[47] S. Szunerits, D. R. Walt, *Anal. Chem*., **74** (2002) 886.
[48] H. S. Isaacs, G. Adzic and C.S. Jeffcoate, *Corrosion,* **56** (2000) 971.
[49] H. S. Isaacs, in *Localized Corrosion*, Eds. B.F. Brown, J. Krugerand R. W. Staehle, NACE , Houston, 1974, p.151.
[50] H. N McMurray, S. R Magill, B. D. Jeffs, *Ironmaking and Steelmaking*, **23** (1996) 183.
[51] R. Akid and D. J. Mills, *Corr. Sci*., **43** (2001) 1203.
[52] P. Doig ans P.E.J. Flewitt, *British Corrosion Journal*, **13** (1978) 118.
[53] E. McCafferty, *J. Electrochem. Soc*., 124 (1977) 1869.
[54] L. F. Jaffe and R. Nuccitelli, *Journal Cell. Bio.,* **63** (1974) 614.
[55] H. S. Isaacs, *Corr. Sci*., **28** (1988) 547.
[56] C. Scheffey, *Rev. Sci. Instrum*., **59** (1988) 787.
[57] B. Vuillemin, X. Philippe, R. Oltra, V. Vignal, L. Coudreuse, L. C. Dufour and E. Finot*, Corros. Sci,* **45** (2003) 1143.
[58] C. R. Crowe and R. G. Kasper, *J. Electrochem. Soc.*, **133** (1986) 879.
[59] K. Ogle, V. Baudu, L. Garrigues, and X. Philippe, *J. Electrochem. Soc.*, **147** (2000) 3654.
[60] P. Doig and P. E. J. Flewitt, *J. Electrochem. Soc*., **126** (1979) 2057.
[61] J. X. Jia, A. Atrens, G. Song, and T. H. Muster, *Materials and Corrosion*, **56** (2005) 468.
[62] S.Aoki, K. Kishimoto and M. Miyasaka, *Corrosion,* **44** (1988) 926.
[63] B. W. Cherry, M. Foo and T. H. Siauw, *Corrosion,* **42** (1986) 654.
[64] R. Morris and W. Smyrl, *AI Ch. E. Journal*, **34** (1988) 723.
[65] T. J. R. Leclere, A. J. Davenport and R. C. Newman, *Corrosion,* **63** (2007) 338.
[66] M. J. Pryor and D. S. Keir, *J. Electrochem. Soc.,* **105** (1958) 629.
[67] J. B. Jorcin, C. Blanc, N. Pebere, B. Tribollet, V. Vivier and J. Vincent, *J. Electrochem. Soc.*, **155** (2008) C46.
[68] P. Bucaille, R. Oltra and T. Warner, *Materials Science Forum*, **242** (1997) 207.

[69] A.J. Bard and L. R. Faulkner, *Electrochemical Methods*, John Wiley, New York, 2001.
[70] J. Newman and K. E. Tomas-Alyea, *Electrochemical Systems*, 3rd Edition, John Wiley & Sons, 2004.
[71] A. C. West, J. Newman, in *Modern Aspects of Electrochemistry No. 23*, Ed. by B.E. Conway, J. O'M. Bockris, and R. E. White, Plenum Press, New York, 1992, p.101.
[72] C. A. Brebbia, *The Boundary Element Method for Engineers*, Pentech Press, London, Plymouth, 1978.
[73] C. A. Brebbia, J. C. F. Telles and L. C. Wrobel, *Boundary Element Techniques: Theory and Applications in Engineering*, Springer-Verlag, Berlin Heildelberg New York-Tokyo, 1984.
[74] E. Bardal, R. Johnsen and P. O. Gartland, *Corrosion*, **40** (1984) 628.
[75] P. Bucaille, R. Oltra, T. Warner, *Materials Science Forum*, **242** (1997) 207.
[76] D. A. Worsley, S. M. Powell, H. N. McMurray, *Corrosion,* **56** (2000) 492.
[77] R. M. Souto, Y. Gonzalez-Garcia, A. C. Bastos, A. M. Simoes, *Corr. Sci*., **49** (2007) 4568.
[78] I. L. Rosenfel'd, in *Proceedings Intern. Congr. Metal, Corrosion, 1st, London Engl.* (1961), p.243 [from *J. Appl. Chem*. (London) **11** (1961) i-242].
[79] T. E. Graedel, *J. Electrochem. Soc.*, **136** (1989) 193.
[80] F. Thébault, B. Vuillemin, R. Oltra, K. Ogle and C. Allely, *Electrochim. Acta,* **53** (2008) 5226.
[81] F. Thebault, PhD, University of Burgundy, 2008.
[82] F. Zhu, X. Zhang, D. Persson, D. Thierry*, Electrochemical and Solid-State Letters*, **4** (2001) B19.
[83] E. G. Webb, T. Suter and R. C. Alkire, *J. Electrochem. Soc.*, **148** (2001) B186.
[84] M. Buchler, T. Watari and W. H. Smyrl, *Corros. Sci.*, **42** (2000). 1661.
[85] J. O. Park, C. H. Paik and R. C. Alkire, *J. Electrochem. Soc.*, **143** (1996) L175.
[86] J. O. Park, C. H. Paik, Y. H. Huang and R. C. Alkire, *J. Electrochem. Soc.*, **146** (1999) 517.
[87] R. M. Rynders, C. H. Paik, R. Ke and R. C. Alkire, *J. Electrochem. Soc.*, **141** (1994) 1439.
[88] M. Buchler, J. Kerimo, F. Guillaume and W. H. Smyrl, *J. Electrochem. Soc.*, **147** (2000) 3691.
[89] P. Leblanc and G. S. Frankel, *J. Electrochem. Soc.*, **149** (2002) B239.
[90] O. Schneider, G. O. Ilevbare, J. R. Scully and R. G. Kelly, *J. Electrochem. Soc.*, **151** (2004) B465.
[91] J. O. Park, C. H. Paik, Y. H. Huang and R. C. Alkire, *J. Electrochem. Soc.*, **146** (1999) 517.
[92] R G. Buchheit, R. P. Grant, P. F. Hlava, B. McKenzie and G. L. Zender, *J. Electrochem. Soc.*, **144** (1997) 2621.
[93] A. Garner and D. Tromans, *Corrosion,* **35** (1979) 55.
[94] O. Schneider, G. O. Ilevbare, J. R. Scully and R. G. Kelly, *J. Electrochem. Soc.*, **151** (2004) B465.
[95] N. Missert, J. C. Barbour, R. G. Copeland and J. E. Mikkalson, *Journal of Metals*, **53** (2001) 34.
[96] J. C. Seegmiller, R. C. Bazito and D. A. Buttry, *Electrochem. Solid State Lett.*, **7** (2004) B1.

4

Preparation of Hierarchical (Nano/Meso/Macro) Porous Structures Using Electrochemical Deposition

Heon-Cheol Shin[*] and Meilin Liu[**]

[*]School of Materials Science and Engineering, Pusan National University, Geumjeong-Gu, Busan, 609-735, Republic of KOREA
[**]Center for Innovative Fuel Cell and Battery Technologies, School of Materials Science and Engineering, Georgia Institute of Technology, Atlanta, GA, 30332-0245, USA

1. INTRODUCTION

Rapid advancements in electronic and telecommunication devices as well as increased concern on global warming have greatly intensified the demands for a new generation of energy storage and conversion devices. One of the grand challenges is how to create devices with energy and power densities far greater than those available today. The key to the successful creation of such a device depends critically on the development of new electrode materials with novel structures that dramatically enhance the charge and mass transfer along surfaces and across interfaces.

Conventional electrochemical energy storage and conversion devices are typically two-dimensional (2-D), a parallel arrangement of planar cathode and anode separated by an electrolyte. In this design, the improvement of energy density is often at the ex-

S.-I. Pyun and J.-W. Lee (eds.), *Progress in Corrosion Science and Engineering II*, Modern Aspects of Electrochemistry 47, DOI 10.1007/978-1-4419-5578-4_4,

pense of the power density. For a conventional battery, for example, as the thickness of the electrode is reduced, the power density increases due to the shortened distance of ionic transport, whereas the energy density falls because of reduced amount of active electrode materials and the increased fraction of other cell components (e.g., separator). Similarly, the power density of a conventional fuel cell is often limited by the electrode polarization resistance of the 2-D configuration, due primarily to the restricted reaction areas/sites and inefficient electrochemical reactions.

Nano-porous structures have attracted much attention in search for the next generation electrochemical energy storage and conversion devices because of their potential to achieve utmost power density without much sacrifice of energy density. Since batteries and fuel cells with nano-porous electrodes are exposed, respectively, to the electrolyte and the active gases in three dimensions, the volume of the active materials can take part in the reactions much more effectively, as compared to planar 2-D design. At the same time, proper design of porous structures for facile transport of active species might make it possible that the energy density is not traded for power density.

A number of studies have focused on the creation of nano-porous structures and their applications to electrochemical energy storage and conversion devices. These include a sol-gel derived, nano-structured aerogel/ambigel composed of a 3-D network of nano-scale particles,[1-4] a 3-D hierarchically-ordered macro-porous solid with the inverted opal structure created by a combination of sol-gel chemistry and templating,[5] an on-chip 3-D arrays based on microelectronics and microelectromechanical systems (MEMS) technology,[6,7] and non-woven fibers by electro-spinning process.[8] While progress is being made in creation of 3-D nano-porous electrodes with improved electrochemical properties,[2,5] many challenges still remain in preparation of new 3-D structures of desired composition and performance.

Hierarchical 3-D graded porous structures offer a possibility for developing batteries and fuel cells of high energy and power density.[9] The highly open structures, prepared by an electrochemical deposition of metal/alloy accompanied by vigorous gas evolution, contain nano-, meso-, and macro-pores with graded pore size, ideally suited for the high-rate operation of batteries and fuel cells. After the pioneering works by Shin and Liu on highly-porous elec-

tro-deposits of copper, tin, and copper-tin alloy,[9-11] many interesting studies (both fundamental and practical) based on this concept have been reported,[12-20] including a couple of successful applications of the copper foam structure to creation of other metals or composites for electrochemical devices.[15,16,18]

This chapter reviews some recent developments in fabrication of hierarchical 3-D porous structures by an electrochemical deposition process. In Section II, three typical porous structures are briefly discussed, together with their unique properties for application to electrochemical devices. Presented in Section III are the preparation of 3-D electrodeposits of metals and alloy with micro-/nano-hierarchical pores. In Section IV, the effect of electrolyte composition on porous structure is discussed. Finally, Section V is devoted to the applications of these porous structures as electrodes in fuel cells and batteries.

II. UNIQUE POROUS STRUCTURES FOR ELECTROCHEMICAL DEVICES

For lithium batteries, porous electrodes with interconnected open pores have several advantages. First, the internal pores can accommodate large volume changes associated with repeated cycling to minimize pulverization or disintegration of active materials during battery operation. Second, the relatively large surface area will reduce the resistance to interfacial reactions and thus accelerate electrode kinetics. Further, it will reduce the solid-sate diffusion length and thus reduce the resistance to enhance mass transport through the electrodes. The following three porous electrode structures are widely used for electrochemical applications.

1. Nano-Powder Based Porous Structures

Most of nano-structured materials are based on nano-sized particles of active materials. For lithium batteries, for example, a good electronic conductor (e.g., carbon) and binders are uniformly blended with nano-sized particles of active electrode materials to enhance the electronic conductivity and binding strength among the particles, respectively.

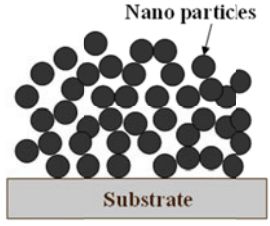

(a)

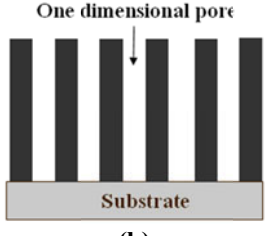

(b)

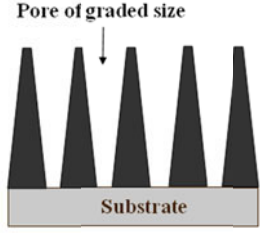

(c)

Figure 1. (a) Simplified porous structure comprising of nano-particles. (b) 1-D channeled porous structure. (c) Porous structure with a graded pore size.

Schematically shown in Fig. 1(a) is a simplified porous structure comprised of nano-particles. The electrode structure includes space to somewhat accommodate the volume change induced by

insertion (alloying)-extraction (de-alloying) of lithium during cycling, possibly suppressing the mechanical disintegration of active particles during operation. Furthermore, significantly-increased active surface area (or surface-to-volume ratio) may reduce the resistance to the interfacial reactions, minimizing electrode polarization.

However, the high performance of this porous electrode may be unsustainable because of the inherent instability of the structure. As soon as the active species around the nano-particles start to be exhausted, the overall electrode process is possibly limited by the transport of active species from the outside into the porous structure. Analogous to ion transport through a porous separator,[21] the *iR* loss ΔE_{iR} across the porous electrode can be expressed as follows:

$$\Delta E_{iR} = \frac{i T^2 L}{\sigma P A} \tag{1}$$

where i is the current transferred; T is the tortuosity; L is the thickness of the electrode; σ is the electrolyte conductivity; P is the porosity, and A represents the apparent (projected) area of the electrode. Equation (1) signifies the effect of structural tortuosity on the energy loss due to mass transfer across the porous structure. Clearly, to achieve high-rate performance, the tortuosity must be minimized.

2. One-Dimensional Porous Structures

The effect of tortuosity becomes insignificant in 1-D monolithic channeled structures, as schematically shown in Fig. 1(b). The straight path for ion transport in the electrolyte gives the fast and open channel for ionic conduction while 1-D bulk structure provides short and continuous pathways for electron transport. The rapid transport of electroactive species makes the overall process facile, leading to increased energy and power densities. Moreover, as far as the wall of the 1-D structure can be controlled to be thin enough, reaction-induced mechanical disintegration of the electrode can be suppressed and at the same time the extremely short

length (virtually, half of wall thickness) of solid-state diffusion accelerates whole energy conversion process.

Long and narrow 1-D nano-porous structures, however, result in large loss of the driving force for the reaction, as evident from Eq. (1). Accordingly, it is quite unlikely that the ionic species moves rapidly inside or out of the 1-D nano-porous structure with narrow and deep pores.[22] This is unfavorable for sustained high-rate operation of the electrochemical devices.

3. Porous Structures with Graded Pore Size

It is readily predicted by Eq. (1) that the transport of ionic species can be much improved when the structure has graded pores. Schematically shown in Fig. 1(c) is a simplified structure with a graded pore size. The graded porous structure with large pores around the orifice makes the reactants in the bulk electrolyte quite accessible to the porous structure and at the same time allows the products to move out of it.

In spite of the reduced volumetric energy density to some extent, as compared to nano-powder based or 1-D porous structure, the graded porous structure must be one of the promising architectures for high-rate and high-efficient operation of electrochemical devices. However, practical and cost-effective ways of fabricating the graded porous structures are yet to be developed for specific applications. The unique electrochemical methods to be presented in the subsequent Sections might open up a new possibility of creating the ideal porous structures needed.

III. PREPARATION OF THREE-DIMENSIONAL HIERARCHICAL POROUS ELECTRO-DEPOSITS

1. Fractals: Unique Porous Structures for Energy Applications

A Fractal is defined as any curve or surface that is independent of scale. If it is blown up, any portion of curve or surface appears identical to the whole curve or surface. The fractal character of the object is quantitatively expressed in terms of fractal dimension. The objects with fractional fractal dimension are frequently ob-

served in the universe, which indicates that the structural and other related properties are intermediate between the properties of the objects with integer dimension.[23-25]

Exemplified fractal structure found in the electro-deposits of metal is the ramified copper, the shape of which is analogous to a tree with a lot of branches.[26] Although highly-branched character of fractal electro-deposit of copper has a great possibility for high-power applications where the large surface area of active materials is favorable, copper fractal has a couple of critical issues to be overcome before its practical use. One originates from the ductility of copper. 3-D electro-deposits of fractal copper are readily formed on the metal substrate. But, the copper trunks and branches with low mechanical strength hardly support the weight of sub-branches or their shaking due to the convective force in the electrolyte, resulting in structural collapses and losing its original fractal structure. The other issue is the overgrowth of branches located inside the structure, reducing the internal pore volume and increasing the resistance to rapid transport of electroactive species through the porous structure.

Under the circumstances, fabrication of self-supported 3-D fractal structures with high porosity and good pore connectivity would be the starting point to utilize the extraordinary character of fractals. The structural integrity (i.e., self-standing structure) may be achieved by tuning the macroscopic structure consisting of numerous branches of copper. Further, overgrowth of branches within the porous structure must be suppressed to retain sufficient porosity for mass transport. These two critical issues will be discussed in the subsequent Section.

2. Formation Mechanism of Hierarchical Porous Structures with Graded Pore Size

Generally, gas evolution is deliberately suppressed during the electrochemical metal deposition process to enhance the qualities of deposits such as their compactness and adhesion to the substrate.[27,28] Thus, the potential for the creation of highly-porous structures by gas evolution during electrochemical deposition of metals has not attracted much attention.

When gas evolution takes place simultaneously with metal deposition, within the constraints of comparable reaction rates of

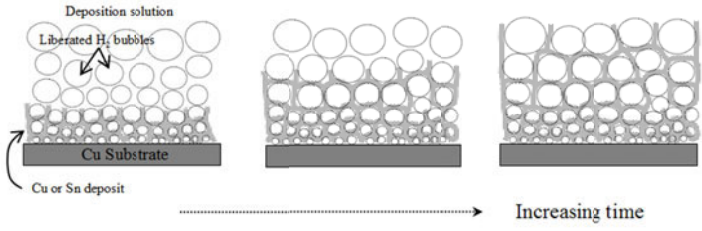

Figure 2. Simplified description of the formation mechanism of the foam with graded pore size and highly-porous walls. Reprinted from H.-C. Shin, J. Dong, and M. Liu, Nanoporous Structures Prepared by an Electrochemical Deposition Process, *Adv. Mater.* **15** (2003) 1610. Copyright (2003) with permission from Wiley-VCH Verlag GmbH & Co. KGaA.

two processes, gas bubble possibly acts as dynamic template of porous electro-deposits. Accordingly, metal deposition is prohibited at the place where there is a bubble and metal can grow only between gas bubbles. Furthermore, the coalescence of the generated bubble with time (or with ascending upward to the electrolyte/air interface) makes the pores of deposits larger with the distance away from the substrate. The resulting structure produced is a foam (or sponge) with graded pore size.[9]

It is important to note that the structures of the foam wall may not be dense, but quite complicated and porous in the case that the metal deposited has a particular growth habit. Copper and tin are two good examples. Their anomalous growth patterns during electro-deposition, which lead to ramified copper and dendritic tin, are frequently explained on the grounds of diffusion-limited aggregation[29] and surface relief phenomenon,[30] respectively. Shown in Fig. 2 is the simplified schematic description of the formation procedure of the graded foam structure with highly-porous walls.

Schematically shown in Fig. 3 is the experimental set-up for preparation of graded foam structures.[31] First, copper was used as the cathode in most of the experiments. Low hydrogen overvoltage of copper is beneficial to the energetic hydrogen evolution reaction in the course of copper deposition. The horizontal placement of copper substrate in the electrolyte bath ensures that the bubbles will move upward vertically upon formation on the surface. The anode is usually the same metal as that to be coated on the cathode. Platinum is sometimes used as the anode, especially

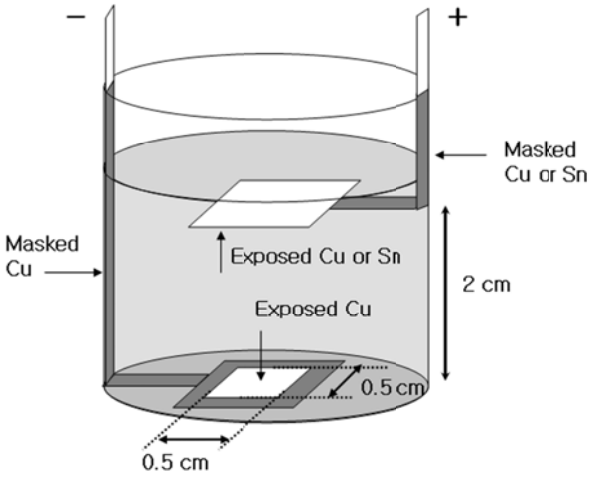

Figure 3. Cell configuration for the preparation of foam structure with graded pore size. Reprinted with permission from *Kor. J. Mater. Res.*, **18** (2008) 163. Copyright (2008) Materials Research Society of Korea.

when the amount of electro-deposit is so small that the change in concentration of metal ions in the electrolyte is relatively small during the deposition. The electrolyte contained metal ions and was acidic, allowing vigorous hydrogen evolution. Both potentiostatic and galvanostatic modes were used for electrochemical deposition. In both cases, the cathodic polarization (overpotential) during deposition was controlled to be 3 to 5 V.

3. Metals and Alloys with Hierarchical Porous Structures

(*i*) *3-D Copper and Tin Electro-Deposits*

Shown in Fig. 4 are some typical copper electro-deposits created by the competitive process of copper deposition and hydrogen evolution under the application of a cathodic current density of 3 A cm^{-2} in the electrolyte solution of 1 M sulfuric acid + 0.5 M copper sulfate. The resulting electro-deposits are characterized

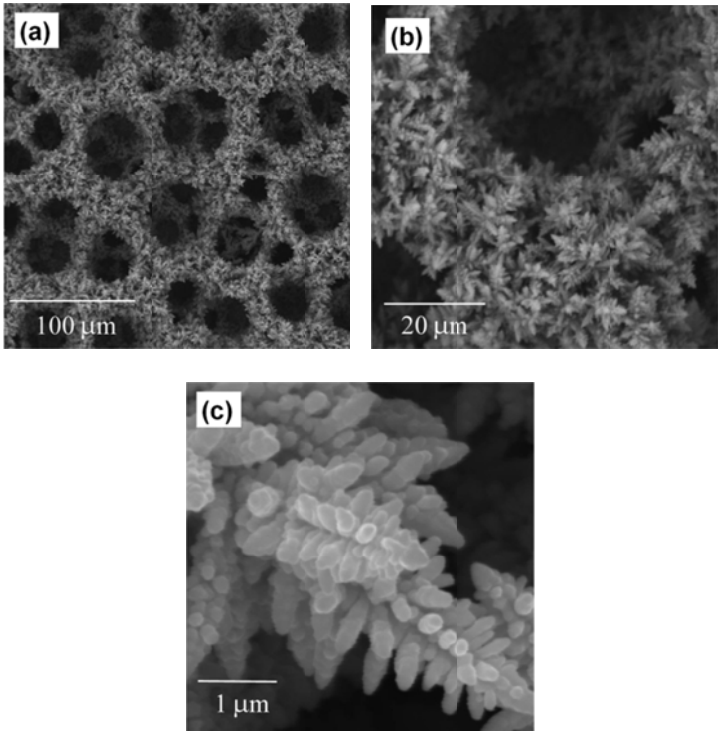

Figure 4. 3-D copper electro-deposits with graded pore size. Reprinted from H.-C. Shin, J. Dong, and M. Liu, Nanoporous Structures Prepared by an Electrochemical Deposition Process, *Adv. Mater.* **15** (2003) 1610. Copyright (2003) with permission from Wiley-VCH Verlag GmbH & Co. KGaA.

by foam structures with micro-sized pores. It is noted that the porous structures sculptured by gas evolution have graded pores; the pore size increases with the distance away from the substrate due to the coalescence of the evolved hydrogen gas. Additionally, the foam walls consist of a number of ramified coppers of the feature size of hundreds nanometers.

The created foam structure retains its integrity during the deposition and the subsequent processes such as drying and structural characterization. The mechanical stability is indebted to the highly cross-linked feature of the ramified coppers. 3-D networked cop-

per branches in all directions throughout the walls lead to a mechanically well-supported structure.

It is important to note that very few large branches are observed throughout the structure, as evident from a cross-sectional view shown in Fig. 5. The absence of over-grown large branches could be explained as follows:

(a) Energetically-moving hydrogen gas retards the conventional iterative branching process. Instead, it induces the continuous activation of new nucleation sites on the copper deposits, resulting in unit copper bundle comprising a couple of branches at most.
(b) There is a virtual depletion of copper ion deep inside the structure due to the difficulty in ion transport through it during vigorous gas evolution, significantly suppressing the growth of internal branches.

Since tin is apt to grow dendritically during the electrochemical deposition, tin electro-deposit is very likely to have a porous wall similar to 3-D copper. Shown in Fig. 6 are some typical tin electro-deposits at a cathodic current density of 3 A cm^{-2} in the electrolyte solution of 1 M sulfuric acid + 0.15 M tin sulfate. The overall foam structure is nearly identical to that of copper.

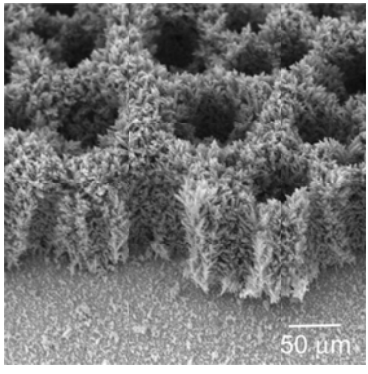

Figure 5. Cross-sectional view of the copper electro-deposits. Reprinted with permission from *Chem. Mater.*, **16** (2004) 5460. Copyright (2004) with permission from American Chemical Society.

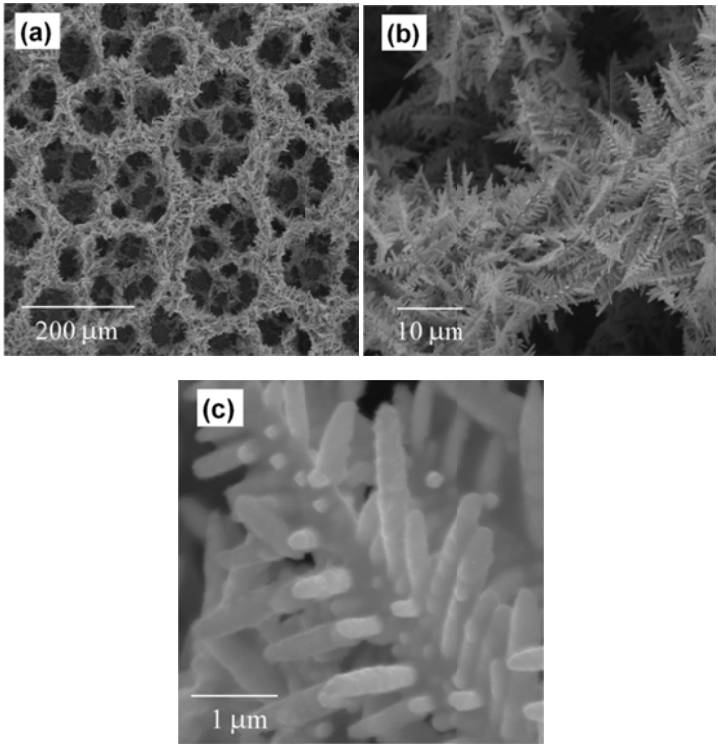

Figure 6. 3-D tin electro-deposits with graded pore size. Reprinted from H.-C. Shin, J. Dong, and M. Liu, Nanoporous Structures Prepared by an Electrochemical Deposition Process, *Adv. Mater.* **15** (2003) 1610. Copyright (2003) with permission from Wiley-VCH Verlag GmbH & Co. KGaA.

Nevertheless, there are following two subtle differences between copper and tin electro-deposits.

One is the porous structure of foam wall. The wall of copper electro-deposits includes a number of small pores between branches, as seen in Fig. 4(b), whereas that of tin electro-deposits shows little pores inside, as seen in Fig. 6(b). As discussed earlier, hydrogen gas plays a critical role, as a dynamic template, in forming porous structure. In the course of copper deposition, hydrogen gas

is liberated on both copper substrate and branches newly-created. It is conceivable that hydrogen gas generated on the substrate is responsible for the large pores of tens of micrometers, which make the overall 3-D foam structure, while hydrogen gas evolved on the electro-deposits creates small pores of about a few micrometers or less inside the foam wall. In contrast, during tin deposition, hydrogen gas is liable to evolve only on copper substrate due to the large hydrogen over-voltage of tin.[32] This makes the foam wall of tin much denser than that of copper.

The other difference between copper and tin electro-deposits is their microstructure. From the transmission electron microscope analyses,[9] it proved that the branches of copper are a polycrystalline structure, including a lot of nano-sized pores inside them, whereas the branches of tin are a single crystal without internal pores and grain boundaries. The polycrystallinity of copper branch is attributed to

(a) the oscillatory character in the nucleation kinetics,[33] and
(b) hydrogen-bubble-induced turbulence around growing copper tips.[9] And, its inner nano-sized pores are likely to originate from the hydrogen gas that is nucleated and adsorbed on freshly-formed copper deposits.

Copper and tin electro-deposits with foam structure can be readily created on any shape of a conductive surface. Shown in Fig. 7 is a typical tin electro-deposit on a copper wire, developed

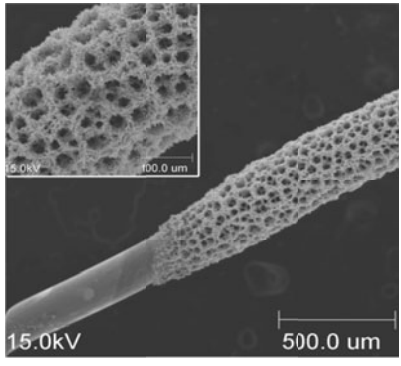

Figure 7. Tin foam structure on a copper wire.

by applying constant voltage of 5 V. Well-defined foam structure with a porous wall was formed throughout the wire length, indicating the flexibility of the surface shape of substrate for creating foam structures.

(*ii*) *3-D Electro-Deposits of Cu-Sn Alloy*

Since copper and tin electro-deposits have similar microscopic features, it would be interesting to explore the structure of electro-deposits of copper-tin alloys. Here, adjusting the ratio of copper to tin ions in the electrolyte solution to get a required stoichiometry may be essential. Fortunately, the fact that large cathodic polarization makes the electrode potential far away from the reduction potential of deposited metal, gives a useful clue for preparing stoichiometric Cu-Sn alloy: the atomic ratio of the metals in the deposits is virtually the same as the ratio of the metal ions in the electrolyte solution. This is supported by the experimental finding that the coulometric efficiency of the deposition was only about 35 %, irrespective of copper and tin, indicating that the deposition rates of copper and tin are comparable during the foam formation process.

Shown in Fig. 8 is a typical copper-tin foam structure prepared in an electrolyte of 1.5 M sulfuric acid containing 0.24 M copper sulfate and 0.20 M tin sulfate. The electro-deposit is characterized by typical foam structure like copper and tin. Moreover, the foam wall is highly-porous and full of numerous small grains. Pores of less than a few microns in foam wall are possibly caused by the hydrogen gas evolution on newly-developed copper-tin deposits, similar to the case of copper deposition. The atomic ratio of copper to tin of the deposit was estimated to be 1.18 using energy-dispersive X-ray spectroscopy and the X-ray diffraction analysis showed the deposit was η'-Cu_6Sn_5, a low-temperature variation of Cu_6Sn_5.[11]

The grain shape of the deposits is particularly noteworthy. Both the ramified character of copper branches and dendritic feature of tin branches totally disappear. Instead, the wall contains spherical grains of the order of hundreds of nanometers. This indicates the growth habit of the deposits is drastically modified when copper and tin are electrochemically co-deposited. Copper-tin alloy is a promising option to substitute the graphite for negative

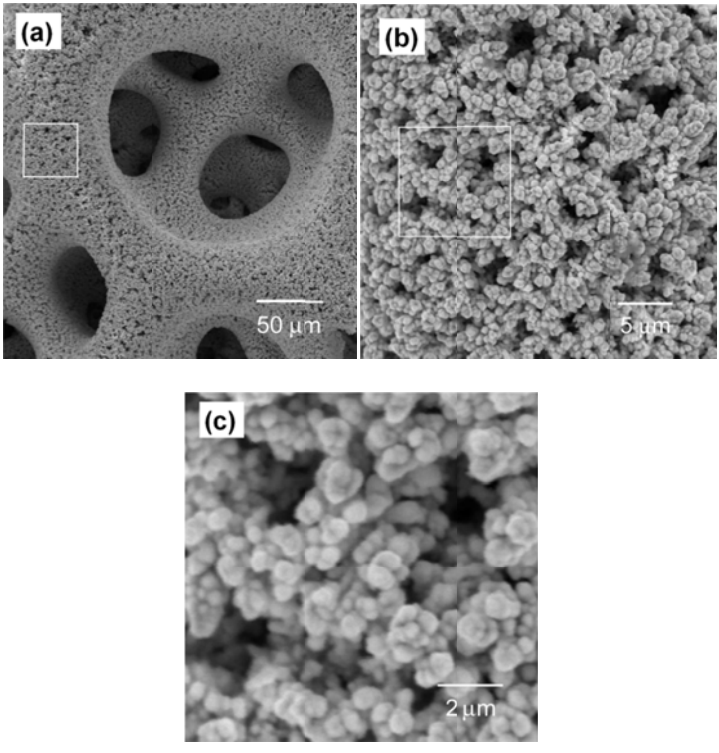

Figure 8. 3-D copper-tin electro-deposits with graded pore size. Reproduced from H.-C. Shin and M. Liu, Three-Dimensional Porous Copper-Tin Alloy Electrodes for Rechargeable Lithium Batteries, *Adv. Funct. Mater.* **15** (2005) 582. Copyright (2005) with permission from Wiley-VCH Verlag GmbH & Co. KGaA.

electrode in lithium ion batteries, due primarily to its high specific capacity.[34-37] In addition, foam structure of the copper-tin alloy is quite beneficial to improve the power density, which depends critically on the mass transport of electroactive species through the porous electrodes and on the area of electrochemically-active electrode surface.[11]

IV. CONTROL OF PORE SIZE AND WALL STRUCTURE OF COPPER HIERARCHICAL POROUS ELECTRO-DEPOSITS

1. Change in the Content of Copper or Tin Ions

It is natural to start with different concentrations of copper or tin ions in the electrolyte solution to modify the foam structure, because the content of metal ions affects the rate of alloy deposition. Figure 9 shows the morphology of copper electro-deposits as a function of the content of copper sulfate. 3-D foam structure was evident at 0.1 to 1.0 M of copper sulfate. The pore size at the surface of the deposits increased with copper sulfate content while the

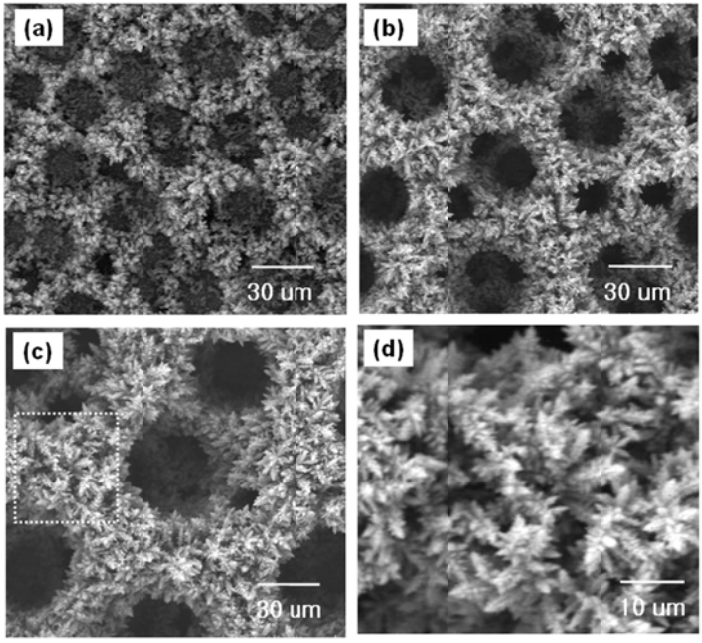

Figure 9. Morphology of copper electro-deposits created at the copper sulfate of (a) 0.1 M, (b) 0.5 M, and (c) 1.0 M. (d) represents the magnified image of the square dot in (c). Reprinted with permission from *Kor. J. Mater. Res.*, **18** (2008) 163. Copyright (2008) Materials Research Society of Korea.

ramified feature of the foam wall remained relatively constant. This strongly indicates that the content of copper ions in the electrolyte doesn't affect the foam structure itself, but changes its formation rate.[10,31]

It is noted that the copper substrate was seen through the structure formed at 0.1 M copper sulfate. This implies the structure consists of one or two pore layers at most and the concentration of copper sulfate is very close to the minimum for the foam creation. On the other hand, there is no sign of the deviation of the electro-deposit from typical foam structure even at 1.0 M copper sulfate, implying that well-defined copper foam structures can be prepared very quickly using concentrated copper sulfate solutions.

Unlike copper electro-deposits, morphological change of tin electro-deposits with the tin sulfate content is quite visible. Figure 10 tells us that the 3-D foam structure was barely developed at the very low content of tin sulfate (0.1 M). The foam structure starts to form in a 0.5 M tin sulfate solution and the structure formed in a 1.0 M solution is characterized by relatively dense foam wall as compared to that prepared in a 0.5 M solution. This means the concentration of tin sulfate in the solution critically influences the foam structure and the details of the wall. Under the experimental conditions studied in this work, well-defined 3-D tin foam structure was formed in solutions with tin sulfate concentrations between 0.1 and 1.0 M.[31]

The effect of metal ion concentration on foam formation behavior for copper and tin can be understood from the larger hydrogen over-voltage of tin than that of copper. As explained in the previous section, there is no virtual hydrogen evolution on the tin electro-deposits. Keeping in mind that hydrogen bubble liberated from the copper electro-deposits passes between the copper deposits and their branches, and thus makes the foam wall highly-porous, the absence of hydrogen evolution on tin deposits is not desirable to form porous walls. It might reduce the porosity of foam wall and at the same time let the internal tin branches overgrow *esp.* in solutions with high concentration of tin sulfate.

It is still not clear why 3-D tin foam structures are difficult to form in solutions with low concentration of tin sulfate, as compared to 3-D copper foam structures. Nevertheless, micrographs shown in Figs. 9(a) and 10(a) reveals that the bundles of copper branches are much smaller than those of tin branches at low con

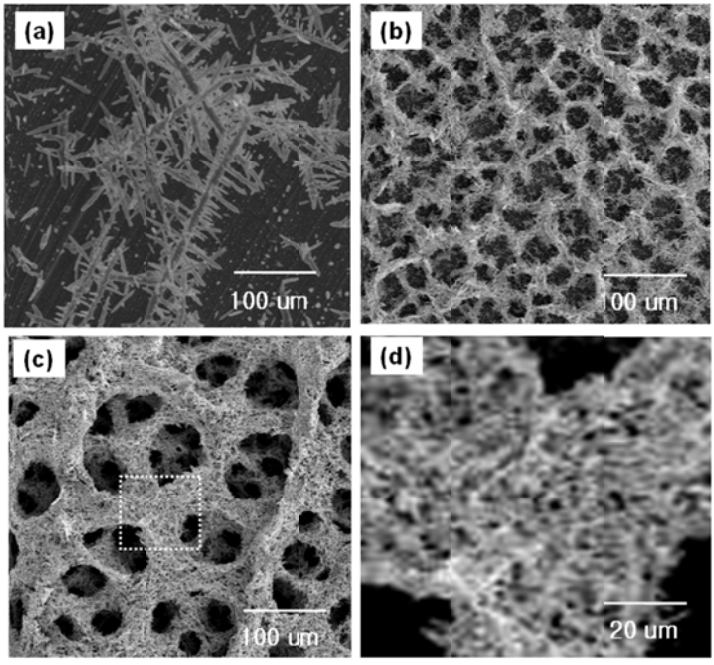

Figure 10. Morphology of tin electro-deposits created at the tin sulfate of (a) 0.1 M, (b) 0.5 M, and (c) 1.0 M. (d) represents the magnified image of the square dot in (c). Reprinted with permission from *Kor. J. Mater. Res.*, **18** (2008) 163. Copyright (2008) Materials Research Society of Korea.

centrations of metal sulfate, suggesting that the nucleation of new copper branches is kinetically much easier than that of tin, leading to much finer bundles of copper branches that enable to effectively form the 3-D network structures. In contrast, in the case of tin, the driving force is mainly consumed on the growth of the existing tin branches, not on nucleation. Further study is needed to investigate into the details of the nucleation and growth kinetics of 3-D network structures.

2. Control of the Pore Size of 3-D Foam Structure

As seen from the mechanism of foam formation illustrated in Fig. 2, the details of the foam structures are critically influenced by the bubble size of the liberated hydrogen. In particular, the coalescence kinetics of hydrogen bubbles is of significant importance since the variation of bubble size during metal deposition process determines the pore size distribution inside the foam. The coalescence of bubble is known to be driven by the hydrophobic force of bubbles.[38,39] When this force is sufficient to overcome the hydrodynamic repulsive force needed to expel water molecules between two bubbles, bubbles start to approach each other and are eventually combined. Accordingly, controlling the hydrophobic force is a key to achieving the control of bubble coalescence and hence the pore size and distribution of the foam structures.

Researchers on the bubble dynamics have suggested that the inhibition of bubble coalescence in aqueous solutions can be realized by the addition of specific additives that affect the water structure and hence the hydrophobicity of bubbles.[38-42] Among the possible additives, acetic acid is known to be a strong bubble-stabilizer.[38,39] Further, it doesn't introduce any metal ions that could be co-deposited as impurity to the copper deposits. Figure 11 shows the effect of acetic acid on the pore size of the foam. The size of surface pores created in the solution containing 0.1 M acetic acid, as shown in Fig. 11(b), was about half of the size of the pores created in the same solution without acetic acid, as shown in Fig. 11(a). This indicates that coalescence of hydrogen bubbles are effectively suppressed by the addition of acetic acid. However, it is noted that the foam layer was about 20 % thinner with the addition of 0.1 M acetic acid, implying that the overall deposition rate may be somewhat suppressed as well.

Shown in Fig. 12 are the morphological changes in copper foam structures with the content of acetic acid. It is noted that the local abnormal growth of foam wall is clearly seen at the acetic acid content more than 0.1 M, as shown in the dotted circles of Fig. 12(a)-(c). In order to further investigate the overgrowth, copper was electro-deposited for 90 s at 0.2 M acetic acid (Fig. 13). Overgrown foam wall is much thicker than the normal ones and its apparent porosity becomes significantly reduced. Also, it is noticeable that 3-D foam structure is hardly developed when the content

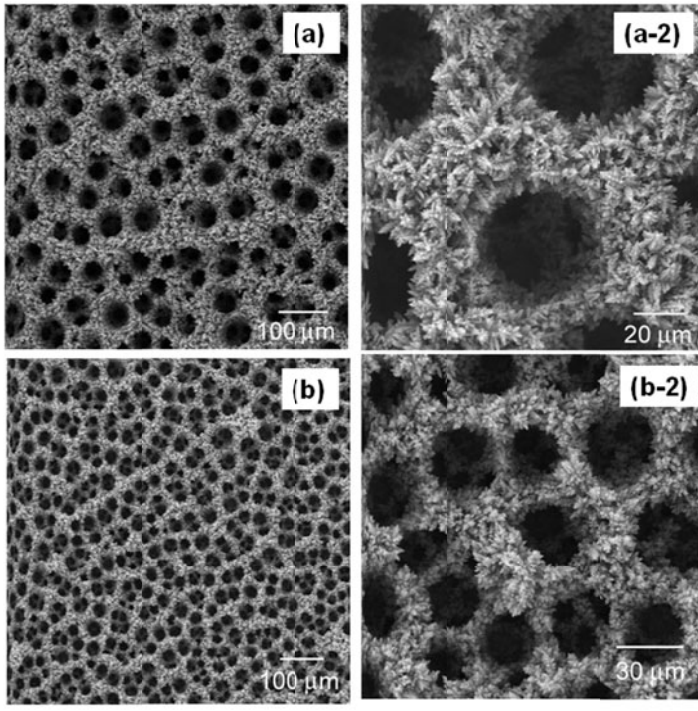

Figure 11. SEM images of 3-D copper electro-deposits created in (a) 0.4 M $CuSO_4$ + 1.5 M H_2SO_4 and (b) 0.4 M $CuSO_4$ + 1.5 M H_2SO_4 + 0.1 M CH_3COOH. (a-2) and (b-2) are the magnified images of (a) and (b), respectively. Reprinted with permission from *Chem. Mater.*, **16** (2004) 5460. Copyright (2004) American Chemical Society.

of acetic acid is more than 0.2 M. Figures 12 (c) and (d) show clearly the resulting discontinuity in network structure. These results imply the concentrated acetic acid lowers the rate of copper deposition and at the same time leads to local over-growth of copper branches, which seriously disrupt the uniformity of foam structure.[31]

The origin of the abnormal over-growth and discontinuity in network structure is yet to be determined. Nevertheless, one of the plausible reasons is the disturbance of the equi-potential surface

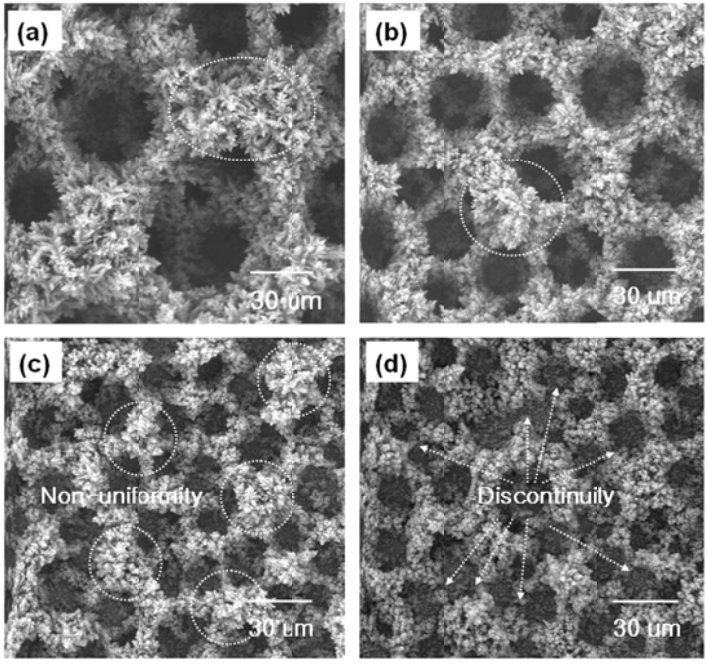

Figure 12. Morphology of copper electro-deposits created in the electrolyte containing (a) 0.05 M, (b) 0.1 M, (c) 0.2 M, and (d) 1.0 M acetic acid. Reprinted with permission from *Kor. J. Mater. Res.*, **18** (2008) 163. Copyright (2008) Materials Research Society of Korea.

and current density distribution during metal deposition by acetic acid.[43] Based on the previous works about the adsorption/desorption of acetic acid on metal surface,[44-46] it is speculated that the acetic acid decreases the electrochemical activity of metal and then slows down the rate of metal deposition. In addition, the energetic movement of hydrogen bubbles and the resulting forced convection of the electrolyte possibly lead to local deficiency in (adsorbed) acetic acid. Thus, discontinuity in network structure occurs in the area with high content of acetic acid and over-grown

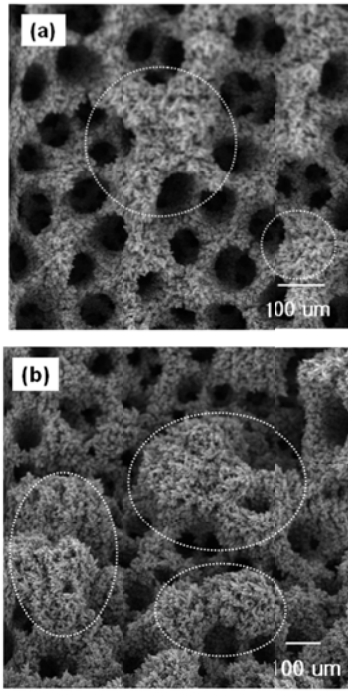

Figure 13. (a) Top view and (b) inclined view of copper foam structure electro-deposited for 90 s in the electrolyte containing 0.2 M acetic acid. Reprinted with permission from *Kor. J. Mater. Res.*, **18** (2008) 163. Copyright (2008) Materials Research Society of Korea.

foam walls develop in the local area with low concentration of acetic acid.

3. Control of Foam Wall Structure

While the 3-D foam structures are very attractive for rapid mass transport and fast electrochemical reactions, many issues still remain for their applications in practical batteries and fuel cells, in-

cluding controlling the size of the branches in the foam wall, the composition of the material, and the mechanical integrity of the porous structure.

A variety of additives have been studied to enhance the quality of the copper electro-deposits.[47-54] In particular, chloride-containing solutions, polyethylene glycol and bis-(3-sulfopropyl) disulfide (SPS), are known to help form void-free, seamless deposits. Among these, chloride ion is worthy of attention because a trace amount of it changes the electron transfer mechanism from outer-sphere reaction (water-water bridge) to inner sphere reaction (chloride bridge)[55] and then accelerates the copper reduction reaction.[55-58] The effect of chloride ion on the wall structure of 3-D copper deposits has been recently reported.[10] Shown in Fig. 14 is the morphological change of copper foam wall with the content of chloride ions in the electrolyte. It is noticeable that the wall structure became denser and the branch size was reduced to less than 50 nm with increasing chloride content. This indicates that the growth habit of copper branches of 3-D foam structure is tunable by addition of relevant ions to the deposition bath, yielding much smaller branch size and higher wall densities.

V. APPLICATIONS OF HIERARCHICAL POROUS STRUCTURES TO FUNCTIONAL ELECTROCHEMICAL DEVICES

1. Copper-Ceria Composite Anode for Solid Oxide Fuel Cell

The copper foam structure has been tested for construction of nano-composite anodes in solid oxide fuel cells. Shown in Fig. 15 are the cross-sectional views of SSC (Samarium Strontium Cobalt Oxide) | GDC (Gadolinium-doped Ceria) | copper foam for the application of copper foam structure to solid oxide fuel cells. The copper foam has been created on the GDC electrolyte covered with thin gold layer. Then, the copper-ceria composite has been prepared by the impregnation of Cu^{2+}/Ce^{3+} solution, followed by high-temperature firing. It is noted that the microstructure of copper-ceria composite was essentially the same as that of Cu foam in spite of the agglomeration of the copper branches in the foam wall during firing, as shown in Fig. 16.

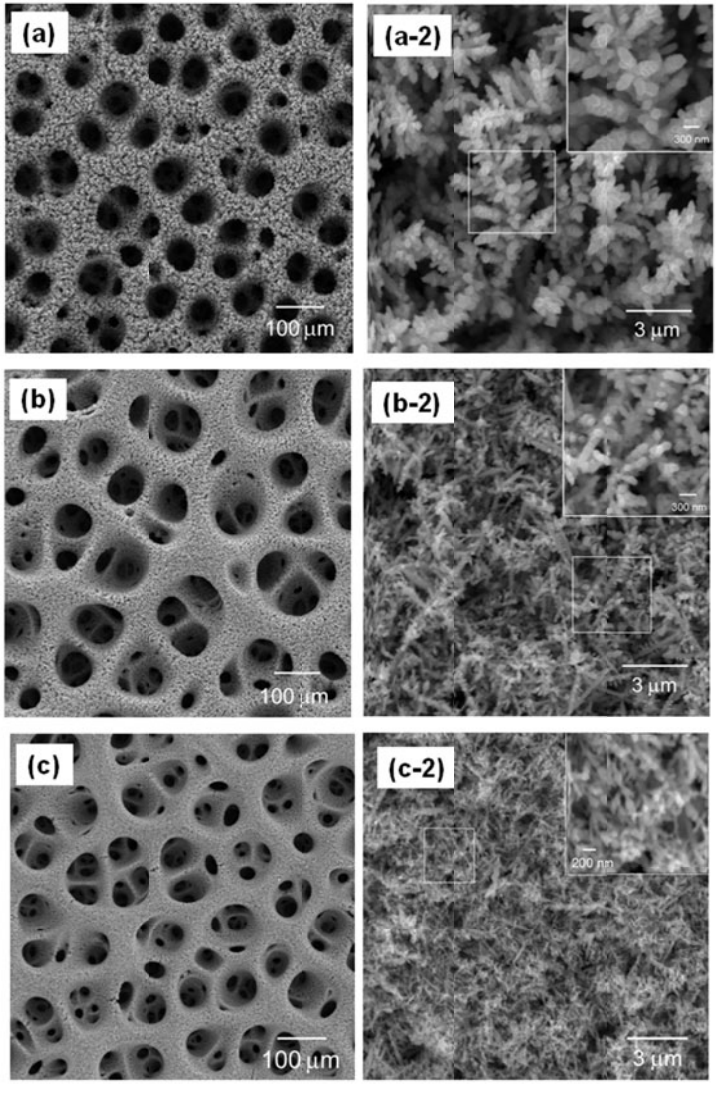

Figure 14. Change in wall structure of the foam with the content of chloride ions. (a) 0 M, (b) 10 mM, and (c) 50 mM HCl. (a-2), (b-2), and (c-2) are the magnified images of (a), (b), and (c), respectively. Reprinted with permission from *Chem. Mater.*, **16** (2004) 5460. Copyright (2004) American Chemical Society.

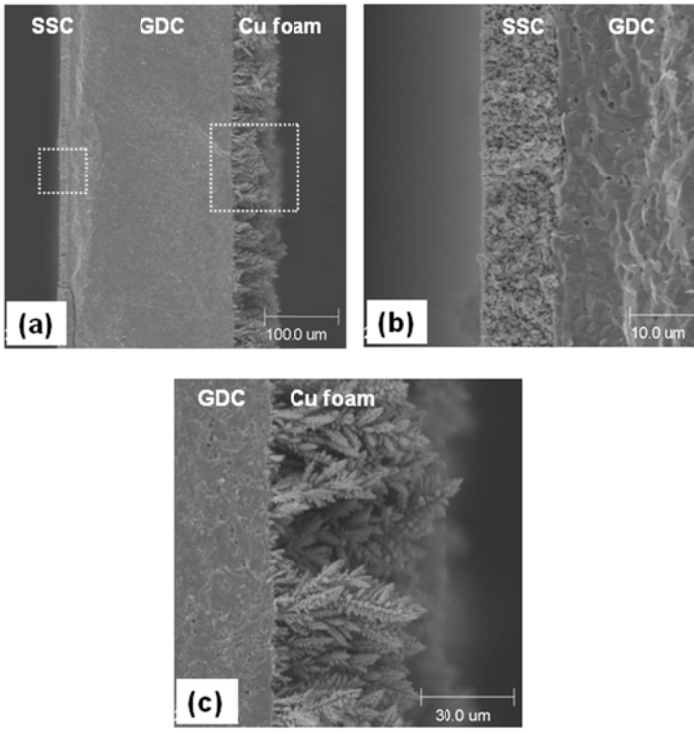

Figure 15. (a) Cross-sectional view of SSC (Samarium Strontium Cobalt Oxide) | GDC (Gadolinium-doped Ceria) | copper foam. (b) and (c) are the magnified images of SSC | GDC and GDC | copper foam, respectively.

Shown in Fig. 17 is the performance of the cell at different operating temperatures. Although the copper-ceria composite with foam structure functions well as the anode for fuel cell operation, the peak power density of 140 $mWcm^{-2}$ at 700°C can be significantly enhanced by improving the microstructure of the anode. It is suspected that, during firing of the copper foam impregnated with Ce^{3+}, the nano-sized branches agglomerate one another and highly-porous feature of the foam wall is seriously damaged and nearly disappeared, leading to significant reduction in pore size, porosity,

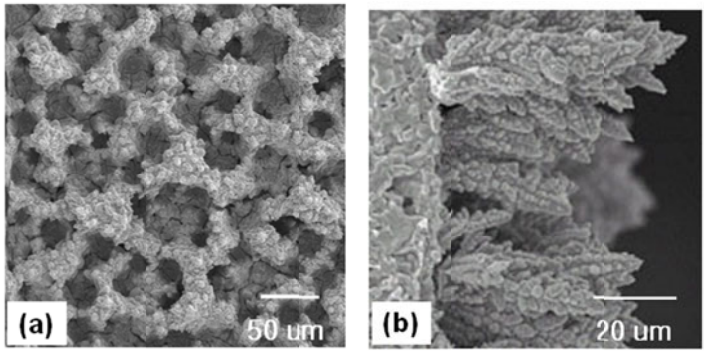

Figure 16. (a) Top and (b) cross-sectional views of copper-ceria composite created on GDC electrolyte.

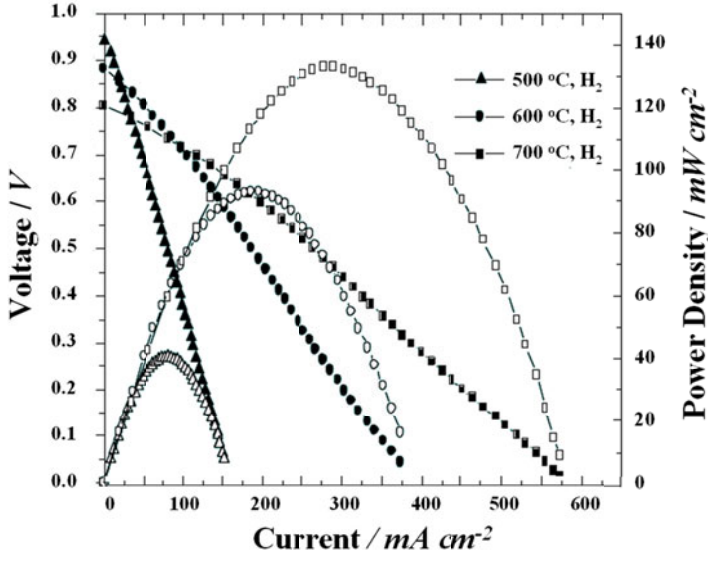

Figure 17. Fuel cell performance obtained from the SSC (anode) | GDC (electrolyte) | copper-ceria (anode) cell, shown in Fig. 15.

surface area, and the length of triple phase boundary (TPB) where electrode, electrolyte, and gas meet. To achieve high performance, it is imperative to develop a process for fabrication of copper foam-based electrode structures on an electrolyte substrate that can preserve the unique microstructure of the copper foam.

2. Tin and Copper-Tin Alloy for Lithium Ion Battery

Metal foam structure with highly-porous wall might find its best application in negative electrode for lithium ion batteries. While foam structure itself is quite beneficial to power density, the structure needs to be accompanied by active materials with high capacity, in order to maximize the battery performance. Tin is one of the most attractive candidates because it has much higher theoretical capacity (991 mA h/g) than graphite (372 mA h/g).[59-61] However, its poor cycling stability due primarily to large volume change during lithium alloying/dealloying process makes it impractical to use pure tin metal as electrode for rechargeable lithium batteries.[59] At this point, it would be interesting to test if the tin foam structure of Fig. 6 can effectively accommodate the volume changes associated with alloying/de-alloying to improve the stability during cycling.

Tin foam and lithium metal are used as the working and counter electrode, respectively. The electrolyte was a 1 M solution of $LiPF_6$ in a 50/50 (v/v) mixture of ethylene carbonate and diethyl carbonate. Figure 18 shows the initial capacity for lithium alloying reached as high as 750 mA h g^{-1}. Unfortunately, however, the capacity loss was unacceptably large with cycling (10%/cycle). While it is likely that the disintegration of tin metal itself due to drastic volume change is suppressed by the capability of the structure to accommodate the alloying/de-alloying-induced stress, the separation of the foam structure from the copper substrate during cycling seems to be critical to poor cycling stability. The strategy for reducing volume change of active material is still necessary to improve the cycling stability of tin-based electrode.

Sn-based intermetallic compounds are one of the most promising options to substitute tin metal. Typically, ductile metal is alloyed with tin to form Sn_xMe_y (Me: ductile metal such as copper,[34-37] nickel,[62-64] and iron[65,66]). While Sn in Sn_xMe_y is readily alloyed with lithium and volume is accordingly expanded, the ab-

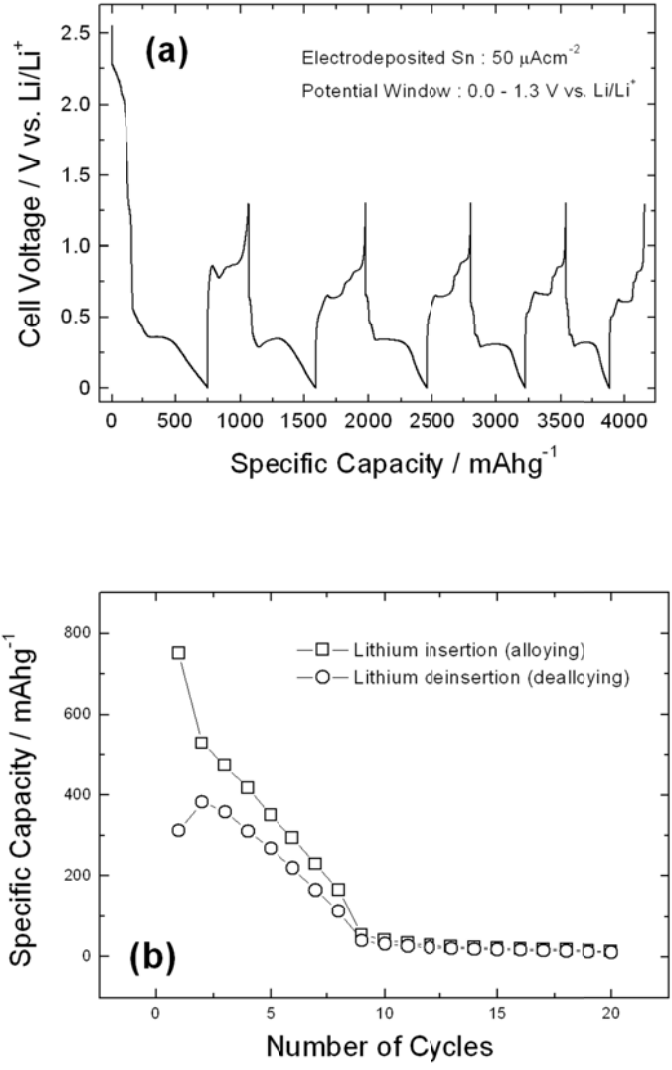

Figure 18. (a) Voltage profiles of the tin foam structure as a negative electrode for lithium ion battery, and (b) dependence of specific capacity on the number of cycles.

rupt volume change is effectively buffered by a soft inactive matrix, Me.[67,68] Since copper-tin alloy proved to readily form the 3-D porous foam structure, the performance of Sn_xCu_y alloy has been investigated. In particular, Cu_6Sn_5 intermetallic compound, envisaged in Fig. 8, has been chosen for the preliminary test.[11]

The capacity retentions of the porous Cu_6Sn_5 as a function of cycle number and discharge rate are shown in Fig. 19(a) and (b), respectively. It is noted that Cu_6Sn_5 foam structure reacts reversibly with lithium to deliver a specific capacity of about 400 mA h g^{-1} up to more than 30^{th} cycle, indicating the cycling stability is much improved as compared to pure tin. In addition, rate capability of Cu_6Sn_5 foam was quite encouraging: More than 50% of the capacity obtained at 1C rate can be delivered at an extremely high current drain of 20C rate.[11]

VI. CONCLUSIONS

One of the critical challenges in fabrication of highly efficient electrochemical energy storage and conversion devices is the preparation of 3-D hierarchical porous electrodes with proper pore size distribution, which promote the transport of electro-active species to (and products away from) the active reaction sites on the internal surfaces. The unique porous structures described in Sections III to V offer some possibility to the creation of unique electrode structures. However, many fundamental issues still remain. For example, while the large pores in the Cu_6Sn_5 foam shown in Figure 8 are great for rapid transport of electrolyte and lithium ions, they are too large to achieve the required volumetric capacity and power density. In addition, the small grains (with size of hundreds nanometers) and the agglomerates of these grains seen in the foam wall may not be best suited to endure the stresses and strains induced by volume changes during cycling. In Section IV, it has been suggested that the pore size was critically affected by the coalescence kinetics of hydrogen bubbles and the appropriate additive to reduce the hydrophobic force really makes smaller pores in the foam structure. The branch structure of foam wall was also tunable by modifying the growth habit of the electro-deposits. The effect of electrolyte additives on foam structure needs to be extensively investigated to further tailor the 3-D foam structure.

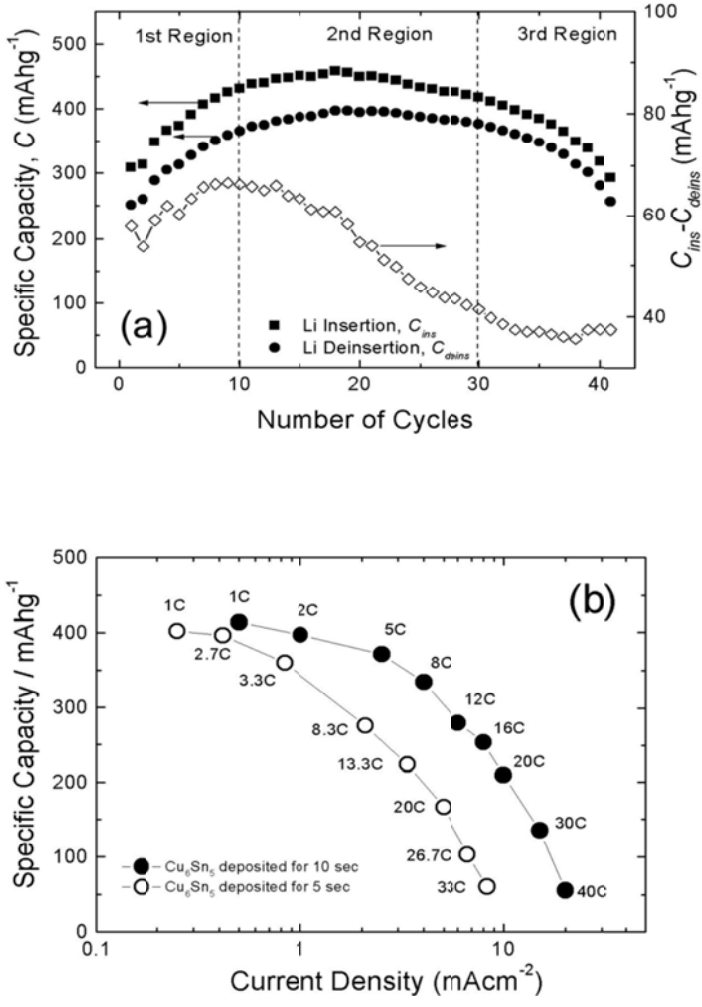

Figure 19. Capacity retentions of the porous Cu_6Sn_5 with (a) the number of cycles and (b) the discharging rate. Reprinted from H.-C. Shin and M. Liu, Three-Dimensional Porous Copper-Tin Alloy Electrodes for Rechargeable Lithium Batteries, *Adv. Funct. Mater.* **15** (2005) 582. Copyright (2005) with permission from Wiley-VCH Verlag GmbH & Co. KGaA.

Combination of foam structure with functional materials is another intriguing topic. Combination of porous metal with active materials used for sensors, fuel cells, and batteries are particularly promising. Exemplary composites include copper-ceria (for the anode in solid oxide fuel cells as suggested in Section V),[69,70] a variety of copper-tin alloys (for anode in rechargeable lithium batteries),[34-37] and copper-sulfur alloys or composites (for cathode in rechargeable lithium batteries.)[71-73] Exploration of hierarchical porous structures of other metals or alloys (in addition to copper, tin, and copper-tin alloys) would be quite challenging. The works might focus on the optimal combination of electrolyte composition, driving force (i.e., polarization) and other deposition parameters where the rates of metal deposition and gas evolution are comparable each other and at the same time, nucleation of metal deposits are extremely vigorous to create highly-branched or -particulated foam wall.

ACKNOWLEDGEMENTS

This work was supported by the Korea Research Foundation Grant funded by the Korean Government (MOEHRD) (KRF-2006-331-D00713). Incidentally, this work was partially supported by a grant-in-aid for the National Core Research Center Program from MOST and KOSEF (No. R15-2006-022-01001-0).

REFERENCES

[1] D. R. Rolison and B. Dunn, *J. Mater. Chem.* **11** (2001) 963.
[2] J. W. Long, R. M. Stroud, and D. R. Rolison, *J. Non-Cryst. Solids* **285** (2001) 288.
[3] J. W. Long, L. R. Qadir, R. M. Stroud, and D. R. Rolison, *J. Phys. Chem. B* **105** (2001) 8712.
[4] J. W. Long, C. P. Rhodes, A. L. Young, and D. R. Rolison, *Nano Letters* **3** (2003) 1155.
[5] J. S. Sakamoto and B. Dunn, *J. Mater. Chem.* **12** (2002) 2859.
[6] K. Kinoshita, X. Song, K. Kim, and M. Inaba, *J. Power Sources* **81/82** (1999) 170.
[7] S. Ranganathan, R. Mccreery, S. M. Majji, and M. Madou, *J. Electrochem. Soc.* **147** (2000) 277.
[8] Q. C. Horn, K. C. White, Y. S. Horn, and J. D. Lennhoff, *204th ECS Meeting*, Orlando, Florida, October 12-16, 2003.
[9] H.-C. Shin, J. Dong, and M. Liu, *Adv. Mater.* **15** (2003) 1610.

[10] H.-C. Shin and M. Liu, *Chem. Mater.* **16** (2004) 5460.
[11] H.-C. Shin and M. Liu, *Adv. Funct. Mater.* **15** (2005) 582.
[12] N. D. Nikolić, K. I. Popov, Lj. J. Pavlović, and M. G. Pavlović, *J. Electroanal. Chem.* **588** (2006) 88.
[13] N. D. Nikolić, K. I. Popov, Lj. J. Pavlović, and M. G. Pavlović, *Surf. Coatings Tech.* **201** (2006) 560.
[14] Y. Li, W.-Z. Jia, Y.-Y. Song, and X.-H. Xia, *Chem. Mater.* **19** (2007) 5758.
[15] T. Jiang, S. Zhang, X. Qiu, W. Zhu, and L. Chen, *Electrochem. Commun.* **9** (2007) 930.
[16] Y. Li, Y.-Y. Song, C. Yang, and X.-H. Xia, *Electrochem. Commun.* **9** (2007) 981.
[17] N. D. Nikolić, Lj. J. Pavlović, M. G. Pavlović, and K. I. Popov, *Electrochim. Acta* **52** (2007) 8096.
[18] T. Jiang, S. Zhang, X. Qiu, W. Zhu, and L. Chen, *J. Power Sources* **166** (2007) 503.
[19] N. D. Nikolić, K. I. Popov, Lj. J. Pavlović, and M. G. Pavlović, *J. Solid State Electrochem.* **11** (2007) 667.
[20] N. D. Nikolić, K. I. Popov, Lj. J. Pavlović, and M. G. Pavlović, *Sensors* **7** (2007) 1.
[21] K. M. Abraham, D. M. Pasquariello, and E. M. Willstaedt, *J. Electrochem. Soc.* **145** (1998) 482.
[22] B. E. Conway, *Electrochemical Supercapacitors: Scientific Fundamentals and Technological Applications*, Kluwer Academic/Plenum Publishers, New York, 1999, p.377.
[23] B. B. Mandelbrot, *The Fractal Geometry of Nature*, W.H.Freeman and Company, New York, 1983.
[24] J. Feder, *Fractals*, Plenum Press, New York, 1988.
[25] J. C. Russ, *Fractal Surfaces*, Plenum Press, New York, 1994.
[26] R. M. Brady and R. C. Ball, *Nature* **309** (1984) 225.
[27] I. Petersson and E. Ahlberg, *J. Electroanal. Chem.* **485** (2000) 166.
[28] B. Kim and T. Ritzdorf, *J. Electrochem. Soc.* **150** (2003) C53.
[29] T. A. Witten and L. M. Sander, *Phys. Rev. Lett.* **47** (1981) 1400.
[30] George T. T. Sheng, C. F. Hu, W. J. Choi, K. N. Tu, Y. Y. Bong, and L. Nguyen, *J. Appl. Phys.* **92** (2002) 64.
[31] D.-K.Kang, J.-H.Heo, and H.-C.Shin, *Kor. J. Mater. Res.* **18** (2008) 163.
[32] D. A.Jones, *Principles and Prevention of Corrosion*, 2nd ed., Prentice Hall, New Jersey, 1996.
[33] V. Fleury, *Nature* **390** (1997) 145.
[34] K. D. Kepler, J. T. Vaughey, and M. M. Thackeray, *Electrochem. Solid-State Lett.* **2** (1999) 307.
[35] G. X. Wang, L. Sun, D. H. Bradhurst, S. X. Dou, and H. K. Liu. *J. Alloys & Compounds* **299** (2000) L12.
[36] Y. Xia, T. Sakai, T. Fujieda, M. Wada, and H. Yoshinaga, *J. Electrochem. Soc.* **148** (2001) 471.
[37] S. D. Beattie and J. R. Dahn, *J. Electrochem. Soc.* **150** (2003) A894.
[38] V. S. J. Craig, B. W. Ninham, and R. M. Pashley, *J. Phys. Chem.* **97** (1993) 10197.
[39] V. S. J. Craig, B. W. Ninham, and R. M. Pashley, *Nature* **364** (1993) 317.
[40] L. A. Deschenes, J. Barrett, L. J. Muller, U. Mohanty, and J. T. Fourkas, *J. Phys. Chem. B* **101** (1997) 5777.

[41] L. A. Deschenes, J. Barrett, L. J. Muller, J. T. Fourkas, and U. Mohanty, *J. Phys. Chem. B* **102** (1998) 5115.
[42] U. Hofmeier, V. V. Yaminsky, and H. K. Christenson, *J. Colloid Interface Sci.* **174** (1995) 199.
[43] M. Paunovic and M. Schlesinger, *Fundamentals of Electrochemical Deposition*, 2nd ed., Wiley-Interscience, The Electrochemical Society (2006).
[44] J. H. White and H. D. Abruna, *J. Electroanal. Chem.* **300** (1991) 521.
[45] E. Herrero and H. D. Abruna, *Langmuir* **13** (1997) 4446.
[46] T. Fukuda and A. Aramata, *J. Electroanal. Chem.* **467** (1999) 112.
[47] J. J. Kelly and A. C. West, *Electrochem. Solid-State Lett.* **2** (1999) 561.
[48] J. J. Kelly, C. Y. Tian, and A. C. West, *J. Electrochem. Soc.* **146** (1999) 2540.
[49] T. P. Moffat, J. E. Bonevich, W. H. Huber, A. Stanishevsky, D. R. Kelly, G. R. Stafford, and D. Josell, *J. Electrochem. Soc.* **147** (2000) 4524.
[50] T. P. Moffat, D. Wheeler, W. H. Huber, and D. Jossel, *Electrochem. Solid-State Lett.* **4** (2001) C26.
[51] T. P. Moffat, D. Wheeler, C. Witt, and D. Jossel, *Electrochem. Solid-State Lett.* **5** (2002) C110.
[52] T. Kobatashi, J. Kawasaki, K. Mihara, and H. Honma, *Electrochim. Acta* **47** (2001) 85.
[53] P. Taephaisitphongse, Y. Cao, and A. C. West, *J. Electrochem. Soc.* **148** (2001) C492.
[54] W.-P. Dow, H.-S. Huang, and Z. Lin, *Electrochem. Solid-State Lett.* **6** (2003) C134.
[55] Z. Nagy, J. P. Blaudeau, N. C. Hung, L. A. Curtiss, and D. J. Zurawski, *J. Electrochem. Soc.* **142** (1995) L87.
[56] S. Rashkov and D. S. Stoichev, *Surf. Technol.* **6** (1978) 155.
[57] L. Bonou, M. Eyraud, R. Denoyel, and Y. Massiani, *Electrochim. Acta* **47** (2002) 4139.
[58] D. M. Soares, S. Wasle, K. G. Weil, and K. Doblhofer, *J. Electroanl.Chem.* **532** (2002) 353.
[59] I. A. Courtney and J. R. Dahn, *J. Electrochem. Soc.* **144** (1997) 2045.
[60] M. Winter and J. O. Besenhard, *Electrochim. Acta* **45** (1999) 31.
[61] R. A. Huggins, *J. Power Sources* **81/82** (1999) 13.
[62] G. M. Ehrlich, C. Durand, X. Chen, T. A. Hugener, F. Spiess, and S. L. Suib, *J. Electrochem. Soc.* **147** (2000) 886.
[63] H. Mukaido, T. Sumi, T. Yokoshima, T. Momma, and T. Osaka, *Electrochem. & Solid-State Lett.* **6** (2003) A218.
[64] Y.-L. Kim, H.-Y. Lee, S.-W. Jang, S.-J. Lee, H.-K. Baik, Y.-S. Yoon, Y.-S. Park, and S.-M. Lee, *Solid State Ionics* **160** (2003) 235.
[65] O. Mao, R. L. Turner, I. A. Courtney, B. D. Fredericksen, M. I. Buckett, L. J. Krause, and J. R. Dahn, *Electrochem. & Solid-State Lett.* **2** (1999) 3.
[66] O. Mao and J. R. Dahn, *J. Electrochem. Soc.* **146** (1999) 414.
[67] M. Winter and J. O. Besenhard, *Electrochim. Acta* **45** (1999) 31.
[68] J. Yang, M. Winter, and J. O. Besenhard, *Solid State Ionics* **90** (1996) 281.
[69] A. C. Tavares, B. L. Kuzin, S. M. Beresnev, N. M. Bogdanovich, E. Kh. Kurumchin, Y. A. Dubitsky, and A. Zaopo, *J. Power Sources* **183** (2008) 20.
[70] H. P. He, A. Wood, D. Steedman, and M. Tilleman, *Solid State Ionics* **179** (2008) 1478.
[71] J. L. Wang, J. Yang, J. Y. Xie, N. X. Xu, and Y. Li, *Electrochem. Commun.* **4** (2002) 499.

[72] J.-S. Chung and H.-J. Sohn, *J. Power Sources* **108** (2002) 226.
[73] J. L. Wang, J. Yang, C. R. Wan, K. Du, J. Y. Xie, and N. X. Xu, *Adv. Funct. Mater.* **13** (2003) 487.

Index

S.-I. Pyun and J.-W. Lee (eds.), *Progress in Corrosion Science and Engineering II*, Modern Aspects of Electrochemistry 47, DOI 10.1007/978-1-4419-5578-4,